Manufacturing, Modelling and Control of a High Speed Permanent Magnet Synchronous Machine including a Thermal Analysis

- Master's Thesis

DAN MØLGAARD MATHIASEN & NICOLAJ THOMAS OLESEN

DEPARTMENT OF MECHANICAL AND MANUFACTURING ENGINEERING

AALBORG UNIVERSITY - 2014

Department of Mechanical and Manufacturing Engineering
Fibigerstræde 16, DK - 9220 Aalborg East
Phone +45 99 40 93 09
lft@m-tech.aau.dk
www.ses.aau.dk

Title:
Manufacturing, Modelling and Control of a High Speed Permanent Magnet Synchronous Machine including a Thermal Analysis.

Semester theme: Master's Thesis
Semester: Third and fourth semester
Project period: 01/09-2013 - 03/06-2014
ECTS: 60

Supervisor:
Peter Omand Rasmussen
Project group:
EMSD4-2.221b

Dan Mølgaard Mathiasen

Nicolaj Thomas Olesen

Number printed: 2
Number of pages: 146
Number of appendixes: 4
Enclosures: CD

Synopsis:
This project concerns the development of a liquid cooled Permanent Magnet Synchronous Machine (PMSM). The application of the PMSM may result in heat problems which are investigated. High operational speed is required, which entails challenges with generation of sinusoidal voltages using a Voltage Source Inverter (VSI). Two prototypes of the PMSM are manufactured, where experiences from the first prototype are used to improve the second prototype.

A 3D thermal lumped parameter model is developed to estimate the temperatures in a thermal test scenario that replicates the operational conditions. Different compensation approaches are analysed to avoid over estimation of temperatures when distributed heat sources are modelled. An electrical and a mechanical model are used to design and test developed control strategies. The VSI is modelled to include the effect of pulse width modulated sinusoidal voltages.

The thermal model is compared to a 2D FEM model and experimental tests. The deviations are acceptable why temperatures in the thermal test scenario are estimated. The electrical models are verified against measured currents, which show acceptable correlation between the current characteristics. Simulations with designed controllers and the VSI show large current ripples and oscillations due to the high speed and a limited switching frequency.

Two issues are revealed during the manufacturing; the liquid cooling is leaky and the rotational losses are higher than expected. Further verification of the thermal model is required to ensure higher certainty of the about the model and estimated temperatures.

By signing this document, each member of the group confirms participation on equal terms in the process of writing the project. Thus, each member of the group is responsible for all the contents in the project.

PREFACE

The thesis is written by group EMSD4-2.221B during the third and fourth semester of the Master Programme in Electro-Mechanical System Design at the department of Mechanical and Manufacturing Engineering, Aalborg University. The thesis is a product of project research carried out in the period; September 1st 2013 to June 3rd 2014. The basic problem of the thesis is: *How to develop and operate a prototype of a high speed PMSM, which is applicable for a low pressure environment?*

Special thanks go to Lars Skovlund Andersen as a representative of Johnson Controls Inc. for his support and involvement in the project and to Tommy Frandsen for his input and feedback during the project. Thanks are also addressed to Skalform A/S and Dantrafo A/S for their support.

The reader should notice that the content of the thesis is not always in the chronological order, due to the simultaneous tasks and the time span of the project. Furthermore the number of involved collaborators results in knowledge gained by internal discussion and knowledge sharing, why some background knowledge is left out as the group cannot take credit for this work. Source references to internal sources or calculations are made when this is relevant.

The report is documented using LaTeX. Data analysis and calculations are carried out in Maple 16 and MATLAB 2012. An appendix CD is attached in the end of the thesis, which contains:

- A digital copy of the thesis
- Electrical and thermal models of the Permanent Magnet Synchronous Motor
- CAD drawings and pictures of the Permanent Magnet Synchronous Motor
- C code used to control the VSI
- Data sheets

Instructions for reading

Source references in the thesis are made according to the Institute of Electrical and Electronics Engineers (IEEE) citation style, with the bibliography placed after the conclusion on page 147. Titles, pictures, equations and tables are numbered. Pictures, equations and tables are in the format x.y, where x indicates the chapter number and y indicates the consecutive number. A nomenclature list is located after the table of contents. Some nomenclatures are assumed to be understood and accepted by the reader. These are: Time derivative $\dot{x}$, vector $\underline{x}$ and matrix $\underline{\underline{x}}$, with x being replaceable.

RESUME

Dette kandidat speciale omhandler udvikling og test af en Permanent Magnet (PM) motor. PM motoren skal anvendes i en ny type vanddampskompressor med individuelt drevne kompressorhjul. Formålet med projektet er at vurdere anvendeligheden af et forslået motor design, der bygger på et tidligere projekt udfærdiget på Aalborg Universitet. Anvendelsen i vanddampskompressoren betyder at PM motoren skal operere ved lavt tryk og høje temperaturer. For at imødegå de termiske udfordringer, der opstår heraf, implementeres et væskekølesystem i motor designet. Motorens operationshastighed er 15.000 omdr./min., hvilket medfører udfordringer i forbindelse med styringsstrategier og generering af en trefaset driftsspænding. Driftsspændingen generes af en frekvensomformer der anvender pulsbreddemodulation til styring af transistorerne i vekselretteren. Udfordringen ligger i at den høje hastighed kræver en driftsspænding med høj grundtonefrekvens, hvilket kræver en høj switchfrekvens i frekvensomformeren for at mindske forvrængningen i den genererede driftsspænding. En høj switchfrekvens er ikke ønskværdig da det medfører forhøjede tab i frekvensomformeren. Dermed skal switchfrekvensen vælges som et kompromis mellem grundtone forvrængning og tab i frekvensomformeren.

To prototyper fremstilles med formålet at teste motor design og egenskaber. Fremstillingen inkluderer samling, vikling og indstøbning af statoren i EPOXY baseret syntetisk harpiks. Den syntetiske harpiks har til formål dels at forbedre den termiske ledeevne i motoren og derudover at forsegle kølesystemet. Fremstillingen af den første prototype viser at indstøbningsprocessen ikke er i stand til at forsegle kølesystemet. Utæthederne forsøges fjernet, men uden held, hvilket udelukker testkørsel med væskekølesystemet. På trods af det utætte væskekølesystem samles den første prototype og det lykkes at køre den op til de ønskede 15.000 omdr./min. Baseret på erfaringerne fra den første prototype opstilles forbedringsforslag til den anden prototype, hvilket bl.a. indebærer at indstøbningsprocessen udføres under vakuum og dele af væskekølesystemet redesignes. Vakuumindstøbningsprocessen forbedrer forseglingen af kølesystemet, men ikke tilstrækkeligt til at prototypen kan samles og testes med væskekølesystem. Yderligere forbedringer forslås, men disse eftervises ikke.

En termisk model af PM motoren opstilles med formålet at forudsige varmefordelingen og temperaturene i motoren under drift. Et termisk test scenarie der repræsenterer det forventede driftsmiljø i vanddampskompressoren opstilles. En 3D termisk koncentreret tabs model opsættes. Metoden udvælges på baggrund af metodens udbredte anvendelighed indenfor termisk modellering af elmotorer og simplicitet. Det findes nødvendigt at undersøge og implementere forskellige kompenseringsteknikker for at undgå overestimering af temperaturene i forbindelse med tildeling af fordelte tab i den koncentrerede tabs model. Den termiske model verificeres ud fra sammenligninger med en 2D FEM model og målte data.

Input parametrene i det termiske test scenarie bestemmes fra eksperimentelle målinger af tabene på den første prototype. De målte tab er højere end forventet, hvilket kan skyldes at syntetisk harpiks på rotor og stator lamineringerne blev fjernet i en drejebænk. I drejebænken tog lamineringerne skade, hvilket formentlig resulterer i højere jerntab. Simuleringerne baseret på de målte tab viser at temperaturene i motoren ikke kan holdes tilstrækkeligt nede i det termiske test scenarie. Derfor udføres simuleringer med de forventede tab, hvorved temperaturene reduceres til et acceptabelt niveau.

En elektrisk model udvikles for at teste og designe kontrol strategier og vurdere motorens respons under forskellige driftsbetingelser. Modellen anvendes bl.a. til at teste motoren med last, hvilket ikke er muligt at teste eksperimentelt da en lastmekanisme ikke er udviklet. Den elektriske model opbygges af spændingsligninger i et roterende dq-reference koordinatsystem og det mekaniske system modelleres som et modvirkende momentbidrag. Problemstillingen omkring den høje operationshastighed kombineret med en begrænset switchfrekvens af frekvensomformeren er grundlaget for at inkludere frekvensomformeren i den elektriske model. Frekvensomformeren implementeres sammen med den valgte rumvektorpulsbreddemodulationsstrategi, for at se effekterne af et lavt antal pulser per omgang. Parametrene for den elektriske og mekaniske model af motoren bestemmes eksperimentelt og parametrene bruges til at verificere modellerne op mod målte data. Verifikationen begrænses af manglende positions sensor og adgang til fase-nul spændingsmålinger, men god overensstemmelse ses på trods af dette mellem de målte og simulerede strømkarakteristikker.

For at omgå den indbyggede styring i frekvensomformeren udvikles to kontrol strategier. En lukket sløjfe kaskade regulator designes men implementeres ikke i forsøgsopstillingen grundet nedprioritering. Det elektriske og mekaniske system lineariseres for at udvikle en hastigheds- og strømregulator. Strømregulatorens formål er at minimere strømmen og dermed tabet i motoren. En åben sløjfe spændingsstyring udvikles på baggrund af den elektriske og mekaniske model og denne styring eftervises i forsøgsopstillingen. Både målte og simulerede resultater viser oscillationer i strømme og hastighed. Simuleringer viser at årsagen til oscillationerne stammer fra åben løkke strukturen, den ubelastede motor og switchfrekvensen. Det konkluderes at en switchfrekvens på 10 kHz er nødvendig for at begrænse oscillationer og strøm-rippler.

CONTENTS

NOMENCLATURE

Parameter	Description	Unit
a	Complex rotation operator	$[-]$
A	Area	$[m^2]$
a_{cent}	Centripetal acceleration	$[m/s^2]$
A_{cond}	Cross sectional area of conductors	$[m^2]$
A_{rotor}	Required outer area of the rotor	$[m^2]$
a,b,c,d,e	Velocity coefficients	$[-]$
A,B,C,D,O	Geometric points	$[-]$
B	Flux density	$[T]$
B_m	Linearised rotational torque constant (viscous friction)	$[Nm/(rad/s)]$
B_{max}	Peak flux density	$[T]$
d_b	Average bearing diameter	$[m]$
d_{cond}	Diameter of conductor	$[m]$
D_i	Duty cycle	$[-]$
$E_{back-emf,LL}$	Back electromotive force, line-to-line	$[V]$
$E_{back-emf,LN}$	Back electromotive force, line-to-neutral	$[V]$
f_{app}	Frequency of applied voltage	$[Hz]$
f_{BW}	Bandwidth	$[Hz]$
f_s	Sample frequency	$[Hz]$
f_{sw}	Switching frequency	$[Hz]$
$G_{c,i}$	Contoller	$[-]$
G_i	Transfer function	$[-]$
$G_{p,i}$	Transfer function of plant	$[-]$
h	Height	$[m]$
h_{conv}	Thermal heat transfer coefficient from convection	$[W/(m^2\ K)]$
h_{rad}	Thermal heat transfer coefficient from radiation	$[W/(m^2\ K)]$
$h_{rad,cyl}$	Thermal heat transfer coefficient from radiation between two concentric cylinders	$[W/(m^2\ K)]$

$h_{rad,plane}$	Thermal heat transfer coefficient from radiation between two planes	$[W/(m^2\ K)]$
h_{step}	Change in x	$[-]$
i_i	Current	$[A]$
$I_{nom,RMS}$	Nominal current	$[A]$
j	Complex operator	$[-]$
J	Moment of inertia	$[kg\ m^2]$
J_{cd}	Current density	$[A/m^2]$
k_{air}	Thermal conductivity of air	$[W/(m\ K)]$
K_{bear}	Bearing loss coefficient	$[Nm/(rad/s)^{(2/3)}]$
$K_{c,in}$	Gain of inner controller	$[-]$
$K_{c,out}$	Gain of outer controller	$[-]$
K_{df}	Dry friction loss coefficient	$[Nm]$
K_e	Eddy current loss coefficient	$[Nm/(T^2\ rad/s)]$
K_h	Hysteresis loss coefficient	$[Nm/T^n]$
k_i	PMSM quantity (e.g current, voltage)	$[-]$
K_i	Opposing rotational torque coefficients	$[-]$
K_i	Integral gain	$[-]$
$k_{insulation}$	Thermal conductivity of insulation plastic	$[W/(m\ K)]$
$K_{l,i}$	Load torque coefficients	$[-]$
K_p	Proportional gain	$[-]$
k_{resin}	Thermal conductivity of resin	$[W/(m\ K)]$
k_{th}	Thermal conductivity	$[W/(m\ K)]$
$k_{th,cont}$	Conductivity though contact element	$[W/(m\ K)]$
K_{vis}	Viscous friction loss coefficient	$[Nm/(rad/s)]$
K_{win}	Windage loss coefficient	$[Nm/(rad/s)^2]$
L	Inductance	$[H]$
L_A	Magnetisation inductance	$[H]$
l_{avg}	Average length of one turn	$[m]$
l_{cond}	Length of conductors	$[m]$
l_{ew}	Length of end windings	$[m]$
l_i	Length	$[m]$
L_{ii}	Self inductance	$[H]$
L_{ls}	Leakage inductance	$[H]$
L_m	Mutual inductance	$[H]$
L_{mdq}	Magnetisation inductance	$[H]$
l_{slot}	Slot length	$[m]$
l_{sw}	Length of slot windings	$[m]$
m	Number of samples	$[-]$
n	Material constant (n=1.5-2.5)	$[-]$
N	Number of winding turns	$[-]$
n_i	Distribution of power losses	$[-]$
n_{tri}	Triangular carrier wave	$[-]$
P_{active}	Active power	$[W]$
$P_{apparent}$	Apparent power	$[V\ A]$
p_b	Number of poles	$[-]$
P_{conv}	Heat flow through convection	$[W]$

P_{core}	Core loss	$[W]$
P_{cu}	Copper loss	$[W]$
P_e	Instantaneous power	$[W]$
P_{eddy}	Power loss due to eddy currents	$[W]$
P_{em}	Electro-magnetic power	$[W]$
P_{ew}	Power loss in end windings	$[W]$
P_{hys}	Power loss due to hysteresis	$[W]$
P_{sw}	Power loss in slot windings	$[W]$
P_{PM}	Losses in PMs	$[W]$
P_{rad}	Heat flow through radiation	$[W]$
$P_{rad,plane}$	Heat flow between two planes through radiation	$[W]$
$P_{rad,cyl}$	Heat flow between two concentric cylinders through radiation	$[W]$
$P_{reactive}$	Reactive power	$[var]$
P_{rot}	Rotational power loss	$[W]$
P_{Rotor}	Losses in rotor	$[W]$
P_{Stator}	Losses in stator	$[W]$
q_i	PWM control signal for the IGBTs	$[-]$
q_{th}	Heat generation	$[W/m^3]$
$R_{eq,i}$	Equivalent resistance	$[\Omega]$
r_i	Radius	$[m]$
$R_{s,theo}$	Theoretical calculated resistance	$[\Omega]$
R_s	Resistance of windings	$[\Omega]$
$R_{s,avg}$	Average phase resistance	$[\Omega]$
$R_{s,T}$	Phase resistance at temperature T	$[\Omega]$
R_{th}	Thermal resistance	$[K/W]$
$R_{th,A}$	Axial thermal resistance	$[K/W]$
$R_{th,C}$	Circumferential thermal resistance	$[K/W]$
$R_{th,cont}$	Thermal contact resistance	$[K/W]$
$R_{th,conv}$	Thermal convection resistance	$[K/W]$
$R_{th,cool}$	Thermal coolant resistance	$[K/W]$
$R_{th,R}$	Radial thermal resistance	$[K/W]$
$R_{th,rad}$	Thermal radiation resistance	$[K/W]$
s	Laplace frequency operator	$[1/s]$
SD	Standard deviation	$[°C]$
T_{comp}	Temperature compensation block	$[K]$
t_{eq}	Effective gap length	$[m]$
T_i	Temperature	$[°C]$
T_i	Temperature	$[K]$
$t_{insulation}$	Thickness of insulation	$[m]$
T_s	Sample time	$[s]$
u_{dc}	DC link voltage	$[V]$
U_{DC}	DC voltage	$[V]$
U_i	Voltage vector	$[V]$
u_{in}	Phase voltage	$[V]$
U_s	Space vector	$[V]$
W_{coil}	Average coil width	$[m]$

x	Position in element	$[m]$
$\bar{x}$	Estimated temperature from FEMM model	$[°C]$
x_i	Estimated temperature from LP model	$[°C]$
X_i	Reactance	$[\Omega]$
x, y, z	Variables	$[-]$
x_0, y_0, z_0	Linearisation point of variables	$[-]$
z	Discrete operator	$[-]$
Z_i	Impedance	$[\Omega]$
	GREEK	
ε	Emissivity of the surface	$[-]$
θ	Angle	$[rad]$
θ_l	Reminding angle of space vector after $\pi/3$ division	$[rad]$
θ_{re}	Electric angle	$[rad]$
θ_s	Angle of space vector	$[rad]$
μ_{cu}	Permeability of copper	$[\Omega\ (s/m)]$
σ_{cu}	Conductivity of copper (57x10e6)	$[S/m]$
σ_{SB}	Stefan-Boltzmann constant (5.67x10e-8)	$[W/(m^2\ K^4)]$
ω_{app}	Frequency of applied voltage	$[rad/s]$
ω_{dc}	Angular velocity of DC motor	$[rad/s]$
ω_{re}	Electric velocity	$[rad/s]$
ω_{rm}	Mechanical angular velocity	$[rad/s]$
δ_{cond}	Skin depth of conductors	$[m]$
λ_{pm}	Permanent magnet flux linkage	$[Wb]$
ν	Temperature dependence coefficient	$[1/K]$
τ_{bear}	Opposing torque due to bearing loss	$[Nm]$
τ_{eddy}	Opposing torque due to eddy currents	$[Nm]$
τ_{em}	Electro-magnetic torque	$[Nm]$
τ_{hys}	Opposing torque due to hysteresis	$[Nm]$
τ_{load}	Load torque	$[Nm]$
τ_{res}	Resulting torque	$[Nm]$
τ_{rot}	Opposing torque due to rotational loss	$[Nm]$
$\tau_{t,el}$	Time constant of electric system	$[s]$
$\tau_{t,m}$	Time constant of mechanical system	$[s]$
τ_{win}	Opposing torque due to windage	$[Nm]$
ϕ	Angle	$[rad]$
Ψ_i	Flux linkage	$[Wb]$
$\mathcal{L}$	Laplace transformation	$[-]$
	SUBSCRIPTS	
A, B, C	Phases	$[-]$
A, R, C	Axial, Radial or Circumferential direction	$[-]$
CL	Closed loop	$[-]$
$conv$	Convection	$[-]$
d	Direct axis of rotating reference frame	$[-]$

dq	Rotating reference frame	[−]
liq	Liquid	[−]
LL	Line-to-Line voltage	[−]
LN	Line-to-Neutral voltage	[−]
n	Phase voltage	[−]
OL	Open loop	[−]
q	Quadrature axis of rotating reference frame	[−]
rad	Radiation	[−]
RMS	Root mean square value	[−]
α	Real axis of stationary reference frame	[−]
$\alpha\beta$	Stationary reference frame	[−]
β	Imaginary axis of stationary reference frame	[−]

CHAPTER

1 INTRODUCTION

This project originates from an ongoing Energy Technology Development and Demonstration Program (EUDP) supported project regarding development of a water vapour chiller with an axial compressor. Such a chiller is shown in figure 1.1. The water vapour chiller has a large potential in the fast growing market for chillers [1], as it is applicable for industrial cooling systems and air conditioning of buildings. A feasibility study was performed in [2] by the Danish Technological Institute, which made the foundation for two demonstration projects in Denmark.

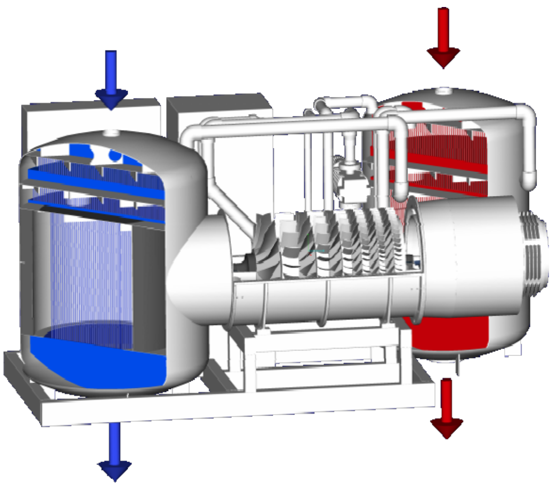

Figure 1.1: The second generation of chiller from the EUDP project [3].

The EUDP supported project aims to develop a cost-competitive and environmentally friendly chiller for the expanding global marked for chillers [1]. The EUDP project has run for two generations. The second generation is shown in figure 1.1 where the axial compressor is shown with six stages and the motor that runs the compressor is placed to the right.

The enhanced focus on the environment and global warming tightens the requirements for the refrigerant in today's chillers, why earlier refrigerants, such as ChloroFluoroCarbons (CFCs), have been replaced by HydroFluoroCarbon (HFC) and natural refrigerants e.g. ammonia [2]. A more attractive alternative to HFCs and ammonia is to use water, as water is non-toxic and non-flammable. Water also has a Global Warming Potential (GWP) of zero and an Ozone Depletion Potential (ODP) of zero. These considerations are the encouragement behind the development of a water vapour chiller.

A drawback of using water as refrigerant is the specific volume is very large at low pressure [2], why the compressor must handle a large amount of gas, up to 100 m^3/s in the feasibility study [2]. The axial compressor is suitable for applications, which require handling of a large amount of gas, as an axial compressor has greater capacity compared to a centrifugal compressor of the same outer diameter [4]. A sketch of a three stage axial compressor is shown in figure 1.2.

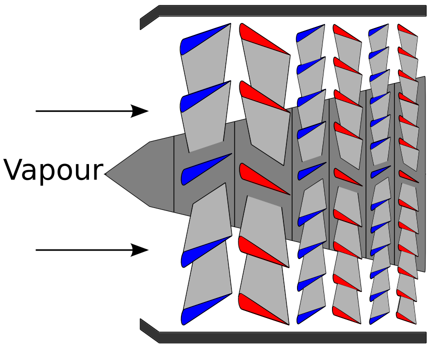

Figure 1.2: An axial three stage compressor.

In figure 1.2 the blue impellers indicates the rotating impellers and the red impellers indicate non-rotating impellers. Each stage first accelerates the water vapour by the rotating impeller after which the kinetic energy is converted to pressure by the stationary impeller. The number of stages increases the pressure ratio [2].

Figure 1.3 and 1.4 show the principle of chillers. The temperatures and pressures in figure 1.4 correspond to the feasibility study in [2]. A typical chiller consists of four main components, as shown in figure 1.3; an expansion valve, an evaporator, a compressor and a condenser. The expansion valve converts High Temperature and Pressure (HTP) liquid to a Low Temperature and Pressure (LTP) liquid. The LTP liquid enters the evaporator, which converts it to a LTP vapour by absorbing heat from the environment, which means the environment is cooled. The LTP vapour is converted to a HTP vapour in the compressor after which the HTP vapour enters the condenser, where the HTP vapour is converted to a HTP liquid. In the condenser, heat is emitted from the chiller. The HTP liquid enters the expansion valve once more and the cycle starts over.

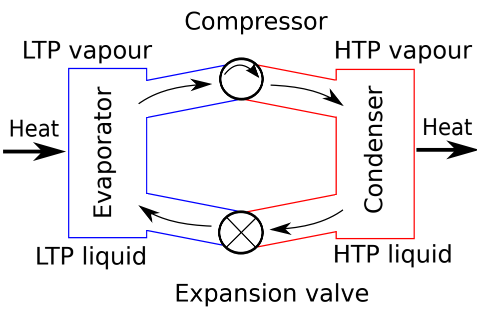

Figure 1.3: Chiller refrigerant cycle.

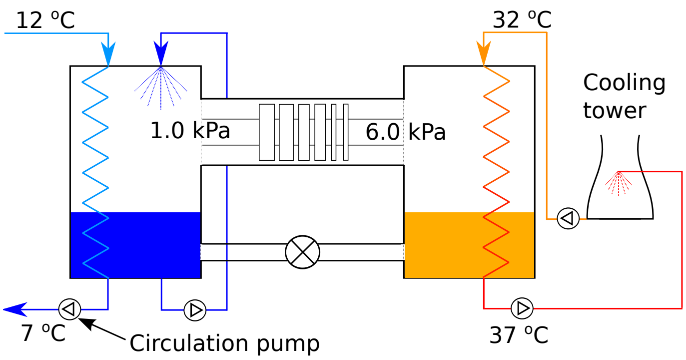

Figure 1.4: Chiller system with indirect heat exchanger [4].

This report concerns the third generation of the water vapour chiller, where a motor is placed within each rotating impeller of the compressor and each stage is individual driven. To accomplish this concept a hub motor with exterior rotor is proposed. The stator of the hub motor is mounted on a through-going stationary shaft and the impeller is mounted on the rotor of the hub motor. Aalborg University (AAU) has had a project regarding development and implementation of a 64 kW hub motor in an electrical vehicle. The proposed motor for the third generation water vapour chiller utilise the same topology as the hub motor used for the electrical vehicle, which is presented in [5]. The hub motor is a Permanent Magnet Synchronous Machine (PMSM) with interior rotor magnets and for this project a downscaled version of the electrical vehicle PMSM is used. Johnson Controls Denmark supports the development and manufacturing of the PMSM for the third generation water vapour chillers.

Scope of the project

The scope of this project is to investigate the applicability of a redesigned PMSM from a former AAU project to be used for the third generation of water vapour chillers.

1.1 Problem analysis

The challenges regarding development and implementation of the hub motor in the water vapour chiller are investigated in this section. The primary challenges are connected to the low pressure environment and the high speed of the compressor.

1.1.1 Operational conditions

The operational conditions for the PMSM are described, which is necessary to assess if the PMSM is applicable in the water vapour chiller.

Compressors in chillers often operate at the same operational speed for longer periods, where the load changes slowly and the dynamics of the system to be cooled are much slower than the dynamics of the PMSM. However the PMSM must be able to operate at various velocities as this is required in the chiller. The PMSM is designed without gears in order to make the PMSM compact. The compressor is intended to run at a maximum speed of 15000 rpm most of the time, which classifies the motor as a high speed motor. High speed motors have the advantage of a high power density, but the operation of high speed motors results in challenges that are not pronounced at lower speeds, e.g. in connection with PWM modulation and control. The load characteristic is similar to a typical fan characteristic where the load is a cubic function of the rotational speed. At maximum speed, the load is 16 Nm.

Operation environment

The expected temperatures and pressures of the operation environment in the axial compressor are stated in table 1.1. The stated temperatures and pressures are of the water vapour, why the temperatures are not a directly applied to the PMSM.

If the PMSM overheats, the efficiency decreases, the insulation of the inductors might melt and the permanent magnets might demagnetize, why the ability to emit and transfer heat is of interest. Heat transfer between two mediums is divided into the following three mechanisms [7] [8]:

- Conduction: Heat transfer within a solid element due to a temperature difference
- Convection: Heat transfer between a solid and a fluid due to motion of the fluid
  - Natural convection is movement of a fluid from density variation

  - Forced convection is movement of a fluid using an external force (e.g a fan)
- Radiation: Heat transfer by electromagnetic waves

Location	**Pressure** [**kPa**]	**Temperature** [°**C**]
Inlet / Stage 1	0.92	8
Stage 1 / Stage 2	1.31	38
Stage 2 / Stage 3	1.81	68
Stage 3 / Stage 4	2.48	98
Stage 4 / Stage 5	3.35	128
Stage 5 / Stage 6	4.48	158
Stage 6 / Outlet	5.93	188

Table 1.1: Temperature and pressure of the water vapour [6].

Forced convection is often the primary heat transfer mechanism in electric motors. Heat transfer coefficients describe how well heat is transferred by heat transfer mechanisms. Some of the common heat transfer coefficients, in connection with electrical motors, are listed in table 1.2.

Heat transfer mechanism	**Coefficient** $[\mathbf{W/(m^2\ K)}]$
Air - Natural convection	5 - 10
Air - Forced convection	10 - 300
Liquid - Forced Convection	50 - 20000
Radiation	0.01-8

Table 1.2: Heat transfer coefficients by rule of thumb [9] .

Based on the PMSM used in the electrical vehicle presented in [5], the rotational loss is estimated to 750 W and the resistive loss is estimated to 250 W in the downscaled PMSM [10]. These losses are to be removed by the aforementioned heat transfer mechanisms. At low pressure, the heat transfer coefficient for convection through air is lowered significantly. Assumed that the coefficient for forced convection is 10 $W/(m^2\ K)$, which is conservative, the temperature of the rotor is $110°C$ and the ambient temperature is $50°C$, the necessary area to remove the generated heat through the rotor by forced convection is given by:

$$A_{rotor} = \frac{1000\ W}{10\ W/(m^2\ K)\ 60\ K} = 1.7\ m^2 \tag{1.1}$$

Where in equation (1.1):

A_{rotor}	Required outer area of the rotor, $[m^2]$

From a CAD drawing of the PMSM, the outer area of the rotor is measured to be less than 0.1 m^2 and therefore liquid cooling must be incorporated to improve the amount of cooling and reduce the risk of overheating. However further investigation must be performed to determine if the liquid cooling is able to keep the PMSM from overheating.

1.1.2 Voltage source inverter

A Voltage Source Inverter (VSI) must be used for start-up and speed control of the PMSM. A VSI outputs three phase controllable voltages of desired amplitude and frequency. Challenges arise due to the use of a VSI along with a high speed motor. Inverters utilise Pulse Width Modulation (PWM) where switches control the output voltage. A higher switching frequency yields a better modulation of the AC voltages but a high switching frequency also results in increased switching losses in the inverter and faster demolition of the switches. To reduce the switching losses and prolong the life span of the inverter, it is desirable to have a low switching frequency. The request of a low switching frequency causes only a few switches per revolution. To run 15000 rpm with an 8 pole PMSM, the modulated AC voltage must have a frequency of:

$$\begin{aligned} f_{app} &= 15000\,rpm\,\frac{p_b}{2} \\ &= 1000\,Hz \end{aligned} \tag{1.2}$$

Where in equation 1.2:

f_{app}	Frequency of applied voltage, $[Hz]$
p_b	Number of poles, $[-]$

Consequently, if the switching frequency is limited to 5 kHz, there are only 5 switches per revolution at maximum speed. The effect of the switching phenomena (e.g. current ripples) plays an important role due to the low number of switches. The VSI must therefore be included in the analysis to investigate the influence of few switches per revolution.

1.1.3 Sensor-less control

It is not desirable to attach an encoder, why a sensor-less control method must be applied when the PMSM is implemented in the chiller. The sensor-less controller estimates the position of the rotor from currents and voltages measurements. By eliminating the encoder the system has better reliability and it is less prone to failures as failure of the encoder is avoided.

The rotor position is a crucial part of today's vector based control algorithms for PMSMs to ensure maxi- mum torque and reduce current in the PMSM, which is desirable to reduce the heat generation. A problem of using a position estimator, which uses current and voltage measurements, is the need for a current and voltage to calculate the position, why the estimator might not work from stand still and in the low velocity range.

CHAPTER

2 PROBLEM STATEMENT

The purpose of this project is to operate a PMSM for a water vapour chiller using a VSI. The PMSM is supposed to operate at 15000 *rpm*, delivering 16 *Nm*, in a low pressure environment. The low pressure environment rises potential heat problems in the PMSM, which must be investigated. To reduce losses and operate the PMSM at 15000 *rpm*, control strategies for the PMSM and VSI are developed and tested. This leads to the problem statement:

How to develop and operate a prototype of a high speed PMSM, which is applicable for a low pressure environment?

2.1 Technical solution

The solution to the problem statement is divided into three main topics; *System description and manufacturing*, *Modelling* and *Control*, which are elaborated in the following sections. At the beginning of this project, the design and CAD drawings of the PMSM parts are available.

2.1.1 System description and manufacturing

The content of this part includes:

- Description of the hardware set-up.
- Presentation of the PMSM.
- Description and analysis of the manufacturing process.

Two prototypes of the PMSM are manufactured. The first prototype is manufactured to gain experience, which is used to improve the second prototype.

2.1.2 Modelling

Three models are developed; an electrical model of the PMSM, an electrical model of the VSI and a thermal model of the PMSM. The models are developed to gain insight in both electrical and thermal aspects of the PMSM, when it is operated at high speed in a low pressure environment.

Electrical models of the PMSM and VSI

The electrical models are developed to obtain the characteristics of the PMSM and VSI. The VSI is modelled to include the effect of the low number of switches per revolution. The electrical models are used to test how the PMSM responds to control strategies. Development of the models involve:

- Modelling of the PMSM
- Modelling of the VSI
- Parameter determination
- Experimental verification

Thermal model of the PMSM

The thermal model is developed to understand and predict the heat distribution and temperatures in the PMSM at different operation conditions. The development of a thermal model involves:

- Investigation of the PMSM power losses
- Determination and modelling of power losses in the PMSM
- Choice of thermal modelling approach
- Experimental verification of model

2.1.3 Control

Two control strategies are developed; a PMSM controller and a PWM strategy. The PMSM controller is used to control the frequency and amplitude of the voltages. The PWM signals are used to control the switches in the VSI directly and thereby gain control over the output of the VSI. Development of the controllers involve:

- Development of PWM strategy
- Implementation of PWM strategy
- Design of PMSM controller
- Test of PMSM controller

2.2 Demarcation

The main focus of the project is to manufacture, model and control the PMSM, why the following demarcations are made:

- The design of the PMSM including the liquid cooling system is predetermined.

- The project only concerns the PMSM and therefore it does not concern or include the chiller system.
- Design and tests of load mechanism. This means all tests are performed at no-load.
- Sensor-less control strategies are not investigated and implementation of the PMSM controller is omitted.

The PMSM controller is not implemented, as it has been prioritised to manufacture and analyse the prototypes of the PMSM rather than implementing a well-documented control strategy. Instead the PMSM controller is tested in the electrical model of the PMSM and VSI to analyse the effect of current ripples on the PMSM controller.

2.3 Thermal test scenario

It is chosen to specify a test scenario as a basis for the thermal analysis of the PMSM as it is not expected that the PMSM is able to operate in the entire range of temperatures from table 1.1. A solution to emit the heat from the impellers must be found to limit the temperature influence from the impellers, but this is considered to be out of the scope of this project cf. the demarcation. It is assessed that the ambient temperature may not exceed $50°C$, to keep the temperatures of the PMSM within an acceptable level. The allowable temperatures of the critical parts are described further in chapter 3. The pressure is set to 2.5 kPa, which corresponds to the pressure between stage 3 and 4. In the test scenario the PMSM is free-standing as shown in figure 2.1 which is chosen as the details about the mounting in the impellers are not specified. In the compressor the impeller is mounted on the rotor which influences the temperatures and heat flow, but this implementation is not further examined as mentioned earlier. The PMSM operates at 15000 rpm and delivers the rated 16 Nm in the thermal test scenario.

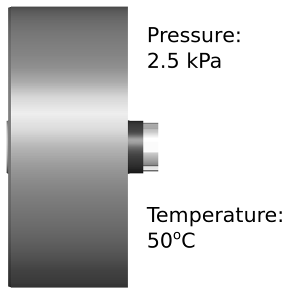

Figure 2.1: Thermal test scenario for the PMSM.

CHAPTER

3 SYSTEM DESCRIPTION

This chapter provides an overview of the system set-up. The system is divided into six overall components as shown in figure 3.1, where the blue lines indicate low voltage signals and the red lines high voltage power lines.

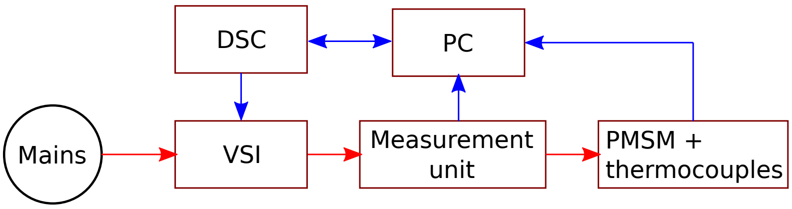

Figure 3.1: Flowchart of the system set-up.

A short description of the components is presented following:

- The mains are the power source and deliver a 50 Hz three phase voltage of 230 V RMS.
- The thermocouples are cast into the PMSM and they measure the temperature of the windings.
- The Digital Signal Controller (DSC) is used to control the PMSM by PWM signals.
- The measurement unit measures the voltages and currents.
- The PC is used to programme the DSC through Code Composer Studio. LabVIEW is used to process the temperature measurements from the thermocouples.
- The VSI is used to control the amplitude and frequency of the voltages for the PMSM.

The components are further described in the following sections.

3.1 PMSM

The PMSM is a liquid cooled hub motor with an inner stator and an outer rotor with interior permanent magnets (PMs). Figure 3.2 shows a CAD model of the PMSM in a radial cross sectional view through the middle of the stator tooth. Both the stator and the rotor are constructed of laminated steel sheet. The rotor housing, end plates, bearings and rotor resin are shown in figure 3.3. The windings around the stator teeth are omitted in the figures for simplicity and the colours are chosen for better separation of the parts.

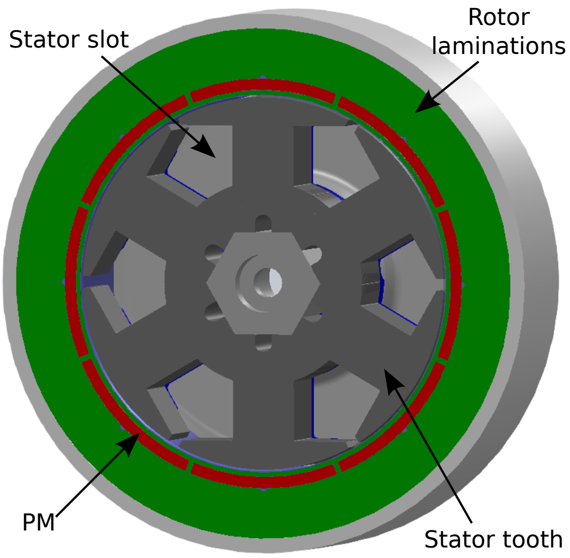

Figure 3.2: Radial sectional view of the PMSM without windings and stator resin.

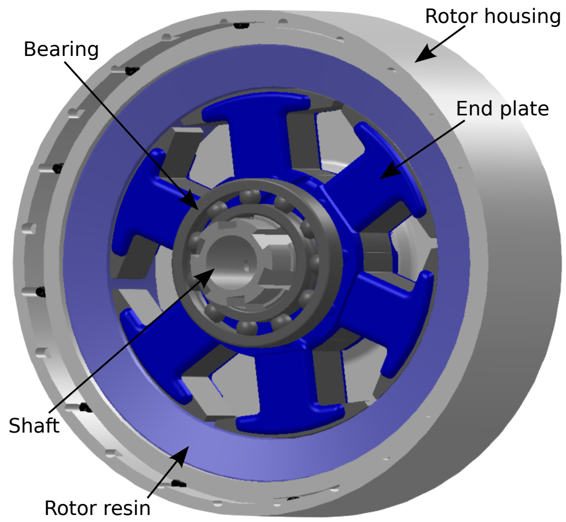

Figure 3.3: Radial view of the PMSM without windings and stator resin.

Figure 3.4 shows an axial sectional view of the PMSM with the windings and stator resin. The resin appears as a shell, however resin fill up the entire volume around and between the windings.

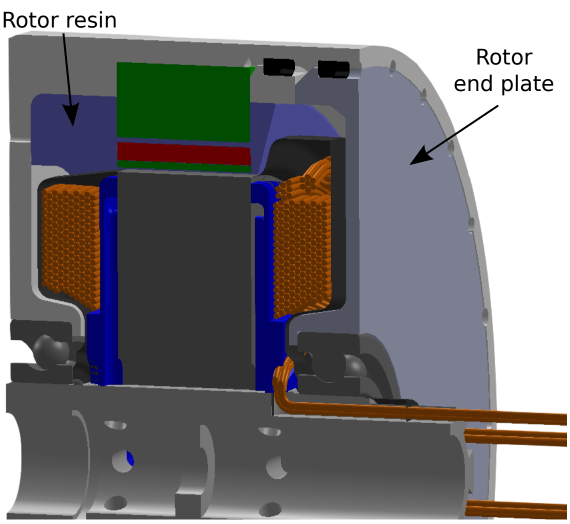

Figure 3.4: Axial sectional view of the PMSM.

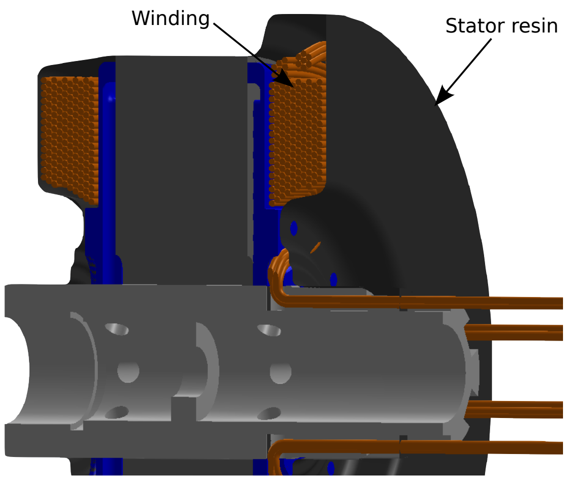

Figure 3.5: Axial sectional view of the stator.

The rotor and the stator are cast into resin to improve emission of heat in the PMSM which is important to reduce the temperatures of the PMSM. The enhanced heat distribution is achieved as resin has a higher conductivity than air. The rotor resin conducts heat from the PMs and the laminations and transfers the heat to the rotor housing. The stator resin is shown in figure 3.5 and the stator resin conducts the heat generated in the windings to the liquid cooling, which runs in the end plate. The stator resin also ensures that no conductors are free to detach and come in contact with the rotor, which could be a problem due to the small clearance between the stator and rotor (0.1 *mm*). Furthermore the stator resin is supposed to seal the liquid cooling system by enclosing the gaps between the stator teeth and end plates and likewise the gaps between the end plates and the shaft. The passage through the shaft is sealed during operation by a bolt. The resin is of thermal class F and the resin casting process of the stator and the rotor is further described in section 4.2.3.

Specifications of the PMSM are listed in table 3.1 and the materials of the main components are listed in table 3.2. Further specifications are listed in appendix A.

Parameter	**Value**
Stator teeth	6
Turns per tooth	17
Rotor poles	8
Nominal current	70 A
Nominal power	25 kW
Nominal speed	15000 rpm
Nominal torque	16 Nm

Table 3.1: PMSM specifications [10].

Item	**Material**
Rotor housing	Aluminium
Rotor end plate	Aluminium
Rotor laminations	0.35 mm steel sheet
PMs	NdFeB
Shaft	Steel
Stator laminations	0.2 mm steel sheet
End plate	POM
Windings	Copper

Table 3.2: Material specifications [10].

3.1.1 Stator laminations and liquid cooling

The stator sheet metal is laminated with a thickness of 0.2 mm to reduce eddy currents. The end plates on the stator are used to lead the coolant. Figure 3.6 shows the coolant channels in the shaft and stator teeth. The coolant flows from the coolant inlet in the shaft into the first end plate, along the shaft, into the second end plate and out of the shaft. This means the coolant in one end plate flows like shown in figure 3.7 and the coolant in the other end flows in the opposite direction. In figure 3.7 the red arrow indicates flow along the shaft, where the coolant flows in the stator coolant channels.

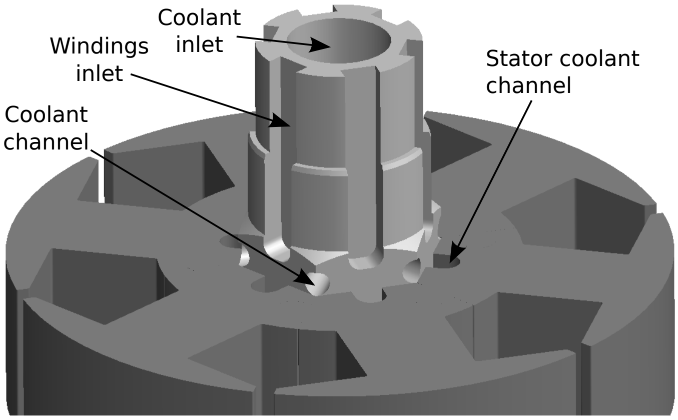

Figure 3.6: Stator and shaft, where the coolant channels are shown.

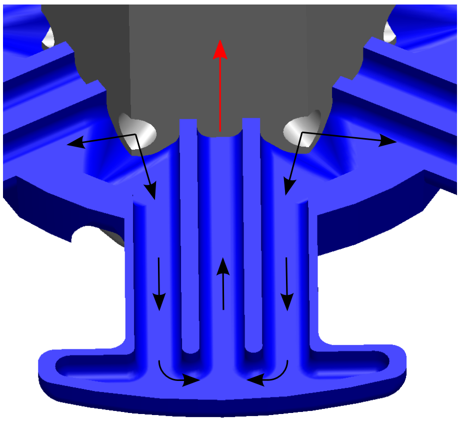

Figure 3.7: Coolant flow in the end plate with coolant channels.

During this project a 0.12 kW circulation pump delivering a flow of maximum 2800 l/min is used for the liquid cooling. The pressure drop through the PMSM is not known, why the actual flow is unknown. The coolant used is 20°C water unless stated otherwise.

3.1.2 Windings

The stator windings are wound manually. The copper conductors are insulated to ensure no electrical contact exists between the conductors. The conductors are of thermal class F, which means they are able to withstand a temperature of $155°C$. During the winding process, the insulation of the conductors may receive small scratches, therefore pieces of insulation plastics are placed between the conductors and the stator to ensure electric insulation. Insulation plastic of the type DuPont Mylar is used.

The current density of the stator windings is often used as a design parameter to avoid overheating. Different guidelines exist, but in [11] a conventional induction machine is allowed to have a current density of 8 A/m^2 and liquid cooling systems allow up to 12 A/m^2. Other guidelines suggest a current density between 15.5 and 18.6 A/m^2 for liquid cooled motors [11], but it all depends on the design of the motor and the performance of the liquid cooling system. As the PMSM operates in a low pressure environment, the current density must be kept under the guidelines for liquid cooled motors, why a maximum allowable current density of 9.5 A/mm^2 is chosen. To ensure a current density $J \leq 9.5\ A/mm^2$ with the rated current of 70 A the required conductor area is:

$$A_{cond} = \frac{I_{nom,RMS}}{J_{cd}} \qquad \Rightarrow \qquad A_{cond} = \frac{70\ A}{9.5\ A/mm^2} = 7.37\ mm^2 \tag{3.1}$$

Where in equation (3.1):

A_{cond}	Cross sectional area of conductors, $[m^2]$
$I_{nom,RMS}$	Nominal current, $[A]$
J_{cd}	Current density, $[A/m^2]$

In section 4.1 the cross sectional area is used to determine the number of conductors in parallel dependent on the choice of conductor diameter. The diameter of the conductors is a balance between a large diameter causing skin effects and a small diameter causing more conductors in parallel, which is practically inconvenient to handle. The skin effect is a frequency dependent phenomenon, where the current density in a conductor tends to increase near the surface and exponential decrease towards the centre of the conductor [12]. This distance from the surface to where the current density is reduced to $1/e = 0.368$ is called the skin depth and it is calculated from equation (3.3). If the skin depth is small and the radius of the conductor is large, the effective cross sectional area of the conductor is reduced, and thus the effective resistance is increased. The copper conductors have a relative permeability near 1 for practical purposes. The frequency, permeability and conductivity, used to calculate the skin depth, are stated and the skin depth is calculated [12]:

$$\omega_{app} = 1000\frac{1}{s}\ 2\pi\ rad \quad ; \quad \mu_{cu} = 1.256 \cdot 10^{-6}\ \frac{\Omega\ s}{m} \quad ; \quad \sigma_{SB} = 5.96 \cdot 10^{7}\ \frac{1}{\Omega\ m} \tag{3.2}$$

$$\delta_{cond} = \sqrt{\frac{2}{\omega\ \mu\ \sigma_{SB}}} = 2\ mm \tag{3.3}$$

Where in equation (3.2) and (3.3):

δ_{cond}	Skin depth of conductors, $[m]$
μ_{cu}	Permeability of copper, $[\Omega\ (s/m)]$
σ_{SB}	Stefan-Boltzmann constant (5.67x10e-8), $[W/(m^2\ K^4)]$
ω_{app}	Frequency of applied voltage, $[rad/s]$

To avoid skin effects, the diameter of the conductor must be chosen such that $d_{cond} \leq 2\ \delta_{cond}$ [12]. Therefore, if the diameter of the conductor is less than 4 mm, the skin effects are negligible. A 4 mm

conductor is not workable enough to be suitable for the windings of the PMSM, why skin effects are not an issue in the choice of conductor diameter.

3.1.3 Bearings and rotor

The deep groove ball bearing from Schaeffler of type FAG 6007 is shown in figure 3.8. The bearings are lubricated with grease. The bearings are inserted in the rotor housing and the rotor end plate. The bearings are rated to 15000 *rpm* and an operating temperature of 70°*C*. The bearings are mounted with a tight press fit as specified from the manufacture.

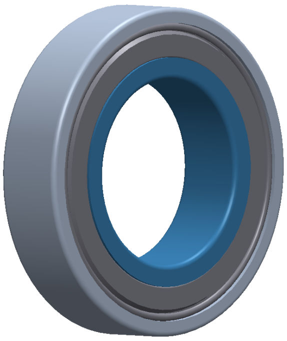

Figure 3.8: CAD drawing of the bearing [13].

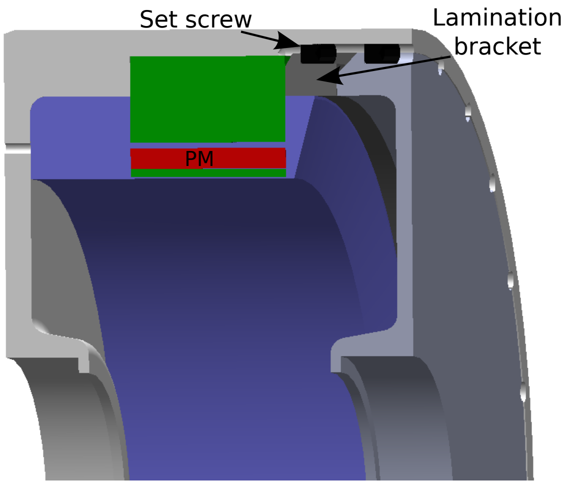

Figure 3.9: Cross sectional view of the rotor parts.

The rotor laminations are segmented with 0.35 *mm* pieces. The lamination bracket in figure 3.9 is used to compress and secure the rotor laminations using set screws. To reduce core losses in the PMs, each PM is laminated in 12 layers. The 8 PMs are interior mounted in the rotor laminations with 1.8 *mm* separation.

3.2 Thermocouples

Type J thermocouples with tolerance class one are used in the PMSM, which result in an uncertainty of 1.1°*C* or 0.4%. The J type thermocouple is robust, compared to types with better accuracy and the robustness is beneficial as the thermocouples might be exposed to some wear during manufacturing of the PMSM. Type J thermocouples are able to measure temperatures from 0°*C* to 750°*C* continuously. The thermocouples are connected to three NI 9211 modules, which are inserted into a NI cDAQ-9172 chassis. Each NI 9211 module has 4 channels, which gives the option to have a total of 12 thermocouples.

NI LabVIEW is used to log the temperatures from the thermocouples. LabVIEW has a build in software to connect to the NI 9211 modules and set up the thermocouples.

3.3 Digital signal controller

The DSC used in this project is a 150 MHz Texas Instruments TMS320F28335. Code Composer Studio is used to programme and control the DSC, where the code is written in *c* (programming language). The generated PWM voltages are used to generate optical PWM signals by an optical board, which the DSC is mounted on. The optical PWM signals are send through optical cables to the IPC2 board, which has replaced the original Danfoss interface on the VSI. A peripheral module in the DSC is used to generate the PWM signals. The code implemented on the DSC is described in chapter 11.

3.4 Measurement unit

An oscilloscope is used to display and log the measured currents and voltages. For this project, a Tektronix DPO 2014 oscilloscope with a current transducer and three Tektronix P5200 voltage differential probes are at disposal. The oscilloscope has a 200 MHz bandwidth and up to 1 GS/s sample rate. The logged data is transferred to the PC via a USB cable.

3.5 Voltage source inverter

A Danfoss FC 302 55 kW VSI is used to power the PMSM. An AC-DC-AC VSI consists of three main components; a rectifier, a DC-link and an inverter, as shown in figure 3.10.

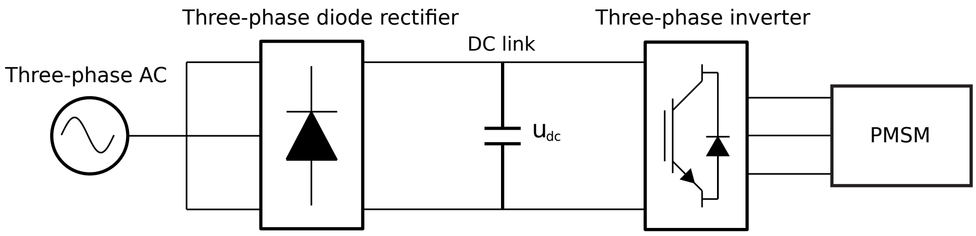

Figure 3.10: A diagram of a VSI [14].

Where in figure 3.10:

u_{dc}	DC link voltage, $[V]$

The build in software is normally limited to an output frequency of 590 Hz due to export control regulations, however the software is revised which means it is limited to an output frequency of 1000 Hz. The build in software is used in section 4.2.6 before the IPC2 board is implemented.

Three phase diode rectifier

The three phase diode rectifier is used to convert the three phase 230 V RMS 50 Hz voltage from the mains to a DC voltage. This is done by passing the supply from the mains through the diode rectifier as shown in figure 3.11. The AC-DC conversion results in ripples as seen in figure 3.11.

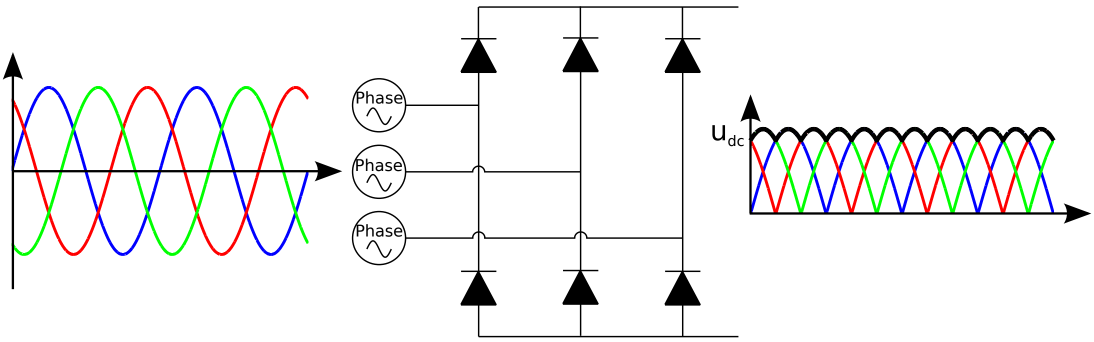

Figure 3.11: A three phase voltage entering a diode rectifier [14].

DC link

The voltage ripples from the rectifier are smoothed out using a capacitor to ensure a constant DC voltage for the inverter. The voltage of the DC link is calculated by:

$$u_{dc} = 230\ V \cdot \sqrt{2} \cdot \sqrt{3} \approx 563\ V \tag{3.4}$$

This calculation assumes an ideal capacitor and diodes. However a small voltage drop across the diodes and non-ideal capacitor reduce the DC-link voltage, why a voltage of 560 V is estimated.

Inverter

The inverter consists of 6 Insulated Gate Bipolar Transistors (IGBTs), which open and close for the DC-link voltage. By controlling the switches a desired output frequency and amplitude can be produced. The transistors are controlled by PWM signals. A diagram of the inverter is shown in figure 3.12.

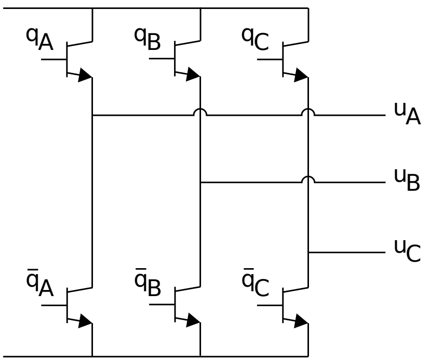

Figure 3.12: A diagram of the inverter [14].

Where in figure 3.12:

q_i	PWM control signal for the IGBTs, $[-]$

The top and bottom transistors of each of the three inverter legs are always in opposite state to avoid shoot through of the DC link. Furthermore a delay (dead time) is introduced between the switches of the top and bottom IGBTs. For the IPC2 board, 4 μs are recommended for the available Danfoss VSI. The switching frequency in the build in software is 3-16 kHz. It is chosen to use a switching frequency of 6 kHz since it is found acceptable through tests in section 4.2.6. The switching frequency is a compromise between switching losses in the VSI and distortion of the output voltages.

CHAPTER

4
MANUFACTURING

The manufacturing process of the PMSM is described in this chapter. The parts for the PMSM are partly supplied from earlier projects at AAU and collaborator companies. The design of the parts and tools are given in advance and therefore the primary task for the group is to assemble, wind and cast the PMSM into resin.

Three stators and two rotors are manufactured. The first stator is a test stator, to check if it is possible to wind the stator with the given number of turns and check the outcome of the resin casting. The test stator is not supposed to run. The first running motor is PMSM-v1 and a stator-v1 and rotor-v1 are manufactured to gain knowledge about; the design, manufacturing, performance and the liquid cooling system. Based on the experiences from PMSM-v1, PMSM-v2 is manufactured, where the experiences are used to improve PMSM-v2.

To give an overview of the following chapter, a short description is stated:

- Manufacturing of test stator
  - Wind the test stator with various conductor diameters
  - Slice the test stator after wax filling and resin casting
- Manufacture the PMSM-v1 and the PMSM-v2
  - Assemble and wind stators
  - Wax injection of the stators
  - Glue and magnetise the PMs
  - Assemble the rotors
  - Resin cast the rotors and stators
  - Assemble the PMSMs and mount the bearings

4.1 Test stator

A test stator is wound on a dummy shaft with two end plates to determine the conductor diameter and to test if the requirements of a minimum conductor area of 7.37 mm^2 and 17 turns, from section 3.1.2, are achievable. The main conclusions are presented in this section and additional pictures and details regarding the test stator are located in appendix B.1.

4.1.1 Choice of conductor diameter

From section 3.1.2 the maximum conductor diameter is calculated to be 4 *mm* to avoid skin effects. Other than this requirement, the diameter of the conductors for the windings is chosen on the basis of the following compromises:

- A smaller conductor diameter means more conductors in parallel which is inconvenient to handle during the winding process because the conductors entangle.
- Larger diameter means fewer conductors in parallel but the conductors are less workable.

From inspection of the available copper wires, it is chosen to wind the test stator with conductors of 0.6 *mm* and 0.8 *mm*. To archive the conductor area of 7.37 mm^2, 26 and 15 conductors are in parallel for the small and large diameter respectively. The test stator is wound and insulation plastics are placed between the stator laminations and windings, to replicate the final manufacturing of the PMSM.

The requirements of 17 windings and a minimum conductor area of 7.37 mm^2 are fulfilled and the result is shown in figure 4.1. A fill factor of approximately 0.42 is obtained, which is within the expectable range. It is assessed that the coil with 0.6 *mm* conductors has a higher fill factor but causes too much entanglement for use in stator-v1. The 0.8 *mm* is too stiff, why a conductor diameter in between the two is desirable. A conductor with a diameter of 0.75 *mm* is chosen for the next stator to reduce entanglement.

Figure 4.1: Conductor diameters of 0.6 *mm* and 0.8 *mm* on the test stator.

4.1.2 Resin casting of test stator

Two types of resin are available, which are heat tested as described in appendix B.3 to choose the most applicable at elevated temperatures. The resin delivered by Huntsman is chosen for the PMSM, due to the better properties during heating and the extra stiffness compared to the other resin delivered by RAMPF. The test stator is cast into resin to check how the resin penetrates into the gaps between the windings, which is important to ensure a good thermal conductivity. To avoid resin penetrating into the cooling channels, they are filled with wax before the resin casting. The wax is poured into the cooling channels without applying pressure. The wax has a melting point around 60°C which makes it possible to melt it off after the resin is cured. The resin casting and wax filling of the test stator are performed by Johnson Controls and Dantrafo A/S.

The resin casting is evaluated by slicing the test stator as described in appendix B.2. In figure 4.2 and 4.3 it is seen the resin has penetrated into the air gaps between the windings as intended.

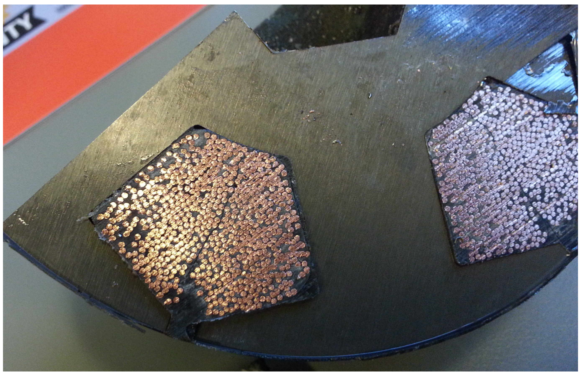

Figure 4.2: Sliced test stator where the slot windings are shown.

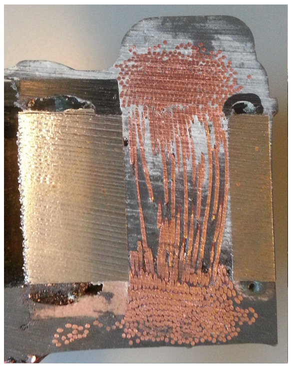

Figure 4.3: Sliced test stator where the resin casting is evaluated.

Figure 4.4 and 4.5 show the wax did not fill the cooling channels entirely, since resin has penetrated into the cooling channels, which blocks the channels. Remainder of wax is also present in the cooling channels, which is because the wax could not be removed as the cooling channels where blocked. To ensure the wax fills the cooling channels, wax injection under pressure should be used for PMSM-v1.

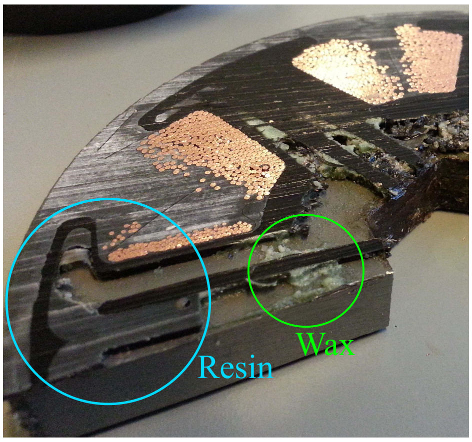

Figure 4.4: Blocked cooling channels by the resin.

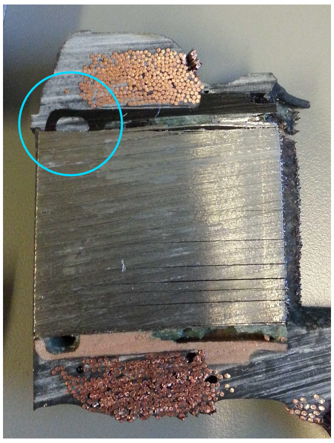

Figure 4.5: Blocked cooling channels by the resin.

4.2 PMSM-v1

The manufacturing process of PMSM-v1 is presented in this section. The drawn experiences are discussed in the end of the section.

4.2.1 Stator-v1

Based on of the experiences from the test stator, a PMSM-v1 with a steel laminated stator is manufactured. A 30 *mm* stator stack of 144 laminations, corresponding to a stacking factor of 0.96, is placed on the shaft. To avoid shorts between the windings and the stator, pieces of insulation plastic are placed in the slot openings as shown in figure 4.6. The pieces of insulation plastic are formed to occupy as little space in the stator slot as possible. They are fastened to the outer stator teeth, to protect the copper conductors from scratches during the winding process. Figure 4.6 shows how the conductors and thermocouples are placed in the inlets in shaft and end plates.

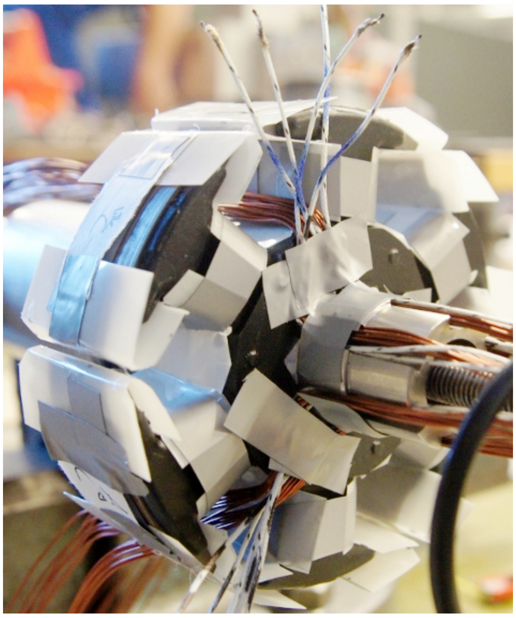

Figure 4.6: The conductors and thermocouples in the inlet and pieces of insulation plastic placed in the stator slots.

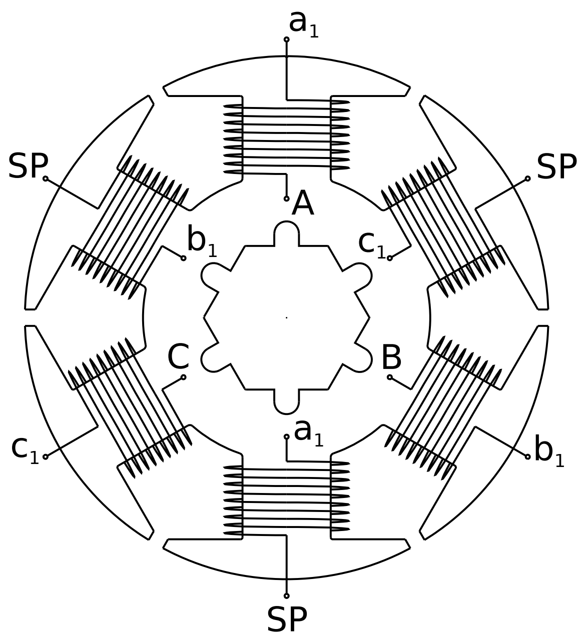

Figure 4.7: Winding diagram of the stator [10].

Figure 4.7 shows a diagram of how the windings are wound on the stator. Capital letter indicates the start of a winding and small letter indicates how two coils are connected into one winding. The three phases are connected in a Star Point (SP) which is located inside the PMSM. The stator with three windings is shown in figure 4.8 where the ends for the star point are tensioned to make the windings settle.

Figure 4.8: Tensioned windings to make them settle.

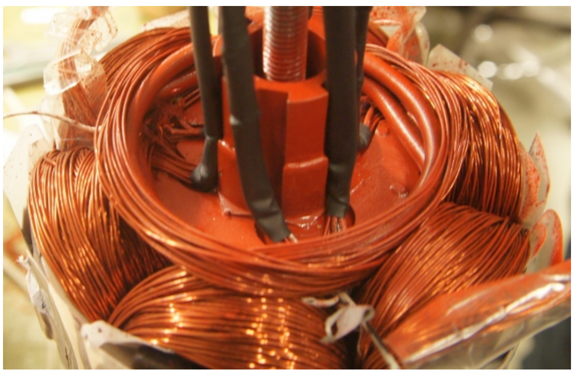

Figure 4.9: Repair of the shorts between the conductors and stator.

To check the stator for shorts prior to assembling of the SP, a DAVO-MEG instrument is used to apply 1000 V and measure the resistance between the windings and the stator. Shorts are measured both between the windings and between the windings and the stator. Fortunately, the shorts are due to the sharp edges on the shaft, that have scathed the conductors in the three phases, why insulation varnish and heat-shrinkable tubing are applied as seen in figure 4.9. The varnish is applied to the conductors and the shaft after which all shorts are sealed.

Wax injection

The wax is injected using pressure at Skalform A/S, which is necessary, based on the experiences from the test stator, to ensure the cooling channels are filled. The stator is mounted in a rectangular tube which is fixed in the injection machine. The wax is injected into the cooling channels through the shaft as seen in figure 4.10. The wax is injected until the excess flows through the small gaps between the stator teeth and end plates as seen in figure 4.11. Judged from the amount of excess wax coming from all the gaps, it is assessed that the wax has filled the cooling channels. The excess wax is removed to enable the resin casting. More pictures from the wax injection are found in appendix B.4.

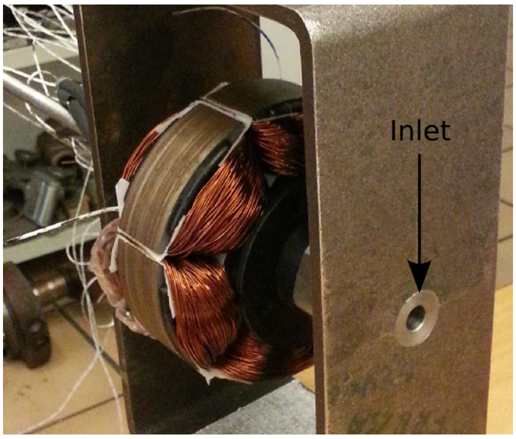

Figure 4.10: The stator mounted in a rectangular tube to enable injection.

Figure 4.11: The excess was that penetrates through the gap between stator tooth and end plate.

4.2.2 Rotor-v1 assembly

The PM segments are glued together, burnished and painted as described in appendix B.5. They are burnished on the ends to ensure they fit in the slots of the rotor laminations. The PMs are painted to avoid corrosion and afterwards they are magnetised at Sintex A/S.

The rotor laminations are placed in the rotor housing and aligned using a snipe nose plier. The laminations are inserted in small batches due to the tight fitting between the rotor housing and laminations. 82 laminations are placed in the rotor housing, which yield a stacking factor of 0.96. This is the same stacking factor as the stator with thinner laminations. Thicker laminations tend to increase the stacking factor, but the tight fit of the rotor laminations is assessed to cause the unaltered stacking factor.

The magnets are inserted in the laminations and due to the tight fit between the PMs and the slots, a press is used as shown in figure 4.12. This caused some of the painting on the magnets to come off, however it is assessed it will not influence the performance of the magnets in this prototype. Furthermore the rotor is cast into resin, which seals the magnets.

Due to the tight fit, small gaps are present between the laminations as shown in figure 4.13. It is sought to minimize the gaps but the laminations are tensioned why they bounce back after each attempt. These gaps might influence the flux path in the rotor and give a smaller inductance in directions with the larger gaps. However it is assessed the gaps do not influence the performance of the PMSM-v1.

Figure 4.12: The magnets being pressed into the rotor laminations.

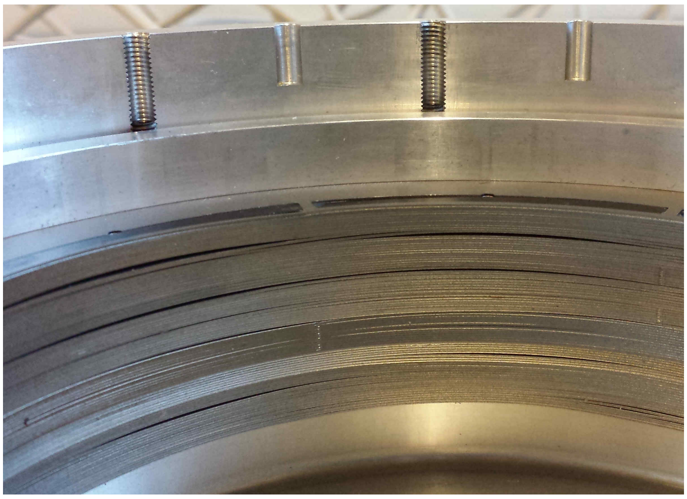

Figure 4.13: Rotor laminations inserted in the rotor where the gaps between the rotor laminations are shown.

4.2.3 Resin casting of PMSM-v1

To cast the stator into resin, the stator is mounted in a mould, shown in figure 4.14 and 4.15, designed to fill resin around the windings and keep resin away from the outer stator teeth, to maintain the clearance between the stator and rotor. The resin is filled through six inlets in the top of the mould and it is filled from one side to allow the air in the mould to escape from the other side as the mould is filled.

A casting mould, shown in figure 4.15, is mounted on the top of the rotor laminations to keep resin in the desired location shown in figure 3.4. The rotor is cast while it rotates to ensure an even distribution of the resin and avoid air pockets. Centrifugal casting is chosen as an attempted to place a thin layer of resin on the inner surface of the laminations. Furthermore manufacturing of a more complicated mould for the rotor is avoided. A thin layer is important to keep the clearance between the stator. A 24 V DC motor is used to rotate the rotor. It is necessary to spin the rotor at high speed, to avoid a conic distribution of the resin. The speed of the available DC motor is almost 490 rpm. The centripetal acceleration at this speed is calculated in equation (4.2), which is found acceptable through experiments.

$$a_{cent} = \frac{(\omega_{dc}\ r)^2}{r} \tag{4.1}$$

$$= \frac{\left(\frac{2\ \pi\ rad}{60\ s} \cdot 490\ rpm\ \cdot 0.0645\ m\right)^2}{0.0645\ m} = 170\ \frac{m}{s^2} \tag{4.2}$$

Where in equation (4.2):

a_{cent}	Centripetal acceleration, $[m/s^2]$
r_i	Radius, $[m]$
ω_{dc}	Angular velocity of DC motor, $[rad/s]$

The resin cures after it is mixed and the higher the temperature, the faster it cures. It is important to keep the temperature below the melting point of the wax, which is 60°C, as long as the resin is low viscous. The resin is mixed at Dantrafo A/S and transported to AAU but due to the logistics the temperature of the resin is decreased. The rotor, stator and resin are placed in the oven as shown in figure 4.15 and preheated before the filling. The resin is filled at 30°C after which refills are performed for two hours. At the last refill, it is discovered that the resin has a lower viscosity compared to the viscosity at the time of filling, which is because the resin was not preheated sufficiently.

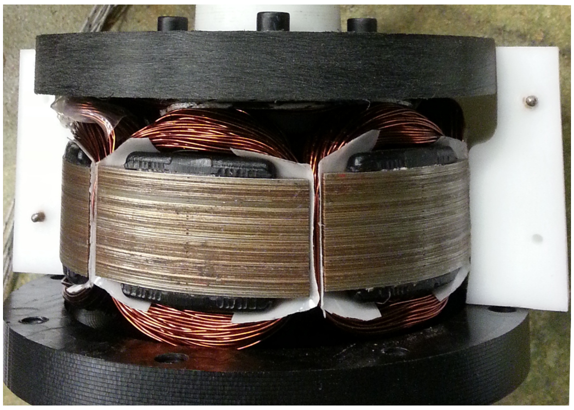

Figure 4.14: The stator mounted in the casting mould.

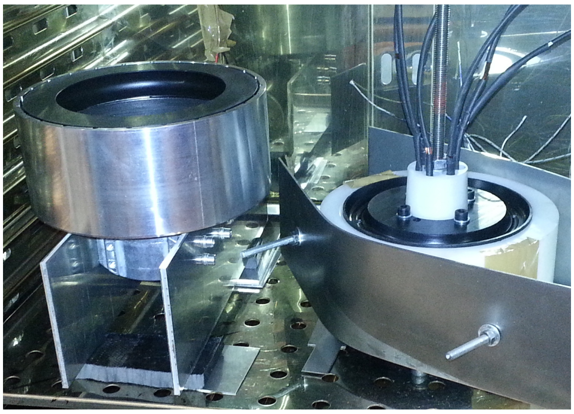

Figure 4.15: The stator and rotor placed in the oven for the resin casting.

The resin cures in the oven, starting at 55°C. After the resin becomes stiff the temperature is increased, ending at 115°C after 48 hours in the oven. Further details of the casting process are listed in appendix B.6. At the elevated temperatures most of the wax melts out of the stator and the remaining wax is removed afterwards by running hot water through the cooling channels.

The casting mould is detached and the result is seen in figure 4.16 and 4.17. Figure 4.16 shows the result of air pockets in the casting mould and resin from the inlets. Figure 4.17 shows the casting mould did not seal tightly around the stator teeth, which caused resin to cover the stator laminations. This resin is unwanted as the clearance between the stator and rotor is only 1 mm. Therefore the resin is removed by machining and the result is shown in figure 4.18.

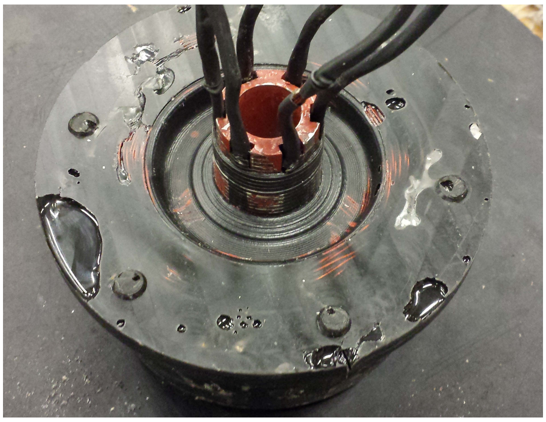

Figure 4.16: The stator cast into resin seen from above.

Figure 4.17: The stator seen from the side with excess resin and gaps in the resin.

A layer of resin is also located on the rotor laminations after the centrifugal casting. However the layer is assessed to be too thick why it is removed in a turning lathe. The disadvantage by using machining and a turning lathe is the risk of creating electric contact between the laminations. As seen in figure 4.18 and 4.19 it was not possible to avoid contact between the machining tool and the laminations, which might lead to higher core losses as electric contact between the laminations are created.

Figure 4.16 shows resin on the shaft where the bearing is to be mounted (more detailed picture available in appendix B.6 in figure B.30). This resin is removed by hand and the surface is burnished afterwards to prepare the mounting of the bearing.

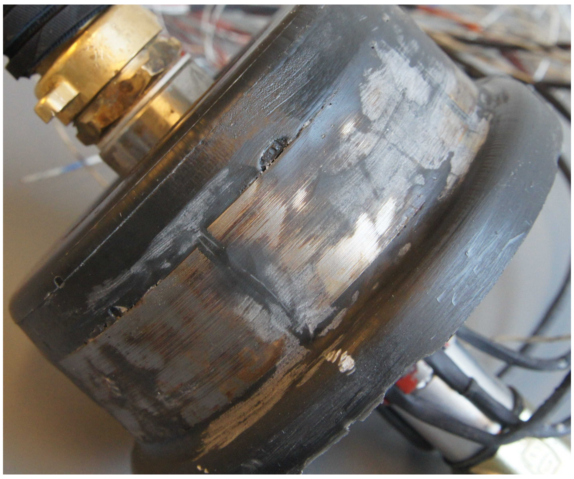

Figure 4.18: The stator after machining.

Figure 4.19: The rotor after the excess resin has been removed by the turning lathe.

4.2.4 Sealing of cooling system

The resin sealing between the end plates and the stator teeth is tested by pouring water through the cooling channels. Leakage is discovered from gaps between the end plates and the stator laminations . The gaps are shown in figure 4.18. To seal the gaps, an epoxy based adhesive is tested, which reveals strong binding to the resin. The resin along the end plates is removed in a thin groove, as shown in figure 4.20 to ensure a strong binding. Figure 4.21 shows how the adhesive is applied.

Figure 4.20: Removal of the resin at the end plates.

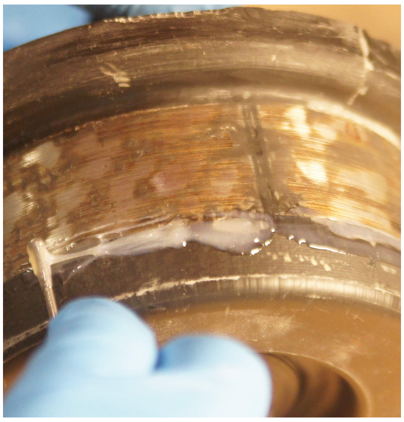

Figure 4.21: Applying of the EPOXY adhesive to the stator.

The adhesive reduces the leaks considerable, but not entirely. A leak repair product is applied to remove the small leakages but without success. The repairs are acceptable to test the cooling system as described in section 8.2. During tests of the cooling, the leakage increases and the adhesive detaches, why the adhesive is removed to ensure clearance between the stator and rotor in the assembling. This rule out liquid cooling in PMSM-v1.

4.2.5 Assembling and mounting PMSM-v1

The PMSM is assembled in six steps as shown in figure 4.22. A guiding shaft with thread is manufactured with a sliding fit tolerance between the shaft and the bearings. The purpose is to guide and centre the stator when mounted in the rotor, to avoid the stator to be snatched by the PMs in the rotor housing. A spacer with the inner diameter of the bearings is manufactured with a thickness of 0.7 *mm* to ensure the desired offset between the end of the shaft and the rotor housing is obtained.

1. The first bearing is cooled and mounted in the preheated rotor end plate.
2. The second bearing is cooled and mounted in the rotor housing.
3. The guiding shaft is screwed into the stator shaft.
4. The stator is lowered into the rotor housing.
5. The spacer is mounted on the guiding shaft.
6. Force is applied to the top of the stator shaft by a hydraulic press while the bottom is supported on the spacer.
7. Force is applied to the inner and outer ring and rotor housing to mount the second bearing on the rotor shaft.

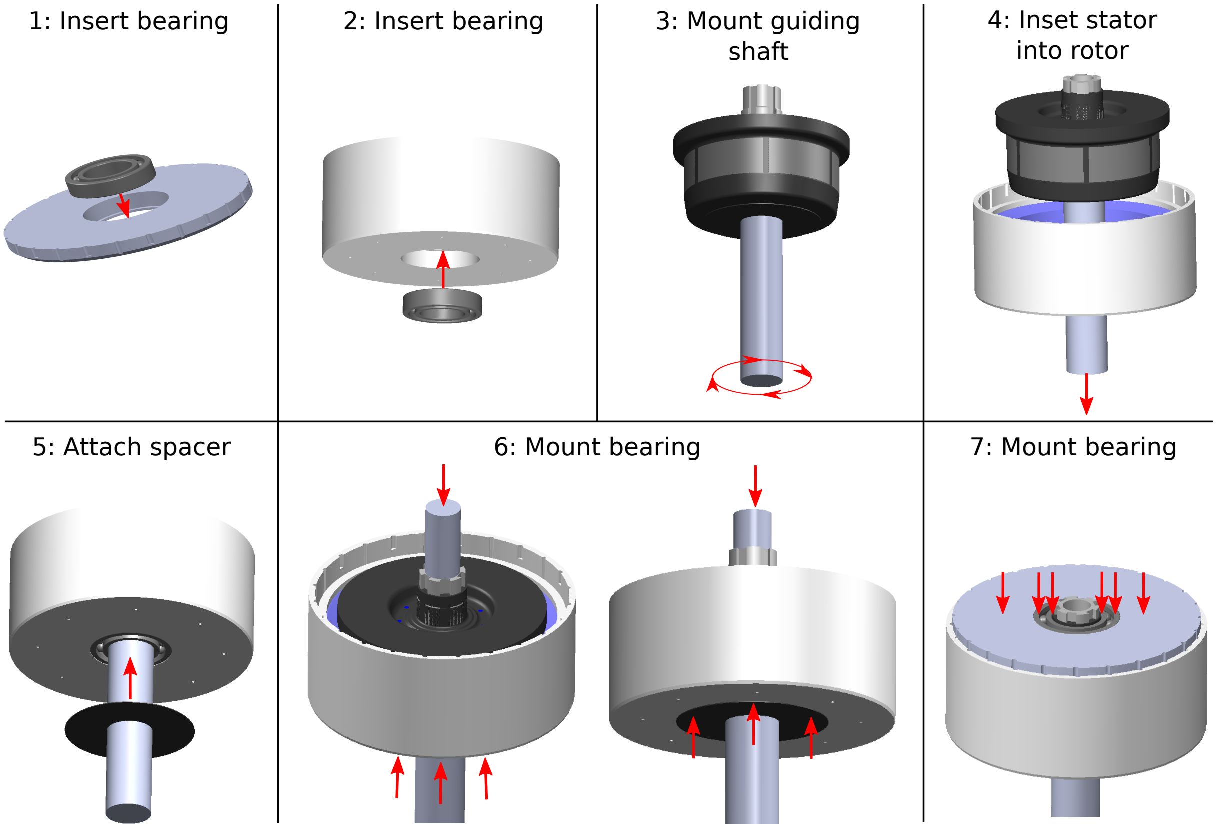

Figure 4.22: The assembling procedure for the PMSM.

Test bench

PMSM-v1 is mounted in a test bench as shown in figure 4.23. The PMSM is mounted to an aluminium shaft with thread in one end and a simple support without thread in the other end as shown in figure 4.24. A bolt is screwed into the aluminium shaft to ensure the PMSM does not detach. The aluminium shafts are fastened to the mounting frame using set screws. The cooling channels enable air cooling using a compressor.

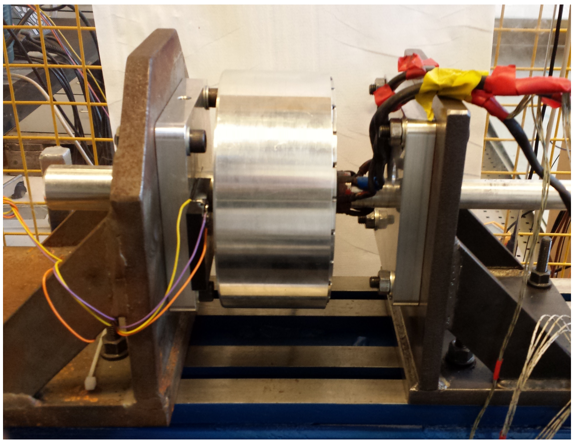

Figure 4.23: The PMSM mounted in the test bench.

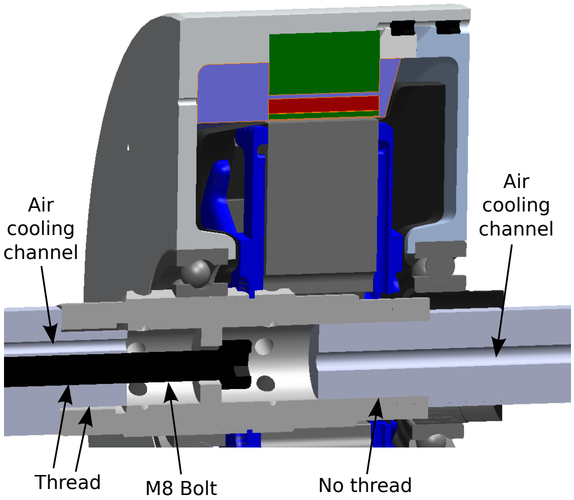

Figure 4.24: Axial sectional view of the mounted PMSM.

4.2.6 Test run and issues

After the assembling and mounting in the test bench, some preliminary tests are performed on the PMSM to test if it is able to run. The build in software of the Danfoss VSI is used to control the PMSM for the test run. Open loop U/F, Voltage Vector Control Plus and a Flux Sensor-less control strategies are tested, but the results are inconsistent and high currents are drawn by the PMSM. Parameter variation and different switching frequencies are attempted with the different control strategies but with limited success. As an attempt, the test bench is grounded to the VSI. This reveals a large current is drawn from the test bench to the ground of the VSI, which indicates a short between the windings and the PMSM. The PMSM is disassembled and the DAVO-MEG instrument is used to search for shorts. Several shorts are discovered where the resin has been removed to enable mounting of the bearings as shown in figure 4.25. As the shorts are located where the bearing is mounted, it is assessed that the short was between the windings and the bearing.

Insulation varnish is applied to remove the shorts and an O-ring is mounted on the shaft. The assembled PMSM is tested for shorts and no shorts are measured.

The PMSM is now able to run, despite of start-up difficulties, and it is able to reach 8000 *rpm* with the build in voltage vector control software. The losses are calculated on the basis of a spin down test and the calculation method is further described in section 8.1. However the measured rotational losses are twice as high as expected from section 1.1.1. Therefore the PMSM is disassembled, to locate the reason for the high losses. It is discovered that the bearing has been mounted too close to the O-ring as the bearing has fret the O-ring, as shown in figure 4.26.

Figure 4.25: Short between the bearing and the windings in the inlet of the shaft.

Figure 4.26: Fret O-ring after the bearing was mounted too close.

A new O-ring and bearing are mounted, but this time the bearing is mounted with an offset of 3.3 *mm* to the stator, to avoid contact. The PMSM is assembled and the rotational losses are measured again, but the losses are still too high. The reason for the losses could be:

- Fittings of the bearings
- Mounting and alignment of the bearings
- Axial forces on the bearings
- Contact between rotor and stator

The reason for the losses are assessed to be the bearings as they get hotter than expected after a short time of operation. It is decided to disassemble the PMSM and loosen the fittings of the bearings and the rotor end plate. The fittings of the bearings are loosened to reduce the losses. 4/100 *mm* is removed from one end of the shaft in a turning lathe and the other end, with inlets for the windings, is handled by hand. 8/100 *mm* is removed from the mounting in the rotor housing in the turning lathe.

During the disassembling of the PMSM, it is discovered that a short has existed between a conductor in the stator and the rotor. Figure 4.27 shows the conductor, which stick out from the stator slot and figure 4.28 shows the signs of the short in the rotor. The conductor was visible after the resin casting, but at that time the solution was to apply insulation varnish. Now it is clear that the varnish did not solve the problem, as the rotor might have scratched the varnish off. Therefore the conductor is planed down to avoid contact but it is not cut, why it is still able to conduct current. The resistance in this phase gets larger but this must be accepted to avoid shorts. Varnish is applied to the planed down conductor.

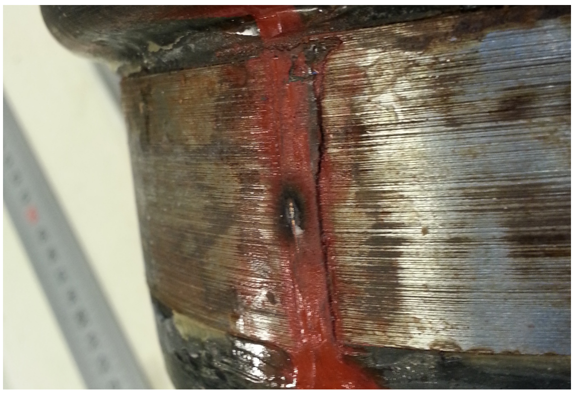

Figure 4.27: Conductor from the stator.

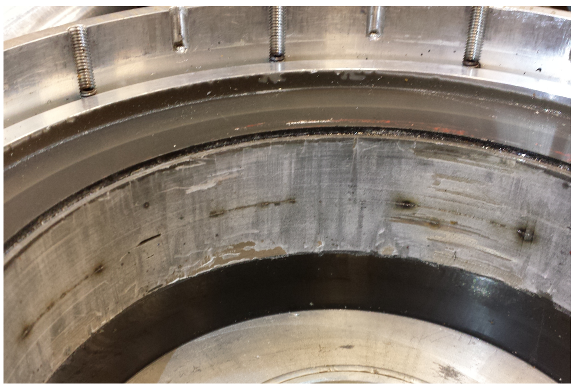

Figure 4.28: Signs on the rotor from shorts.

Despite of the loosened fittings resulted in reduced losses, one of the bearings generates more heat than the other. A thermocouple is placed on the inner race of each bearing as shown in figure 4.29. Several tests have been performed to reduce the risk of error measurement from the mounting of the thermocouples. The thermocouples measure the outer temperature of the bearing, but since a temperature difference between the bearings is of interest it is not an issue. In figure 4.30 the temperature of the bearings are shown from a 4500 rpm test where no cooling is applied. The bearing with the high temperature is the one near the windings inlet as shown in figure 4.29. However the heating is not caused by losses in the windings, as the windings are cold.

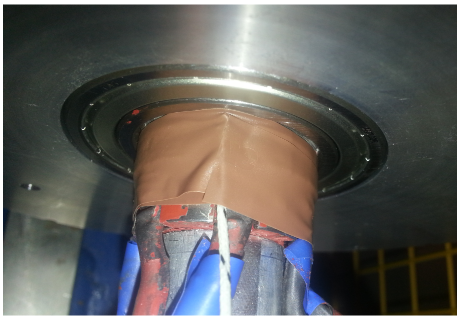

Figure 4.29: Thermocouple to measure the temperature of the bearing.

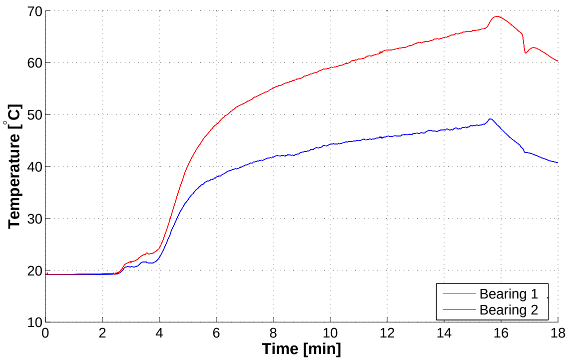

Figure 4.30: Temperature of bearings during test run with original fittings.

The temperature difference between the bearings still exists, which may be caused by:

- The hot bearing is mounted on the shaft with grooves for the windings inlet, which causes deformation of the inner bearing ring.
- The heat from the cold bearing is easily lead through the shaft, as this end is mounted with thread and the shaft at the hot bearing is mounted with a loose press fitting.

It is assessed that the different mounting of the shaft has a small influence, as neither of the shafts or the windings heats up during the short test run. Figure 4.31 shows the bearing mounted on the inlet groove. The inlets are filled with resin, why the sketch is exaggerated because the resin supports the inner ring of the bearing.

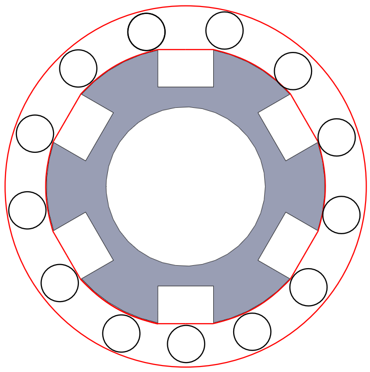

Figure 4.31: An exaggerate sketch of the deformed inner ring.

Spin down tests performed as described in section 8.1 reveals a reduction of 38% in rotational losses at 4500 rpm with the looser fittings. Despite the reduced losses, the temperatures of the bearings exceed the operating temperature of 70°C within 2 minutes at 15000 rpm without cooling. However it has to be investigated if the liquid cooling is able to keep the temperature down, due to the coolant in the shaft. The air cooling is discarded as some of the grease in the bearings is forced out at high speed. Two holes are drilled in the rotor end plate to reduce the pressure, but they are not sufficient at high speed.

At the end of the project, a conductor broke because a short circuit occurred between the conductor and the mounting shaft. Figure 4.32 shows the broken conductor and the broken heat-shrinkable tubing that, along with a scratch in the conductor, caused the short circuit. The missing conductor results in a 1/17 increased phase resistance and thereby a small unbalance. The consequence of an unbalanced system is described in appendix C, however the tests described in the remaining report are performed prior this short circuit.

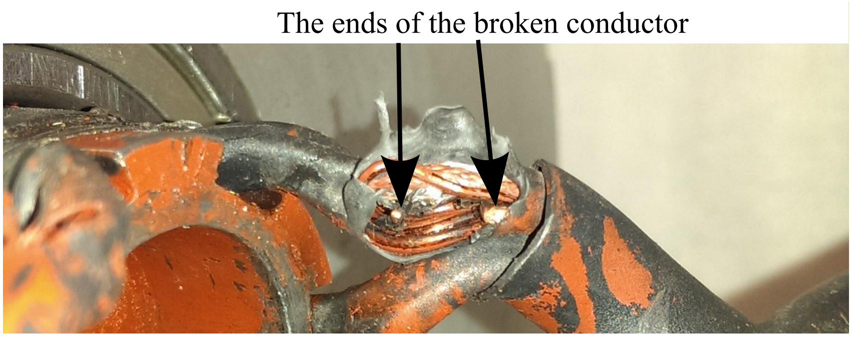

Figure 4.32: Broken conductor due to short circuit.

4.2.7 Experiences

An overview of the important experiences of PMSM-v1 is stated following and afterwards the experiences are elaborated.

- Avoid shorts
- Improve resin casting process
  - Avoid resin on outer stator laminations and inner rotor laminations
  - Preheat resin, stator and rotor to ensure the resin is low viscous
  - Apply vacuum or a shaking table while casting the stator to avoid air pockets in the resin
- Redesign sealing of the cooling system
- Reconsider bearing type or bearing fittings in order to minimize the losses

The shorts between the windings and shaft must be prevented for the next stator by applying heat-shrinkable tubing and insulation varnish. To ensure no electric contact between the shaft and windings, the section of the windings near the shaft inlet must be coated with heat-shrinkable tubes.

During the resin casting, it is important to avoid resin on the end of the stator teeth and on the inner rotor laminations, to leave out machining afterwards. The poor casting (air pockets and misplaced resin) might be caused by the high viscosity of the resin at the time the stator mould was filled. Based on this it might have been beneficial to preheat the stator to $55°C$ before filling the mould. Furthermore it may be beneficial to apply vacuum and/or a shaking table to minimize air bubbles in the resin.

It is assessed that even though the casting is improved, another way to seal the gaps between the end plates and stator teeth is necessary to prevent leakage from the cooling channels. This leads to an alternation of the sealing method.

4.3 PMSM-v2

The second PMSM prototype is presented in this section. Only the considerable alternations of the manufacturing process are presented. The manufacturing of stator-v2 includes a new design of the end plates and an improved resin casting process both attempts to avoid the leakages from stator-v1. Rotor-v2 is assembled and cast the same way as rotor-v1.

4.3.1 End plates

To improve the sealing of the liquid cooling system, a design with a "closed" end plates is proposed, to seal the gaps between the end plates and the stator teeth. Three solutions are proposed to create a sealed end plate:

- Use an "open" end plate (like on PMSM-v1) and weld a thin plastic sheet on the back.
- Use an open end plate and bind it to the stator lamination.
- 3D print a closed end plate in ABS.

The two first solutions are attempted by Johnson Controls and Ejnar A. Wilson A/S. The welding of the end plate fails, as the welding material fills the cooling channels and it is not possible to bind the end plate to the stator laminations. Due to the failures, 3D printing with ABS p430 polymer is chosen due to the ease of the process and the mechanical strength of the material. A CAD model of the closed end plate is shown in figure 4.33. The result is shown in figure 4.34 and the tolerances and strength of the material are satisfying.

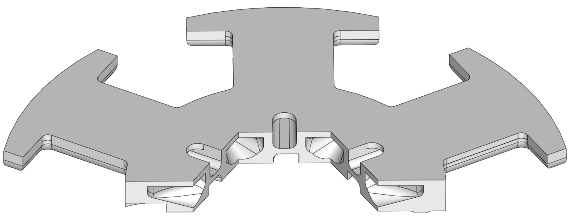

Figure 4.33: CAD model of the closed end plate.

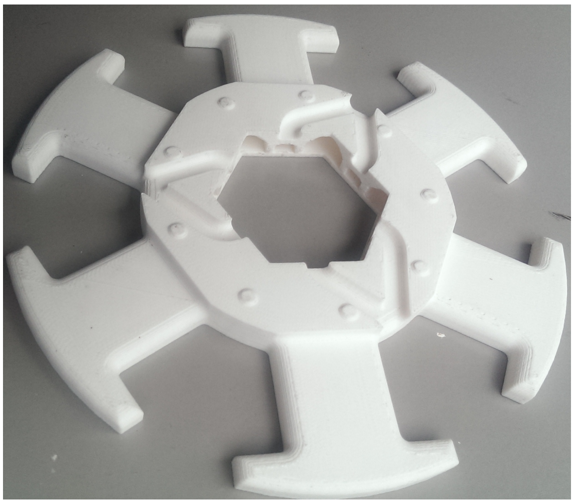

Figure 4.34: 3D printed closed end plate.

A leakage test is performed which reveals the 3D printed material is not tight when air is blown through the channels by a compressor. The reason for the leakage is the process of 3D printing, where material is added in thin layers (0.1 *mm*), which results in small gaps due to insufficient bonding between each layer. It might be possible to seal the end plate by applying a solvent, e.g. acetone, to the outer surface but it is decided to trust in the improved resin casting is able to seal the small leakages.

Residual stresses induced by the 3D printing process might be critical when the material is heated [15]. The residual stresses are induced as the plastic shrinks when it is cooled, and as the layers are cooled at diverse time, they shrink relatively to each other, which causes the residual stress. These stresses may result in deformation if the material is heated because the strength is reduced. However the end plates are cast into resin, why it is assessed the resin supports the end plates and therefore they will not deform during operation. The critical point is when the resin is cast, since the end plates are heated and the resin is not hardened. Prior to the resin casting, the end plates are heat tested up to $75°C$, which has no influence on the stiffness of the end plates.

The end plates are $1.5\ mm$ higher than the end plates from PMSM-v1, which means the stator lamination stack has to be reduced from $30\ mm$ to $27\ mm$. The number of laminations is reduced from 144 to 131, which means the stacking factor is 97%. The reduced stator stack causes a reduced inductance.

4.3.2 Resin casting

The purpose of the resin is to seal the gaps between the shaft and the end plates and seal the small leakages from the end plates. The resin casting process is improved based on the experiences from the PMSM-v1. Before the stator is placed in the mould, duct tape is added to the stator laminations to ensure the resin does not attach to them. In figure 4.35 the stator being wound is shown and in figure 4.36 the stator with the duct tape is shown. The end plates are glued to the stator laminations to ensure a good heat transfer between the two surfaces.

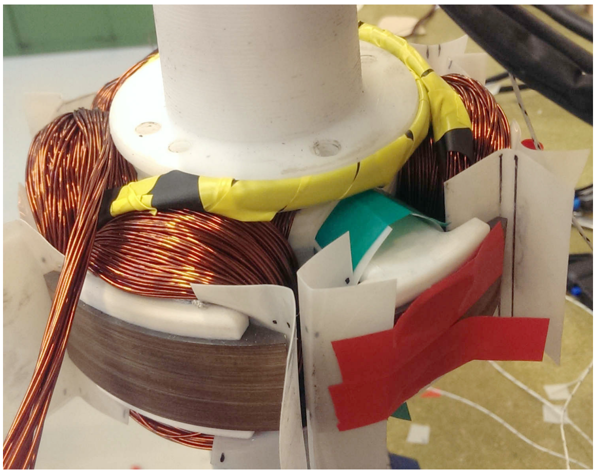

Figure 4.35: Stator-v2 being wound.

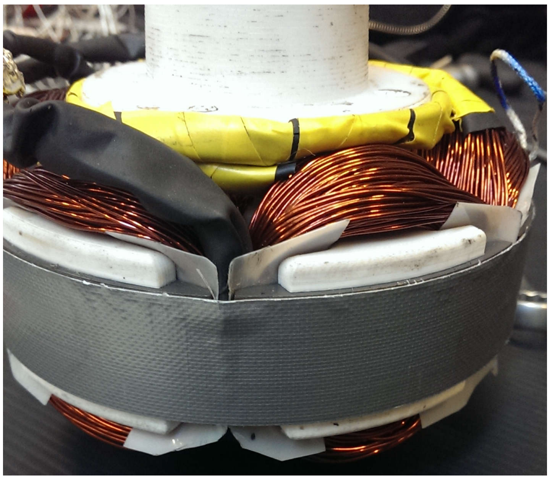

Figure 4.36: Stator-v2 with duct tape attached to the laminations.

A flowchart of the resin casting process is shown in figure 4.37. The resin is mixed at AAU to avoid the transportation time from Dantrafo A/S. The unmixed resin, rotor and stator are preheated to $55°C$ to ensure a low viscosity of the resin. The resin has a lower viscosity at around $80°C$, however at this temperature the wax, which prevents the resin from filling the cooling channels, melts. The resin is mixed and afterwards degassed in a vacuum chamber. Vacuum causes the air and gas bubbles in the resin to expand and reach the surface. The degassing is performed until no more gas bubbles are observed and the entrapped air and gasses are removed.

The resin is filled into the stator mould and it is put into the vacuum oven where the temperature is set to $55°C$. The pressure in the oven is lowered to around $10\ mbar$ (according to the vacuum meter in the oven). Air pockets in the resin are sucked out when vacuum is applied. The stator is refilled and vacuum is applied three times, each with duration of $45\ min$, to ensure the mould is full and the air pockets are removed.

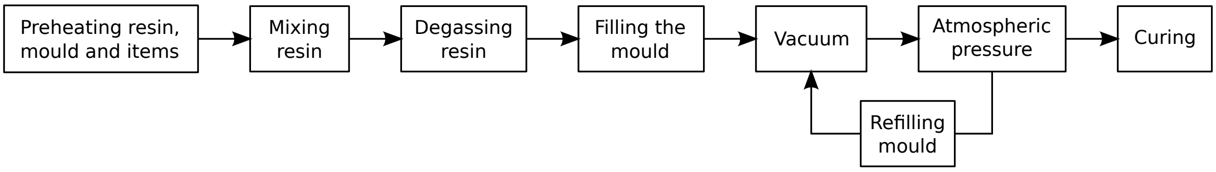

Figure 4.37: Flowchart of the resin casting process.

After the refill, gas bubbles due to degassing of the resin persist, which might be due to a lower pressure in the oven than during the first degassing in a vacuum chamber. Atmospheric pressure makes the gas bubbles contract. It is important to release vacuum before the resin starts to cure, to avoid the bubbles in the cured stator. After approximately three hours where vacuum and atmospheric pressure is alternated, it is assessed that all air pockets are removed. Vacuum is released and the remaining gas bubbles contract as expected. The stator cures at atmospheric pressure for the remaining time. Pictures from the casting process are shown in appendix B.7.

In figure 4.38 and 4.39 the stator-v2 is shown after the resin casting process, where the mould is removed. No resin is present on the laminations after the duct tape is removed. Few air pockets persist and the outcome of the casting process is a great improvement compared to stator-v1. Resin is still located on the surfaces for the bearings.

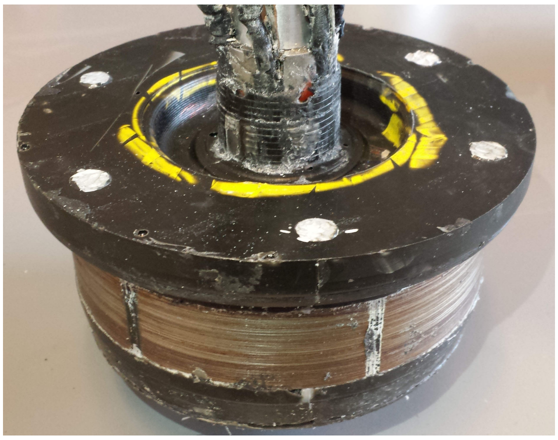

Figure 4.38: Stator-v2 after resin casting.

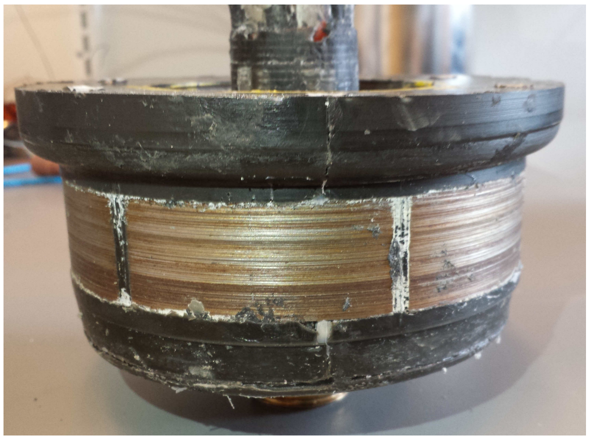

Figure 4.39: Stator-v2 where the laminations are shown.

Few air pockets still exist in the bottom of the stator as shown in figure 4.40 and 4.41. Two pockets are critical (indicated with blue arrows) as they are near the end plate. Resin has covered the end plate in the pocket to the left, while the white end plate is visible in the end plate to the right. These air pockets are due to the mould being filled from the top, why the air pockets have to travel a longer distance out of the mould compared to the air in the top. It must be tested if these two pockets result in leakage.

Figure 4.40 and 4.41 also show sign from silicone, which was used to seal the stator mould before the mould was assembled. The sealing was necessary as a new tight mould was not manufactured, why the mould from stator-v1 was reused. However the pockets from where the silicone has been are only superficial, why it has no impact on the sealing of the cooling system.

To improve the casting of rotor-v2, it is decided to reduce the amount of resin to avoid a thick resin layer on the laminations. Figure 4.42 shows the desired location of the resin. The resin must be placed above and beneath the laminations. The tricky part is to fill the volume between the rotor mould and the top of the laminations, as the opening is around 1 *mm*. It is attempted to use an injection needle to fill this

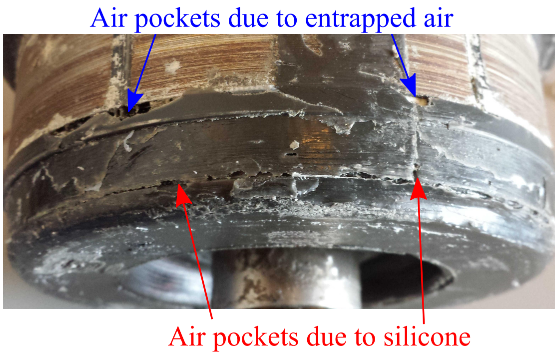

Figure 4.40: Stator-v2 bottom where air pockets and remains of silicone are shown.

Figure 4.41: Stator-v2 bottom where superficial air pockets due to the remains of silicone are shown.

gap, however it is difficult to avoid resin on the laminations and to judge if the resin enters the small gap while the rotor is spinning.

Figure 4.43 shows the result of the resin casting. A thin layer of resin is located on the laminations, which is spill from the filling of the top with the injection needle. This layer must be removed, but it is assessed to be an easy task due to the thin layer and no turning lathe is required.

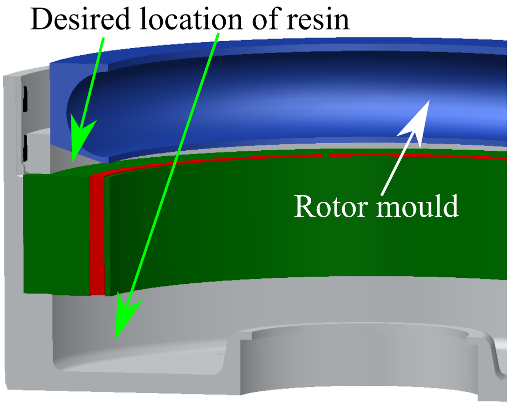

Figure 4.42: Rotor with the rotor mould.

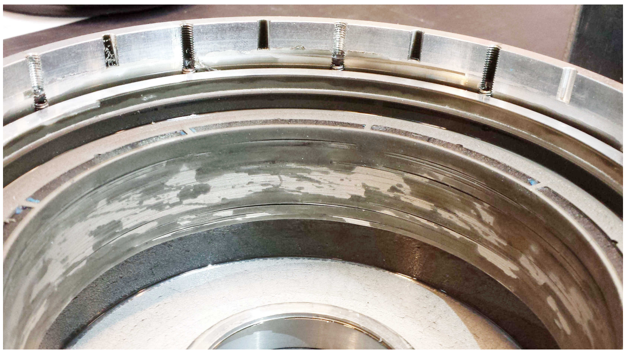

Figure 4.43: Rotor-v2 where the laminations are shown.

The attempt to fill the top of the laminations failed, as the laminations and the PMs are not covered by the resin. The missing resin reduces the emission of heat and the PMs are not sealed. It is not considered to be an issues since the losses in the PMSM are mainly located in the stator teeth, windings, and the bearings as discussed in chapter 8, why the temperature of the rotor is not expected to be critical.

The small amount of excess resin on the stator and rotor was removed by heating with a heat gun and then cut the resin off using a utility knife, why no shorts are made between the laminations of PMSM-v2.

4.3.3 Test of liquid cooling

To test the sealing of stator-v2, the cooling system is connected to the stator and heated by a DC current in the windings. Only a small leakage between the laminations is discovered. The water penetrates from the cooling channel in the stator teeth and through the laminations as shown in figure 4.44. Fortunately the leakage is small and it might be sealed by using a leak repair product.

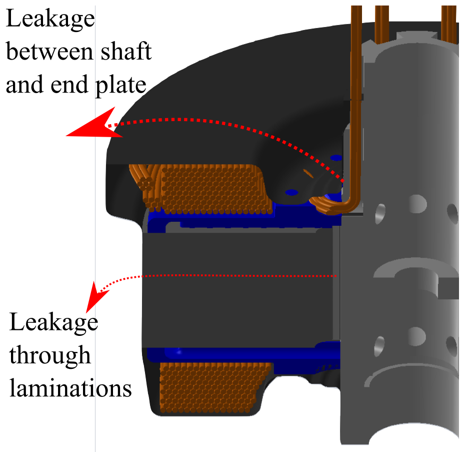

Figure 4.44: The two places where leakage occur in stator-v2.

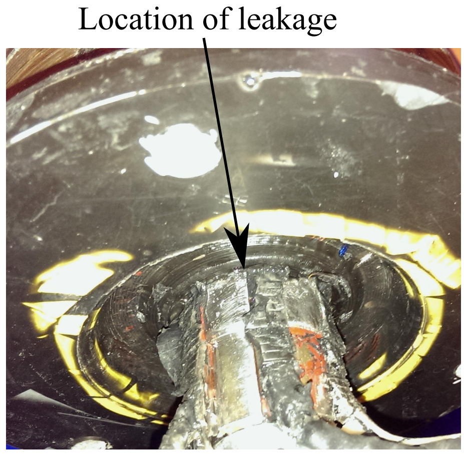

Figure 4.45: Location of leakage after the excess resin was removed from the shaft.

However as the resin located on the surface used to mount the bearing is removed, leakage starts where the end plate is mounted on the shaft as shown in figure 4.44 and 4.45. This is due to only a thin layer of resin is present on the top of the end plate to make the PMSM as compact as possible. During the removal of the excess resin, the resin that seals the small leakage between the end plate and shaft might have been loosened. The leakage cannot to be stopped by a leak repair product and due to a limited time period of this project further solutions to seal stator-v2 are not tested. Even if the leakage is sealed from the outside, water is still present around the conductors which causes a short circuit if a conductor has a small scratch. Despite the leakages, the sealing of stator-v2 is an improvement compared to stator-v1 and the two air pockets at the end plates did not result in leakage from the end plates.

4.3.4 Experiences from PMSM-v2

The experiences gained through the manufacturing of PMSM-v2 are summarised below:

- New rotor mould is required.
- Further improvement of the cooling system design is required to prevent leakages.
- Consider a redesign of the cooling system with pipes instead of relying on the resin casting.

To ensure a better resin casting of the rotor, a redesign of the rotor mould is required. A possible solution is depicted in figure 4.46, where the resin is filled from two ways, to ensure the area above and beneath the laminations are filled, while the inner surface of the laminations are free of resin. Centrifugal casting is still applied to ensure the resin is evenly distributed.

Improvements of sealing could be performed by adding a thicker layer of resin between shaft and end plate. This makes the PMSM equivalent longer to the amount of added resin, as the remaining dimensions in the PMSM cannot be reduced. The cooling channel through the stator might be sealed by a pipe that goes into each end plate or a redesigned 3D printed end plate. The concept is shown in figure 4.47, where each end plate is printed with channels that goes through the stator and fits into each other. However it has not been tested if it is possible to print the end plate in one piece or if the channels or pipes must be mounted afterwards.

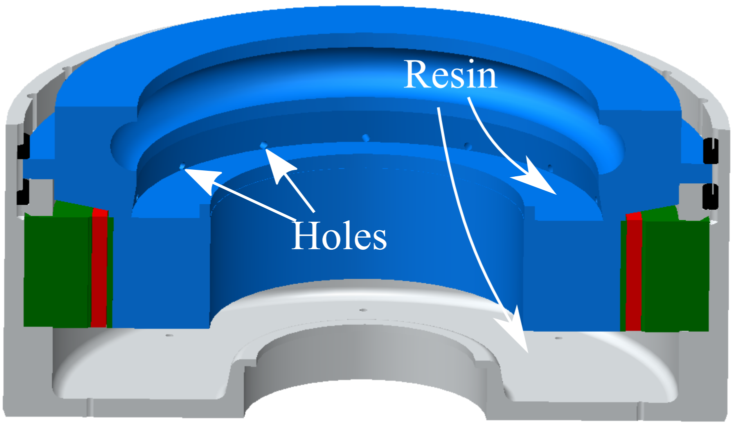

Figure 4.46: Redesigned rotor mould to ensure a better casting of the rotor.

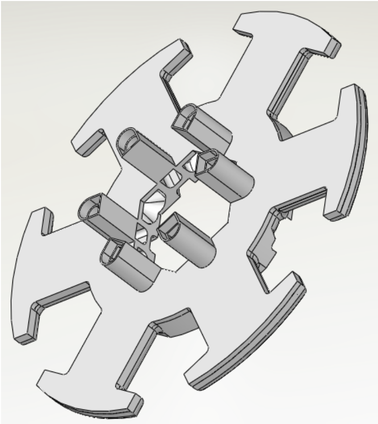

Figure 4.47: End plate that seals the leakage between the laminations.

CHAPTER

5 ELECTRICAL MODEL

In this chapter a mathematical model of the PMSM is developed based on the components and design of the PMSM. The voltage equations for the stator windings are derived in the stationary ABC coordinate frame. To simplify the model, the voltage equations are first transformed to a stationary $\alpha\beta$ frame and secondly to a rotor fixed dq reference frame. The model is derived based on [16] [17] [18] [19].

The voltage equations are derived from physical considerations of the PMSM, depicted in figure 5.1. The windings are considered as symmetric concentrated coils with resistances and inductances. The diagram of the stator is shown in figure 5.2.

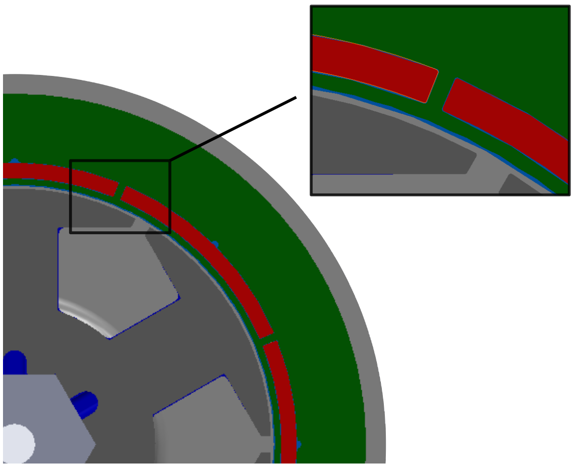

Figure 5.1: Sectional view of the PMSM.

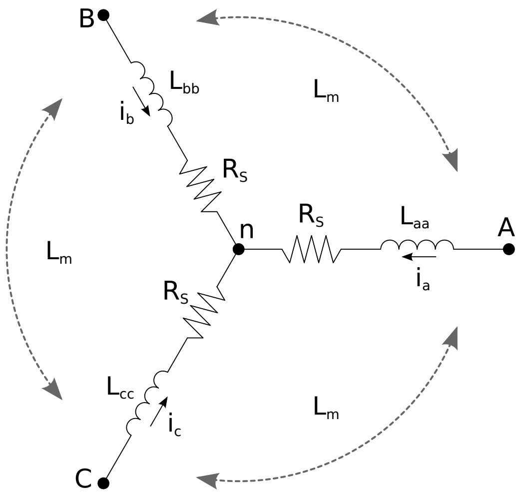

Figure 5.2: Equivalent stator diagram.

Where in figure 5.2:

i_i	Current, $[A]$
L_{ii}	Self inductance, $[H]$
L_m	Mutual inductance, $[H]$
R_s	Resistance of windings, $[\Omega]$

Simplifications

In order to reduce the complexity of the PMSM model, some simplifications are made [20]:

- Higher order harmonics are neglected
- The gaps between the magnets, shown in figure 5.1, are neglected
- Magnetic saturation and anisotropy effects are neglected
- The stator resistance, reactance and the permanent-magnet flux from the rotor are considered to be constant
- Core losses are not included in the electric model

Based on these simplifications the model is developed.

5.1 Voltage equations

The voltage equations are set up for the stationary phase reference frame in this section. Figure 5.2 shows an equivalent circuit of the stator windings in a wye-connection. The windings are modelled with three equal resistances and inductors in series. The instantaneous voltages for the three stator windings are described by equation (5.1) and (5.2).

$$\underline{u_{abc}} = R_s\, \underline{i_{abc}} + \frac{d}{dt}\underline{\Psi_{abc}} \tag{5.1}$$

$$\underline{u_{abc}} = \begin{bmatrix} u_{an} \\ u_{bn} \\ u_{cn} \end{bmatrix} \quad ; \quad \underline{i_{abc}} = \begin{bmatrix} i_a \\ i_b \\ i_c \end{bmatrix} \quad ; \quad \underline{\Psi_{abc}} = \begin{bmatrix} \Psi_a \\ \Psi_b \\ \Psi_c \end{bmatrix} \tag{5.2}$$

Where in equation (5.1) and (5.2):

u_{in}	Phase voltage, $[V]$
Ψ_i	Flux linkage, $[Wb]$

The flux linkage has two contributions, one from the current in the stator windings and one from the permanent-magnet flux from the rotor:

$$\underline{\Psi_{abc}} = \underline{\Psi_{abc(s)}} + \underline{\Psi_{pm(r)}} \tag{5.3}$$

$$\underline{\Psi_{abc}} = \begin{bmatrix} L_{aa} & L_{ab} & L_{ac} \\ L_{ba} & L_{bb} & L_{bc} \\ L_{ca} & L_{cb} & L_{cc} \end{bmatrix} \underline{i_{abc}} + \lambda_{pm} \begin{bmatrix} cos(\theta_{re}) \\ cos\left(\theta_{re} - \frac{2\pi}{3}\right) \\ cos\left(\theta_{re} - \frac{4\pi}{3}\right) \end{bmatrix} \tag{5.4}$$

Where in equation (5.4):

θ_{re}	Electric angle, $[rad]$
λ_{pm}	Permanent magnet flux linkage, $[Wb]$

Simplifying inductance matrix

The inductance matrix can be simplified due to the uniform air gap which makes the self inductances equal. The self inductances are defined as the sum of the leakage inductance and magnetisation inductance [16], when neglecting the rotor position dependency [17]:

$$L_{aa} = L_{bb} = L_{cc} = L_{ls} + L_A \tag{5.5}$$

Where in equation (5.5):

L_A	Magnetisation inductance, $[H]$
L_{ls}	Leakage inductance, $[H]$

The PMSM is assumed to be symmetric, which means the phases are equally distributed with 120° between and the coils have the same number of turns. This leads to a simplified mutual inductance as stated in equation (5.6).

$$L_m = L_{ab} = L_{ba} = L_{ac} = L_{ca} = L_{bc} = L_{cb} \tag{5.6}$$

The inductance matrix from equation (5.4) can be expressed as:

$$\underline{\underline{L}} = \begin{bmatrix} L_{aa} & L_{ab} & L_{ac} \\ L_{ba} & L_{bb} & L_{bc} \\ L_{ca} & L_{cb} & L_{cc} \end{bmatrix} \Rightarrow \underline{\underline{L}} = \begin{bmatrix} L_{ls}+L_A & L_m & L_m \\ L_m & L_{ls}+L_A & L_m \\ L_m & L_m & L_{ls}+L_A \end{bmatrix} \tag{5.7}$$

The inductance matrix can be reduced, because the windings are connected in a star connection, and thus Kirchoff's current law can be applied at the star point:

$$i_a + i_b + i_c = 0 \tag{5.8}$$

By multiplication of the mutual inductance and a rearrangement, three expressions are derived:

$$L_m\, i_b + L_m\, i_c = -L_m\, i_a \tag{5.9}$$

$$L_m\, i_a + L_m\, i_c = -L_m\, i_b \tag{5.10}$$

$$L_m\, i_a + L_m\, i_b = -L_m\, i_c \tag{5.11}$$

Equation (5.9), (5.10) and (5.11) are used to reduce the inductance matrix in equation (5.7). The mutual inductance can be defined as stated in equation (5.12) when neglecting the rotor dependency. The factor -1/2 derives from the angle between the phases. Using equation (5.12) the inductance matrix stated in equation (5.7) is reduced to equation (5.13).

$$L_m = -\frac{1}{2}L_A \tag{5.12}$$

$$\underline{\underline{L}} = \begin{bmatrix} L_{ls}+L_A-L_m & 0 & 0 \\ 0 & L_{ls}+L_A-L_m & 0 \\ 0 & 0 & L_{ls}+L_A-L_m \end{bmatrix} \Rightarrow \underline{\underline{L}} = \begin{bmatrix} L_{ls}+\frac{3}{2}L_A & 0 & 0 \\ 0 & L_{ls}+\frac{3}{2}L_A & 0 \\ 0 & 0 & L_{ls}+\frac{3}{2}L_A \end{bmatrix} \tag{5.13}$$

Simplified voltage equations

From the simplified inductance matrix the final voltage equations for the PMSM can be expressed as stated in equation (5.14) and (5.16). Equation (5.14) is written out in equation (5.17).

$$\boxed{\underline{u_{abc}} = R_s\, \underline{i_{abc}} + \frac{d}{dt}\underline{\Psi_{abc}}} \tag{5.14}$$

$$\underline{\Psi_{abc}} = \begin{bmatrix} L_{ls}+\frac{3}{2}L_A & 0 & 0 \\ 0 & L_{ls}+\frac{3}{2}L_A & 0 \\ 0 & 0 & L_{ls}+\frac{3}{2}L_A \end{bmatrix} \underline{i_{abc}} + \lambda_{pm} \begin{bmatrix} cos(\theta_{re}) \\ cos\left(\theta_{re}-\frac{2\pi}{3}\right) \\ cos\left(\theta_{re}-\frac{4\pi}{3}\right) \end{bmatrix} \tag{5.15}$$

$$\boxed{\underline{\Psi_{abc}} = \underline{\underline{L}}\, i_{abc} + \lambda_{pm}\, \underline{\gamma}} \tag{5.16}$$

$$\underline{u_{abc}} = R_s\, \underline{i_{abc}} + \underline{\underline{L}}\, \frac{d}{dt}\underline{i_{abc}} + \lambda_{pm}\frac{d}{dt}\underline{\gamma} \tag{5.17}$$

5.2 Stationary reference frame, αβ

In order to transform the instantaneous quantities (current, voltage or flux linkage) into the stationary reference frame αβ, equation (5.18) is used, where the complex operator, a, is defined as stated in equation (5.19).

$$\begin{aligned} \underline{k_{\alpha\beta}} &= \frac{2}{3}\begin{bmatrix} 1 & a & a^2 \end{bmatrix}\begin{bmatrix} k_A & k_B & k_C \end{bmatrix}^T \\ &= \frac{2}{3}\left[k_A + a\, k_B + a^2\, k_C\right] \end{aligned} \tag{5.18}$$

$$a = e^{j\frac{2\pi}{3}} \qquad \Rightarrow \qquad a^2 = e^{j\frac{4\pi}{3}} \tag{5.19}$$

$$k_\alpha = Re\left(k_{\alpha\beta}\right) \qquad ; \qquad k_\beta = Im\left(k_{\alpha\beta}\right) \tag{5.20}$$

Where in equation (5.18) and (5.19):

a	Complex rotation operator, $[-]$
j	Complex operator, $[-]$
k_i	PMSM quantity (e.g current, voltage), $[-]$

A graphical representation of the αβ frame is shown in figure 5.3. The green lines indicate the phases, which are combined into a complex space vector, $k_{\alpha\beta}$. The real part of $k_{\alpha\beta}$ is defined as k_α and the imaginary part is defined as k_β.

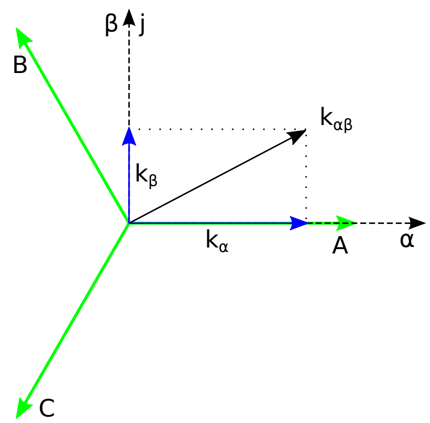

Figure 5.3: ABC quantities transformed into the stationary reference frame (Clark transform).

Voltage equations in the stationary reference frame

Using equation (5.18) the voltage equation from section 5.1 can now be rewritten to space vector form, where the terms are stated in equation (5.24) and (5.25).

$$\underline{u_{\alpha\beta}} = \frac{2}{3}\left(u_{an} + a\, u_{bn} + a^2\, u_{cn}\right) \tag{5.21}$$

$$= R_s\, \frac{2}{3}\left(i_a + a\, i_b + a^2\, i_c\right) + \frac{d}{dt}\left(\frac{2}{3}\left(\Psi_a + a\, \Psi_b + a^2\, \Psi_c\right)\right) \tag{5.22}$$

$$\boxed{\underline{u_{\alpha\beta}} = R_s\, \underline{i_{\alpha\beta}} + \frac{d}{dt}\underline{\Psi_{\alpha\beta}}} \tag{5.23}$$

$$\underline{i_{\alpha\beta}} = \frac{2}{3}\left(i_a + a\, i_b + a^2\, i_c\right) \tag{5.24}$$

$$\underline{\Psi_{\alpha\beta}} = \frac{2}{3}\left(\Psi_a + a\, \Psi_b + a^2\, \Psi_c\right) \tag{5.25}$$

Including the definitions of $\underline{\Psi_{abc}}$ stated in equation (5.7), equation (5.25) can be rewritten as stated in equation (5.26). Using the equation (5.27), further reduction of the last term is shown in equation (5.28) to (5.31).

$$\begin{aligned}\underline{\Psi_{\alpha\beta}} =& \frac{2}{3}\ (L_{ls} + \frac{3}{2}L_A)\ (i_a + a\, i_b + a^2\, i_c) \\ &+ \frac{2}{3}\left(\lambda_{pm}\left(cos(\theta_{re}) + a\ cos\left(\theta_{re} - \frac{2\pi}{3}\right) + a^2\ cos\left(\theta_{re} - \frac{4\pi}{3}\right)\right)\right)\end{aligned} \tag{5.26}$$

$$cos(\theta_{re}) = \frac{1}{2}\left(e^{j\ \theta_{re}} + e^{-j\ \theta_{re}}\right) \tag{5.27}$$

$$\frac{1}{3}\lambda_{pm}\left(e^{j\theta_{re}} + e^{-j\theta_{re}} + e^{j\frac{2\pi}{3}}\left(e^{j\left(\theta_{re} - \frac{2\pi}{3}\right)} + e^{-j\left(\theta_{re} - \frac{2\pi}{3}\right)}\right)\right) + e^{j\frac{4\pi}{3}}\left(e^{j\left(\theta_{re} - \frac{4\pi}{3}\right)} + e^{-j\left(\theta_{re} - \frac{4\pi}{3}\right)}\right) \tag{5.28}$$

$$= \frac{1}{3}\lambda_{pm}\left(e^{j\theta_{re}} + e^{-j\theta_{re}} + \left(e^{j\theta_{re}} + e^{j\left(-\theta_{re} + \frac{4\,\pi}{3}\right)}\right) + \left(e^{j\theta_{re}} + e^{j\left(-\theta_{re} + \frac{8\pi}{3}\right)}\right)\right) \tag{5.29}$$

$$= \frac{1}{3}\lambda_{pm}\ \left(3e^{j\theta_{re}} + e^{-j\theta_{re}} + e^{-j\theta_{re}}\left(e^{j\frac{4\,\pi}{3}} + e^{j\frac{8\,\pi}{3}}\right)\right) \tag{5.30}$$

$$= \lambda_{pm}\ e^{j\theta_{re}} \tag{5.31}$$

Inserting the reduced term into the expression for $\underline{\Psi_{\alpha\beta}}$ yields:

$$\underline{\Psi_{\alpha\beta}} = \frac{2}{3}\ (L_{ls} + \frac{3}{2}L_A)\ (i_a + a\, i_b + a^2\, i_c) + \lambda_{pm}\ e^{j\theta_{re}} \tag{5.32}$$

$$\boxed{\underline{\Psi_{\alpha\beta}} = (L_{ls} + \frac{3}{2}L_A)\ \underline{i_{\alpha\beta}} + \ \lambda_{pm}\ e^{j\theta_{re}}} \tag{5.33}$$

Equation (5.23) and (5.33) states the space vector model of the PMSM.

5.3 Rotating reference frame, dq

The PMSM quantities can be transformed from the stationary reference frame ($\alpha\beta$) into a rotating reference frame (dq), which generally can rotate with an arbitrary velocity. However in PMSMs the rotating velocity of the reference frame has to be fixed to the rotor velocity ($\dot{\theta}_{re}$) in order to eliminate the time varying inductances [16].

A graphical representation of the dq transformation is shown in figure 5.4. The dashed $\alpha\beta$-axis indicates the stationary reference frame, and the dq-axis indicates the rotating reference frame. k_{dq} indicates a PMSM quantity in the dq frame. k_d is defined as the real part of k_{dq} and k_q is defined as the imaginary part.

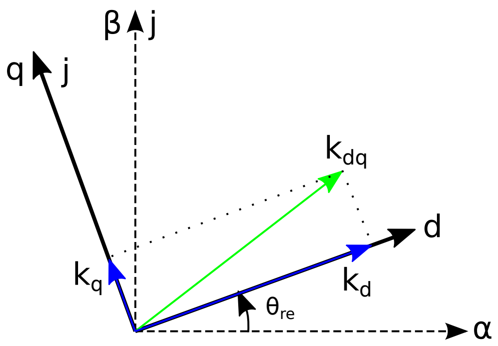

Figure 5.4: Park transformation.

$$\underline{k_{dq}} = \underline{k_{\alpha\beta}}\, e^{-j\theta_{re}} \Rightarrow \tag{5.34}$$

$$k_d = Re(\underline{k_{dq}}) \quad ; \quad k_q = Im(\underline{k_{dq}}) \tag{5.35}$$

$$\begin{bmatrix} k_d \\ k_q \end{bmatrix} = \begin{bmatrix} cos(\theta_{re}) & -sin(\theta_{re}) \\ sin(\theta_{re}) & cos(\theta_{re}) \end{bmatrix} \begin{bmatrix} k_\alpha \\ k_\beta \end{bmatrix}$$

Voltage equations in the rotating reference frame

To transform equation (5.23) into the rotating reference frame, equation (5.34) can be used, which is stated in equation (5.36). Using the chain rule equation (5.36) can be rewritten to (5.37) [17].

$$\underline{u_{\alpha\beta}}\, e^{-j\theta_{re}} = R_s\, \underline{i_{\alpha\beta}}\, e^{-j\theta_{re}} + e^{-j\theta_{re}} \frac{d}{dt} \underline{\Psi_{\alpha\beta}} \tag{5.36}$$

$$= R_s\, \underline{i_{\alpha\beta}}\, e^{-j\theta_{re}} + \frac{d}{dt} \underline{\Psi_{\alpha\beta}}\, e^{-j\theta_{re}} + j\, \omega_{re}\, \underline{\Psi_{\alpha\beta}}\, e^{-j\theta_{re}} \tag{5.37}$$

$$\boxed{\underline{u_{dq}} = R_s\, \underline{i_{dq}} + \frac{d}{dt} \underline{\Psi_{dq}} + j\omega_{re}\, \underline{\Psi_{dq}}} \tag{5.38}$$

Where in equation (5.37):

ω_{re}	Electric velocity, $[rad/s]$

In equation (5.38) the quantities are defined as stated in equation (5.39) to (5.41). Inserting equation (5.33) into equation (5.41) leads to equation (5.42), which is reduced to equation (5.43) using the definition stated in equation (5.34).

$$\underline{u_{dq}} = \underline{u_{\alpha\beta}}\, e^{-j\theta_{re}} \tag{5.39}$$

$$\underline{i_{dq}} = \underline{i_{\alpha\beta}}\, e^{-j\theta_{re}} \tag{5.40}$$

$$\underline{\Psi_{dq}} = \underline{\Psi_{\alpha\beta}}\, e^{-j\theta_{re}} \tag{5.41}$$

$$= (L_{ls} + \frac{3}{2} L_A)\, \underline{i_{\alpha\beta}}\, e^{-j\theta_{re}} + \lambda_{pm}\, e^{j\theta_{re}}\, e^{-j\theta_{re}} \tag{5.42}$$

$$\boxed{\underline{\Psi_{dq}} = (L_{ls} + \frac{3}{2} L_A)\, \underline{i_{dq}} + \lambda_{pm}} \tag{5.43}$$

Due to a uniform air gap between the rotor and stator and the small space between the permanent magnets, the inductances in the d- and q-direction are assumed to be equal. The magnetizing inductances are defined as stated in equation (5.44) [16]. This leads to equation (5.45).

$$L_{mdq} = \frac{3}{2}\, L_A \tag{5.44}$$

$$L = L_d = L_q = L_{ls} + \frac{3}{2}\, L_A = L_{ls} + L_{mdq} \tag{5.45}$$

Where in equation (5.44):

L_{mdq}	Magnetisation inductance, $[H]$

Separating into d- and q-axis

The voltage and flux linkage equations are separated into the d- and q-axis, using the expressions stated in equation (5.46) to (5.48). The separated voltage and flux linkage equations are stated in equation (5.53), (5.54), (5.50) and (5.51), which defines the rotating reference frame model of the PMSM.

$$\underline{u_{dq}} = u_d + j\, u_q \tag{5.46}$$

$$\underline{i_{dq}} = i_d + j\, i_q \tag{5.47}$$

$$\underline{\Psi_{dq}} = \Psi_d + j\, \Psi_q \tag{5.48}$$

$$\boxed{\underline{u_{dq}} = R_s\, \underline{i_{dq}} + \frac{d}{dt}\underline{\Psi_{dq}} + j\omega_{re}\, \underline{\Psi_{dq}}} \tag{5.49}$$

$$u_d = R_s\, i_d + \frac{d}{dt}\Psi_d - \omega_{re}\, \Psi_q \tag{5.50}$$

$$u_q = R_s\, i_q + \frac{d}{dt}\Psi_q + \omega_{re}\, \Psi_d \tag{5.51}$$

$$\boxed{\underline{\Psi_{dq}} = L\, \underline{i_{dq}} + \lambda_{pm}} \tag{5.52}$$

$$\Psi_d = L\, i_d + \lambda_{pm} \tag{5.53}$$

$$\Psi_q = L\, i_q \tag{5.54}$$

5.4 Electro-magnetic torque

The developed electro-magnetic torque is calculated by considering the electrical power supplied to the PMSM and the mechanical power delivered by the PMSM. The power supplied to the PMSM is calculated from the voltages and currents in the dq-frame [16]:

$$P_e = \frac{3}{2}(u_d\, i_d + u_q\, i_q) \tag{5.55}$$

Where in equation (5.55):

P_e	Instantaneous power, $[W]$

The expressions for the voltages are inserted in equation (5.55) from equation (5.50) and (5.51), and the expression for the instantaneous power is rewritten as:

$$P_e = \frac{3}{2}\left(\left(R_s\, i_d + \frac{d}{dt}\Psi_d - \omega_{re}\, \Psi_q\right)\, i_d + \left(R_s\, i_q + \frac{d}{dt}\Psi_q + \omega_{re}\, \Psi_d\right)\, i_q\right) \Leftrightarrow \tag{5.56}$$

$$P_e = \underbrace{\frac{3}{2}\, R_s\, (i_d^2 + i_q^2)}_{Resistive\ heating} + \underbrace{\frac{3}{2}\left(\frac{d}{dt}\Psi_d\, i_d + \frac{d}{dt}\Psi_q\, i_q\right)}_{Change\ of\ energy\ in\ the\ magnetic\ field} + \underbrace{\frac{3}{2}\, \omega_{re}\, (\Psi_d\, i_q - \Psi_q\, i_d)}_{Energy\ conversion} \tag{5.57}$$

The first term express resistive power losses in the conductors, the second term is a change in the energy of magnetic field and the third term express the conversion from electrical energy to mechanical energy:

$$P_{em} = \frac{3}{2}\left(\omega_{re}\ \Psi_d\ i_q - \omega_{re}\Psi_q\ i_d\right) \tag{5.58}$$

Where in equation (5.58):

P_{em}	Electro-magnetic power, $[W]$

The relation between the angular velocity of the dq reference frame and the mechanical angular velocity of the rotor is:

$$\omega_{rm} = \frac{2}{p_b}\ \omega_{re} \tag{5.59}$$

Where in equation 5.59:

p_b	Number of poles, $[-]$
ω_{rm}	Mechanical angular velocity, $[rad/s]$

To calculate the torque, the relation between the power and the torque is used:

$$\tau_{em} = \frac{P_{em}}{\omega_{rm}} \tag{5.60}$$

Where in equation (5.60):

τ_{em}	Electro-magnetic torque, $[Nm]$

Equation (5.58) and (5.59) are inserted into Eq. (5.60), which yields:

$$\tau_{em} = \frac{3}{2}\ \frac{p_b}{2}\left(\Psi_d\ i_q - \Psi_q\ i_d\right) \tag{5.61}$$

The expression for the electro-magnetic torque is derived by inserting Ψ_d and Ψ_q from equation (5.53) and (5.54):

$$\tau_{em} = \frac{3}{2}\ \frac{p_b}{2}\left(\left(\frac{2}{3}\ L\ i_d\ + \lambda_{pm}\right)\ i_q - \left(\frac{2}{3}\ L\ i_q\right)\ i_d\right) \Leftrightarrow \tag{5.62}$$

$$\boxed{\tau_{em} = \frac{3}{2}\ \frac{p_b}{2}\ \lambda_{pm}\ i_q} \tag{5.63}$$

From equation (5.63) it is seen that the electro-magnetic torque is generated from the q-axis current and the flux linkage by the permanent magnets. Thus it is possible to control the electro-magnetic torque by controlling the q-axis current and it is desirable to minimise the d-axis current.

5.5 Torque contributions

To describe the interaction between the electro-magnetic and mechanical system, the torque contributions are described. The electro-magnetic system delivers the electro-magnetic torque, which interacts with the other torque contributions and inertia of the mechanical system that results in acceleration. This is described by Newton's 2nd law for rotational motion:

$$\tau_{res} = J\ \frac{d}{dt}\omega_{rm} \tag{5.64}$$

$$\frac{d}{dt}\omega_{rm} = \frac{\tau_{res}}{J} \tag{5.65}$$

Where in equation (5.65):

J	Moment of inertia, $[kg\ m^2]$
τ_{res}	Resulting torque, $[Nm]$

The resulting torque is the sum of the torque contributions from:

- Electro-magnetic torque
- Core loss torque
  - Hysteresis
  - Eddy current
- Friction loss torque
  - Dry friction
  - Viscous friction
  - Windage
- Load torque

Another torque developed in PMSMs is cogging torque. Cogging torque is developed as the reluctance of the stator is non uniform, due to the stator slots, which causes a torque due to flux variations from the rotor PMs. The torque is dependent on the number of PMs and the design of the stator teeth and it is notable at lower speeds. Cogging torque does not provide a work, as the average torque contribution is zero for one revolution, thus it is not included in the resulting torque. Likewise, reluctance torque is not included in the model, as the inductance in the d- and q-axis are considered being equal. The torques contributions that contribute to the resulting torque are described in the following sections.

5.5.1 Core loss torque

The core losses are modelled as a torque contribution. Another possibility is to model the core losses in the electric model but as the core losses are speed dependent, it is chosen to model the speed depend losses as a torque contribution. The core losses consist of hysteresis loss and eddy current loss.

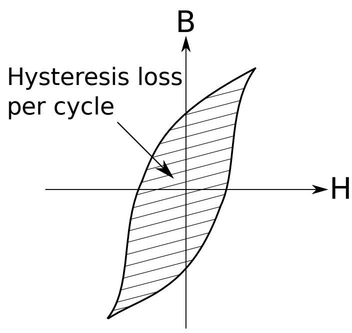

Figure 5.5: B-H loop to visualise the hysteresis loss.

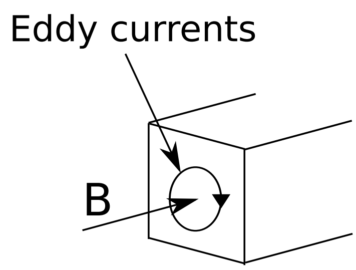

Figure 5.6: Eddy currents induced in a core.

Hysteresis loss

Hysteresis loss occurs when a ferromagnetic material is exposed to a varying magnetic field as it requires energy to magnetise and demagnetise the material magnetisation path is depend on the position on the B-H loop shown in figure 5.5. This results in an energy loss per magnetisation cycle expressed by [21]:

$$P_{hys} = K_h\ B_{max}^n\ \frac{\omega_{re}}{2\ \pi} \tag{5.66}$$

Where in equation (5.66):

B_{max}	Peak flux density, $[T]$
K_h	Hysteresis loss coefficient, $[Nm/T^n]$
n	Material constant (n=1.5-2.5), $[-]$
P_{hys}	Power loss due to hysteresis, $[W]$

The power loss is included as a torque contribution:

$$\tau_{hys} = -\frac{P_{hys}}{\omega_{rm}} \tag{5.67}$$

$$= -\frac{K_h\, B_{max}^n\, p_b}{4\,\pi} \tag{5.68}$$

Where in equation (5.67) and (5.68):

τ_{hys}	Opposing torque due to hysteresis, $[Nm]$

Thus, the hysteresis loss torque is velocity independent.

Eddy current loss

Eddy current loss occurs as a result of a magnetic field passing through an electrical conductor, which induces current that flows within the core as shown in figure 5.5. The eddy currents cause power loss, which is described by the classical Steinmetz formula [21]:

$$P_{eddy} = K_e\, B_{max}^2 \left(\frac{\omega_{re}}{2\,\pi}\right)^2 \tag{5.69}$$

Where in equation (5.69):

K_e	Eddy current loss coefficient, $[Nm/(T^2\ rad/s)]$
P_{eddy}	Power loss due to eddy currents, $[W]$

The power loss is included as a torque contribution:

$$\tau_{eddy} = -\frac{P_{eddy}}{\omega_{rm}} \tag{5.70}$$

$$= -\frac{K_e\, B_{max}^2\ \ p_b}{8\,\pi^2}\ \omega_{re} \tag{5.71}$$

Where in equation (5.70) and (5.71):

τ_{eddy}	Opposing torque due to eddy currents, $[Nm]$

The torque from eddy current loss is proportional to the electrical velocity of the PMSM. To reduce the eddy current loss, laminated sheet metal is used for both rotor and stator.

5.5.2 Windage loss torque

Windage loss is often included in high speed machines, as it is proportional to the velocity squared. Windage loss depends on the smoothness of the object as it is the friction force between a moving object and the air. Windage loss torque is expressed by:

$$\tau_{win} = -K_{win}\,\omega_{rm}^2 \tag{5.72}$$

Where in equation (5.72):

K_{win}	Windage loss coefficient, $[Nm/(rad/s)^2]$
τ_{win}	Opposing torque due to windage, $[Nm]$

5.5.3 Bearing loss torque

The loss in the bearings is dependent on the viscosity of the grease, diameter of the bearings and a bearing constant. The factor K_{bear} express that the torque from the bearings decrease with rising speed [21]. The friction loss torque is expressed as:

$$\tau_{bear} = -K_{bear}\ \omega_{rm}^{2/3} \tag{5.73}$$

Where in equation 5.73:

K_{bear}	Bearing loss coefficient, $[Nm/(rad/s)^{(2/3)}]$
τ_{bear}	Opposing torque due to bearing loss, $[Nm]$

5.5.4 Rotational loss torque

The knowledge of the most common torque contributions and their origin is desirable, but when it comes to estimation of the losses and experimental measurements it is often difficult to predict and verify the losses independently based on a measured total loss. The reason for the difficult prediction is that the losses are dependent on the specific motor design. The rotational loss is a collection of all the opposing torque contributions in a single expression stated in equation (6.17).

$$\tau_{rot} = -K_1\ \omega_{rm}^2 - K_2\ \omega_{rm} - K_3\ \omega_{rm}^{2/3} - K_4 \tag{5.74}$$

Where in equation (5.74):

K_i	Opposing rotational torque coefficients, $[-]$
τ_{rot}	Opposing torque due to rotational loss, $[Nm]$

The losses of the PMSM are investigated further in section 8.1.

5.5.5 Load torque

The load torque is the torque contribution from the load which the PMSM drives, in this case the compressor. The load torque is modelled as a quadratic load, which is a typical fan type load characteristic.

$$\tau_{load} = -K_{l,1}\ \omega_{rm}^2 - K_{l,2}\ \omega_{rm} - K_{l,3} \tag{5.75}$$

Where in equation (5.75):

$K_{l,i}$	Load torque coefficients, $[-]$

This load is not included in τ_{rot} as the load is not included in the test set-up.

5.6 Simulation model

A block diagram of the model is shown in figure 5.7. The equations of the PMSM are derived and implemented in Matlab Simulink. The equations implemented are:

- Voltage equations, (5.50) and (5.51)
- Flux linkage equations, (5.53) and (5.54)
- Torque equations, (5.63) and (5.65)
- Relation between mechanical and electrical velocity, (5.59)

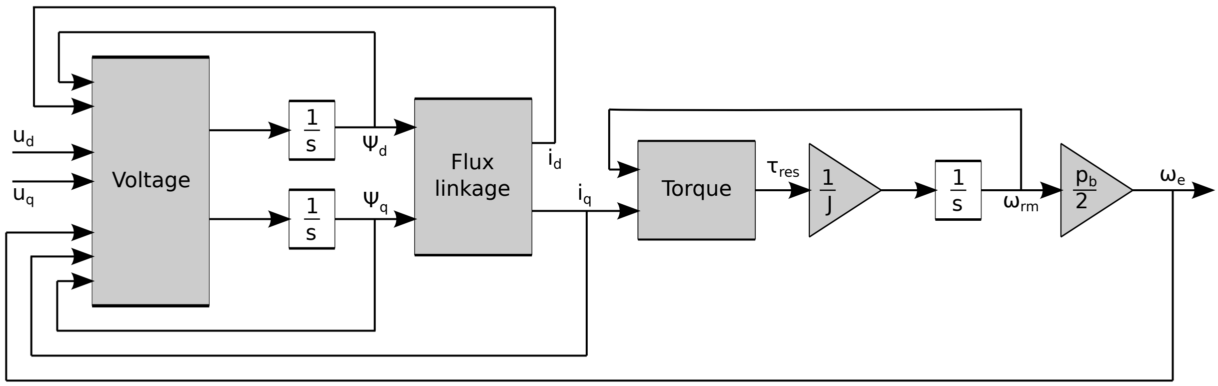

Figure 5.7: Block diagram of the PMSM model.

5.7 VSI model

A full switch model of the inverter is implemented in Matlab Simulink using the PLECS Blockset Package. The PLECS Blockset Package is chosen over the Matlab SimPowerSystems due to a faster simulation time. The model is shown in figure 5.8 with ideal IGBTs with an integrated diode. The neutral point in the VSI is located between the two capacitors with half of the DC voltage across it. The DC link is set to 560 V cf. section 3.5.

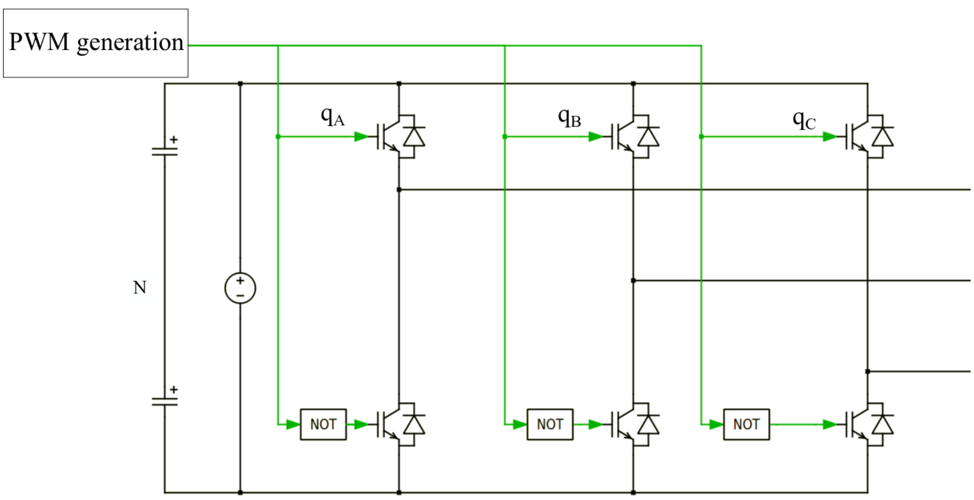

Figure 5.8: PLECS full switch model of the inverter.

Where in figure 5.8:

q_i	PWM control signal for the IGBTs, $[-]$

The switching signals to the IGBTs are generated by the PWM technique from chapter 11. Ideal IGBTs are chosen due to the excessive simulation time connected with the non-ideal IGBTs. Ideal switches are characterised by [12]:

- Able to block arbitrarily large voltages in the off-state.
- Have zero voltage drop when they conduct arbitrarily large currents in the on-state.
- Require no time to switch from on- to off-state.
- Require no power from the control source to trigger the switch.

The most significant of these simplifications is assessed to be the discarded turn on and off time. The turn on and off time leads to power losses due to voltage and current build up and fall. Furthermore dead time is not included in the VSI model, however this could have been implemented despite of the ideal IGBTs. Small variations in the DC link might occur, but this is not modelled. Since dead time is not included and the IGBTs and DC links are modelled as ideal, higher order harmonics due to these phenomena are not included in the VSI output [12]. However the output from the VSI model yields a better modelling of the reality compared to passing ideal sinusoidal voltages to the PMSM model, especially at high speed where the number of switches per revolution is low.

5.7.1 Power losses of VSI

The losses in the VSI are described to identify the losses and determine their origin. The knowledge is important when the switching frequency is determined and measurements including the VSI are performed. In a non-ideal VSI, power losses occur in the loss generating components. The losses are categorised as conduction loss and switching loss. The conduction loss occurs when the switch is in the on-state and the switching losses occur when the switches changes state.

- Conduction loss
  - The loss connected with the small voltage drop when the diode or IGBT conducts current. The loss depends on the size of the conducted current, the on-time and the size of the on-state voltage drop.
- Switching losses
  - Turn on: The loss occurs when an inductive load is driven due to rise time of the voltage and currents. It includes the reverse recovery loss from the diode. It is measured from the time where the on-signal is given and to the time where the IGBT is in the fully on-state.
  - Turn off: The same arguments apply as for the turn-on loss but for fall time of current and voltage instead. It is measured from the time where the off-signal is given and to the time where the IGBT is in the fully off-state.

Furthermore a small leakage current might occur when the switch is turned off, but this current is negligible [12]. The switching losses vary with the switching frequency and the time it takes to turn on and off the IGBTs [12]. The turn-on and turn-off times are in the range of 1 μs in general for IGBTs [12].

CHAPTER

6 PARAMETER DETERMINATION

The parameters for the PMSM model are determined in this chapter. All the parameters are determined from tests performed on PMSM-v1. The parameters of PMSM-v2 are not determined as it was not assembled in this project. The parameters of PMSM-v2 might deviate from PMSM-v1, e.g. the rotational torque parameters, due to no shorts between the rotor and stator laminations, but examination of this is left for future work. The parameters determined are:

- Phase resistance - R_s
- Flux linkage - λ_{pm}
- Inductance - L
- Inertia - J
- Rotational torque coefficients - $K_1,\ K_2,\ K_3,\ K_4$

Line-to-line vs line-to-neutral

The star point is located inside the PMSM as described in section 4.2, why it is not possible to measure the line-to-neutral voltage in connection with the parameter determination. It is possible to convert a peak or RMS value of a line-to-line voltage to a line-to-neutral voltage by division of $\sqrt{3}$ if the voltage is sinusoidal. However it is not possible to recreate the original line-to-neutral sine wave of the voltage if it contains e.g. third order harmonics as these cancel out in the line-to-line measurement. Furthermore when line-to-line voltage measurements are performed, it is not possible to associate all parameters to a certain phase.

6.1 Phase resistance test

The resistance in each of the phases is determined in this section. It is possible to associate the resistance to a certain phase as a DC voltage source and measurements on all three phases are performed. The resistance is temperature dependent which is taken into account. The resistance is first calculated from experimental tests and afterwards compared to an analytical calculated resistance.

6.1.1 Experimental determination

The resistance of the windings in each phase is determined from DC tests where the voltage and current are varied. The tests are performed where one phase (primary) is in series with two parallel phases (secondary) as shown in figure 6.1. An equivalent resistance of this circuit is calculated by the measured voltage and current.

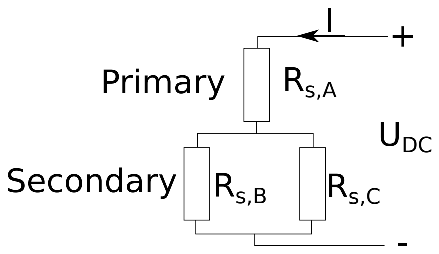

Figure 6.1: Equivalent circuit when phase A is the primary phase.

Where in figure 6.1:

R_s	Resistance of windings, $[\Omega]$
U_{DC}	DC voltage, $[V]$

The equivalent resistances are calculated by ohm's law and then the resistance of each phase is calculated by solving the 3 equations in equation (6.1).

$$R_{eq,A} = R_{s,A} + \frac{1}{\frac{1}{R_{s,B}} + \frac{1}{R_{s,C}}} \quad ; \quad R_{eq,B} = R_{s,B} + \frac{1}{\frac{1}{R_{s,A}} + \frac{1}{R_{s,C}}} \quad ; \quad R_{eq,C} = R_{s,C} + \frac{1}{\frac{1}{R_{s,B}} + \frac{1}{R_{s,A}}} \tag{6.1}$$

Where in equation (6.1):

$R_{eq,i}$	Equivalent resistance, $[\Omega]$

Resistance at 21 $^\circ C$

Tests are performed at different voltages for each phase connected as the primary phase. The voltage is varied from 0.4 V to 2.9 V, which varies the current from 17 A to 140 A, and the data for each phase is plotted in figure 6.2. The DC source is turned on for a short moment to reduce the temperature increment in the windings. The temperature is measured by the thermocouples placed in the windings. Thermocouples are placed in five different positions in the windings as described in section 8.2. Each thermocouple output a spot temperature and each of the temperatures are watched. The average equivalent resistance is calculated for each phase in the primary configuration to reveal if the resistance varies between the phases. The three average equivalent resistances at 21$^\circ C$ are:

$$R_{eq,A} = 0.0205\ \Omega \quad ; \quad R_{eq,B} = 0.0203\ \Omega \quad ; \quad R_{eq,C} = 0.0200\ \Omega \tag{6.2}$$

The equivalent resistances are average values from five measurements for each phase. The five measurements deviates maximum 2% from the average resistance of the same phase which is acceptable. The three phase resistances are:

$$R_{s,A} = 0.0138\ \Omega \quad ; \quad R_{s,B} = 0.0136\ \Omega \quad ; \quad R_{s,C} = 0.0132\ \Omega \tag{6.3}$$

$$R_{s,avg} = 0.0135\ \Omega \tag{6.4}$$

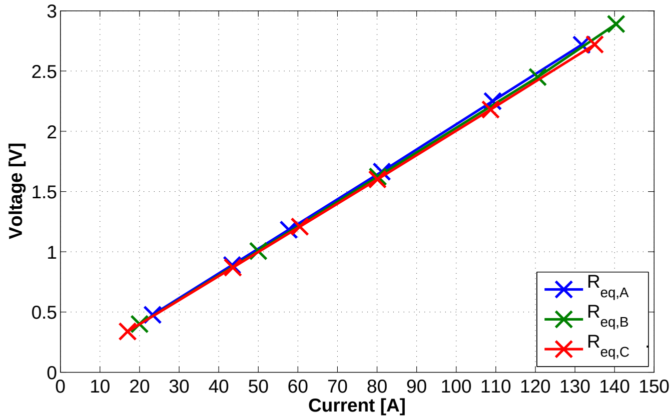

Figure 6.2: Voltage and current measurements at $21°C$.

Where in equation (6.4):

$R_{s,avg}$	Average phase resistance, $[\Omega]$

The deviation between the phase resistances for phase A and C is 4.5%, which could be caused by varying lengths of the windings, the connections in the socket or variations in temperature. An average of the three phase resistances is calculated to be used for the electrical model and control of the PMSM.

Temperature dependency of the resistance

Temperature dependency has an influence on the calculated power loss, which is needed in connection with thermal tests on the PMSM. The resistance of the windings increases due to change in the electric conductivity as the windings heat up as expressed in equation (6.5). The temperature coefficient, ν, is a physical property of copper ($\nu = 3.81 \cdot 10^{-3}/K$ [22]) that describes the correlation between temperature and resistance. The reference resistance of the windings is measured at $T_0 = 21°C$.

$$R_{s,T} = R_{s,avg}\left(1 + \nu\left(T - T_0\right)\right) \tag{6.5}$$

Where in equation (6.5):

$R_{s,T}$	Phase resistance at temperature T, $[\Omega]$
T_i	Temperature, $[K]$
ν	Temperature dependence coefficient, $[1/K]$

6.1.2 Theoretical determination

The theoretical phase resistance is calculated by the conductivity of copper, the length of the winding and the cross sectional area of the windings [22]. Each winding is approximately 6 meters long and with the area of the windings, the theoretical resistance is calculated as:

$$R_{s,theo} = \frac{l_{cond}}{\sigma_{cu}\, A_{cond}} \tag{6.6}$$

$$= \frac{6\ m}{57 \cdot 10^6 S/m \cdot 7.5 \cdot 10^{-6}\ m^2} = 0.0140\ \Omega \tag{6.7}$$

Where in equation (6.6):

A_{cond}	Cross sectional area of conductors, $[m^2]$
l_{cond}	Length of conductors, $[m]$
$R_{s,theo}$	Theoretical calculated resistance, $[\Omega]$
σ_{cu}	Conductivity of copper (57x10e6), $[S/m]$

This is a derivation of -3.8% between the measured and the theoretical resistance, which could be caused by the length of the windings, which was not measured accurately during the manufacturing process, measurement uncertainties or by the lack of data sheet for the copper, which might have a slightly different conductivity than the utilised. Other sources of errors could be the connection of the cable clamps and the star point, however that will cause the measured resistance to be higher than the theoretical resistance. The deviation is assessed to be within the acceptable range and the measured resistance is used in the PMSM model and the temperature dependency is used in the determination of the power loss.

6.2 Flux linkage test

The permanent magnet flux linkage constant, λ_{pm}, is determined from a spin down test, where the PMSM runs 15000 rpm. The power supply is cut and the PMSM is free-wheeling while the line-to-line voltages are logged by an oscilloscope. The measured voltage at the terminals is the induced voltage from the permanent magnets (back-emf), as no current flows in the windings due to the open circuit.

Velocity estimation

A velocity is required to determine the permanent magnet flux linkage constant. The velocity can be determined by manual reading of a time period of the induced back-emf or by programming a zero-crossing detection algorithm, which reads the periods of the induced sine voltages. The manual reading is disregarded due to the inconvenience in manual readings for several data sets and the automated algorithm makes it possible to utilise a large data set to calculate a mean value and calculate the flux linkage constant for a wide range of velocities.

The velocity is calculated from the voltages by locating every zero-crossing and then the frequency is calculated from the time period between two zero-crossings:

$$\omega_{re} = \frac{1}{time\ period} 2\pi \qquad ; \qquad \omega_{rm} = \omega_{re} \frac{2}{p_b} \tag{6.8}$$

Where in equation (6.8):

p_b	Number of poles, $[-]$
ω_{re}	Electric velocity, $[rad/s]$
ω_{rm}	Mechanical angular velocity, $[rad/s]$

The resolution of the oscilloscope is set to 1.25 million data points for the 100 seconds data set. This causes in average only 12.5 data points for each sine wave at maximum velocity. The poor resolution results in the velocity calculation fluctuating between 14420 rpm and 15630 rpm, which is seen in figure 6.3 that shows the calculated velocities in a spin down test. In figure 6.4 the zero crossing detections are shown at maximum velocity, where the resolution influences the location of the detected zero crossing.

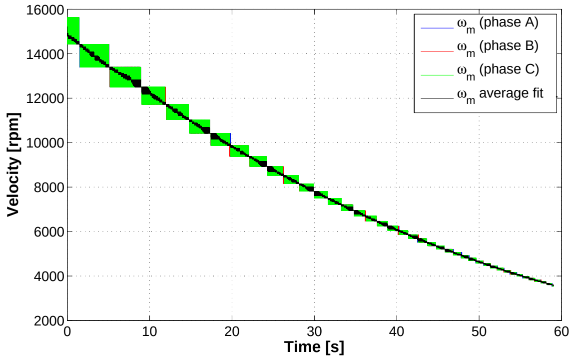

Figure 6.3: Calculated velocity by zero-crossing detection.

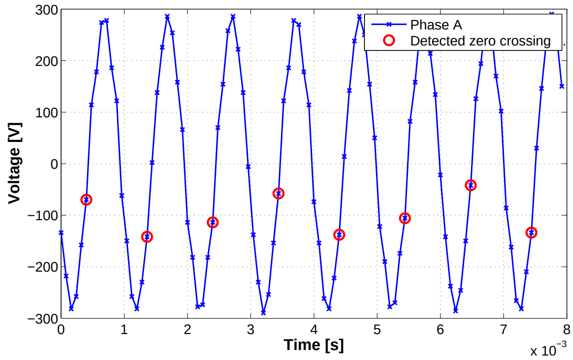

Figure 6.4: Detected zero-crossings.

To utilise the velocity calculations, a moving average filter is applied to the velocities calculated for each phase. Another method is to utilise linear interpolation between the data points to reduce the velocity fluctuation, however the same velocity is obtained with the moving average filter. The linear interpolation increases the calculation time compared to the moving average filter, why linear interpolation is discarded. Figure 6.5 shows the velocities with the moving average filter compared to the voltages.

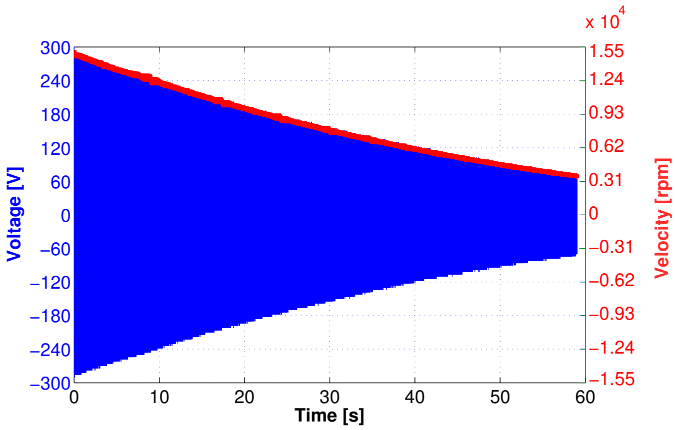

Figure 6.5: Back-emf and velocity calculation.

At 1000 Hz the PMSM runs 15000 rpm and the estimated velocity is 14840 rpm which is a deviation 1% why the calculation method is found valid. The curvature of the velocity estimation corresponds to the curvature of the voltages, which is expected cf. equation (6.9). Furthermore the velocity calculated from tests with higher resolution (shorter time span) corresponds to the average velocity. At low velocity the data from the 15000 rpm spin down test is fluctuating, which causes the zero crossing detection to malfunction. Therefore the velocity is not calculated a low velocities.

Permanent magnet flux linkage calculation

To calculate λ_{pm}, the amplitude of the voltages and velocity is used. The velocity is assumed to be constant during each electric period, which is acceptable due to the inertia of the rotor and furthermore it is assumed the system is balanced. λ_{pm} is calculated from equation (6.9), where $E_{back-emf,LN}$ and $E_{back-emf,LL}$ are the peak amplitudes of the voltage. The back-emf from the permanent magnets is assumed to be sinusoidal to convert the measured line-to-line amplitude to a line-to-neutral amplitude of the voltage.

$$\lambda_{pm} = \frac{E_{back-emf,LN}}{\omega_{re}} \qquad \Rightarrow \qquad \lambda_{pm} = \frac{E_{back-emf,LL}}{\sqrt{3}\,\omega_{re}} \tag{6.9}$$

Where in equation (6.9):

$E_{back-emf,LL}$	Back electromotive force, line-to-line, $[V]$
$E_{back-emf,LN}$	Back electromotive force, line-to-neutral, $[V]$
λ_{pm}	Permanent magnet flux linkage, $[Wb]$

The permanent magnet flux linkage calculated for the three line-to-line measurements are shown in figure 6.6. The line-to-line measurements do not make it possible to associate the flux linkage to each phase, why the nomenclatures (1), (2) and (3) are used to distinguish the three measurements. The time interval is shortened to improve the resolution of the measurements. The test is performed with a rotor temperature of $65°C$.

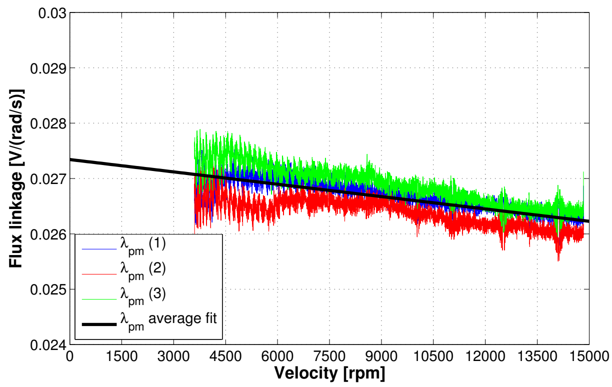

Figure 6.6: Calculated peak flux linkage constant from a 15000 rpm spindown test.

The measurements in figure 6.6 show that the flux linkage constant calculated from line-to-line measurement (2) is lower than (1) and (3). This may be caused by some of the stator teeth were twisted a bit during the tension of the windings, as described in section 4.2, which causes a higher reluctance or by uncertainties in the voltage probe that measures the voltage used to calculate λ_{pm} (2).

The average flux is fitted to a first order polynomial as the flux linkage seems to decrease with increasing velocity. This might be caused by the velocity dependent eddy currents that generate an opposing flux in the stator core. However the variation is 4% with the average fit, why an average flux linkage constant λ_{pm} of 0.0267 Wb is chosen at $65°C$.

In figure 6.7 the flux linkage is calculated from two spin down tests, one where the PMSM is approximately $25°C$ and one where the rotor is approximately $65°C$. The tests show that the flux linkage decreases when the temperature increases. This is expected as the PMs produce less flux at high temperatures. Figure 6.8 shows the velocities for the two spin down tests at different temperatures. The temperature of the rotor influences the duration of the spin down, which is expected cf. section 5.5, where the opposing torque generated by the core loss depends on the size of the flux density. Attention must be focused on the temperature dependency when spin downs are performed to determine the rotational torque parameters in section 6.5 and the rotational loss in section 8.1.

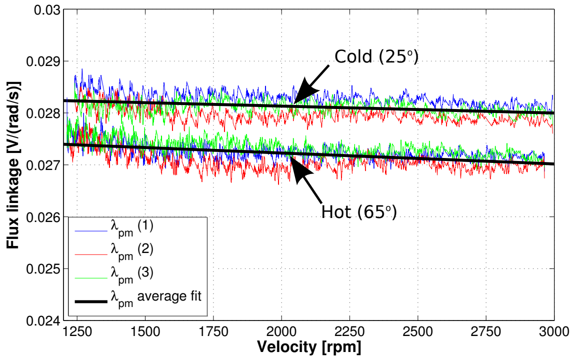

Figure 6.7: Calculated flux linkage from two 3000 *rpm* spindown tests at different temperatures.

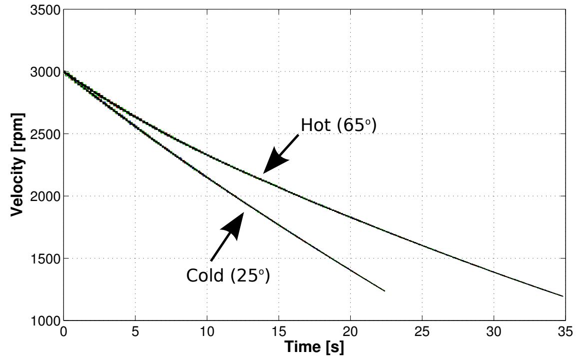

Figure 6.8: Calculated velocity from two 3000 *rpm* spindown tests at different temperatures.

6.3 Inductance test

The test set-up for the inductance test is shown in figure 6.9, where current is applied to all phases to ensure the mutual inductances are included in the calculated inductances. The power analyzer is used to measure the RMS current and a voltmeter is used to measure the RMS line-to-line voltage. Due to the small impedance it is chosen to use the power analyzer to measure the current and a voltmeter to measure the voltage at the terminals of the PMSM. The measured voltage from the power analyzer does not include the voltage drop due to the resistance in the cables to the PMSM, why the voltmeter is used. The PMSM is assumed to be symmetric, why only one RMS line-to-line voltage and one RMS current is measured.

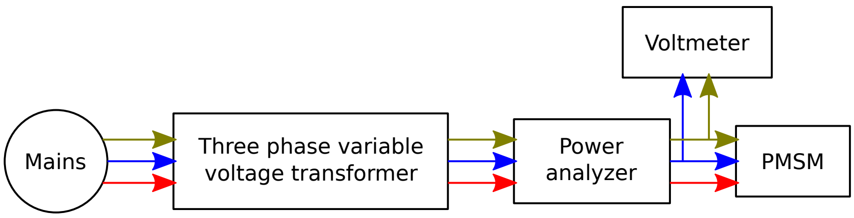

Figure 6.9: Test set-up for inductance test.

The inductance tests are performed where the rotor is aligned in the d-direction and the q-direction. The d-alignment is performed using a DC power supply, where phase A is connected to the positive potential and B and C are connected to the negative potential. The PMSM is locked in the position and the voltage and current measurements are performed with the set-up in figure 6.9.

The q-alignment of phase A is performed by connecting the positive potential of the DC supply to phase B and the negative potential to phase C. Once more, the PMSM is locked and the voltage and currents are measured.

From this test method the calculated inductance includes both the magnetising and leakage inductances. The measured RMS line-to-line voltages and RMS currents are stated in table 6.1.

The inductance is calculated from the impedance triangle and complex power triangle shown in figure 6.10. The calculations are stated in equation (6.10) to (6.15), where the stator resistance, $R_{s,avg}$, determined in section 6.1, is used.

Quantity	**Measurements with d-aligned**						
I_{RMS} [A]	2.965	6.17	8.844	11.608	14.733	17.756	19.924
$U_{RMS,LL}$ [V]	0.717	1.496	2.151	2.796	3.472	4.075	4.478
Quantity	**Measurements with q-aligned**						
I_{RMS} [A]	2.975	6.061	8.902	11.872	14.949	18.028	18.449
$U_{RMS,LL}$ [V]	0.708	1.449	2.106	2.782	3.448	4.058	4.272

Table 6.1: Measured quantities for the inductance determination.

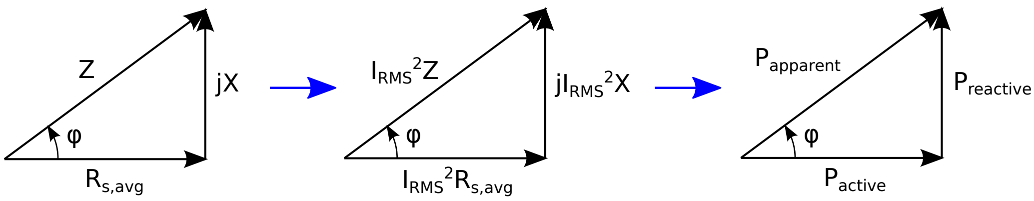

Figure 6.10: Impedance triangle to complex power triangle.

Where in figure 6.10:

P_{active}	Active power, $[W]$
$P_{apparent}$	Apparent power, $[VA]$
$P_{reactive}$	Reactive power, $[var]$
X_i	Reactance, $[\Omega]$
Z_i	Impedance, $[\Omega]$
ϕ	Angle, $[rad]$

$$P_{apparent} = \frac{U_{RMS,LL}}{\sqrt{3}} I_{RMS} \tag{6.10}$$

$$P_{active} = R_{s,avg}\, I_{RMS}^2 \tag{6.11}$$

$$\phi = arccos\left(\frac{P_{active}}{P_{apparent}}\right) \tag{6.12}$$

$$P_{reactive} = P_{apparent}\, sin(\phi) \tag{6.13}$$

$$X = \frac{P_{reactive}}{I_{RMS^2}} \tag{6.14}$$

$$L = \frac{X}{\omega_{app}} \tag{6.15}$$

Where in equation (6.15):

ω_{app}	Frequency of applied voltage, $[rad/s]$

To reduce uncertainty of measurements an average reactance and an average inductance are calculated from the measurements stated in table 6.1. The inductance in the both the d- and the q-direction are calculated as stated in table 6.2. The inductances are similar, which means the reluctance in the rotor is uniform (gaps between the magnets are neglectable).

Reactance [Ω]	**Inductance** [mH]
$X_d = 0.1361$	$L_d = 0.433$
$X_q = 0.1342$	$L_q = 0.427$
$X_{dq} = 0.1352$	$L_{dq} = 0.43$

Table 6.2: Calculated reactances and inductances.

6.4 Moment of inertia

The inertia of the rotor is determined from the CAD drawing of the PMSM. Each rotor component is weighed and then the density of the CAD component is fitted so the total weight of the component corresponds to the measured weight. This is done to reduce inaccuracies e.g. stacking factor and material density. In table 6.3 the rotor components are stated, together with the weight and inertia. All quantities are the total weight and inertia.

Component	**Weight** $[g]$	**Inertia** $[kg\ m^2]$
Rotor housing	1171.9	0.00781
Rotor end plate	333.0	0.00165
Rotor laminations [30 *mm*]	1856.6	0.01137
Permanent magnets [x8]	363.8	0.00174
Rotor resin	446.7	0.00236
Set screws	11.7	0.00009
Lamination bracket	91.9	0.000635
Bearings [x2]	300.0	0.000114
Total	4534	0.02577

Table 6.3: Measured weights and corresponding inertia of rotor components.

The inertia of the rotor resin is found by weighing the rotor before and after the resin casting. The weight is then fitted to correspond to the CAD model from which the inertia is calculated. The inertia of the bearings is assessed to be 75% of the total inertia of the bearings, since the inner bearing ring does not rotate.

6.5 Rotational torque parameters

The torque parameters are determined from a spin down test performed with a rotor temperature of $65°C$. The parameters are determined based on the velocity of the PMSM, which is calculated as described in section 6.2. The torque is expected to be expressed by equation (6.17) (rewritten from section 5.5), where the angular acceleration has to be determined.

$$\tau_{rot} = J\,\dot{\omega}_{rm} \tag{6.16}$$

$$= K_1\,\omega_{rm}^2 + K_2\,\omega_{rm} + K_3\,\omega_{rm}^{2/3} + K_4 \tag{6.17}$$

Where in equation (6.17):

K_i	Opposing rotational torque coefficients, $[-]$
τ_{rot}	Opposing torque due to rotational loss, $[Nm]$

Two different methods are used to determine the angular acceleration; one where the velocity is fitted to a polynomial which is differentiated and one where the calculated velocity is numerically differentiated without fitting. MATLAB is used to fit the velocity to the polynomial. The velocity is fitted to the polynomial stated in equation (6.18), which is derived from integrating the right site of equation (6.17). The numerical differentiation is performed using a central difference approach, which is given by equation

(6.19) and afterwards a moving average filter is applied.

$$\omega_m = a\,x^3 + b\,x^2 + c\,x^{5/3} + d\,x + e \tag{6.18}$$

$$\frac{df}{dx} \approx \frac{f(x+h_{step}) - f(x-h_{step})}{2h_{step}} \tag{6.19}$$

Where in equation (6.18) and (6.19):

a,b,c,d,e	Velocity coefficients, $[-]$
h_{step}	Change in x, $[-]$
x	Point, $[-]$

The velocity and the acceleration for the two methods are shown in figure 6.11 and 6.12. The acceleration from the numerical differentiation contains more noise, but the polynomial seems to correlate in the spin down. However the numerical differentiation reveals resonance peaks in the acceleration, which are suppressed by the polynomial fit (the importance of this becomes evident later in this section).

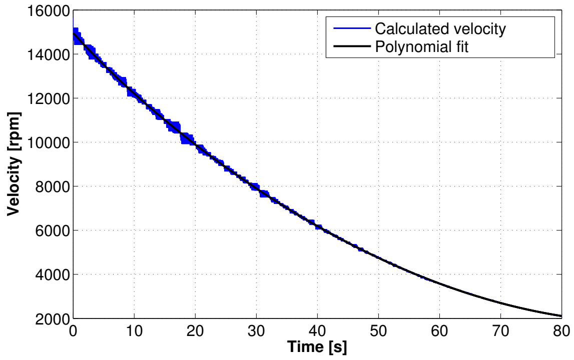

Figure 6.11: Velocity calculation and a fitted polynomial.

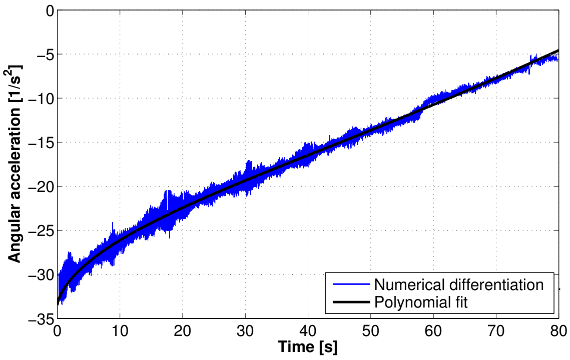

Figure 6.12: Angular acceleration calculated by numerical differentiation and based on the polynomial fit.

The calculated torque based on figure 6.12 is shown in figure 6.13, where the parameters for the fitted torque curve are:

$$K_1 = 5.018 \cdot 10^{-7}\,Nm\,s^2; \qquad K_2 = -0.003189\,Nm\,s \tag{6.20}$$

$$K_3 = 0.03848\,\frac{Nm\,s}{\sqrt{1/s}}; \qquad K_4 = -0.5999\,Nm \tag{6.21}$$

From the coefficients it is noted the torque contribution constants K_2 and K_4 are negative, which does not make physically sense, as these coefficients are associated with losses. Furthermore this means the torque characteristic does not make sense if it is extrapolated to low velocities. A full spin down could not be logged due to the available equipment for data logging but spin downs from different velocities are shown in figure 6.16.

Several spin down tests, shown in figure 6.15 and 6.16, have been performed to investigate the measured torque curve. A resonance peak is observed around 13000 rpm to 15000 rpm in the tests by utilising the numerical differentiation. The velocity where resonance occurs can be altered by changing how the PMSM is fixed, which indicate it is mechanical resonance that might be excited by unbalance in the rotor. The blue arrows in figure 6.14 indicate the fixing that affects the resonance peak. The resonance peak results in audible vibrations which affect the rotational torque due to the changing radial forces on the bearings.

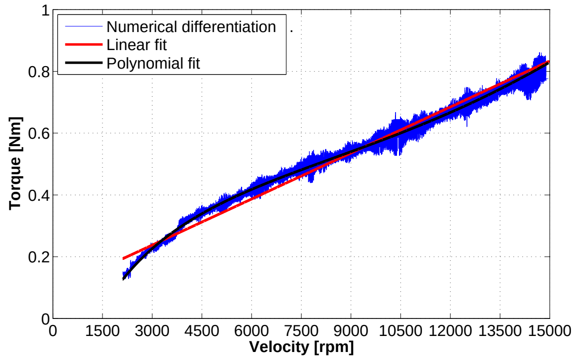

Figure 6.13: No-load torque curve.

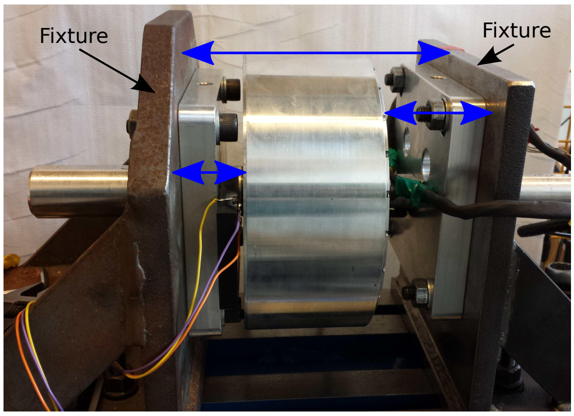

Figure 6.14: PMSM fixture in the test bench.

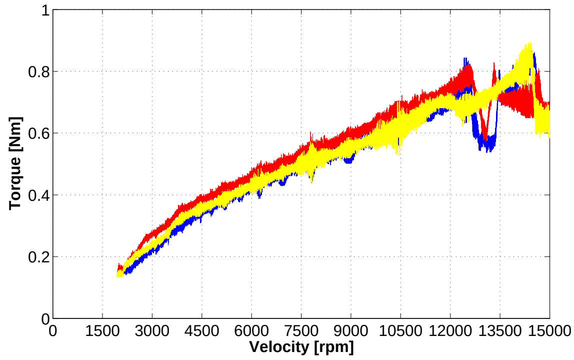

Figure 6.15: No-load torque curve with several spin down tests determined by numerical differentiation

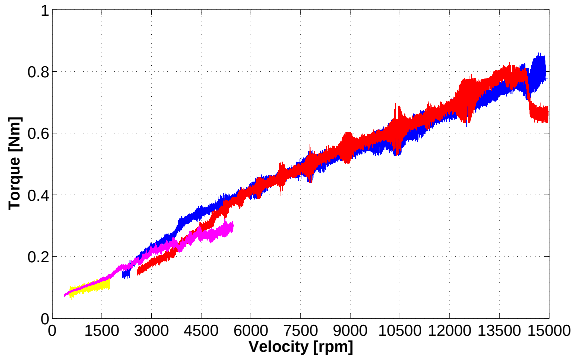

Figure 6.16: No-load torque curve with several spin down tests determined by numerical differentiation.

To circumvent the influence of the resonance peak and the negative torque coefficients, it is chosen to set K_1 and K_3 to zero and thereby use a linear torque curve. This means the torque from the windage loss in equation (5.72) and bearing in equation (5.73) are not included. Figure 6.13 shows a linear fit to the torque curve, which is assessed to be an acceptable fit. The linear torque simplifies the linearisation of the mechanical system in chapter 12. The linear torque equation is:

$$\tau_{rot} = K_1 \omega_{rm} + K_2 \tag{6.22}$$

$$= 0.0004745 \, \frac{Nm}{s} \omega_{rm} + 0.08858 \, Nm \tag{6.23}$$

This torque curve corresponds to a mechanical system with only viscous and dry friction.

CHAPTER

7

VERIFICATION OF ELECTRICAL MODEL

The electrical models of the PMSM and VSI are verified in this chapter. Due to the lack of an encoder, it is not possible to dq-transform the measured voltages and currents, why the verification is performed in the ABC coordinate reference frame. Furthermore it is not possible to measure the line-to-line voltages and feed them to the model since the model is based on line-to-neutral voltages. The missing dq-transformation and star point limit the possibilities to verify the models. The PMSM model is well-established in literature [16]-[19] and therefore it is therefore expected to represent the PMSM well. The chapter is divided into two parts, test of the VSI and verification of the PMSM.

7.1 Test of VSI

In this section the VSI is tested and the limitations of the VSI model are investigated. A DC test is performed where the reference output for the VSI is an average DC voltage of 8 V, which parks the PMSM in a fixed position. The switching frequency of the VSI is varied in order to see the effect of switching frequency when a low voltage is generated. During the test run in section 4.2.6, it was discovered that the switching frequency had great impact on the ability of the PMSM to start up.

A phase current is measured at each switching frequency and the results are shown in figure 7.1. The switching frequency has a great impact on the amplitude of the measured currents. A higher switching frequency reduces the current ripples along with the average value of the DC current. Figure 7.1 shows that the current ripples increase significantly when the switching frequency is lowered. At a switching frequency of 3500 Hz, the ripples are around 14 A, whereas at a switching frequency of 8000 Hz the ripples are less than 1 A.

The lowered current might be caused by the dead time in the VSI or the switching losses described in section 5.7.1. The dead time and switching losses reduce the output voltage and thereby the currents. The dead time in the VSI is 4 μs, which is independent on the switching frequency, however the total dead time increases as the switching frequency increases. As the output voltage is low in the test, the dead time has higher influence because the on-time of the switches is short. The on-time for the switches in this test is 7.1 μs calculated from equation (11.7) and a switching frequency of 6000 Hz, which makes the dead time 56% of the on-time. The turn-on time of IGBTs is in general around 1 μs [12], which is

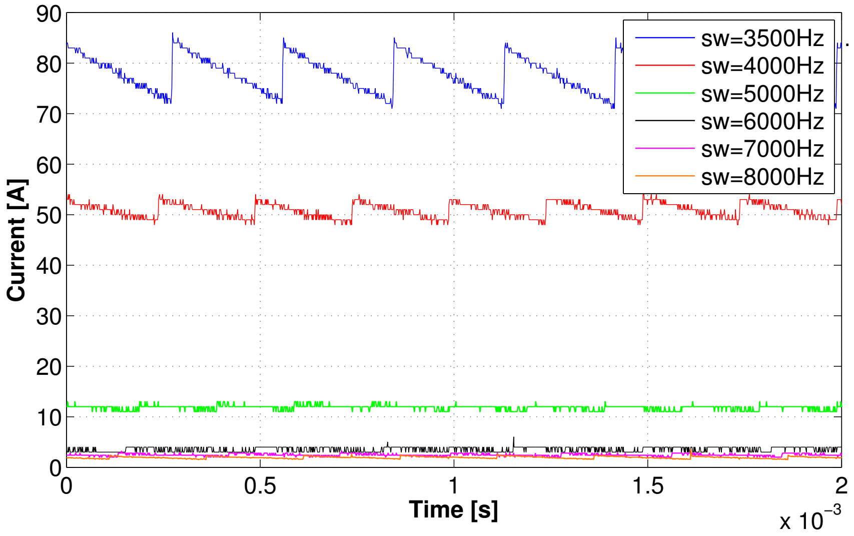

Figure 7.1: Current in one phase at different switching frequencies.

14% of the on-time.

The on-time increases as the switching frequency is lowered or the output voltage is increased. Therefore both dead time and turn-on time have a smaller influence on the VSI output when the amplitude of the voltage is increased, since both gets smaller compared to the on-time. It is therefore not expected to see these effects at higher velocities and the effects of dead time and switching losses are therefore not included in the VSI model, but a compensation must be included when the PMSM is operated at low voltages.

7.2 PMSM verification

To verify the PMSM and VSI models, both the models and the PMSM is ramped up in velocity and then a step in voltage is performed to excite system dynamics. The current is measured during the step, which is compared to the model. Two tests are performed, one where the velocity is ramped to 4500 *rpm* and another where the velocity is ramped to 8250 *rpm*. The switching frequency in both tests is 6000 *Hz*.

An open loop U/F ramp, developed in section 11.2, is used to ramp the PMSM. The open loop control results in current oscillations as shown in figure 7.2 and 7.3 for the test at 4500 *rpm*.

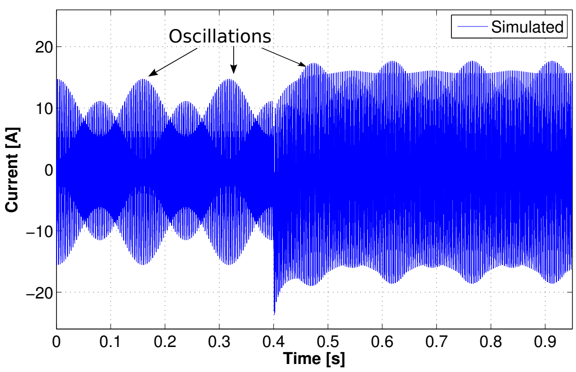

Figure 7.2: Simulated currents at steady state velocity and a step in voltage amplitude.

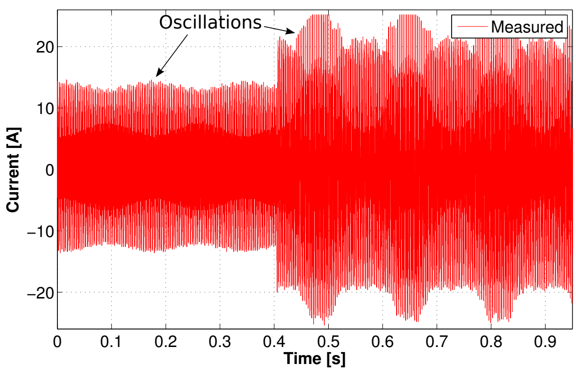

Figure 7.3: Measured currents at steady state velocity and a step in voltage amplitude.

At steady state velocity, both the simulated and measured currents suffer from oscillations both before and after the step. Repeated measurements show that the oscillations are not consistent. It is therefore discarded to verify the models with the open loop ramp over a wide time range, as the oscillations dominates the currents. It is assessed to be the open loop control structure that causes the oscillations. The oscillations are reduced by the PMSM controller as discussed in chapter 12. As the PMSM controller is not implemented, it is not possible to verify the model from a voltage step with the PMSM controller. Another verification must be performed, despite this is not desirable.

Instead of comparing the dynamics from a voltage step, the PMSM and VSI models are verified by comparing the switching dynamics of the currents. This is relevant as the reason for including the VSI is to model the current ripples. Zooms of figure 7.2 and 7.3 are shown in figure 7.4 and 7.5 respectively, where the PMSM operates at 4500 rpm.

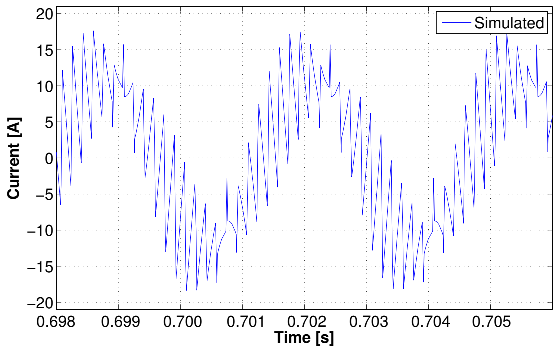

Figure 7.4: Zoom of the simulated currents from figure 7.2.

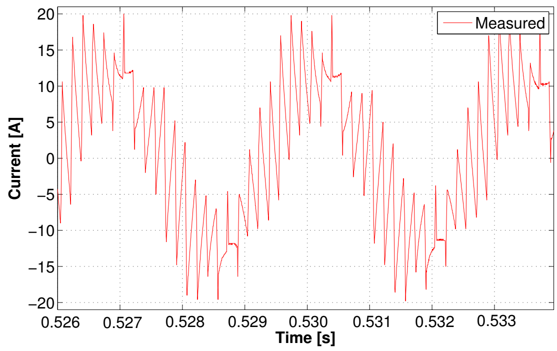

Figure 7.5: Zoom of the measured currents from figure 7.3.

The amplitude of the fundamental frequency in figure 7.5 is larger than the simulated, which is due to the slow oscillations from the open loop control structure. The amplitude of the current ripples and their characteristic correlate.

Figure 7.6 shows the measured and simulated currents at 8250 rpm, where the current ripples are increased due to the lower number of switches per revolution. The effect of the switching is well modelled as the current spikes and distortion is captured by the model. The amplitudes differ but this might be caused by the slow oscillations from the open loop control structure. The use of ideal switches and lack of dead time is not seen in this test, which is expected as the on-time of the switches is high compared to the test in section 7.1.

The switching dynamics are well captured and no improvements are performed based on this test as the results are found satisfactory.

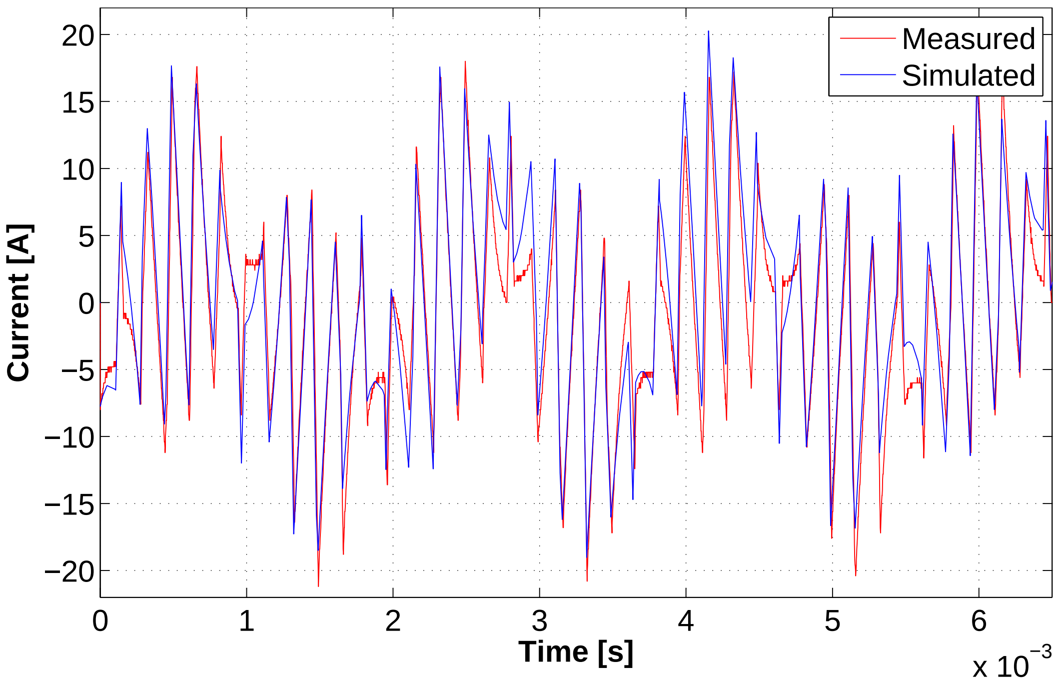

Figure 7.6: Comparison of the measured and logged currents at 8250 *rpm*.

CHAPTER

8

HEAT DEVELOPMENT AND REMOVAL

The heat development is investigated by analysis of the power losses in the PMSM. A test of stator-v1 is performed to investigate the performance of the cooling system, to give an indication of the capability of heat removal.

8.1 Power losses of PMSM-v1

The power losses of the PMSM at rated speed and load is calculated in this section. The losses in the PMSM consist of resistive loss in the windings, core losses and mechanical loss in the bearings. Estimation of the power losses is a crucial task as the estimated losses are used as input to the thermal model developed in chapter 9.

Resistive losses

The resistive losses in the windings are calculated at the rated current of 70 A RMS and a phase resistance at 140°C from equation (6.5):

$$R_{s,T} = 0.0135\ \Omega \left(1 + 0.00381 \frac{1}{°C} (140°C - 21°C)\right) = 0.0196\ \Omega \tag{8.1}$$

Where in equation (8.1):

$R_{s,T}$	Phase resistance at temperature T, [Ω]

The total resistive loss of the three windings are calculated by:

$$P_{cu} = 3\ R_{s,T}\ I^2_{nom,RMS} \tag{8.2}$$

$$= 3 \cdot 0.0196\ \Omega\ (70A)^2 = 288\ W \tag{8.3}$$

Where in equation (8.3):

$I_{nom,RMS}$	Nominal current, [A]
P_{cu}	Copper loss, [W]

Rotational losses

The rotational losses are determined from the rotational torque (from section 6.5) and the velocity (from section 6.2), as stated in equation (8.4). The rotational losses are presented in figure 8.1 where the temperature of the rotor is approximately 65°C.

$$P_{rot} = \tau_{rot}\ \omega_{rm} \tag{8.4}$$

Where in equation (8.4):

P_{rot}	Rotational power loss, $[W]$
τ_{rot}	Opposing torque due to rotational loss, $[Nm]$
ω_{rm}	Mechanical angular velocity, $[rad/s]$

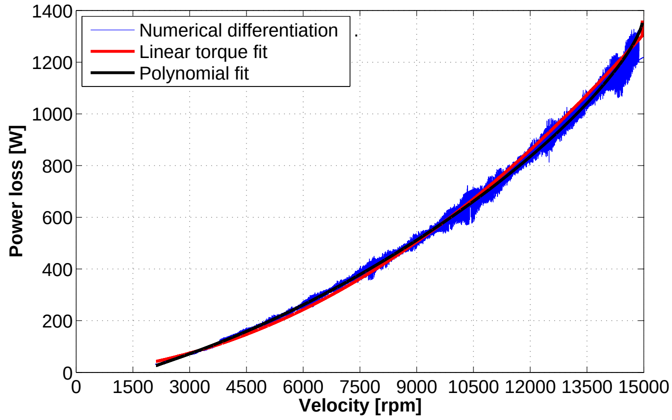

Figure 8.1: Power loss calculated from the spin down test.

The rotational loss is approximately 500 W higher than the expected 750 W from section 1.1. It might be caused by contact between the laminations due to the use of machining and turning lathe during the manufacturing as described in section 4.2.3 or the bearing losses are higher than expected due to the mounting of the bearings as described in section 4.2.

Losses in bearings depend mainly on the friction in the bearing, the speed, mounting and the loading conditions. The losses in the bearings are calculated by the manufacturer (Schaeffler), at the operational conditions, to be 51 W for each bearing.

Distribution of losses

It is chosen to distinguishing between the slot and the end windings for the distribution of the resistive loss as thermocouples are placed in both places. Figure 8.2 depicts the definition of a slot and end winding. The copper loss is distributed by the ratio of the lengths, which is a simplification as the curvature of the end winding results in a slightly lower ratio.

$$P_{sw} = \frac{30\ mm}{51\ mm}\, P_{cu} \qquad ; \qquad P_{ew} = \frac{21\ mm}{51\ mm}\, P_{cu} \tag{8.5}$$

Where in equation (8.5):

P_{ew}	Power loss in end windings, $[W]$
P_{sw}	Power loss in slot windings, $[W]$

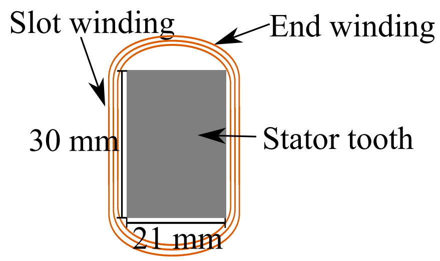

Figure 8.2: Section view of a stator tooth and a coil.

The distribution of the core loss depends on the geometry of the stator and rotor, the thickness of the laminations in the stator and rotor, the flux density distribution, the number of slots etc. A good prediction of the distribution requires an in-depth analysis of all factors for the PMSM and this is not prioritised in this project. To distribute the core loss between the parts which have the largest amount of core loss, the distribution from similar type and size of motor is used. In [23] a PMSM with interior rotor, interior permanent magnets, 699 W core loss, rated speed around 6000 rpm, stator diameter of 198 mm, core length of 200 mm and 9 stator slots is investigated which yields a distribution of:

$$n_{Rotor} = 2/30 \qquad n_{PM} = 1/30 \qquad n_{Stator} = 27/30 \tag{8.6}$$

Where in equation (8.6):

n_i	Distribution of power losses, $[-]$

The 10% loss assigned in the rotor is used as an approximation of the core loss distribution, despite the number of factors, which influence the distribution, are unknown for the PMSM presented in [23]. The three core losses are thus calculated as:

$$P_{Rotor} = n_{Rotor}\, P_{core} \qquad P_{PM} = n_{PM}\, P_{core} \qquad P_{Stator} = n_{Stator}\, P_{core} \tag{8.7}$$

Where in equation (8.7):

P_{PM}	Losses in PMs, $[W]$
P_{Rotor}	Losses in rotor, $[W]$
P_{Stator}	Losses in stator, $[W]$

The core losses consist of the loss from hysteresis and eddy currents but additionally the windage loss is included in the distribution of the measured losses as no calculation of the windage loss are performed and thus it cannot be separated. This might influence the simulated temperatures for the thermal model where the losses are assigned to each part of the PMSM as windage loss is not located in the laminations. In section 6.5 the size of windage loss was assessed to be negligible, why the inclusion of windage loss in the core losses is acceptable.

8.2 Thermal AC test of stator-v1

A thermal AC test is performed prior to the assembling of the PMSM to estimate the performance of the cooling system. The test is performed by applying 50 Hz AC while the temperatures of the windings are measured. The core losses are small due to the weak magnetic field (no rotor is present) and low frequency. The core losses are estimated to be 1.1 W [10], why they are neglected. The locations of the thermocouples are shown in figure 8.3.

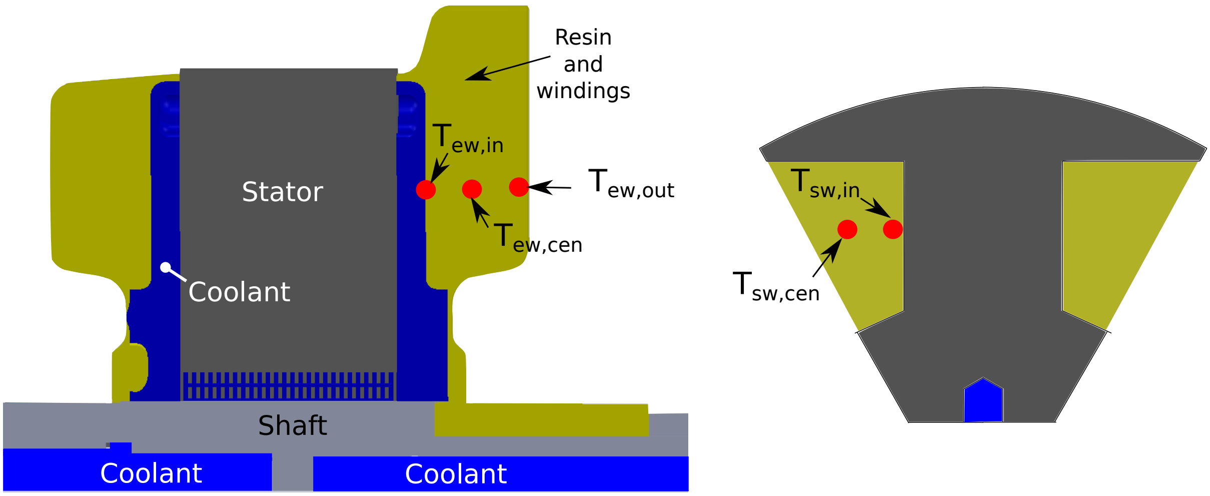

Figure 8.3: Cross sectional view of the stator, where the thermocouples are shown.

Three cooling methods are tested; a test with no cooling (NC), where only the natural convection dissipates heat from the stator to the ambient, two tests with forced cooling are performed, one with forced liquid cooling (LiqC) and one with forced air cooling (AirC). The test arrangement for the liquid cooling is shown in figure 8.4. The forced air cooling tests are performed with a compressor blowing air through the stator cooling channels.

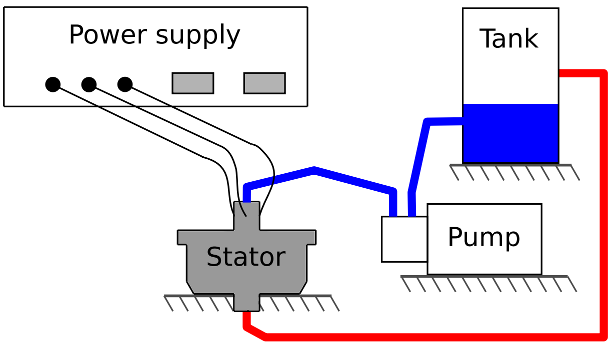

Figure 8.4: Thermal test set-up for the stator.

In table 8.1 an overview of the tests are presented together with the measured temperatures, with an ambient temperature of $20°C$. ΔT is the difference between the maximum temperature in the windings and the coolant. The temperatures in the slot windings are left out, since they are close to the temperature in the end windings ($\pm 1°C$). The applied power is calculated from the applied current and the resistance of the windings (including the temperature dependency) from section 6.1.

Test 1 is performed to compare the three cooling methods at the same current. To compare the tests $\Delta T/P_{cu}$ are calculated, which provides information on how effective the cooling methods are to keep the temperature in the stator low with respect to the same input power. Natural convection and radiation is only able to provide a $\Delta T/P_{cu}$ of $112\frac{°C}{100\ W}$. AirC and LiqC reduce the temperature significantly as expected.

The liquid cooling is able to provide a $\Delta T/P_{cu}$ of approximately $20\frac{°C}{100\ W}$. The $\Delta T/P_{cu}$ from AirC varies between $33.5\frac{°C}{100\ W}$ to $48.6\frac{°C}{100\ W}$ in all tests, however in test 2 and 3 it is almost constant. This might indicate the full potential of the forced air convection is not taken advantage of in test 1, which could be due to manual adjustments of the pressure and alignment of the compressor pistol for air cooling. From

Quantities	Test 1 NC	Test 1 AirC	Test 1 LiqC	Test 2 AirC	Test 2 LiqC	Test 3 AirC	Test 3 LiqC
I_{RMS} [A]	43.7	43.7	43.7	58	58	66	70
P_{cu} [W]	109	84.0	81.0	174	149	249	231
$T_{coolant}$ [$°C$]	(20)	18.5	19.4	18.7	18.2	19.2	20.3
$T_{ew,in}$ [$°C$]	140	39.1	28.7	85.8	36.8	117	49.3
$T_{ew,cen}$ [$°C$]	142	46.1	34.9	101	48.9	140	68.5
$T_{ew,out}$ [$°C$]	140	46.1	35.3	101	49.5	140	69.5
ΔT [$°C$]	(120)	28.1	15.9	82.7	31.3	121	49.2
$\Delta T/P_{cu}$ [$\frac{°C}{100\ W}$]	(112)	33.5	19.6	47.5	21.0	48.6	21.3

Table 8.1: Steady state temperatures from thermal AC tests of the stator.

the calculated $\Delta T/P_{cu}$ it is seen the LiqC is around 2.4 times better than AirC to dissipate heat from the stator and around 5.5 times better than NC.

From test 3 (LiqC), the temperature of the windings is just below $70°C$ at rated current. The insulation on the windings has a maximum operation temperature of $155°C$ and the resin has a maximum operating temperature of $150°C$, which allow a temperature rise of $80°C$ before the critical temperature is reached.

The total losses in the PMSM is estimated to $1000\ W$ from section 1.1, which means the temperature in the windings approach $210°C$, if all losses are applied to the windings. It is necessary to obtain a $\Delta T/P_{total}$ of under $15\frac{°C}{100\ W}$ to ensure the PMSM does not overheat in this test scenario. However out of the total loss, the rotational loss is 750 W, which is primary located in the stator teeth. This is beneficial as it is easier to dissipate heat from the stator, due to the high conductivity of the stator laminations and the large contact area to the liquid cooling. Otherwise the temperature of coolant could be lowered, but this requires extra energy. Further tests have to be conducted in order to verify if the cooling system is able to keep the temperatures beneath $150°C$ when the rotational losses are included. The tests are performed at atmospheric pressure without the rotational losses, why further analysis must be performed to assess the temperatures in the thermal test scenario.

CHAPTER

9

THERMAL MODEL

A thermal model of the PMSM is derived in this chapter. Since the PMSM is going to operate in a low pressure environment, failure due to overheating is of concern. The thermal model is used to analyse the heat distribution and temperatures of the PMSM. In figure 9.1 and 9.2, a sketch of the heat flow is presented. Red arrows designate heat conduction and yellow arrows designate both radiation and convection. Due to the low pressure environment, the external radiation and convection is reduced, why the primary way for the PMSM to emit heat is through the liquid cooling. Heat is developed as a

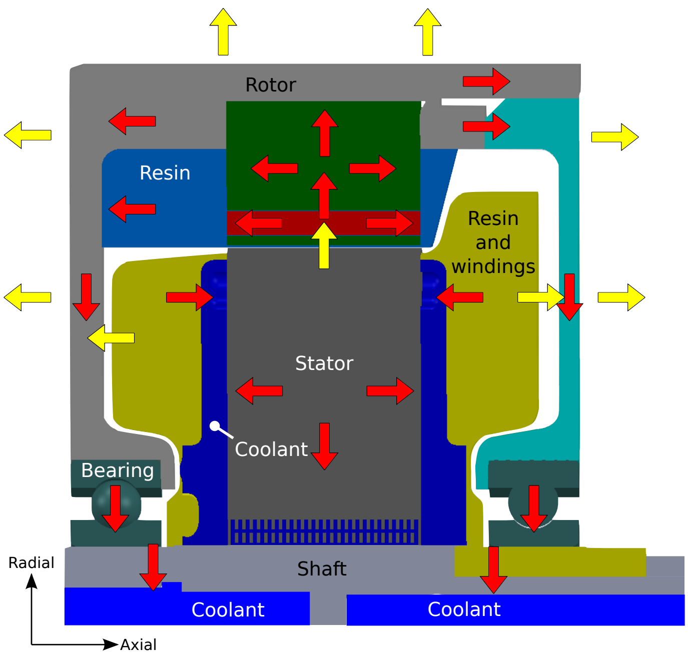

Figure 9.1: Axial cross sectional view of one half of the PMSM, with the overall heat flow shown.

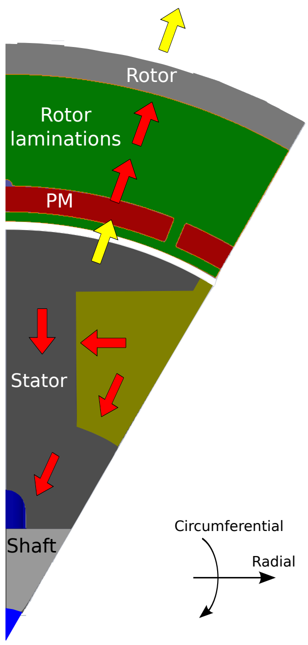

Figure 9.2: Radial cross sectional view of 1/12 of the PMSM, with the overall heat flow shown.

consequence of the losses, which occur in the windings, stator, bearings and rotor. A critical aspect for the PMSM is that radiation and convection might not be sufficient to emit the heat developed in the rotor, why the heat must be conducted through the rotor housing and bearings to reach the coolant in the shaft.

The liquid cooling cools the end windings in the axial plane, but the slot windings are not directly cooled. To emit the heat from the slot windings, a part of the heat is conducted into the axial plane to the cooling channels in the end plate and the other part is conducted through the stator to the cooling channels in the radial plane. This causes a 3-D heat flow that must be taken into account to avoid over-prediction of the temperatures in the radial plane.

Several approaches exist to model the thermal behaviour of electric motors e.g. exact analytical calculation (distributed loss model), Finite Element Method (numerical analysis) and lumped parameter model (concentrated loss model) [24]:

- Exact analytical calculation solves the time depend governing equation for a heat transfer problem [25][26]. This is a severe task for a complex thermal system such as a PMSM.
- Finite Element Method (FEM) solves the governing equation by discretizing the geometry into a finite number of elements and then the problem is solved by numerical solvers for each element. If the discretization level is sufficient, the approximated solution closely matches the analytical solution [27]. Power losses are distributed as a power per volume source.
- The lumped parameter model divides the PMSM into larger elements with a node in each element. Connecting the nodes forms a thermal network. Each element has a thermal resistance and thermal capacitance which is calculated analytically. Power losses are treated as a heat source, located in the nodes.

It is chosen to further investigate the lumped parameter model as the method has proved good results on other types of electric motors and due to simplicity [28] [29]. The lumped parameter model is used to model the PMSM in 3D and a FEM is used to verify the lumped parameter model by 2D simulations.

Literature review

A literature review is carried out to investigate the previous work on thermal models of electric machines. Previous work, which is applicable for the modelling of the PMSM, is presented with the focus on the achieved results and methods used for the thermal models.

In the lumped parameter method several approaches exist to compensate for heat sources, which is necessary as omission of compensation elements leads to overestimation of the temperatures in the nodes where the losses are assigned [30]. Some of the approaches are widely used, however their accuracies are uncertain [24] [25] [26] therefore several approaches are to be investigated to choose the most accurate.

No publications are found on hub motors, however several publications are found on interior rotor PMSMs, some of the most applicable are presented in [29] [7] [30]. No literature is found on motors with liquid cooling on the stator end laminations, however other designs of liquid cooling are presented in [7] [30].

In [29] a 10-node model lumped parameter model of a PMSM is developed without radiation. The PMSM has no cooling system, only convection removes heat from the motor. The power losses are applied directly to the concerned nodes without compensation. The lumped parameter model is compared to a FEM model and experimental tests. The lumped parameter model overestimates the temperature in the stator and in the rotor by 4.5%, however the temperature in the windings are underestimated by 15.7%.

In [7] a model of a PMSM with liquid cooled stator frame is presented. Two lumped parameter models are developed; a simple 7-node model and a complex 15-node model. The thesis focuses mainly on the analytical calculations of the resistances and the node placement. The results from the simple and complex models are compared to a FEM model. Both the simple and the complex lumped parameter model have a maximum deviation of 4% but the complex model proved to be slightly more accurate.

In [30] a lumped parameter 7-node model of a PMSM is developed. The model includes compensation elements for the heat sources and forced liquid cooling on the stator. The lumped parameter model is compared to a FEM model, where it is stated the lumped parameter model only deviates with maximum 1%.

To sum up the modelling challenges are:

- The liquid cooling on the stator corresponding to a 3-D heat flow.
- Compensation for heat sources in a thermal network with complex geometry.
- No well-documented thermal model for a water cooled hub PMSM exists.

In section 9.1 the basic lumped parameter method is described and methods for modelling the heat sources are investigated. Section 9.2 describes the 3-D lumped parameter model of the PMSM and the thermal resistances are calculated in section 9.3.

9.1 Lumped parameter approach

The thermal lumped parameter method is similar to an electric circuit and the analogy is stated in table 9.1. The network can be analysed by laws which are analogue to the laws of an electric circuit.

Electric parameter	**Unit**	-	**Thermal parameter**	**Unit**	**Symbol**
Current	[A]	-	Heat flow	[W]	P
Voltage	[V]	-	Temperature	$[°C]$	T
Resistance	[Ω]	-	Resistance	$[K/W]$	R_{th}
Capacitance	[F]	-	Capacitance	$[J/K]$	C_{th}
Conductivity	$[A/(V\ m)]$	-	Conductivity	$[W/(m\ K)]$	k_{th}

Table 9.1: Analogy between electric and thermal parameters.

In order to model transient responses thermal capacitances are added to each element to capture the change of internal energy. Transient analysis can be performed with both the lumped parameter model and the FEM, but since the PMSM is going to operate at the same speed for longer periods, as described in section 1.1, the transient analysis is disregarded for this report and only steady state performance is concerned.

The lumped parameter model is developed based on the geometry of the PMSM and material properties. An element with one-dimensional heat distribution, without an internal heat source, is shown in figure 9.3. The node temperature, T_n, can be calculated by Fourier's law, which is analogous to Ohm's law, as stated in equation (9.1). Furthermore thermal equilibrium is required in the nodes (analogous to Kirchhoff's current law), which means the total heat flow into a node equals the total heat flow out from a node as stated in equation (9.2).

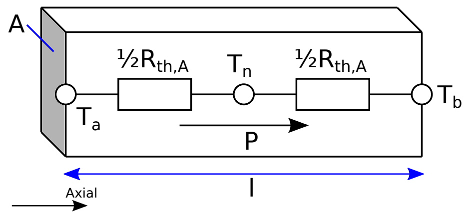

Figure 9.3: Bar element with one-dimensional heat flow.

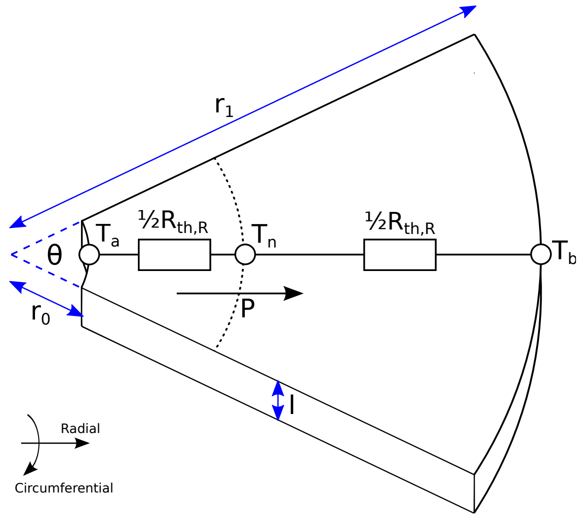

Figure 9.4: Hollow cylinder segment with one-dimensional heat flow.

Where in figure 9.3 and 9.4:

A	Area, $[m^2]$
l_i	Length, $[m]$
r_i	Radius, $[m]$
θ	Angle, $[rad]$

$$T_a - T_n = P\,\frac{R_{th}}{2} \qquad \wedge \qquad T_n - T_b = P\,\frac{R_{th}}{2} \tag{9.1}$$

$$\sum P_{in} = \sum P_{out} \tag{9.2}$$

It is chosen to place the node in the resistive centre of the element, which is not necessary in the geometric middle of the element as illustrated in figure 9.4. The node location depends on the geometry (assuming the thermal conductivity of the element is constant). By choosing the resistive centre, the number of thermal resistances to be calculated, is reduced. The node configuration in figure 9.3 and 9.4 can easily be extended to two or three-dimensional heat flow as shown in figure 9.5, where the element from figure 9.4 is shown with two-dimensional heat flow.

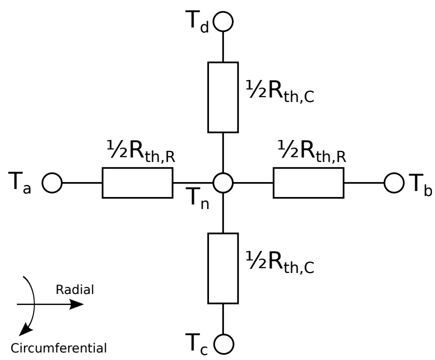

Figure 9.5: Two-dimensional heat flow node configuration of circular element.

9.1.1 Thermal resistances

The thermal resistances are important parameters in a thermal model why the resistance calculation procedures are stated in the following section. The resistance calculations are presented for conduction, convection and radiation. Convection and radiation are included as thermal resistances as it is desirable from a model technical viewpoint. If the radiation and convection are modelled as a constant heat flow, the temperature dependency of these phenomena is not modelled and if a variable heat flow is used, the MATLAB solver ends up in an algebraic loop.

Conduction resistance

Conduction resistance is the internal resistance in an element. The thermal resistances are calculated based on the geometry of the element and the thermal conductivity of the material. The thermal conduction resistance is calculated in three directions; axial, radial and circumferential for a bar and a hollow cylinder. The axial resistance of a bar element is shown in figure 9.3 and calculated as stated in equation (9.3). The radial resistance of a hollow cylinder segment is shown in figure 9.4 and calculated as stated in equation (9.4) [7]. The circumferential resistance of a hollow cylinder segment is calculated as stated in equation (9.5) [7].

$$R_{th,A} = \frac{l}{k_{th}\,A} \tag{9.3}$$

$$R_{th,R} = \frac{ln(r_0/r_1)}{\theta\,k_{th}\,l} \tag{9.4}$$

$$R_{th,C} = \frac{\theta}{2\,k_{th}\,l}\frac{r_1+r_0}{r_0-r_1} \tag{9.5}$$

Where in equation (9.3) to (9.5):

$R_{th,A}$	Axial thermal resistance, $[K/W]$
$R_{th,C}$	Circumferential thermal resistance, $[K/W]$
$R_{th,R}$	Radial thermal resistance, $[K/W]$

Convection resistance

Convection transfers heat to the surroundings and internally between the stator and the rotor. The convection depends on many factors, such as rotational speed, surface structure, geometry, forced flow, pressure, temperature, humidity etc. [7]. Therefore simplified models exist to model convection in electric motors. The heat flow generated by convection is described as [7]:

$$P_{conv} = \frac{T_a - T_b}{R_{th,conv}} \tag{9.6}$$

Where in equation (9.6):

P_{conv}	Heat flow through convection, $[W]$
$R_{th,conv}$	Thermal convection resistance, $[K/W]$

T_a represents the temperature of the surface which emits heat and T_b represents the temperature of the ambient. The thermal resistance for convection is calculated as:

$$R_{th,conv} = \frac{1}{h_{conv}\,A} \tag{9.7}$$

Where in equation (9.7):

h_{conv}	Thermal heat transfer coefficient from convection, $[W/(m^2\ K)]$

The convection heat transfer coefficient, h_{conv}, includes the air flow modelling. Simplified models seek to estimate the heat transfer coefficient, which takes the aforementioned factors into account.

Radiation resistance

Radiation is often neglected at atmospheric pressure as the main heat flow is through convection and conduction. Heat transfer by radiation occurs between the rotor and stator parts (internal radiation) and from the rotor to the surroundings (external radiation) due to a temperature difference. The amount of heat transfer depends on the temperature, the emissivity of the material and surface area.

The amount of radiation emitted from a small object and absorbed by an infinite large object is given by [31]:

$$P_{rad} = \sigma_{SB}\, A\, \varepsilon \left(T_a^4 - T_b^4\right) \tag{9.8}$$

Where in equation (9.8):

P_{rad}	Heat flow through radiation, $[W]$
ε	Emissivity of the surface, $[-]$
σ_{SB}	Stefan-Boltzmann constant (5.67x10e-8), $[W/(m^2\ K^4)]$

To calculate the radiation resistance, Fourier's law is used as shown in equation (9.9) and the heat transfer coefficient is derived and shown in equation (9.11).

$$R_{th,rad} = \frac{(T_a - T_b)}{\sigma_{SB}\, A\, \varepsilon \left(T_a^4 - T_b^4\right)} \tag{9.9}$$

$$R_{th,rad} = \frac{1}{A\, h_{rad}} \tag{9.10}$$

$$h_{rad} = \frac{\sigma_{SB}\, \varepsilon \left(T_a^4 - T_b^4\right)}{T_a - T_b} \tag{9.11}$$

Where in equation (9.9) to (9.11):

h_{rad}	Thermal heat transfer coefficient from radiation, $[W/(m^2\ K)]$
$R_{th,rad}$	Thermal radiation resistance, $[K/W]$

Radiation between two surfaces also depends on the view angle. The view angle expresses how much of the radiation leaving one surface that reaches the other surface. If the surfaces are aligned and closely positioned, the view factor approaches 1 as all radiation reach the other surface. For the PMSM, the view factor is set to 1 as the parts with heat transfer by radiation are close and aligned.

For two parallel planes with different temperature and emissivity, the heat transfer by radiation is given by equation (9.12) and for two concentric cylinders, the heat transfer is given by equation (9.13) [31].

$$P_{rad,plane} = \frac{\sigma_{SB}\, A \left(T_a^4 - T_b^4\right)}{\frac{1}{\varepsilon_a} + \frac{1}{\varepsilon_b} - 1} \tag{9.12}$$

$$P_{rad,cyl} = \frac{\sigma_{SB}\, A_a \left(T_a^4 - T_b^4\right)}{\frac{1}{\varepsilon_a} + \frac{1-\varepsilon_b}{\varepsilon_b}\left(\frac{r_a}{r_b}\right)} \tag{9.13}$$

Where in equation (9.12) and (9.13):

$P_{rad,cyl}$	Heat flow between two concentric cylinders through radiation, $[W]$
$P_{rad,plane}$	Heat flow between two planes through radiation, $[W]$

The heat transfer coefficients for two planes and cylinders are given by:

$$h_{rad,plane} = \frac{\sigma_{SB}\left(T_a^4 - T_b^4\right)}{\left(T_a - T_b\right)\left(\frac{1}{\varepsilon_a} + \frac{1}{\varepsilon_b} - 1\right)} \quad ; \quad h_{rad,cyl} = \frac{\sigma_{SB}\left(T_a^4 - T_b^4\right)}{\left(T_a - T_b\right)\left(\frac{1}{\varepsilon_a} + \frac{1-\varepsilon_b}{\varepsilon_b}\left(\frac{r_a}{r_b}\right)\right)} \tag{9.14}$$

Where in equation (9.14)

$h_{rad,cyl}$	Thermal heat transfer coefficient from radiation between two concentric cylinders, $[W/(m^2\ K)]$
$h_{rad,plane}$	Thermal heat transfer coefficient from radiation between two planes, $[W/(m^2\ K)]$

Contact resistance

Contact resistance originates at the interface between two parts due to the unavoidable small surface imperfections. Surface roughness, hardness of the materials, interface pressure and air pressure has a significant influence on the contact resistance [32]. Contact resistances are often significant compared to conduction resistances and are therefore critical in the prediction of the temperature in the PMSM [32]. Contact resistances are modelled by an equivalent effective gap length, which represent the small separation between the parts as shown in figure 9.6.

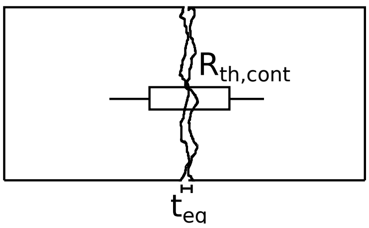

Figure 9.6: Two parts in contact, which result in a gap with an equivalent thickness.

Where in figure 9.6:

$R_{th,cont}$	Thermal contact resistance, $[K/W]$
t_{eq}	Effective gap length, $[m]$

Typical effective gap lengths in motors are presented in [32], the relevant lengths are listed in table 9.2.

Materials interface	Effective gap length [mm]
Ceramic-Metal	0.0031 - 0.0173
Aluminium - Aluminium	0.0005 - 0.0025
Stainless - Stainless	0.0070 - 0.0153
Stainless - Aluminium	0.0058 - 0.0087
Iron - Aluminium	0.0006 - 0.0060

Table 9.2: Effective interface gap lengths [32].

The thermal contact resistances are calculated like conduction where the equivalent thickness is used:

$$R_{th,cont} = \frac{t_{eq}}{k_{cont}\ A} \tag{9.15}$$

Where in equation (9.15):

$k_{th,cont}$	Conductivity though contact element, $[W/(m\ K)]$

9.1.2 Test of compensation approaches

Losses in the PMSM (e.g. copper losses and iron losses) are treated as a heat source within the concerned element. If one of the loss generating parts in the PMSM is represented by multiple elements, the losses are distributed among those elements according to their volumes.

The conventional lumped parameter approach assigns the total power loss in the node, however this approach over-estimates the temperature in the node [30] [24] [25]. The conventional approach is not considered in the rest of the report, due to its poor estimation of the temperatures. To improve the prediction of the temperatures, compensation elements are added to elements with an internal heat source. Different compensation element approaches exist and some common approaches are listed in table 9.3 [25] [24].

Approach	**Nodes**	**Compensation**
T-equivalent	Centric	Add a compensation resistance of $-\frac{1}{6}R_{th,i}$ as shown in figure 9.9
Improved conventional	Centric	Assign half of the heat source as shown in figure 9.7
Novel GD	Centric	Add a compensation temperature of $T_{comp,i} = -\frac{1}{2}P_i\ R_{th,i}$ as shown in figure 9.8
Improved novel GD	Moving	Add a compensation temperature of $T_{comp,i} = -\frac{1}{2}P_i\ R_{th,i}$

Table 9.3: Heat source modelling approaches.

The T-equivalent estimates the average temperature of the element by adding a thermal resistance to the element. The improved conventional and novel GD approaches estimate the temperature in the node location.

The improved conventional approach assigns half of the power loss in the node to avoid overestimation of the temperatures. However in a thermal network, the temperatures in the other nodes are underestimated due to the missing second half of the power [33].

The novel GD (Gerling and Dajaku) approach is a relative new approach, therefore literature is limited. The authors claim this approach is more accurate than the conventional and T-equivalent approaches, however no details are provided how to implement this approach in a complex network, like a PMSM. Literature only states how to implement this approach on a simple 1-D bar element [25].

The improved novel GD approach moves the node towards the location with the highest temperature in the element by iteration [26]. The improved novel GD approach is discarded since the programming of the moving nodes is considered to be comprehensive.

The improved conventional, T-equivalent and the novel GD approach are examined further in order to determine their level of accuracy. The node configurations of the three approaches are shown in figure 9.7 to 9.9.

In order to select the most accurate approach, three scenarios are set up in the following sections. The first scenario is found in [25], however this scenario is simple and it does not indicate how the approaches perform in a network. The first scenario is used to determine the accuracy in a single element. The second

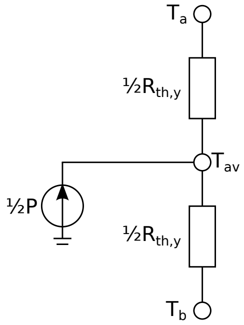

Figure 9.7: Improved conventional approach.

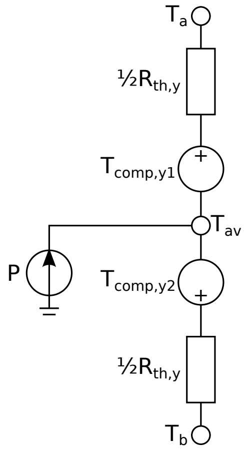

Figure 9.8: Novel GD approach.

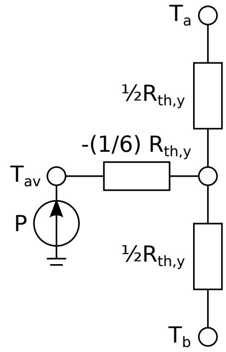

Figure 9.9: T-equivalent approach.

scenario is developed to investigate how the approaches perform in a network with several elements. The third scenario is developed to investigate how the approaches perform when several heat sources are located next to each other and when symmetry is applied. The two developed scenarios are more complex than the scenario presented in [25] and they yield better basis for assessment of the accuracy in the PMSM model.

Scenario with 1-D heat flow

The first scenario is a simple bar with a heat source in the middle and two fixed temperatures at the end of the bar, which corresponds to the node configuration shown in figure 9.7 to 9.9. For this simple case the analytical solution is calculated as stated in equation (9.16) [25]. Furthermore the results are compared to the results from a FEM model which is developed in appendix D.1.1. Table 9.4 states the test parameters and figure 9.10 and 9.11 show the test results.

$$T_{analytical} = -\frac{q_{th}}{2k_{th}}x^2 + \left(\frac{T_b - T_a}{l} + \frac{q\,l}{2k_{th}}\right)x + T_a \qquad (9.16)$$

Where in equation 9.16:

q_{th}	Heat generation, $[W/m^3]$
x	Position in element, $[m]$

Parameters	**A**	**l**	**k_{th}**	**$R_{th,y}$**
Values	600 mm^2	100 mm	40 $\frac{W}{m\,K}$	4.167 K/W

Test	**T_a**	**T_b**	**P**	**q**
Test 1	$0°C$	$0°C$	60 W	1 $\frac{MW}{m^3}$
Test 2	$0°C$	$70°C$	60 W	1 $\frac{MW}{m^3}$

Table 9.4: Parameters for heat source modelling approach [25].

Figure 9.10 and 9.11 show that the analytical and the FEM solution are consistent as expected. Therefore it is considered acceptable to use FEM as a reference to evaluate the compensation approaches. From the figures it is seen the novel GD and the improved conventional approaches estimate the same temperatures,

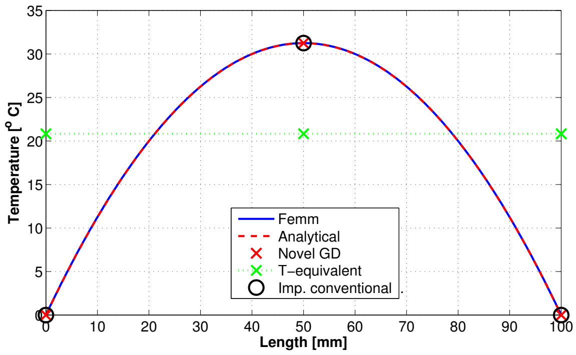

Figure 9.10: Comparison of results from test 1 [25].

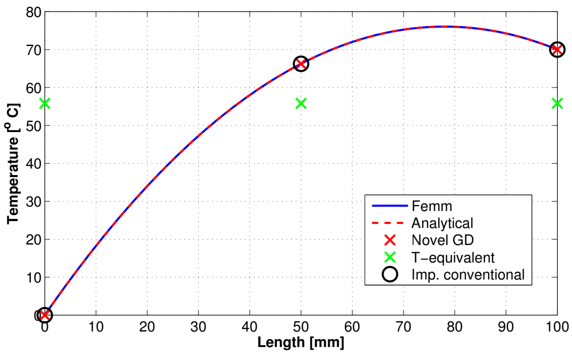

Figure 9.11: Comparison of results from test 2 [25].

which correlate with the analytical and FEM solutions. This test shows the improved conventional and novel GD approaches are accurate in a simple scenario. The average temperature from the FEM solution of test 1 is 21°C and 56°C from test 2, why the T-equivalent approach also performs well in this scenario.

Scenario with 2-D heat flow

According to [24] [26] [30] problems arise for the improved conventional approach in a network with several elements, like an electric machine. Therefore a second test scenario is presented in figure 9.12, where two heat sources are present. In this scenario an analytical solution has not been derived, therefore the reference results are from a FEM model. The FEM model is developed in appendix D.1.2 and the parameters for the test are stated in table 9.5.

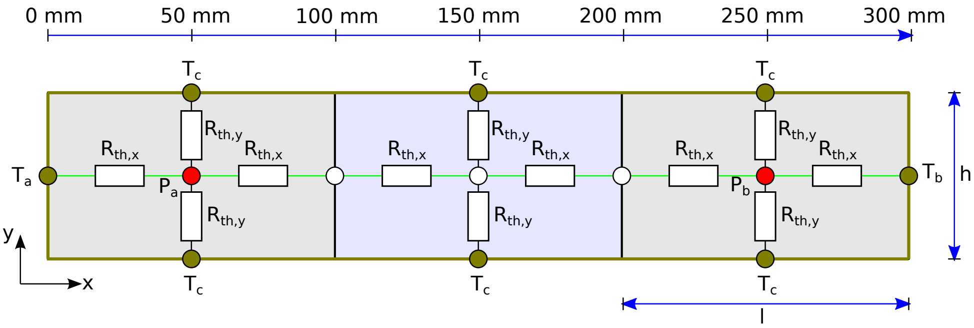

Figure 9.12: Test scenario with 2-D heat flow.

Where in figure 9.12:

h	Height, $[m]$

Parameters	**t**	**h**	**l**	$\mathbf{k_{th,x}}$	$\mathbf{k_{th,y}}$	$\mathbf{R_{th,x}}$	$\mathbf{R_{th,y}}$
Values	600 mm	100 mm	100 mm	$40\frac{W}{m\ K}$	$20\frac{W}{m\ K}$	2.08 K/W	4.17 K/W

Test	$\mathbf{T_a}$	$\mathbf{T_b}$	$\mathbf{T_c}$	$\mathbf{P_a}$	$\mathbf{P_b}$	$\mathbf{q_a}$	$\mathbf{q_b}$
Test 3	20 °C	80 °C	30 °C	60 W	30 W	$1\ \frac{MW}{m^3}$	$0.5\ \frac{MW}{m^3}$
Test 4	20 °C	80 °C	30 °C	30 W	60 W	$0.5\ \frac{MW}{m^3}$	$1\ \frac{MW}{m^3}$

Table 9.5: Parameters for test scenario with 2-D heat flow.

The test results from the 2-D heat flow tests are shown in figure 9.13 to 9.16. The FEM references shown in figure 9.13 and 9.15 are the temperatures along the line between the nodes T_a (at 0 mm) and

T_b (at 300 mm) (h/2 in y-axis). The average element temperatures from the T-equivalent approach are compared to the average element temperature from the FEM model. Table 9.6 states the temperature deviations between the approaches and the FEM model. The Standard Deviation (SD) is calculated from the temperature deviations by the equation 9.17. The standard deviation states how much the estimated temperatures deviate from the mean value, why a small value is desirable [34].

$$SD = \sqrt{\frac{1}{m}\sum_{i=1}^{m}(x_i - \bar{x})^2} \tag{9.17}$$

Where in equation (9.17):

m	Number of samples, $[-]$
SD	Standard deviation, $[°C]$
$\bar{x}$	Estimated temperature from FEMM model, $[°C]$
x_i	Estimated temperature from LP model, $[°C]$

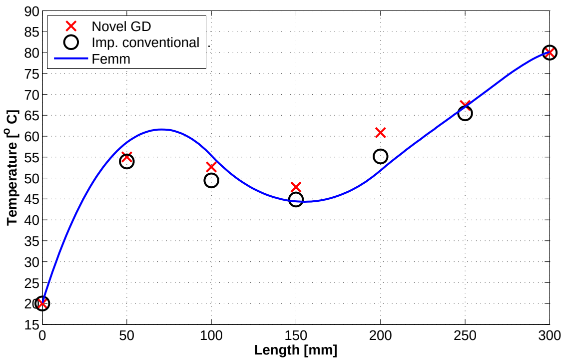

Figure 9.13: Temperature estimations from novel GD and improved conventional approaches in test 3.

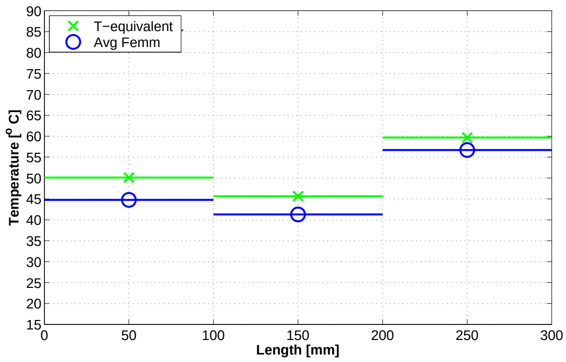

Figure 9.14: Temperature estimations from T-equivalent in test 3.

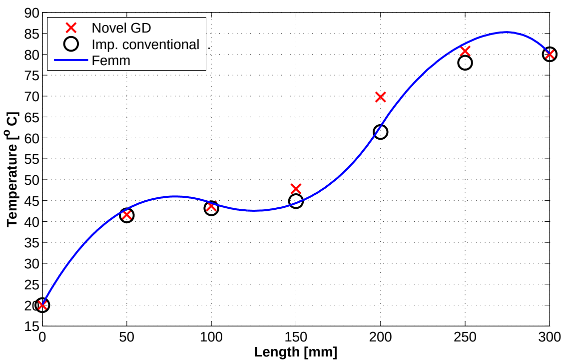

Figure 9.15: Temperature estimations from novel GD and improved conventional approaches in test 4.

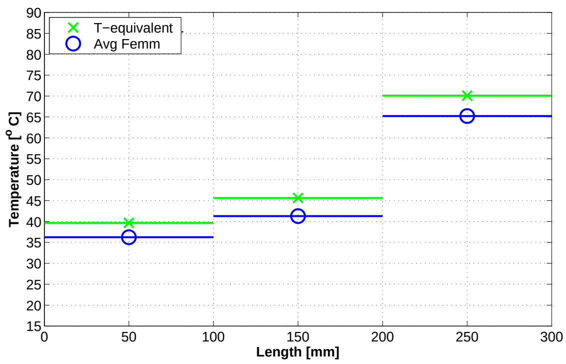

Figure 9.16: Temperature estimations from T-equivalent in test 4.

The results in table 9.6 shows that the improved conventional approach in average underestimates the temperatures, while the novel GD approach overestimates the temperatures and it is slightly closer to the FEM solution. The under- and overestimation are anticipated, since the total power in the improved conventional approach is half the power in the novel GD approach. The middle element has no power sources, why it has no temperature compensation and that cause a higher temperature in the novel GD approach. The improved conventional has a better SD than the novel GD approach, which has a maximum deviation of 9.27$°C$, compared to -6.51$°C$ for the improved conventional approach.

Compensation approach	T_{50mm}	T_{100mm}	T_{150mm}	T_{200mm}	T_{250mm}	Average	SD
Test 3							
Imp. conventional [$°C$]	-4.02	-6.51	0.41	3.58	-1.44	-1.60	3.5
Novel GD [$°C$]	-2.95	-3.28	3.39	9.27	0.46	1.38	4.6
T-equivalent [$°C$]	5.33		4.34		2.99	4.22	0.96
Test 4							
Imp. conventional [$°C$]	-1.49	-1.30	0.50	-1.09	-4.47	-1.57	1.6
Novel GD [$°C$]	-1.31	-0.75	3.47	7.28	-1.68	1.40	3.47
T-equivalent [$°C$]	3.44		4.34		4.89	4.22	0.60

Table 9.6: Temperature deviation between compensation approaches and FEM solution.

The temperatures from T-equivalent approach deviate in average with 4.22$°C$, which is the poorest accuracy of the three approaches. However the T-equivalent approach has the lowest SD and thus it seems to be more consistent. From the results stated in table 9.6 all the compensation approaches perform acceptable and thus the next test must be used to select the most suitable approach.

Scenario with several heat sources and symmetry

The third scenario is set up to verify how to model elements where symmetry is applied and to verify the compensation approaches in an element where several heat sources are located next to each other. The scenario is set up as shown in figure 9.17 where the parameters are the same as test 4 from table 9.5. The hatched area illustrates the area excluded due to symmetry. The heat sources are located in the hight h, since the power flows from the centre and out to the edges. The FEM model is developed in appendix D.1.3. The results are shown in figure 9.18 and 9.19, where the FEM references and the estimated temperatures are the temperatures along the green line in figure 9.17.

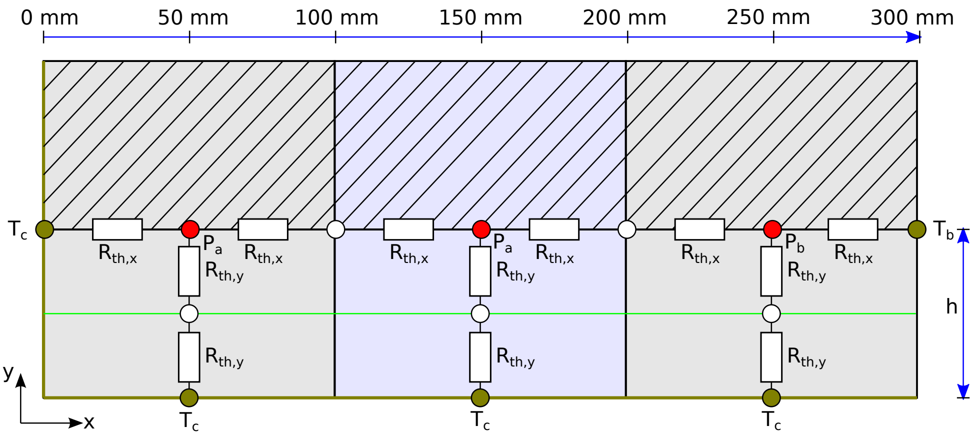

Figure 9.17: Test scenario with 2-D heat flow and where symmetry is applied.

From figure 9.18 it is seen the novel GD approach is able to estimate the FEM results accurately. From the test it is seen that the novel GD approach is most accurate in the nodes containing heat sources. The improved conventional approach underestimates the temperatures by up to 30$°C$, which is not acceptable. The underestimation is caused by several heat sources being located next to each other and the compensation approach, where half the power source is missing, and not by symmetry, as proved from the test in appendix D.1.4, where a similar element is shown without symmetry.

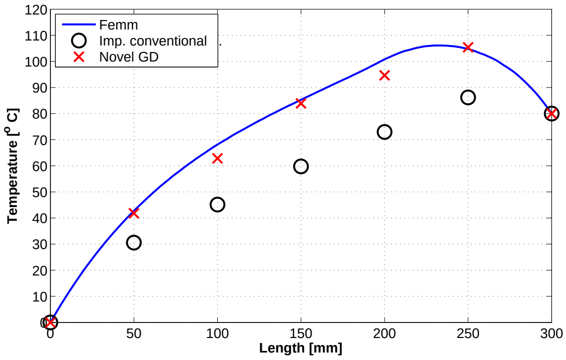

Figure 9.18: Temperature estimation from improved conventional and novel GD approaches in the scenario where symmetry is applied.

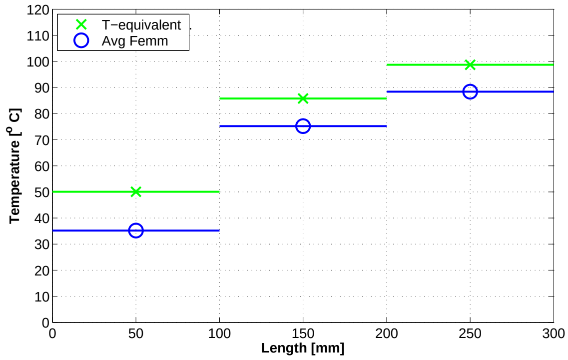

Figure 9.19: Average temperature estimation from T-equivalent and FEM model in the scenario where symmetry is applied.

Like the previous scenarios the T-equivalent approach overestimates the average temperature, however the percentage-wise overestimation is increased as shown in figure 9.19. One solution to improve the T-equivalent approach could be to decrease the -1/6 compensation resistance factor to around -1/5, however it is not investigated further.

Choice of compensation approach

From the test scenarios it is seen the improved conventional approach performs well, besides from the last scenario. The T-equivalent approach generally overestimates the temperatures, especially in the last scenario, which is undesirable as multiple heat sources beside each other is used in the thermal model of the PMSM. The novel GD approach performs well in all test scenarios, why it is chosen as the compensation approach for the lumped parameter model.

9.2 Lumped parameter model of the PMSM

A lumped parameter model of the PMSM is developed in this section. First the simplifications are discussed and afterwards the thermal network is presented.

9.2.1 Thermal simplifications

An axial cross sectional view of one half of the PMSM is shown in figure 9.20 and a 1/12 radial cross sectional view is shown in figure 9.21. These figures form the foundation of the thermal model of the PMSM.

The following simplifications are made in the lumped parameter model:

- The PMSM is considered to be thermally symmetric
- The liquid cooling is modelled as a constant temperature.
- The geometry of the PMSM is simplified.

The PMSM is considered as symmetric from a thermal point of view, why symmetry is used to reduce the number of elements. A 1/24 part of the PMSM is modelled, which equals a quarter tooth. If the

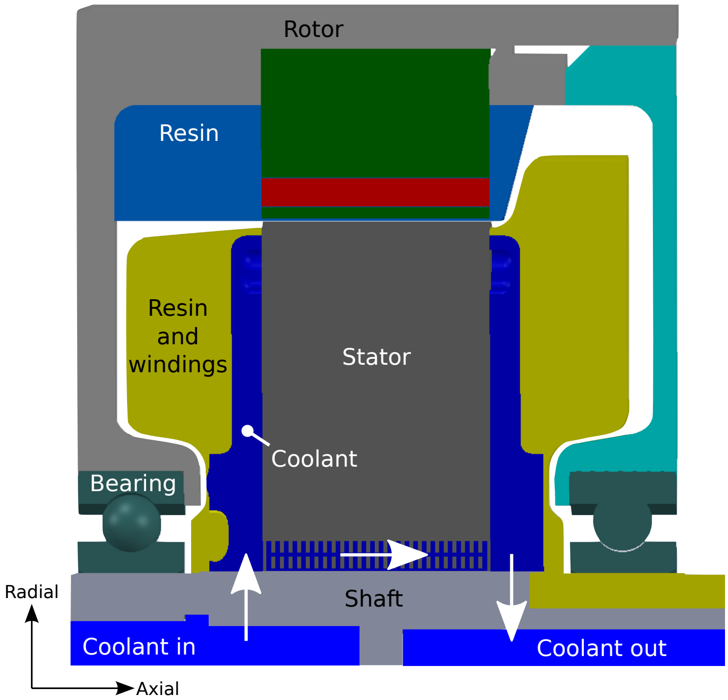

Figure 9.20: Axial cross sectional view of one half of the PMSM.

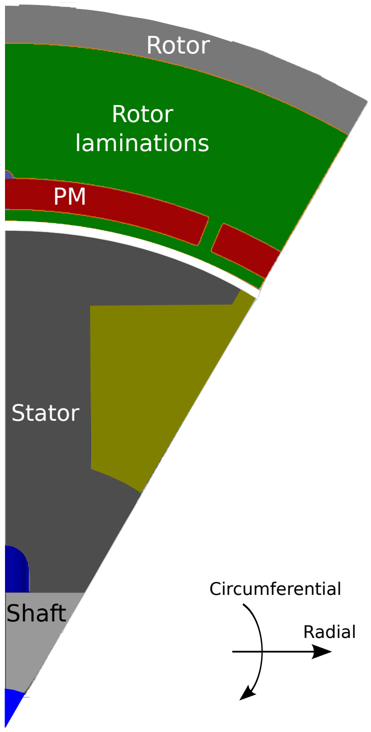

Figure 9.21: Radial cross sectional view of 1/12 of the PMSM.

geometry and heat flow are symmetric, there is no heat flow across the line of symmetry. The PMSM is not entirely symmetric for two main reasons:

- The geometry of the stator and rotor resin
- The geometry of the rotor

The resin contributes with an increased thermal mass, however in steady state the thermal mass has no influence on the calculated temperatures. Due to the low conductivity of the resin, the main heat flow paths are in the aluminium (in the rotor) and in the windings. For these reasons, the shape of the resin is considered to be symmetric.

The liquid cooling is modelled as a constant temperature, which is a simplification, since the liquid heats up as it flows through the cooling path. The heating of the liquid cooling causes an uneven axial temperature of the PMSM, however the effect is considered to be neglectable. The liquid cooling is assumed to cover the entire stator teeth, which is a simplification since the areas of the stator teeth are a bit larger than the coolant channels in the end plates.

Some of the PMSM geometries are simplified to ease the analytical calculations of the resistances. However since the internal resistances of the elements are small compared to the contact resistances, the inaccuracies introduced is considered not to influence the results.

Convection and radiation

From the test scenario in section 2.3 the pressure is 2.5 kPa, which is relevant as the convection and radiation heat transfer coefficients depend on the temperature of the specimen and pressure of the environment. In [35], the heat transfer coefficients of natural convection and radiation are studied as a function of specimen temperature and pressure. The specimen in [35] is a horizontal copper cylinder with a 6.35 *mm* diameter and a length of 160 *mm*. Data is available for pressures of 1 *kPa* and 10 *kPa*, which is assessed to be applicable to give an indication of the heat transfer coefficients at 2.5 *kPa*. An excerpt of the heat transfer coefficients are shown in figure 9.7 and table 9.8. As seen in the table, the heat transfer coefficient of radiation is not affected by the pressure, only the temperature of the specimen.

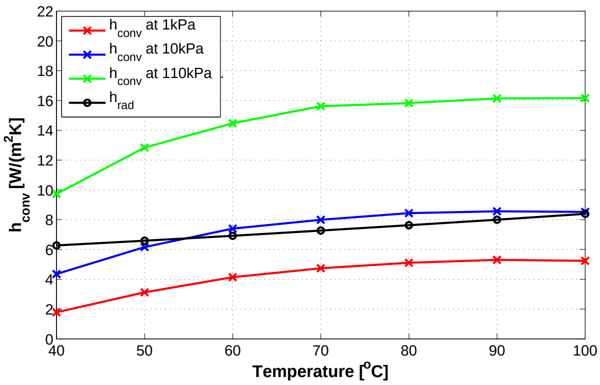

Table 9.7: Heat transfer coefficient as a function of specimen temperature [35].

		Pressure		
		1 kPa	**10 kPa**	**110 kPa**
$40°C$	h_{conv}	1.78	4.35	9.73
	h_{rad}	6.27	6.27	6.27
$100°C$	h_{conv}	5.24	8.52	16.16
	h_{rad}	8.39	8.39	8.39

Table 9.8: Heat transfer coefficients at various specimen temperatures and pressures [35].

Table 9.8 is used to assess the heat transfer from convection and radiation in the thermal test scenario. The heat transfer coefficient for radiation must be calculated for each part of the PMSM, as it depends on the emissivity of the material. However it is seen from the table that radiation must be considered for materials with high emissivity and temperature.

The rotor housing has low an emissivity (0.05-0.1 [9]), why the external radiation from the rotor housing is neglected, as the low emissivity results in a low heat transfer by radiation according to equation (9.8). Internal radiation is included as the emissivity of resin and the laminations are higher.

Internal and external convection are included in the thermal model in the test scenario, even though they are reduced according to table 9.8, as they are to be included during the verification of the model at atmospheric pressure and room temperature in section 10.3. Different approximations of the convection heat transfer coefficient are stated in [36]. However the approximated results are questionable, due to the number of approximated input parameters. Therefore it is chosen to simply estimate the heat transfer coefficient for convection by the data from table 9.8. This is a conservative approach since the coefficients are for natural convection rather than forced convection. However the air in the PMSM can only escape through the bearings. The entrapment reduces the forced convection, why the natural convection coefficient is found acceptable.

At specimen temperature of $100°C$ and a pressure of 2.5 *kPa* it is assessed that h_{conv} approximates around 6 $W/(m^2\ °C)$. At atmospheric pressure a heat transfer coefficient for convection of 16 $W/(m^2\ °C)$ is chosen. Radiation and convection is further handled in section 9.3.4.

9.2.2 Thermal network

An axial cross section of a quarter of the PMSM and a radial cross section view of a half tooth with nodes are shown in figure 9.22. Red nodes indicate heat sources and blue nodes indicate the temperature of the ambient and the coolant. The radial plane is modelled to include the heat transfer path between the slot windings and the stator tooth. The shaft is neglected in the radial plane as the heat flow is assessed to be neglectable. The stator tooth is divided into 3 nodes, to enable the calculations of the thermal resistance.

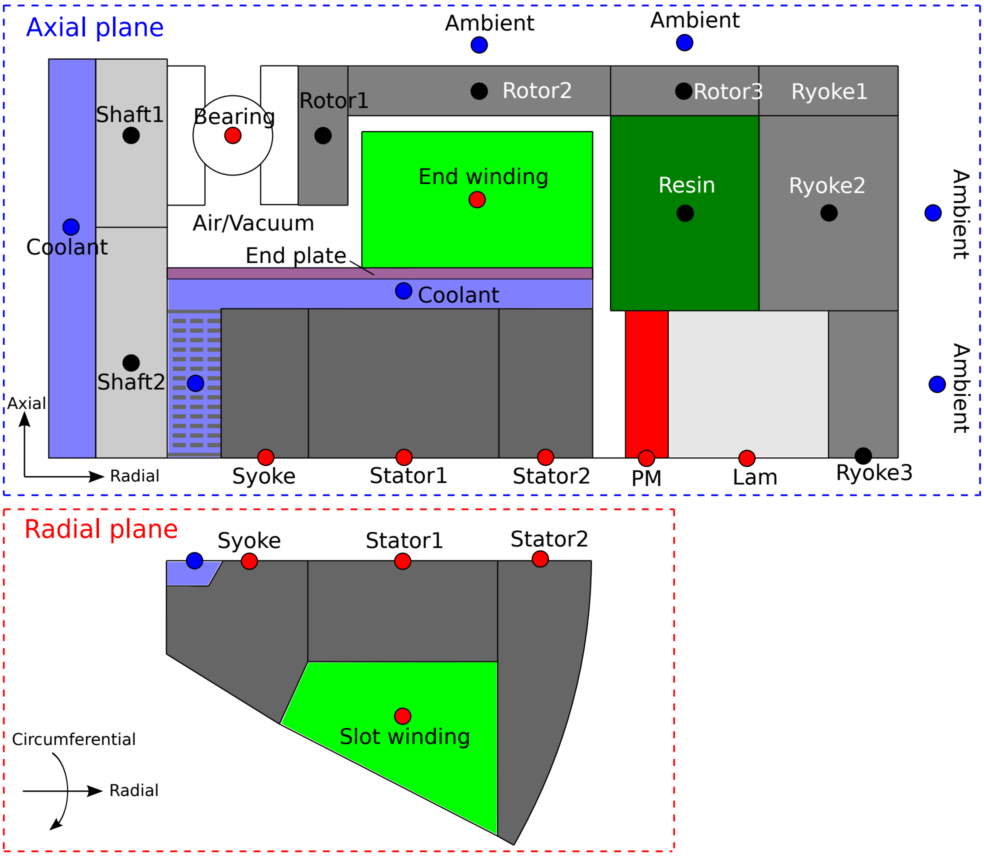

Figure 9.22: Axial cross sectional view of a quarter of the PMSM and radial cross sectional view a half stator tooth with nodes.

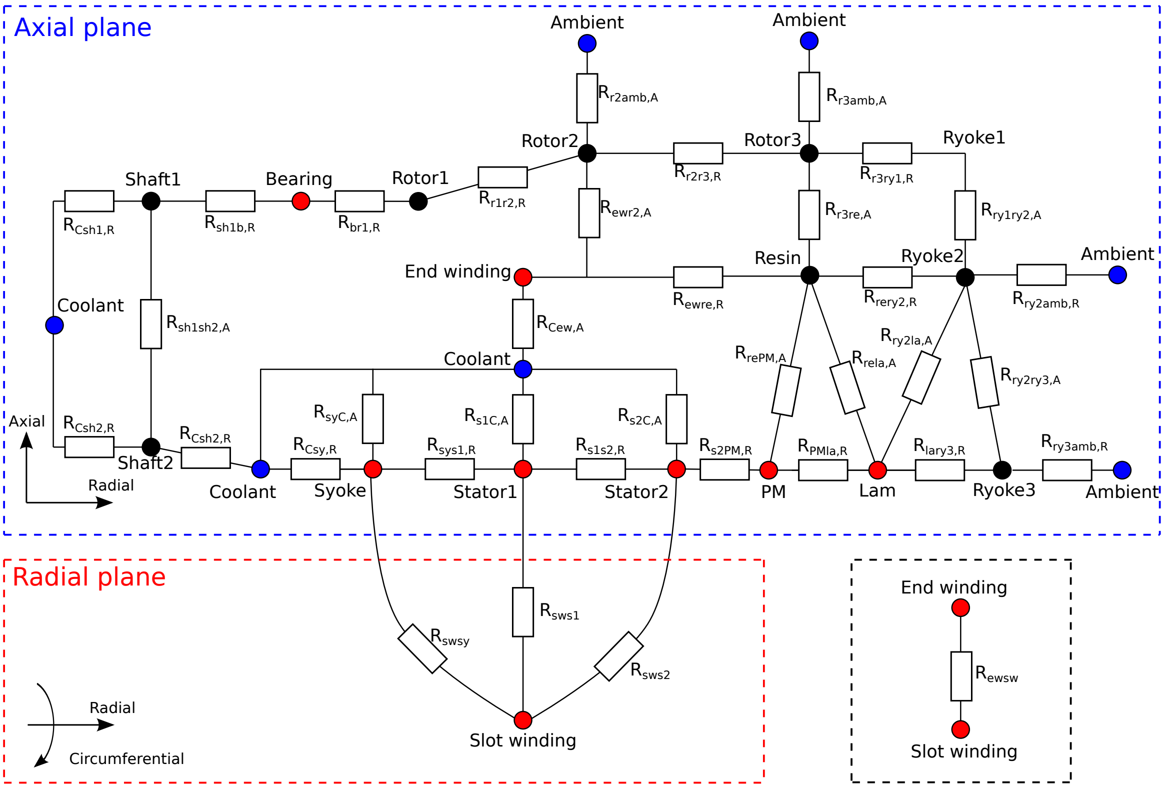

Figure 9.23: Axial and radial thermal network of the PMSM.

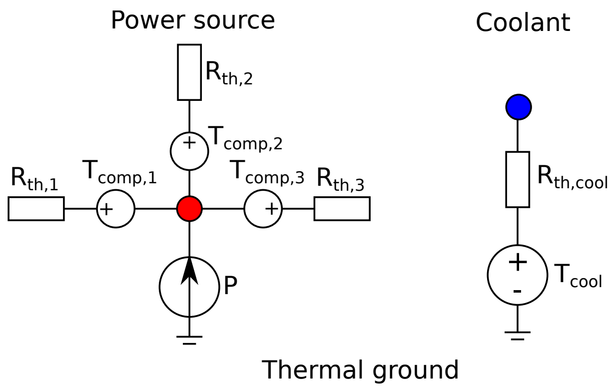

Figure 9.24: Symbolic nomenclature for thermal power source and coolant

A thermal network of the PMSM is derived on the basis of figure 9.22 and the thermal network is shown in figure 9.23. The figure shows the connection between the axial and radial plane in the thermal network. The thermal resistances are equivalent resistances, which means they may consist of several thermal resistances, as further discussed in section 9.3.1 to 9.3.3.

The subscripts indicate where the resistances are located, which are based on the node-names shown in figure 9.22. Equivalent resistances are abbreviated from the nodes as e.g. $R_{sh1sh2,A}$ from shaft1-shaft2 in axial direction and $R_{s2PM,R}$ from stator2-PM in radial direction. Some general subscripts used to identify the resistance locations are:

- xy,z: Equivalent resistance between node x and y in z direction, where z is:
  A: Resistance in axial direction
  R: Resistance in radial direction
  C: Resistance in circumferential direction
- X / Y: Contact resistance between element X and Y

Figure 9.24 depicts the modelling of power sources and liquid cooling. The resistance $R_{th,cool}$ is included to take the heat transfer coefficient for liquid cooling into account.

9.3 Resistance determination

The thermal resistances, shown in figure 9.23, are calculated in this section. Only resistances where considerable simplifications are made, are discussed in this section, the rest of the calculations are shown in appendix D.2. The resistance calculations are performed as described in section 9.1.1.

Thermal conductivities

The thermal conductivities used to calculate the resistances are stated in table 9.9. The thermal conductivity of the stator and rotor laminations are dependent on the direction of the heat flow, due to the contact resistances between each lamination. The axial conductivity is 20-40 times smaller than the radial conductivity, which is dependent on; clamping pressure, lamination thickness, stacking factor, lamination surface finish and interlamination insulation material [37]. A factor of 20 is chosen, in the absence of better or experimental data. The silicon content in the lamination steel decreases the thermal conductivity. Steel with a silicon content of 1%-4% has a thermal conductivity of 38-20 $W/(m\ K)$ [37]. The stator laminations have a silicon content of 2.5%, why a conductivity of 30 $W/(m\ K)$ is used.

Element	**Material**	**Conductivity** $[W/(m\ K)]$	**Source**
Windings	Copper	401	[38]
Resin	Casting resin	0.61	[39]
Stator lam (Radial/Axial)	2.5% Si Steel	R:30/A:1.5	[37]
Shaft	Stainless steel (416)	25	[40]
Rotor	Aluminium	237	[38]
PM	NdFeB	7.7	[41]
Rotor lam (Radial/Axial)	Steel M235-35A	R:40/A:2	[42]

Table 9.9: Materials and thermal conductivities of the PMSM parts.

The thermal conductivity of air varies with the pressure and temperature. In [43] a database containing thermal properties of fluids at various temperatures and pressures exist. Atmospheric air consists of 78% and 21% oxygen, why the conductivities of oxygen and nitrogen are used to calculate a conductivity of air by the content ratio. The conductivities of air at the test scenario pressure and atmospheric pressure at two temperatures are listed in table 9.10. The variation of the conductivity as a function of pressure is negligible and a conductivity of 0.031 $W/(m\ K)$ is chosen as the temperature of the air in the PMSM is expected to be around 100°C.

Temperature $[°C]$	**Pressure** $[kPa]$	**Conductivity** $[W/(m\ K)]$
100	2.5	0.0308
25	101.32	0.0259
100	101.32	0.0310

Table 9.10: The thermal conductivity of air at different pressures and temperatures, calculated on the basis of the database in [43].

Contact resistances

Contact resistance play a significant role due to the low conductivity of air. To circumvent the low conductivity, the stator has been cast into resin, as described in section 4.2.3. The resin has penetrated into the gaps with a large effective gap length, why the conductivity of air from equation (9.15) is replaced by the conductivity of resin, which is higher.

In tight fittings with small effective interface gap lengths, it is assessed that the resin does not penetrate. Other interfaces are not in contact with the resin. Which conductivities that have been used for the contact resistances between the parts in the PMSM are described in the related coming sections.

9.3.1 Stator and windings resistances

The thermal resistances of the stator and windings are calculated in this section. In [7] different geometrical approximations of the stator are investigated, to identify the deviation in the calculated resistances for each of the geometrical approximations. The geometry of the stator tooth is approximated to consist of cuboids, hexahedron or cylinder segments. It is found that the deviation between the methods is at most 1.3% for the total resistance of the tooth and at most 15% for the elements in the tooth.

Figure 9.25 shows half a stator tooth from a radial cross section view. The tooth is simplified to four cylindrical elements and one rectangular element in the radial plane. The radii and lengths are chosen such that the original volume of each element is preserved. The dimensions and volumes are calculated from a CAD model. It is seen from figure 9.26 that there is no connections between the three stator nodes (Syoke2, Stator1 and Stator2). The nodes are connected in the axial plane, as shown in figure 9.28, which is why they are not included the radial plane.

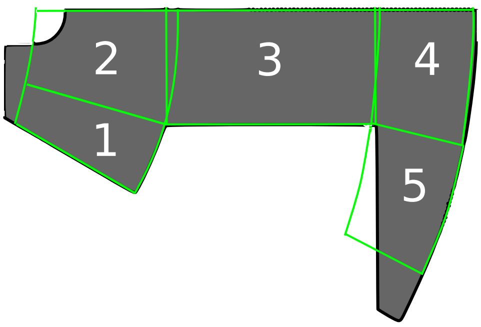

Figure 9.25: Geometrical simplifications used to calculate the internal conduction resistances.

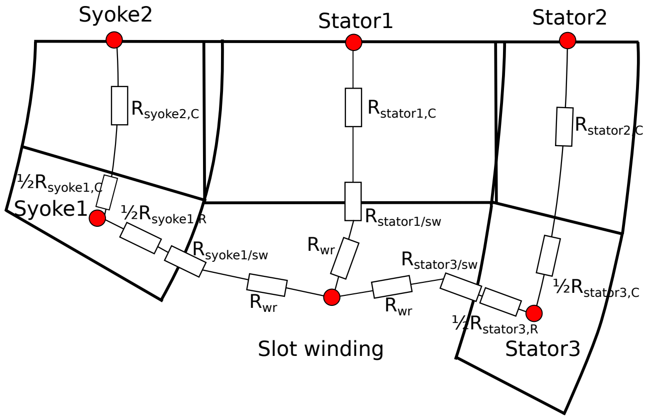

Figure 9.26: Resistances in the radial cross section view.

The simplified element 5 in figure 9.25 leads to a larger radial resistance and a smaller circumferential resistance, but as the total resistance through this element is of interest, the geometrical simplifications are assessed to be valid for this model. The same argument holds for the sum of resistances of element 1 and 2. The interface between element 2 and 3 and element 3 and 4 overlap, but the extra conduction resistance from the overlap is neglectable.

The windings and the resin are simplified to one element that consists of resin and copper. The resistance of this element R_{wr} is determined from the dimensions in the axial plane shown in figure 9.28 and the fill factor for the windings. The copper is neglected, due to its high conductivity, and 60% of the end windings is assumed to be resin, which is used to calculate the internal winding resistance as an axial resistance.

$$R_{wr} = 0.6 \, \frac{8.5 \cdot 10^{-3} \; m}{500 \cdot 10^{-6} \; m^2 \; 0.61 \; W/(m \; K)} = 16.7 K/W \tag{9.18}$$

It is assumed that this resistance applies for all of the resistances from the middle slot to the stator tooth.

Contact resistance between slot windings and stator

The contact resistance between the windings in the slot and the stator tooth depends on the insulation plastic, how well the resin has filled the air gaps in the windings and on how tight the windings are wound. From the sliced PMSM shown in figure 9.27 and appendix B.2, it is seen that the resin has filled the air gaps in the windings.

The properties of the insulation plastic is found from a DuPont Nomex paper Type 410 insulation paper with a conductivity of 0.1 $W/(m \; K)$ and a thickness of 0.25 mm [44], as no thermal properties of the utilised DuPont Mylar insulation plastic are available, however it is assessed the thermal properties are similar. Due to the low conductivity of the insulation paper, the influence of the tightness of the windings

Figure 9.27: A radial sliced slot in the middle of the stator stack.

is neglected as the gaps are filled with resin which has a 9 times higher conductivity compared to the insulation paper.

$$R_{stator1/sw} = \frac{t_{insulation}}{A\ k_{insulation}} \tag{9.19}$$

$$= \frac{0.25 \cdot 10^{-3}\ m}{320 \cdot 10^{-6}\ m^2\ 0.1\ W/(m\ K)} = 7.8\ K/W \tag{9.20}$$

Where in equation 9.19:

$k_{insulation}$	Thermal conductivity of insulation plastic, $[W/(m\ K)]$
$t_{insulation}$	Thickness of insulation, $[m]$

To calculate the two remaining contact resistances in the radial plane shown in figure 9.26, equation (9.19) is used, where the only change is the contact area:

$$R_{stator3/sw} = \frac{0.25 \cdot 10^{-3}\ m}{250 \cdot 10^{-6}\ m^2\ 0.1\ W/(m\ K)} = 10\ K/W \tag{9.21}$$

$$R_{syoke1/sw} = \frac{0.25 \cdot 10^{-3}\ m}{100 \cdot 10^{-6}\ m^2\ 0.1\ W/(m\ K)} = 25\ K/W \tag{9.22}$$

Contact resistances between end plate and end windings

The contact resistance between the end plate and the end winding is calculated in the same way as equation (9.19) but with the area between the end plate and end winding.

$$R_{ep/ew} = \frac{0.25 \cdot 10^{-3}\ m}{313 \cdot 10^{-6}\ m^2\ 0.1\ W/(m\ K)} = 8.0\ K/W \tag{9.23}$$

Stator and windings resistances overview

The remaining thermal resistances from figure 9.26 and 9.28, are calculated in appendix D.2 and stated in table 9.11.

The dominating resistances are in the axial direction ($R_{syC,A}$, $R_{s1C,A}$, $R_{s2C,A}$) due to the low conductivity of the laminations in the axial direction. Also the equivalent resistances, containing contact resistances ($R_{sysw,R}$, $R_{s1sw,C}$, $R_{s2sw,R}$), are dominating due to the size of the contact resistances.

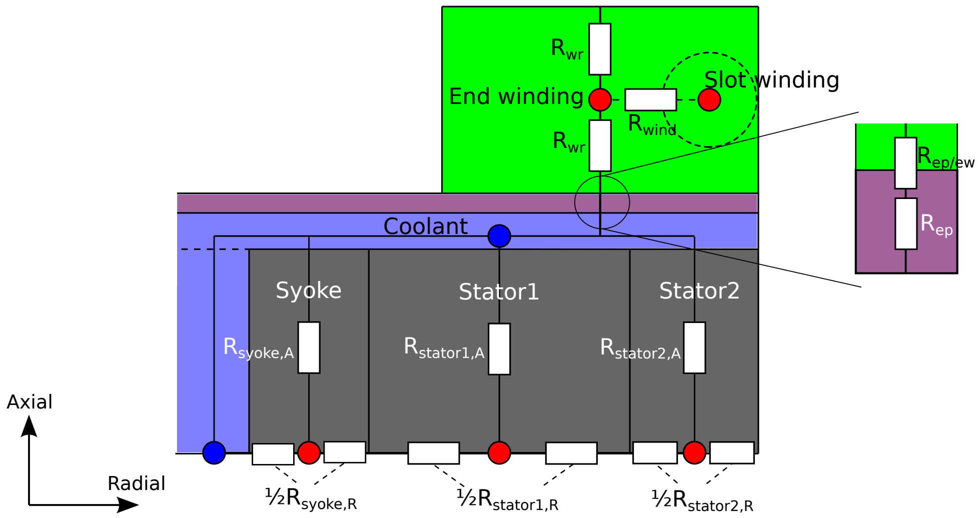

Figure 9.28: Resistances in the axial cross section view.

Thermal resistance		Features	Value $[K/W]$
$R_{Csy,R}$	=	$\frac{1}{2}R_{syoke,R}$	2.86
$R_{sys1,R}$	=	$\frac{1}{2}R_{syoke,R}+\frac{1}{2}R_{stator1,R}$	4.97
$R_{s1s2,R}$	=	$\frac{1}{2}R_{stator1,R}+\frac{1}{2}R_{stator2,R}$	3.03
$R_{syC,A}$	=	$R_{syoke,A}$	49.0
$R_{s1C,A}$	=	$R_{stator1,A}$	45.3
$R_{s2C,A}$	=	$R_{stator2,A}$	45.9
$R_{Cew,A}$	=	$R_{wr}+R_{ep/ew}+R_{ep}$	21.9
R_{ewsw}	=	R_{wind}	0.77
R_{swsy}	=	$R_{wr}+R_{syoke1/sw}+\frac{1}{2}R_{syoke1,R}+\frac{1}{2}R_{syoke1,C}+R_{syoke2,C}$	41.6
R_{sws1}	=	$R_{wr}+R_{stator1/sw}+R_{stator1,C}$	17.9
R_{sws2}	=	$R_{wr}+\frac{1}{2}R_{stator3/sw}+\frac{1}{2}R_{stator3,R}+\frac{1}{2}R_{stator3,C}+R_{stator2,C}$	27.0

Table 9.11: Thermal resistances of the stator and windings.

9.3.2 Shaft and bearings resistances

In the following sections the resistances of the shaft and bearings are stated. The resistances are shown in figure 9.23 for the bearings and the shaft. The simplifications made during these resistances are concerning the geometry of the shaft. The shaft is simplified as two hollow cylinders where the dimensions preserve volume of each element.

Thermal resistance of the bearing

In [28] a thermal model of a ball bearing is presented and the thermal network is depicted in figure 9.30 along with a CAD drawing of the actual bearing. The thermal resistance R_0 represents the heat flow through the metal cap sealing. This heat flow is neglected due to the small thickness of the metal shield and the focus is put on determination of the thermal resistance $R_{bear,R}$ [28].

The thermal resistance $R_{bear,R}$ depends on the equivalent contact surface between the balls and the inner and outer race of the bearing, which also includes lubrication. The thermal resistance also depends on the angular velocity, as the thermal resistance decreases as the velocity rises. A function that depends on

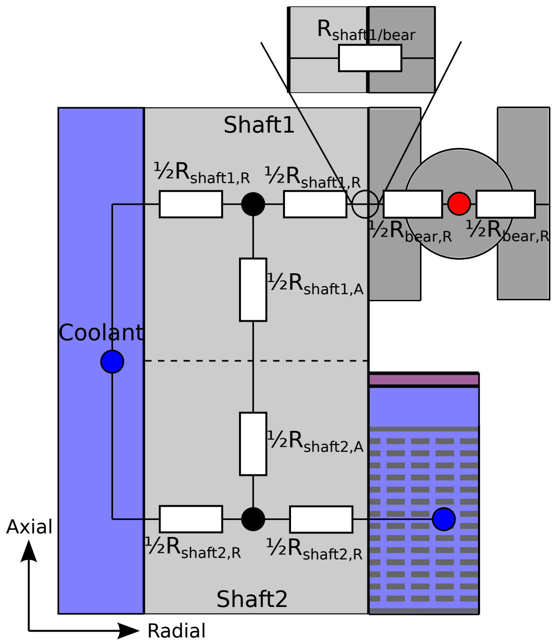

Figure 9.29: Thermal resistances of the shaft and bearings.

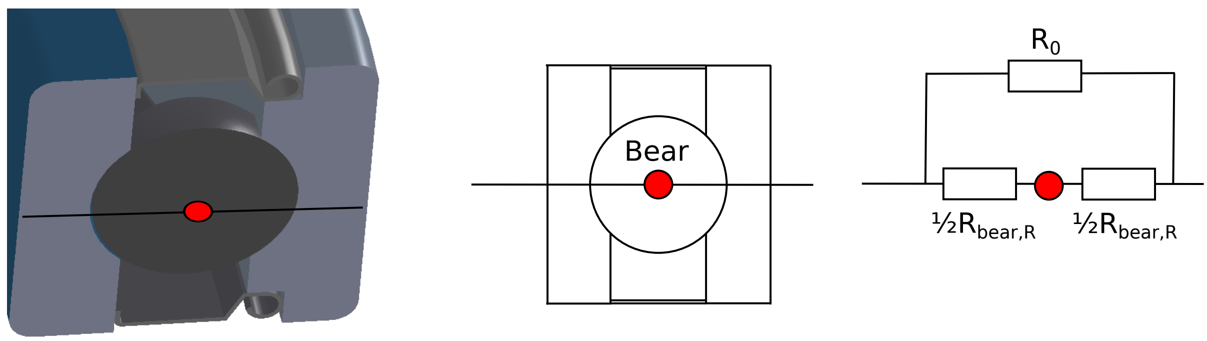

Figure 9.30: Thermal model of ball bearings [13].

the velocity and bearing size is set up on the basis of experimental measurements in [28] but the function is only valid within the size and linear velocity limitations:

$$46\ mm \leqslant d_b \leqslant 77.5\ mm \quad \wedge \quad \omega_{rm}\ d_b \leqslant 14.5\ m/s \tag{9.24}$$

Where in equation 9.24:

d_b	Average bearing diameter, $[m]$
ω_{rm}	Mechanical angular velocity, $[rad/s]$

For the PMSM these values are $d_b = 48\ mm$ and $\omega_{rm}\ d_b = 75\ m/s$. Therefore it is chosen to calculate the resistance of the bearing at the minimum value of d_b and the maximum linear velocity, by the function stated in equation (9.26) [28]. This is a conservative consideration, as the thermal resistance decreases as the velocity rises.

$$\begin{aligned} R_{bear,R} &= 0.45\ K/W\ \big(0.12 - 1\ m^{-1}\ 0.046\ m\big)\big(33 - 1\ s/m\ \ 14.5 m/s\big)\ 12 && (9.25) \\ &= 7.4 K/W && (9.26) \end{aligned}$$

The factor of 12 is due to the symmetry conditions in the radial plane. This resistance is used as an approximation of the thermal resistance trough the bearing, even though the higher velocity of the PMSM decreases the resistance.

Contact resistances between shaft and bearings

The contact resistance between the shaft and the bearing is taken to be the interface gap between two parts of stainless steel from table 9.2. The smallest gap length is chosen due to tight fitting of the bearing on the shaft. The resistance is calculated by the radial resistance formula and the conductivity of air.

$$R_{shaft1/bear} = \frac{ln\left(\frac{r_1+t_{eq}}{r_1}\right)}{\theta\ k_{air}\ l} \tag{9.27}$$

$$R_{shaft1/bear} = \frac{ln\left(\frac{17.5\cdot 10^{-3}\ m+0.0070\cdot 10^{-3}\ m}{17.5\cdot 10^{-3}\ m}\right)}{\frac{\pi}{6}\cdot 0.031\ W/(m\ K)\cdot 14\cdot 10^{-3}\ m} = 1.8\ K/W \tag{9.28}$$

Where in equation (9.27):

k_{air}	Thermal conductivity of air, $[W/(m\ K)]$

Shaft and bearings resistances overview

The remaining thermal resistances from figure 9.29, are calculated in appendix D.2 and stated in table 9.12.

Thermal resistance		Features	Value $[K/W]$
$R_{Csh1,R}$	=	$\frac{1}{2}R_{shaft1,R}$	1.2
$R_{Csh2,R}$	=	$\frac{1}{2}R_{shaft2,R}$	0.83
$R_{sh1sh2,A}$	=	$\frac{1}{2}R_{shaft1,A}+\frac{1}{2}R_{shaft2,A}$	14.6
$R_{sh1b,R}$	=	$\frac{1}{2}R_{shaft1,R}+R_{shaft1/bear}+\frac{1}{2}R_{bear,R}$	10.4

Table 9.12: Thermal resistances for shaft and bearings.

The resistances in the shaft are small, and as no heat is generated in the shaft, the influence of the resistances is limited. The heat flow from the bearing to the coolant is primarily through the resistances in the radial direction of Shaft1, due to the larger resistance in the axial direction.

9.3.3 Rotor resistances

In the following section the resistances of the rotor are calculated. The resistances are shown in figure 9.23. A detailed figure of the resistances is shown in figure D.10 in appendix D.2.3.

Contact resistance between bearing and rotor

The contact resistance between the bearing and the rotor is calculated from the effective gap length between aluminium and steel from table 9.2 and the smallest effective gap length is chosen due to the tight fitting between the rotor and the bearing. The conductivity of air is used and the contact resistance is calculated as a radial resistance:

$$R_{bear/rotor1} = \frac{ln\left(\frac{r_1+t_{eq}}{r_1}\right)}{\theta\ k_{air}\ l} \tag{9.29}$$

$$R_{bear/rotor1} = \frac{ln\left(\frac{31\cdot 10^{-3}\ m+0.0058\cdot 10^{-3}\ m}{31\cdot 10^{-3}\ m}\right)}{\frac{\pi}{6}\cdot 0.031\ W/(m\ K)\cdot 14\cdot 10^{-3}\ m} = 0.8\ K/W \tag{9.30}$$

Contact resistance between rotor yoke and laminations

The thermal contact resistance between the rotor yoke and the laminations is difficult to determine, because it depends on the alignment of the laminations, the fitting in the rotor housing, the temperature and the materials. The effective gap length is larger compared to the effective gap lengths from table 9.2. The thermal expansion of the laminations and the rotor housing causes the effective gap length to increase during heating of the parts, due to the different thermal expansion coefficients of aluminium and steel. In [32] effective interface gap lengths between housing and laminations are presented based on measurements performed on different sizes and types of motors. It is suggested to use the average of the calculated gap, which is 0.037 *mm*. This is assessed to be a good approximation from the assembling process of the rotor, as the rotor laminations had a tight fit in the rotor housing. The conductivity of air is used, as it is assessed the centrifugal casting process did not force resin to fill the small gap. The contact resistance is calculated as:

$$R_{ryoke2/lam} = \frac{ln\left(\frac{r_1+t_{eq}}{r_1}\right)}{\theta\ k_{air}\ l} \tag{9.31}$$

$$R_{ryoke2/lam} = \frac{ln\left(\frac{87.5\cdot 10^{-3}\ m+0.037\cdot 10^{-3}\ m}{87.5\cdot 10^{-3}\ m}\right)}{\frac{\pi}{6}\cdot 0.031\ W/(m\ K)\cdot 15\cdot 10^{-3}\ m} = 1.7\ K/W \tag{9.32}$$

Contact resistance between permanent magnets and rotor laminations

The thermal contact resistance between the permanent magnets and the laminations could be calculated based on the largest effective interface gap length between ceramics and steel of 0.0173 *mm* from table 9.2. However an assessment of the fitting of the permanent magnets in the rotor laminations during the assembling process reveals a larger gap, which is assessed to be 0.1 *mm*. This gap also includes the gap that occurs as a consequence of the laminated permanent magnets. It is assessed that the gap is filled with resin. The contact resistance is calculated as:

$$R_{PM/lam} = \frac{ln\left(\frac{r_1+t_{eq}}{r_1}\right)}{\phi\ k_{resin}\ L} \tag{9.33}$$

$$R_{PM/lam} = \frac{ln\left(\frac{70.23\cdot 10^{-3}\ m+0.1\cdot 10^{-3}\ m}{70.23\cdot 10^{-3}\ m}\right)}{\frac{\pi}{6}\cdot 0.61\ W/(m\ K)\cdot 15\cdot 10^{-3}\ m} = 0.3\ K/W \tag{9.34}$$

Where in equation (9.33):

k_{resin}	Thermal conductivity of resin, $[W/(m\ K)]$

As the gap is filled with resin, this contact resistance is low compared to the other contact resistances.

Rotor resistances overview

The remaining thermal resistances from figure 9.29, are calculated in appendix D.2 and stated in table 9.13, afterwards they are discussed.

Thermal resistance		**Features**	**Value** $[K/W]$
$R_{br1,R}$	=	$\frac{1}{2}R_{bear,R} + R_{bear/rotor1} + \frac{1}{2}R_{rotor1,R}$	8.26
$R_{r1r2,R}$	=	$\frac{1}{2}R_{rotor1,A} + \frac{1}{2}R_{rotor1,R} + \frac{1}{2}R_{rotor2,R}$	0.54
$R_{r2r3,R}$	=	$\frac{1}{2}R_{rotor2,R} + \frac{1}{2}R_{rotor3,R}$	0.63
$R_{r3ry1,R}$	=	$\frac{1}{2}R_{rotor3,R} + \frac{1}{2}R_{ryoke1,R}$	0.30
$R_{r3re,A}$	=	$\frac{1}{2}R_{rotor3,A} + \frac{1}{2}R_{resin,A}$	28.3
$R_{ry1ry2,A}$	=	$\frac{1}{2}R_{ryoke1,A} + \frac{1}{2}R_{ryoke2,A}$	0.10
$R_{rery2,R}$	=	$\frac{1}{2}R_{resin,R} + \frac{1}{2}R_{ryoke2,R}$	17.4
$R_{rePM,A}$	=	$\frac{1}{2}R_{resin,A} + R_{PM,A}$	42.9
$R_{rela,A}$	=	$\frac{1}{2}R_{resin,A} + \frac{1}{2}R_{lam,A}$	38.8
$R_{ry2la,A}$	=	$\frac{1}{2}R_{ryoke2,A} + R_{ryoke2/lam} + R_{lam,A}$	12.5
$R_{ry2ry3,A}$	=	$\frac{1}{2}R_{ryoke2,A} + \frac{1}{2}R_{ryoke3,A}$	0.34
$R_{PMla,R}$	=	$\frac{1}{2}R_{PM,R} + R_{PM/lam} + \frac{1}{2}R_{lam,R}$	6.67
$R_{lary3,R}$	=	$\frac{1}{2}R_{lam,R} + R_{lam/ryoke3} + \frac{1}{2}R_{ryoke3,R}$	2.10

Table 9.13: Thermal resistances for the rotor.

The resistances from conduction are small compared to the contact resistances and as the heat flow in the rotor is expected to be small, further simplifications of the rotor housing geometry could have been made without affecting the temperatures. The resistances from the resin are large due to the low conductivity of resin.

9.3.4 Radiation and convection resistances in the test scenario

In this section the radiation and convection resistances are stated for the conditions in the test scenario. The resistances are presented in table 9.14 and assigned as depicted in figure D.10. Convection resistances are abbreviated by *conv* and radiation resistances by *rad*. The radiation resistances are calculated from assessed temperatures of the PMSM, as they are temperature dependent. A stator and winding temperature of 140°C and a rotor temperature of 110°C are used to calculate the radiation resistances. The resistances $R_{stator2/PM,rad}$ and $R_{ew/resin,rad}$ are calculated as radiation between cylindrical surfaces and $R_{stator2/PM,rad}$ is calculated as radiation between two parallel planes, both described by equation (9.14). A heat transfer coefficient of 6 $W/(m^2\ °C)$ is used for the convection.

As seen from table 9.14 the resistances are higher than the resistances for the rest of the PMSM as expected. The radiation resistances are calculated by equation (9.10). To include the temperature dependency in the thermal model, the radiation resistance is calculated by iterations of equation (9.10) and temperatures from the simulation model. First simulations are made where the radiation resistance is high. The simulated temperature of the rotor is used in the next iteration to calculate a new radiation resistance, which is implemented in the simulation model. The new radiation resistance causes the temperature in the rotor to decrease and the procedure is repeated until the calculated resistance is almost constant.

Thermal resistance		**Value** $[K/W]$
$R_{stator2/PM,rad}$	=	309
$R_{ew/rotor2,rad}$	=	1400
$R_{ew/resin,rad}$	=	114
$R_{stator2/PM,conv}$	=	350
$R_{ew/rotor2,conv}$	=	333
$R_{ew/resin,conv}$	=	223
$R_{rotor2,conv}$	=	199
$R_{rotor3,conv}$	=	145
$R_{ryoke2,conv}$	=	141
$R_{ryoke3,conv}$	=	229

Table 9.14: Thermal resistances of radiation and convection.

CHAPTER

10

VERIFICATION OF THERMAL MODEL

The thermal model of the PMSM is verified in this chapter. A 2-D FEM model is developed in section 10.1 to verify the lumped parameter model in the axial and radial plane against the FEM model. The lumped parameter model is compared to a FEM model of the PMSM in section 10.2. The comparison is performed to investigate the simplifications in the geometry of the lumped parameter model and the performance of the chosen compensation approach. After this comparison, it is compared to measurements performed on stator-v1 in section 10.3. The stator is tested to verify the lumped parameter thermal model of the stator by experimental tests. No thermal tests are performed on the PMSM during operating due to the leakage described in section 4.2. The final results from the thermal test scenario, from section 2.3, are presented in section 10.5.

10.1 FEM model

The FEMM software package is used to model the 2D FEM model of the PMSM in the axial and radial planes. Some of the basic options are described in appendix D.3. FEMM is a free software, which is capable of solving 2D planar and axisymmetric magnetic, electrostatic, heat, and current flow problems [45]. FEMM solves heat flow problems as a heat conduction problem described by:

$$-\nabla(k_{th}\,\nabla T) = q_{th} \tag{10.1}$$

Were in equation (10.1):

k_{th}	Thermal conductivity, $[W/(m\ K)]$
T_i	Temperature, $[°C]$
q_{th}	Heat generation, $[W/m^3]$

FEM provide approximate solutions to the analytical solution, but as seen in section 9.1.2, the FEM solutions are very close to the analytical solution. The accuracy of the method in more complex scenarios, compared to the 1D bar element, depends on the discretization level, the specified boundaries and the input data, why the FEM cannot be used unassisted to validate the lumped parameter model of the PMSM. FEMM does not make it possible to connect the axial and radial plane by e.g. boundary conditions, why the FEM model is used to verify the lumped parameter model for each plane separately.

As for the lumped parameter, a 1/24 of the PMSM is modelled and a 1/24 of the power losses are used as input.

FEM model of the PMSM

The planar definition causes a mismatch between the volumes of the FEMM and the volumes of PMSM in the axial plane as the symmetry segment of the PMSM is a sector of a circle. The mismatch between volumes in the axial plane is taken into account when the FEM properties are calculated as the properties of the lumped parameter are used to determine the FEM properties. The axial problem is specified as a planar problem with a thickness, t_{plan}, of 100 mm, whereas the radial problem is specified with a thickness of 15 mm, corresponding to half of the stack length. To build the PMSM in FEMM the following properties are modelled as:

- Losses are modelled as a distributed volumetric heat generation.
- Conductivities are calculated based on resistances from section 9.3.
- Liquid cooling and ambient temperature are modelled as boundary temperatures.
- The heat transfer coefficients from radiation and convection are taken into account by extra elements with conductivities calculated from the lumped parameter model resistances.

Each element in the lumped parameter model corresponds to an element in the FEM model as shown in figure 10.1. Thus by referring to an element in the FEM model, the reference is not to the discretisation elements. Mesh refinement is performed until the solution converges. The convergence is assessed based on the change in temperature between each mesh refinement.

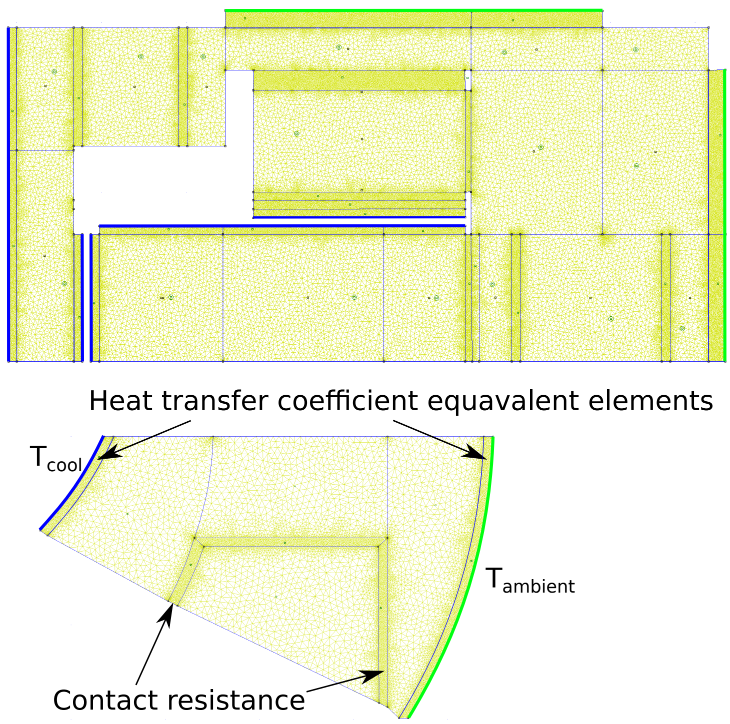

Figure 10.1: PMSM geometry in FEMM with elements and material properties.

The conductivities of the materials in the axial plane are calculated on the basis of the thermal resistances and geometry of the lumped parameter model, to ensure the thermal resistances of the two models correspond and thus including the influence from the third dimension in the conductivities. The thermal conductivity for each element of the PMSM is calculated as:

$$k_{th} = \frac{l}{A\ R_{th}} \tag{10.2}$$

Where in equation (10.2):

A	Area, $[m^2]$
l_i	Length, $[m]$
R_{th}	Thermal resistance, $[K/W]$

It is not possible to specify a contact resistance between two elements in FEMM as it is in other commercial programmes. To circumvent the inability to specify the contact resistances, equivalent elements with a thickness of 1 mm and conductivities that result in the contact resistances from the lumped parameter model, are implemented. The conductivities of these equivalent elements are calculated as:

$$k_{th,cont} = \frac{1\ mm}{A\ R_{th,cont}} \tag{10.3}$$

Where in equation (10.3):

$k_{th,cont}$	Conductivity though contact element, $[W/(m\ K)]$
$R_{th,cont}$	Thermal contact resistance, $[K/W]$

10.2 Comparison of FEM model and lumped parameter model

The temperatures from the lumped parameter model are compared to the temperatures of the FEMM model. The lumped parameter model is disassembled such that the axial and the radial plane are separated. The disassembling is done since the FEM model cannot be connected between the two planes as the lumped parameter model can. To compare the two models, some arbitrarily chosen input parameters are used, which are listed in table 10.1. The results are shown in table 10.2 where the nomenclature corresponds to those in figure 9.23.

Parameter	**Value**	**Description**
h_{conv}	$16\ W/(m^2\ K)$	Heat transfer coefficient of convection to the surroundings
h_{liquid}	$7000\ W/(m^2\ K)$	Heat transfer coefficient of the liquid cooling
$T_{ambient}$	$20°C$	Temperature of the ambient air
T_{cool}	$30°C$	Temperature of the liquid cooling
P_{cu}	$270\ W$	Copper losses
P_{core}	$650\ W$	Core losses

Table 10.1: Arbitrary chosen input values.

The deviations in table 10.2 are generally higher than those from section 9.1.2, where the compensation approaches were tested on a well-defined and simple geometry. The primary source to the deviations is assessed to be the transition surfaces between two elements of different size. In the FEMM, the elements do not have contact on the entire transition surface, if the elements are of different size, but this is not taken into account in the lumped parameter model. The difference results in an extra thermal resistance, which results in higher temperatures in the FEMM.

Node	**FEMM** [°C]	**LP** [°C]	**Deviation** [%]
Axial plane			
T_{PM}	66.9	62.0	-7.3
T_{lam}	62.9	58.27	-7.4
T_{ryoke2}	60.6	55.0	-9.2
T_{rotor3}	60.5	54.7	-9.6
T_{bear}	56.9	52.0	-8.6
T_{syoke}	66.1	66.0	-0.2
$T_{stator1}$	90.3	84.0	-7.0
$T_{stator2}$	96.9	89.2	-7.9
T_{ew}	126	120	-4.8
Radial plane			
T_{syoke}	91.5	94.5	3.4
$T_{stator1}$	127	128	0.8
$T_{stator2}$	143	137	-4.2
T_{ew}	155	149	-3.9

Table 10.2: Temperatures from the lumped parameter model and FEMM in the disassembled axial and radial planes. The temperature locations are shown in figure 9.22 and 9.23 on page 90.

The geometrical simplifications of the stator tooth and slot winding in the radial plane of the lumped parameter model might cause an over prediction in the radial plane.

The fact that the tendency for the lumped parameter model to underestimate temperatures makes it possible to compensate for this when the lumped parameter model is compared to experimental tests, by fitting e.g. the amount of convection and radiation or the resistances in the PMSM.

10.3 Experimental verification of thermal stator model

Experimental tests performed on stator-v1 are used to verify the thermal model of the stator. The rotor is not tested experimentally as no temperature measurements are available for the rotor. A thermographic camera is tested, but light reflection and estimation of the emissivity dominates measured temperatures why it is discarded. Other attempts like outer placed thermocouples on the rotor could be attempted however a well-defined power loss is needed to establish a good comparison, why it is discarded. Furthermore most of the losses are placed in the stator which causes a higher heat flow.

The ideal test scenario is to test the thermal model in the operational conditions, but as no vacuum chamber is at disposal, the experimental verification is performed at room temperature (19°C) and atmospheric pressure (101.32 kPa). The thermal model of the PMSM is adjusted according to the pressure and temperature from the test set-up. The following adjustments are made:

- Adjustment of the ambient temperature and pressure
- Adjustment of the heat transfer coefficients for convection and radiation.
- The rotor is removed from the lumped parameter model.

As the rotor is removed, the radiation resistances are calculated from equation (9.9) as the heat transfer is not between two surfaces, why it is assumed the surroundings absorb the entire radiation. Figure 10.2

shows the thermal resistances when the rotor is removed. The temperatures of the shaft are of no interest as it does not conduct heat in this scenario however it is included to show the resistances of the liquid cooling along the shaft. The radiation resistances, listed in table 10.3, are calculated for a winding and stator temperature of $140°C$ and $110°C$ respectively. A heat transfer coefficient for convection of 16 $W/(m^2\ C)$ is chosen as described in section 9.2.

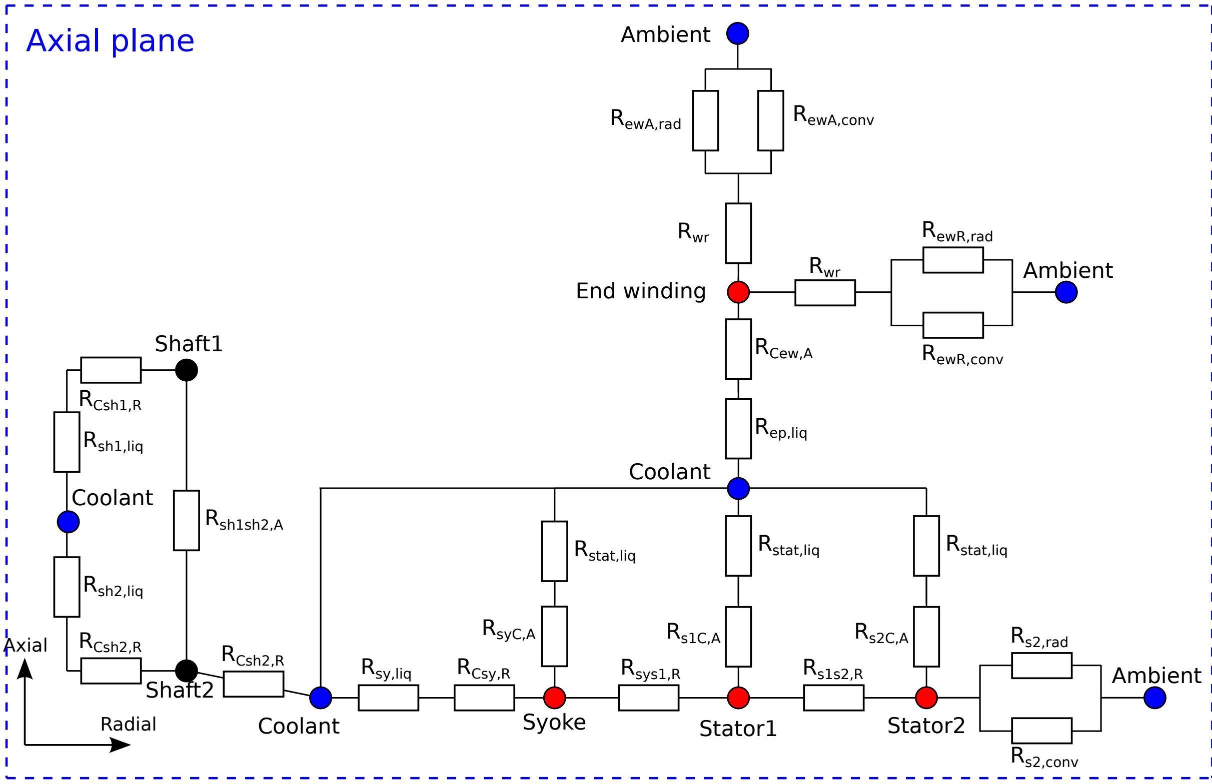

Figure 10.2: Thermal network with the resistances of convection, radiation and liquid cooling heat transfer. The radial plane is not shown.

Thermal resistance		Value $[K/W]$
$R_{s2,rad}$	=	473
$R_{s2,conv}$	=	131
$R_{ewA,rad}$	=	217
$R_{ewA,conv}$	=	125
$R_{ewR,rad}$	=	145
$R_{ewR,conv}$	=	84.0

Table 10.3: Thermal resistances of radiation and convection at atmospheric pressure and without rotor. The resistances are shown in figure 10.2.

10.3.1 Results from AC test

The test set-up and results from section 8.2 are used to verify the thermal model of the stator. The five measured temperatures in the slot and the end windings are compared to the corresponding temperatures from the lumped parameter model. Three tests are used to verify the model, one with air cooling and two with liquid cooling.

Air cooling

The first test is performed to validate the convection and radiation in the lumped parameter model of the stator. In this test, a copper loss of 249 W and forced air cooling are applied to the stator. The temperatures of the stator are in the range of the temperatures of Test 1 without cooling from section 8.2. As no cooling is applied in Test 1, the input effect of 109 W is emitted by convection and radiation. To verify the modelling of radiation and convection, the 109 W of heat transfer is compared to the simulated heat transfer. The results are listed in table 10.4.

Node	**Measured** $[°C]$	**LP** $[°C]$	**Deviation** $[\%]$
$T_{ew,out}$	140	132	-5.7
$T_{ew,cen}$	140	140	0.0
$T_{ew,in}$	117	123	5.1
$T_{sw,cen}$	139	140	0.7
$T_{sw,in}$	116	124	6.9

Heat transfer	**Measured** $[W]$	**LP** $[W]$	**Deviation** $[\%]$
Radiation		29.8	
Convection		70.2	
Sum	109	100	-8.3%

Table 10.4: Air cooling test with AC power source of 249W. The temperature locations are shown in figure 8.3 on page 72.

The heat transfer coefficient for convection from section 9.2 was determined to be 16 $W/(m^2\ K)$ at temperatures above 100$°C$. The sum of heat transfer by convection and radiation is 100 W with this heat transfer coefficient, which is a derivation of -8.3%. The radiation and convection are applied to the nodes shown in figure 10.2 and calculated from the corresponding areas. This explains why the model has a lower heat transfer as the total area of the PMSM is larger than the one used to calculate the radiation and convection heat transfers. One possibility is to increase the heat transfer coefficients to compensate for the smaller area, but it is decided to disregard this fitting and use the heat transfer coefficients from section 9.2 in the remaining tests.

Liquid cooling

Two tests with liquid cooling are used to verify the thermal model. The results from a test with an AC power input of 81 W are presented in table 10.5 and the results with an input 231 W are shown in table 10.6. The test with an input effect of 81 W results in low temperatures, which are far from the expected temperatures in the thermal test scenario. This is not desirable, but the current was limited in the available test set-up and the test is included to have more than the 231 W test, which corresponds to the nominal current. The results are discussed in the following section along with the results of the air cooling test.

Discussion of results

The heat transfer coefficients for convection are taken from section 9.2 and listed in table 10.7. The heat transfer coefficients for air cooling and liquid cooling are fitted from the tests. Liquid cooling resistances are abbreviated by liq. The heat transfer coefficient for forced air cooling is determined by fitting of the

Node	Measured [°C]	LP [°C]	Deviation [%]
$T_{ew,out}$	35.3	36.3	2.8
$T_{ew,cen}$	34.9	37.1	6.3
$T_{ew,in}$	28.7	30.4	5.9
$T_{sw,cen}$	34.7	36.7	5.8
$T_{sw,in}$	27.1	29.2	7.7

Heat transfer	
Radiation	2.70 W
Convection	5.60 W

Table 10.5: Liquid cooling test with AC power source of 81 W. The temperature locations are shown in figure 8.3 on page 72.

Measured [°C]	LP [°C]	Deviation [%]
69.5	65.8	-5.3
68.5	68.9	0.6
49.3	50.5	2.4
68.2	67.8	-0.6
43.9	47.2	7.5

Heat transfer
8.60 W
24.3 W

Table 10.6: Liquid cooling test with AC power source of 231 W corresponding to nominal current.

coefficient. It is fitted until $T_{ew,cen}$ corresponds to the measured temperature.

Parameter	Value $[W/(m^2\ K)]$	Description
$h_{conv,40C}$	9.73	Natural convection at 40°C
$h_{conv,70C}$	15.6	Natural convection at 70°C
$h_{conv,100C}$	16.0	Natural convection at 100°C
h_{air}	55	Forced convection from compressor
h_{liq}	5000	Liquid cooling

Table 10.7: Input heat transfer coefficients for the three thermal tests of the stator.

The resistances connected to h_{liq} are negligible compared to the other resistances between the windings and the liquid cooling. The thermal resistances related to the heat transfer coefficient of water cooling are listed in table 10.8.

Thermal resistance	Value $[K/W]$	Description
$R_{stat,liq}$	0.32	Axial resistance between stator tooth and coolant
$R_{ep,liq}$	0.30	Axial resistance between end plate and coolant
$R_{sy,liq}$	1.8	Radial resistance between stator yoke and coolant
$R_{sh1,liq}$	4.9	Radial resistance between shaft1 and coolant
$R_{sh2,liq}$	1.0	Radial resistance between shaft2 and coolant

Table 10.8: Resistances corresponding to R_{htc} calculated from the heat transfer coefficient for liquid cooling. The resistances are shown in figure 10.2

The resistance of the end plate alone is more than 10 times greater compared to the resistance for liquid cooling on the end plate, why it could be left out and thus the temperature of the liquid could be applied directly to the boundary of the elements. However the resistance is important when air cooling is applied as h_{air} is a hundred times smaller than h_{liq}, which results in a hundred times higher resistance. Therefore the resistance calculated from the heat transfer coefficient is included in all models.

The ratio between radiation and convection from table 10.4 to 10.6 varies as expected, because h_{conv} varies with the temperature and the amount of radiation varies with the temperature to the power of four.

Sources of errors, which apply to all of the thermal tests, are listed and elaborated afterwards:

- Placement of the thermocouples in the windings during the manufacturing process
- Air pockets in the resin
- Contact between thermocouples and windings
- The placement of the outer thermocouple ($T_{ew,out}$) does not exactly correspond to the outer temperature in the model
- Thermal conductivities are temperature dependent
- The water leakage might affect some of the thermocouples
- Read outs from the logged temperatures (e.g. define steady state temperatures and noise)

If air pockets are present inside the windings, due to poor quality of the resin casting, and a thermocouple is placed inside an air pocket, the thermocouple has a poor contact compared to the thermocouples placed in the resin, which results in a lower measured temperature. Even though air pockets are not present, the thermocouples placed in the inner and outer winding might have different contact to the windings compared to the centre placed thermocouple. The inner thermocouple might have poor contact due to the looser windings along the slot, as shown in figure B.9, and the outer thermocouple because only one turn of the winding keeps it in place. This could be the reason for the overestimation of $T_{sw,in}$ in all three tests, an another reason could be water leakage that flows near the inner slot of the stator tooth. The reason why $T_{ew,out}$ is underestimated could be that the thermocouple is placed well below the surface of the resin, while the temperature of the lumped parameter model is read from the surface of the resin.

Apart from the source of errors, the tolerances of the thermocouples add to the deviation. The type J thermocouples have limits of errors of $\pm 1.1°C$ or 0.4% (whichever is greater), which is a notable error at lower temperatures and when two temperatures, e.g. $T_{ew,out}$ and $T_{ew,cen}$, are compared. The deviations of the temperatures are below 8% which is acceptable to assess the temperature of the PMSM in the test scenario.

To further validate the stator model, it is necessary to know the temperatures other places than in the windings. Thermocouples could have been placed on the stator teeth, shaft and both ends of the stator, which would give a better indication of how the entire model agreed with the measured temperatures. The thermocouples in both ends could give an indication of the symmetry assumption. Thermocouples in the stator teeth could give indication about the relation between axial and radial conductivity of the stator laminations. A better alternative compared to place thermocouples on the surfaces of the stator teeth is to place thermocouples inside the stator teeth by e.g. cutting a slot in some of the stator laminations. Placing thermocouples on the surface is hindered by the leakage from the stator, as the water running from the stator makes the temperature measurements on the surface unusable.

To validate the amount of heat transferred by convection and radiation, tests without forced cooling at temperatures corresponding to those with liquid cooling would have been beneficial.

The result from section 10.2, where the lumped parameter model was compared to the FEM model and the lumped parameter model turned out to underestimate the temperatures, is not seen in this tests as the heat transfer coefficients and internal resistance in the windings are fitted to compensate for the underestimation.

10.4 DC symmetry test

To test the symmetry condition in the radial plane, the 1/24 model is expanded to an 1/4 model, to test the heat flow in an asymmetric heat distribution, where each neighbouring tooth is connected. The model is shown in figure 10.3, where it is seen how the 1/24 stator models are connected to the 1/4 model by thermal resistances.

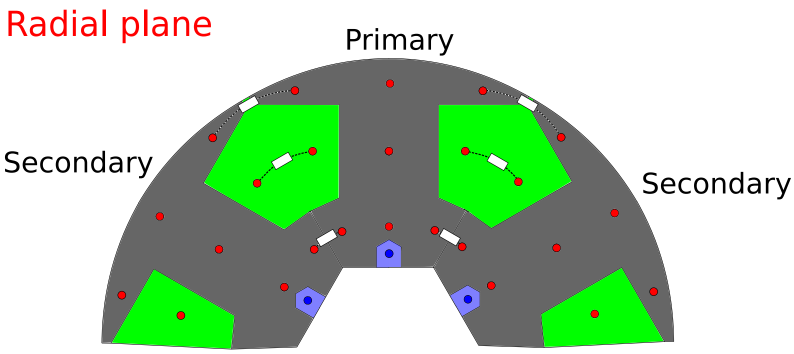

Figure 10.3: A half of the stator in the radial plane for the DC test.

The results are presented in table 10.9 where the measurements are performed with liquid cooling and a DC current of 117 A is applied as shown in figure 6.1. The current yields a resistive loss of 263 W for the primary phase and 55.4 W for each of the secondary phases (374 W for the entire stator). Two tests are performed to obtain the results in table 10.9, as the temperature measurements from the primary and secondary phases are made from the same phase but in two configurations. The reason for this is the phase, from which the temperatures are measured, contains more working thermocouples than the other phases.

Node	**Measured** [$°C$]	**LP** [$°C$]	**Deviation** [%]
Primary			
$T_{ew,out}$	120	132	10.0
$T_{ew,cen}$	144	140	-2.8
$T_{ew,in}$	102	98.3	-3.6
$T_{sw,cen}$	144	139	-3.7
$T_{sw,in}$	83.5	104	24.6
Secondary			
$T_{ew,out}$	86.7	72.1	-16.8
$T_{ew,cen}$	79.0	76.1	-3.7
$T_{ew,in}$	55.7	62.7	12.6
$T_{sw,cen}$	78.9	74.0	-6.2
$T_{sw,in}$	56.9	58.5	2.8

Table 10.9: Measured and simulated temperatures in the DC test. The temperature locations are shown in figure 8.3 on page 72.

The temperature $T_{ew,out}$ deviates 10.0% and -16.8% in the primary and secondary phase configuration respectively. This could be caused by the thermocouple is not placed in the middle of the tooth, which explains why the measured temperature is lower than the model in the primary configuration. This is also seen in the secondary phase as the measured temperature is higher than the simulated, which indicates the thermocouple is placed closer to the primary phase.

Two of the inner thermocouples deviate 24.6% and 12.6% which could be due to water leakage that cools the inner thermocouples. Apart from the discussed temperatures, the remaining temperatures are within an acceptable range why the expanded model is found acceptable. The test reveals the uncertainty of the thermocouple placement.

10.5 Estimation of temperatures in the test scenario

The thermal model of the PMSM is used to estimate the temperatures of the PMSM in thermal test scenario from section 2.3. Coolant with a constant temperature of $20°C$ is assumed to be available. The input parameters for the thermal model are listed in table 10.10 and the temperatures are shown in figure 10.4. The input parameters are determined based on the tests of PMSM-v1 and the nominal current of $70\ A$ is used to calculate the resistive loss.

Input parameter	Value	Source
Rotational loss	$1300\ W$	Section 8.1
Resistive loss	$279\ W$	Section 8.1
Loss in each bearing	$51\ W$	Section 8.1
Heat transfer coefficient for convection	$6\ W/(m^2\ °C)$	Section 9.2
Heat transfer coefficient for liquid cooling	$5000\ W/(m^2\ °C)$	Section 10.3.1
Ambient temperature	$50°C$	Section 2.3
Coolant temperature	$20°C$	

Table 10.10: Input parameters for estimation of temperatures in the test scenario.

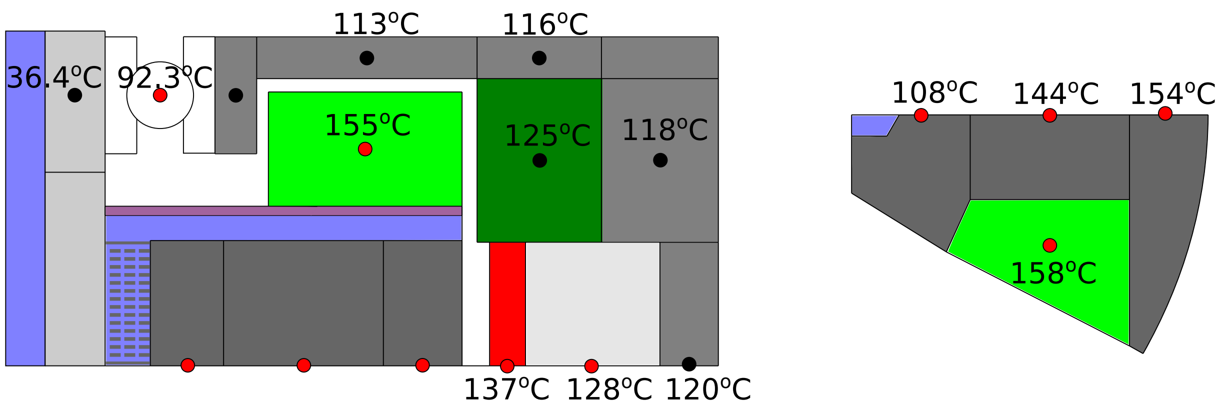

Figure 10.4: Estimated temperatures with the input parameters from table 10.10.

The temperatures of the windings are on the limit of the thermal class ($155°C$). Furthermore the temperature of the bearing exceed the operating temperature of $70°C$. Based on these considerations it is assessed the PMSM is not able to operate at rated current and speed in the test scenario without overheating. However, the rotational loss determined by the spin down test is higher than the expected 750 W from section 1.1. The laminations of PMSM-v2 are not processed after the resin casting why the rotational loss might be reduced to be within the expected range of $750\ W$. A simulation with $750\ W$ rotational losses is performed and the temperatures are shown in figure 10.5.

The reduced rotational loss decreases the temperatures in both the stator and the rotor. The winding temperatures are decreased by approximately 20% and the stator tooth by approximately 33%. Figure

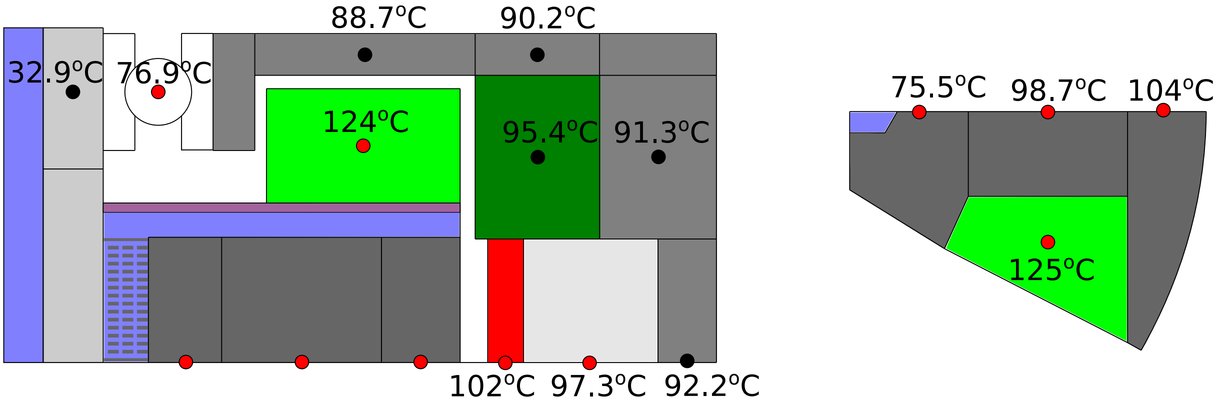

Figure 10.5: Estimated temperatures with the core loss reduced to 750 W.

10.5 shows the temperature of the windings is reduced to $124°C$, which leaves a safety margin. A safety margin is desirable since the thermal model is not tested in a low pressure environment or verified during operation. Extensive temperature measurements are also required to achieve higher accuracy of the model. Furthermore the PMSM is likely to operate above rated values for short periods, why the steady state temperatures must keep a safety margin to the maximum allowable temperatures.

The temperature of the bearing is still above the rated operating temperature, however as discussed in section 9.3.2, the thermal resistance of the bearing at operational speed is conservative. Therefore if the actual thermal resistance of the bearing is lower than the calculated, the temperature of the bearing decreases. Nevertheless it is assessed that the PMSM with the liquid cooling has the possibility to operate in the test scenario if the rotational loss is reduced. However a test with the PMSM operating with liquid cooling enabled would be of great importance to further verify the thermal model but it has not been possible due to leakages from both stator-v1 and stator-v2. Furthermore the assessment is based on a coolant temperature of $20°C$ which might not be available.

10.6 Discussion of the thermal model

The thermal model is used to discuss the simulated temperatures in different scenarios. First, convection and radiation are neglected to test the influence of these often neglected heat transfer mechanisms in vacuum. Secondly, the distribution of the rotational loss is altered and the effect is investigated as no measurements or calculation of the distribution has been performed. In this test convection and radiation is included. Thirdly, it is investigated if it is beneficial to reduce the total amount of losses in the PMSM.

10.6.1 Thermal model without convection and radiation

The rotational loss is 750 W is used as input but all external and internal connections from convection and radiation are removed. The temperatures from the test are presented in figure 10.6.

The temperature increase is due to the extended heat path as no heat is emitted to the ambient through the rotor. The temperatures are increased by around 10% in the rotor, why the high convection and radiation resistances influence the estimated temperatures in vacuum. The temperatures in the stator are only slightly increased, which indicates the external convection affects the temperatures more than internal convection and radiation in the thermal test scenario. The internal heat transfer is reduced due to the small temperature difference between the stator and rotor parts.

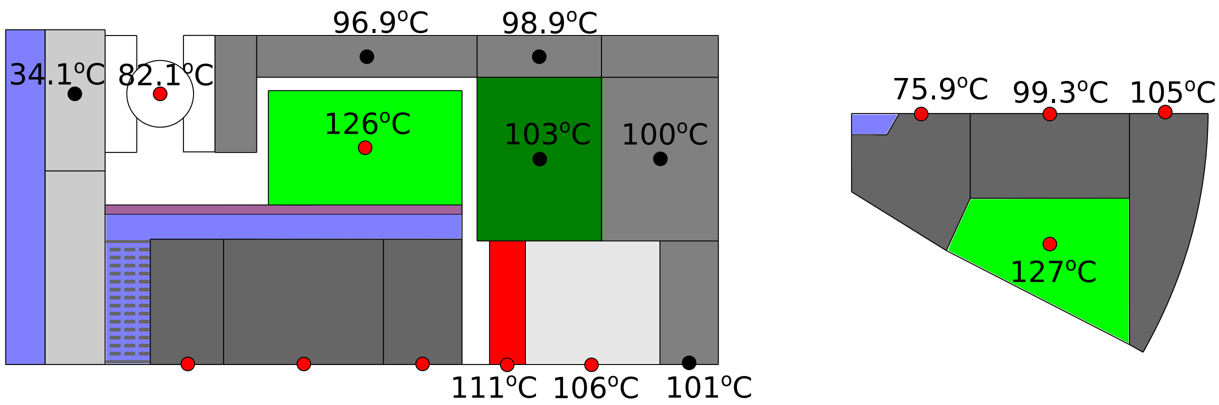

Figure 10.6: Estimated temperatures without convection and radiation.

10.6.2 Distribution of rotational loss

The distribution of the rotational loss from section 8.1 is changed in this section. As the PMs are segmented and the rotor is laminated, the losses in the rotor are expected to be smaller than estimated in section 8.1. A simulation is performed where the entire rotational loss is located in the stator teeth and the temperatures are shown in figure 10.7.

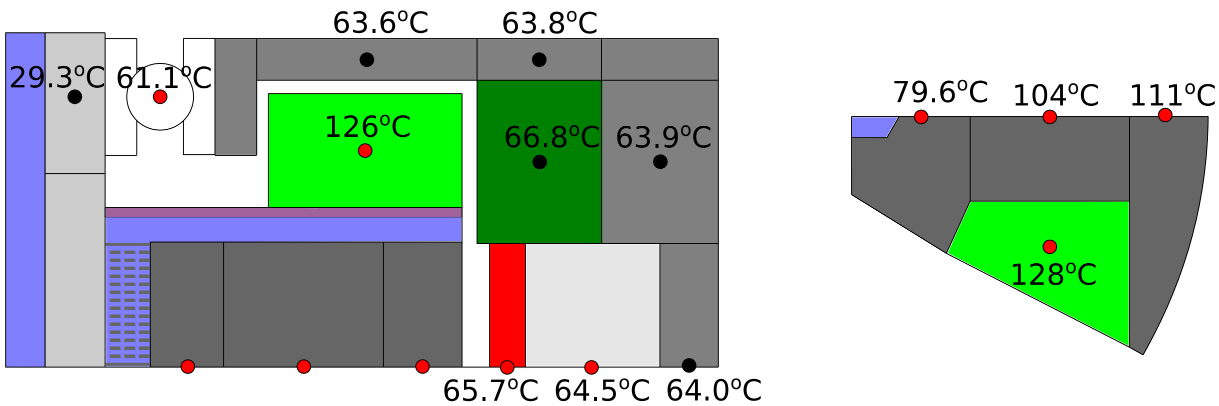

Figure 10.7: Estimated temperatures when all rotational loss is placed in the stator teeth.

The temperatures in the stator are insignificantly affected due to the extra loss but the temperatures of the rotor are highly affected, which is because the stator is more effectively cooled compared to the rotor. The rotor is heated by the internal radiation and convection from the stator and the bearing.

10.7 Minimization of losses

The total loss in the PMSM might be minimised, by altering the design of the PMSM. Throughout the section, the i_d current is assumed to be zero. From the data sheet of the stator laminations [46], the core losses (hysteresis and eddy current loss) at 1000 Hz are proportional to the flux density by:

$$P_{core} \propto B^{1.95} \tag{10.4}$$

Where in equation (10.4):

B	Flux density, $[T]$

It is investigated how the resistive loss in the windings depends on the flux density in order to compare the two dependencies. The required electro-magnetic torque to drive the PMSM is proportional to the current as stated in equation 10.5. The flux linkage from the PMs can be expressed by the number of turns, flux density and area as stated in equation 10.6.

$$\tau_{em} \propto \lambda_{pm}\, i_q \tag{10.5}$$
$$\tau_{em} \propto N\, B\, A\, i_q \tag{10.6}$$

Where in equation (10.5) and (10.6):

i_i	Current, $[A]$
N	Number of winding turns, $[-]$
λ_{pm}	Permanent magnet flux linkage, $[Wb]$
τ_{em}	Electro-magnetic torque, $[Nm]$

If the number of turns and the area are unchanged, the current to generate a constant electro-magnetic torque is proportional to:

$$i_q \propto \frac{1}{B} \tag{10.7}$$

The resistive loss is determined by the current and the resistance. The resistive loss is proportional to the flux density by:

$$P_{cu} \propto \frac{1}{B^2} \tag{10.8}$$

An optimum solution for minimization of the total loss (the sum of P_{core} and $P_{resistive}$) exists. Figure 10.8 is a sketch of equation (10.4) and (10.8). The flux density in the PMSM is altered by e.g. changing the air gap between the stator and rotor or by choosing weaker PMs. The design of the PMSM that yields the minimum loss is not determined and neither is the distance to the minimum. Other calculations based on 2D FEM simulations of the flux in the PMSM suggest that reduction of the flux density reduces the total loss [10], however a thorough analysis is required to estimate the actual numbers.

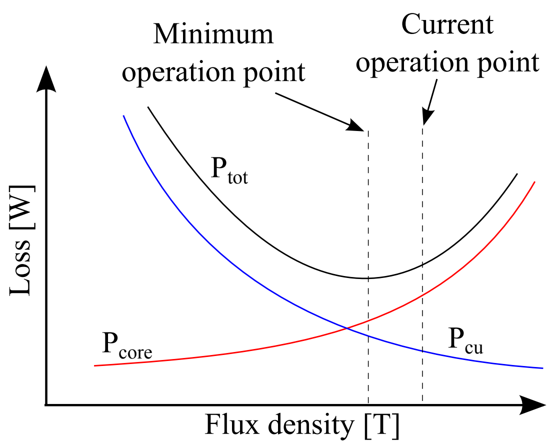

Figure 10.8: Sketch of the losses in the PMSM and the current operating point.

The simulated results in the test scenario, presented in figure 10.5, show the winding temperatures are already high. Therefore the actual reduction in total loss must be determined to see if it is beneficial, from a thermal point of view, to move more losses into the windings. This might be beneficial if the reduction of the total loss is high enough to reduce the overall temperatures in the PMSM.

CHAPTER

11 IMPLEMENTATION

The PWM strategy used to control the switches in the VSI is first described, after which the PWM strategy is implemented on the DSC along with an experimentally designed open loop U/F control strategy. At the end of the chapter, the implemented software and U/F controller is tested on the PMSM.

11.1 PWM strategy

Space Vector Pulse Width Modulation (SVPWM) is a widely used approach to generate PWM signals for PMSMs. SVPWM is easy to implement on a DSC and the frequency and amplitude of the three phase output voltages are controllable. Furthermore SVPWM has low total harmonic distortion compared to other modulation techniques [50]. It is therefore chosen as the PWM generating technique.

The PWM signals are generated by comparing a modulation signal with a carrier signal, which turns the IGBTs in the VSI on and off. First the generation of the modulation signal is described and afterwards the carrier signal and implementation are described.

Modulation signal generation

SVPWM generates three phase modulation signals by rotating a space vector, U_s, in the $\alpha\beta$ coordinate system. The length of the space vector defines the peak amplitude of the phase voltages and the angular speed defines the frequency of the output voltages. The maximum length of the space vector is $U_{s,max} = u_{DC}/\sqrt{3}$, since SVPWM is able to fully utilise the DC-link [51]. By ramping the length and speed of the space vector it is possible to start up and control the PMSM.

As seen from figure 11.1 the dashed circle, in which U_s rotates, is equally divided into 6 sectors. With a two level inverter with three phase legs, eight combinations of the six switches are available. The blue arrows, that define the beginning and end of each sector, are the six active voltage vectors corresponding to the six switch combinations that generate an output voltage. Two zero vectors are also available, where no output voltage is generated. The switching states that generate the voltage vector and the corresponding phase voltages are listed in table 11.1. The nomenclature of the switch states corresponds to the nomenclature of the switch pairs in figure 5.8 where an 1 indicates the switch is turned on and a

0 indicates the switch is turned off. By shifting through each row of active voltage vectors (U_1 to U_6) in the columns with the phase voltages (u_{an},u_{bn},u_{cn}), a pulsed three phase sinusoidal voltage is generated.

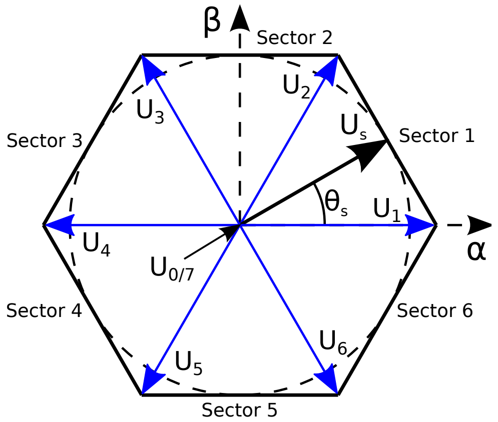

Figure 11.1: Space vector representation.

Where in figure 11.1:

U_i	Voltage vector, $[V]$
U_s	Space vector, $[V]$
θ_s	Angle of space vector, $[rad]$

Voltage vector	Switch state			Phase voltages		
	$\mathbf{q_A}$	$\mathbf{q_B}$	$\mathbf{q_C}$	$\mathbf{u_{an}}$	$\mathbf{u_{bn}}$	$\mathbf{u_{cn}}$
$\mathbf{U_0}$	0	0	0	0	0	0
$\mathbf{U_1}$	1	0	0	$2\ u_{DC}/3$	$-u_{DC}/3$	$-u_{DC}/3$
$\mathbf{U_2}$	1	1	0	$u_{DC}/3$	$u_{DC}/3$	$-2\ u_{DC}/3$
$\mathbf{U_3}$	0	1	0	$-u_{DC}/3$	$2\ u_{DC}/3$	$-u_{DC}/3$
$\mathbf{U_4}$	0	1	1	$-2\ u_{DC}/3$	$u_{DC}/3$	$u_{DC}/3$
$\mathbf{U_5}$	0	0	1	$-u_{DC}/3$	$-u_{DC}/3$	$2\ u_{DC}/3$
$\mathbf{U_6}$	1	0	1	$u_{DC}/3$	$-2\ u_{DC}/3$	$u_{DC}/3$
$\mathbf{U_7}$	1	1	1	0	0	0

Table 11.1: Voltage vectors for each state and their phase voltages.

The SVPWM algorithm rotates the space vector by a combination of the active and zero vectors. In figure 11.2 the space vector is placed between two active voltage vectors. In this position the space vector is generated by combining three voltage vectors U_1, U_2 and $U_{0/7}$. To generate this space vector, each of the three voltage vectors in sector 1 are applied for a time interval within each sample to yield the voltage vector:

$$U_s = \frac{T_1}{T_s}U_1 + \frac{T_2}{T_s}U_2 + \frac{T_{0/7}}{T_s}U_{0/7} \tag{11.1}$$

$$= D_1\ U_1 + D_2\ U_2 + D_{0/7}\ U_{0/7} \tag{11.2}$$

The time interval normalised with respect to the sampling time is the duty cycles D_1, D_2 and $D_{0/7}$. The duty cycles are used in all sectors to scale the two active voltage vectors and apply the zero voltage vector for the remaining time in a sample period. The number of space vectors generated per revolution of the space vector is dependent on the switching frequency. A high switching frequency yields a high number of space vectors per revolution, thus a better modulation of the desired sinusoidal output voltages.

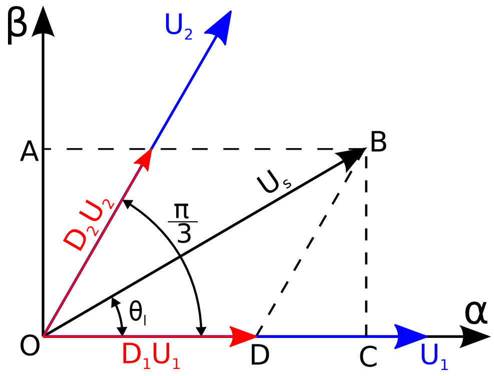

Figure 11.2: Space vector in sector 1.

Where in figure 11.2:

A, B, C, D, O	Geometric points, $[-]$
D_i	Duty cycle, $[-]$
θ_l	Reminding angle of space vector after $\pi/3$ division, $[rad]$

To reduce the switching losses and harmonics in the output voltage, the switching scheme has to follow the rules listed below [50]:

- The voltage vector U_s rotates in a circle
- Only one of q_A, q_B or q_C changes to move to the next sector
- Only two active vectors (e.g. U_1 and U_2) are generated per period $(1/f_{sw})$
- The initial state of a sample must be the same as the end state of the previous sample

The duty cycles to generate the space vector in equation (11.2) are derived by geometrical consideration of figure 11.2 with the five points A, B, C, D and O. The term $D_1\ U_1$ from equation (11.2) is expressed by:

$$D_1\ U_1 = U_s\ cos(\theta_l) - |DC| \tag{11.3}$$

It is possible to express the length $|DC|$ by the angle θ_l and the length of the space vector $|U_s|$ by trigonometric considerations, which results in:

$$D_1\ U_1 = \frac{2}{\sqrt{3}}\ U_s\ sin\left(\frac{\pi}{3} - \theta_l\right) \tag{11.4}$$

The term $D_2\ U_2$ is expressed by:

$$D_2\ U_2 = \frac{|AO|}{cos(\frac{\pi}{6})} = \frac{U_s\ sin(\theta_l)}{\frac{\sqrt{3}}{2}} \tag{11.5}$$

$$= \frac{2}{\sqrt{3}}\ U_s\ sin(\theta_l) \tag{11.6}$$

The lengths of the two active vectors U_1 and U_2 equal $\frac{2}{3}u_{DC}$, which is inserted in equation (11.4) and (11.6). The duty cycle D_0 is calculated from the duty cycle of the two active vectors:

$$D_1 = \sqrt{3}\ \frac{|U_s|}{u_{DC}}\ sin\left(\frac{\pi}{3} - \theta_l\right) \tag{11.7}$$

$$D_2 = \sqrt{3}\ \frac{|U_s|}{u_{DC}}\ sin(\theta_l) \tag{11.8}$$

$$D_0 = \frac{1 - (D_1 + D_2)}{2} \tag{11.9}$$

To generate a sinusoidal wave, it must be determined which sector the space vector is located in as it moves around the circle. The sector is determined from the angle θ_s and the duty cycle for each phase (D_A, D_B and D_C) is determined from table 11.2.

Duty cycle	$\mathbf{D_A}$	$\mathbf{D_B}$	$\mathbf{D_C}$
Sector 1	$D_0+D_1+D_2$	D_0+D_2	D_0
Sector 2	D_0+D_1	$D_0+D_1+D_2$	D_0
Sector 3	D_0	$D_0+D_1+D_2$	D_0+D_2
Sector 4	D_0	D_0+D_1	$D_0+D_1+D_2$
Sector 5	D_0+D_2	D_0	$D_0+D_1+D_2$
Sector 6	$D_0+D_1+D_2$	D_0	D_0+D_1

Table 11.2: Duty cycle of each phase in all sectors.

In figure 11.3, 11.4 and 11.5 an example is shown where the space vector U_s has a magnitude of 230 V and a frequency of 50 Hz. Figure 11.3 shows the duty cycles D_1, D_2 and D_0 when the space vector takes one revolution in the circle and goes through the six sectors.

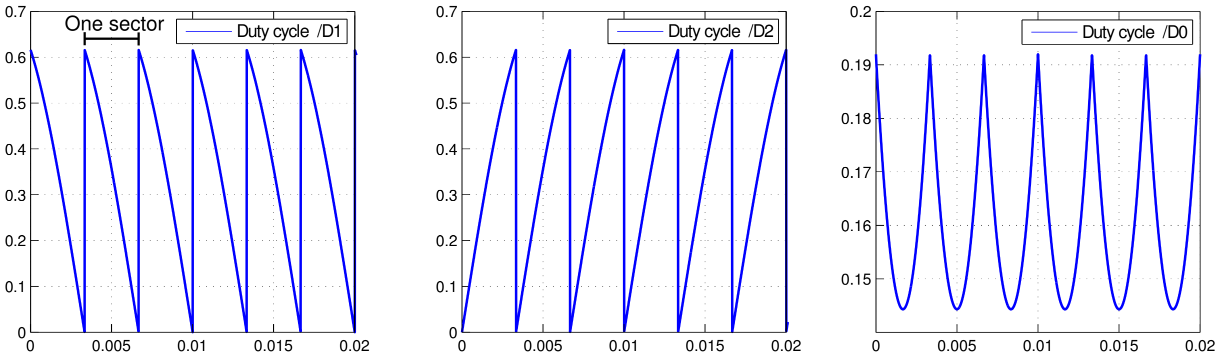

Figure 11.3: Duty cycles of the voltage vectors in a the sectors.

The resulting duty cycles for each phase calculated by table 11.2 are shown in figure 11.4. This is the modulation signals for each phase.

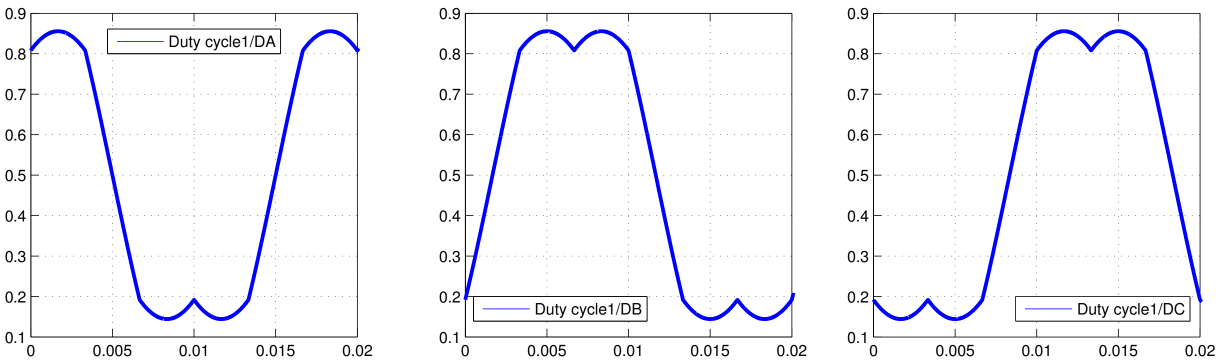

Figure 11.4: Duty cycle for each phase.

PWM generation by carrier wave

D_A, D_B and D_C are compared to a triangular carrier wave, n_{tri}, (up-down counter) which generates the PWM signals (q_A, q_B and q_C) for the IGBTs as stated in equation (11.10). The frequency of the carrier wave defines the switching frequency of the VSI.

$$q_A = \begin{cases} 1 & \text{if } D_A \geq n_{tri} \\ 0 & \text{if } D_A < n_{tri} \end{cases} \qquad q_B = \begin{cases} 1 & \text{if } D_B \geq n_{tri} \\ 0 & \text{if } D_B < n_{tri} \end{cases} \qquad q_C = \begin{cases} 1 & \text{if } D_C \geq n_{tri} \\ 0 & \text{if } D_C < n_{tri} \end{cases} \tag{11.10}$$

Where in equation (11.10):

n_{tri}	Triangular carrier wave, $[-]$
q_i	PWM control signal for the IGBTs, $[-]$

The duty cycle D_A from figure 11.4 is shown in figure 11.5 compared to the carrier wave (the frequency of the carrier wave is reduced to 500 Hz).

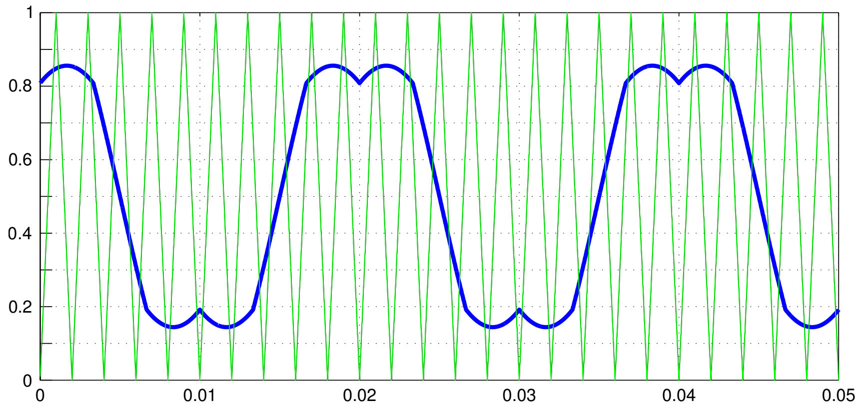

Figure 11.5: Duty cycle of phase A compared to carrier wave.

Implementation of SVPWM

The SVPWM algorithm can be summarized as:

- Determine sector based on θ_s and calculate the angle in the sector, θ_l ($0\ rad - \frac{\pi}{3}\ rad$)
- Calculate duty cycles (D_1, D_2 and D_0) of voltage vectors U_1, U_2 and $U_{0/7}$ in the sector
- Calculate duty cycles for the phases (D_A, D_B and D_C) based on sector
- Calculate PWM signals (q_A, q_B and q_C) by comparing D_A, D_B, D_C with the carrier wave

The amplitude and position of the space vector is determined by the U/F control described later in this chapter.

11.2 DSC software

To run the PMSM, software has been developed and implemented on the DSC. Figure 11.6 shows the algorithm, implemented on the DSC, to ramp the PMSM to the desired speed. The rotor is first aligned in the zero position of the space vector, to ensure a consistent start-up each time. The alignment is required since the rotor position is unknown. To align the rotor, a voltage generating a current of 4 A is applied for 1.2 s, which is determined through experiments.

After the rotor is parked, two ramps are performed; Ramp1 and Ramp2. Ramp1 is designed to compensate for the voltage drop in the VSI in the low velocity range (discussed in chapter 7). Therefore the

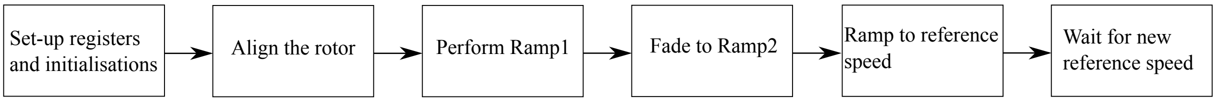

Figure 11.6: Overview of the software implemented on the DSC.

voltage is increased by an offset and Ramp1 is experimentally designed to be:

$$|U_s| = 0.17 \frac{V}{Hz}\ \omega_{re} + 7.5\ V \tag{11.11}$$

The U/F relation of $0.17\ \frac{V}{Hz}$ is experimentally determined by multiple test runs with the PMSM. The relation is a trade-off between stability and high currents. When the speed increases the voltage drop becomes insignificant as discussed in chapter 7. Therefore Ramp2 is faded in to reduce the current during the ramp. Ramp2 is given by:

$$|U_s| = 0.17 \frac{V}{Hz}\ \omega_{re} \tag{11.12}$$

A linear fade between the two ramps is performed over 80 Hz to avoid a step down in the voltages, which may cause oscillations. The transition start at 170 Hz and ends at 250 Hz, from where Ramp2 is used to ramp the PMSM to the desired speed. The two ramps and the fading between the two of them are shown in figure 11.7.

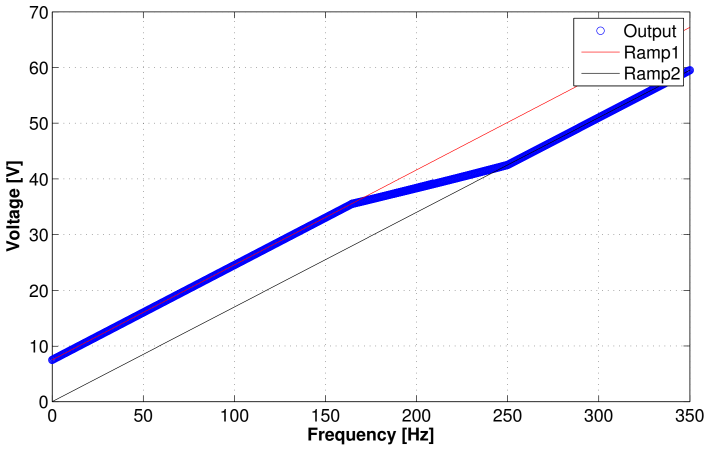

Figure 11.7: The two ramps implemented on the DSC.

The frequency is ramped with a slope of $3.6\ \frac{Hz}{s}$, which is assessed to be a good compromise between reliability and acceleration time judged from experimental tests. However the ramp time is significantly slower than the 20 s it takes for the PMSM controller developed in chapter 12 to ramp the PMSM to nominal speed. The difference is assessed to be caused by the difference between a closed loop and open loop control structure along with idealisation of the models.

11.3 Test run with open loop U/F control

The PMSM is ramped to 471 $\frac{rad}{s}$ within 84 s with a switching frequency of 6.0 kHz and the current is shown in figure 11.8. Apart from the ramp, the parking is seen in the first 1.2 s and after the ramp, the PMSM runs at steady state. The transition between Ramp1 and Ramp2 starts at 30 s and ends at 44 s.

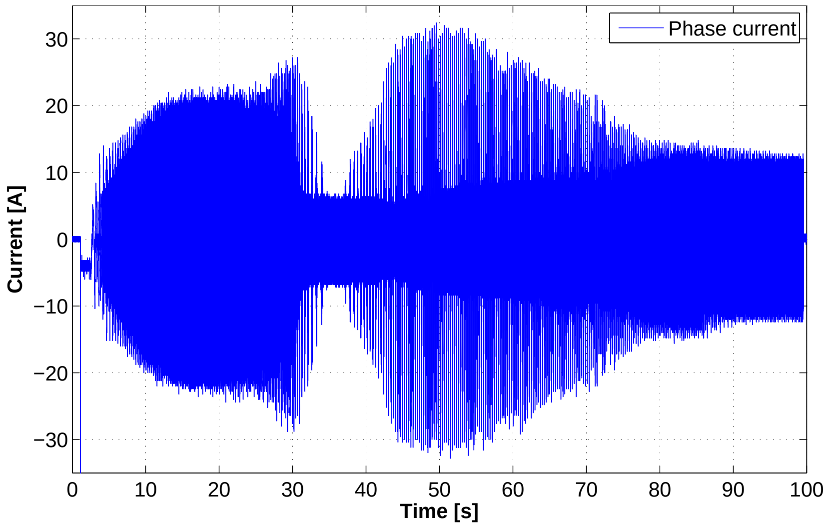

Figure 11.8: Measured current during the ramp to 471 $\frac{rad}{s}$.

The current drawn seems high since the PMSM is not loaded, but a decreased U/F relation results in higher oscillations and ultimately the PMSM loses synchronisation. However in the transition interval, the U/F relation is decreased and this also decreases the oscillations, why more experiments could be performed with a decreased U/F relation in Ramp2 if a decreased current is of importance during the ramp.

Figure 11.9 and 11.10 are an extract of figure 11.8 and they show the oscillations in the current. The start-up is shown in figure 11.9 starting with the constant parking current. Figure 11.10 shows the oscillations in the current while the PMSM is ramped. The oscillations are caused by the open loop control structure as discussed in 7.2 as the simulated ramps suffer from the same oscillations. However the mechanical resonance discovered in section 6.5 might increase the oscillations.

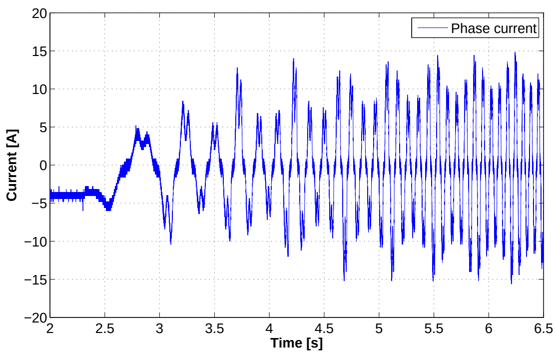

Figure 11.9: Logged current during the start-up.

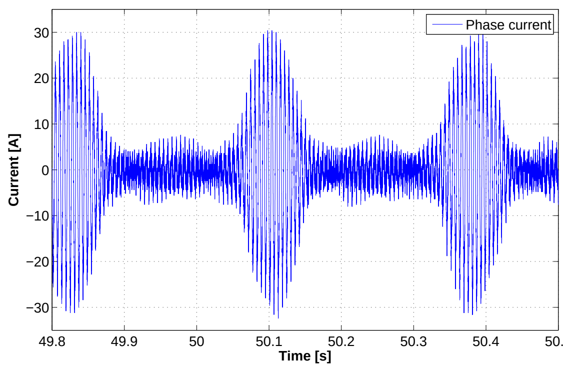

Figure 11.10: Oscillations in the logged current during the ramp.

The open loop U/F controller is able to successfully ramp the PMSM to 15000 *rpm* and the currents during the ramp resemble the currents from figure 11.8.

CHAPTER

12

PMSM CONTROLLER

The development of the PMSM controller is described in this chapter. The PMSM controller is developed to generate reference voltages for the VSI in a no load test scenario. As stated in section 1.1 the PMSM is going to operate for long periods with a slow varying load, why no performance criteria are set up. The no load scenario is chosen as no load mechanism is designed and the controllers are designed to be implemented, despite this is not achieved in this project. However the procedure for designing the controllers to the system with load is the same as stated in this chapter. Knowing the controllers should be redesigned for a load scenario, it is chosen not to tune the controllers and investigate more than one control strategy. The PMSM controller is used to avoid the oscillations, discussed in chapter 7, caused by the open loop U/F controller, described in chapter 11.

The electric and mechanical models of the PMSM are linearised in order to enable application of linear controller design and the linear models are verified against the non-linear model. A linear controller design with a thoroughly tested control structure for a PMSM is chosen to ease the controller design. A closed loop velocity controller with an inner current loop is designed.

12.1 Linearisation

The electric and the mechanical systems are linearised and transfer functions for both systems are determined in this section. The transfer functions are used to design the PMSM controller.

12.1.1 Linearisation of electrical model

The voltage equations in the dq-frame are linearised to enable application of linear control theory, which eases the controller design. The non-linear voltage equations (5.50) and (5.51) are repeated below:

$$u_d = R_s\, i_d + L\frac{d}{dt}\, i_d - \omega_{re}\, L\, i_q \tag{12.1}$$

$$u_q = R_s\, i_q + L\frac{d}{dt}\, i_q + \omega_{re}\,(L\, i_d + \lambda_{pm}) \tag{12.2}$$

Where in equation (12.1) and (12.2):

i_i	Current, $[A]$
L	Inductance, $[H]$
R_s	Resistance of windings, $[\Omega]$
u_{in}	Phase voltage, $[V]$
λ_{pm}	Permanent magnet flux linkage, $[Wb]$
ω_{re}	Electric velocity, $[rad/s]$

The equations are linearised by a first order Taylor's approximation for three variables:

$$f(x,y,z) \approx f(x_0,y_0,z_0) + \frac{\partial f(x_0,y_0,z_0)}{\partial x}(x-x_0) + \frac{\partial f(x_0,y_0,z_0)}{\partial y}(y-y_0)\frac{\partial f(x_0,y_0,z_0)}{\partial z}(z-z_0) \quad (12.3)$$

Where in equation (12.3):

x,y,z	Variables, $[-]$
x_0,y_0,z_0	Linearisation point of variables, $[-]$

The linearisation point is chosen in the end of this section. As a linear model is of interest, the constant contributions are left out and thus the linearised voltages are expressed by:

$$\overline{u}_d = R_s\, i_d + L\frac{d}{dt}\, i_d - L\,\omega_{re,0}\, i_q - L\,\omega_{re}\, i_{q,0} \quad (12.4)$$

$$\overline{u}_q = R_s\, i_q + L\frac{d}{dt}\, i_q + L\,\omega_{re,0}\, i_d + \omega_{re}\,(L\, i_{d,0} + \lambda_{pm}) \quad (12.5)$$

The differential equations are Laplace transformed from the time domain to the frequency domain:

$$\begin{aligned}\mathcal{L}(\overline{u}_d) &= U_d(s)\\ &= R_s\, I_d(s) + L\, s\, I_d(s) - L\,\omega_{re,0}\, I_q(s) - L\, i_{q,0}\,\Omega_{re}(s) \quad (12.6)\\ \mathcal{L}(\overline{u}_q) &= U_q(s)\\ &= R_s\, I_q(s) + L\, s\, I_q(s) + L\,\omega_{re,0}\, I_d(s) + (L\, i_{d,0} + \lambda_{pm})\,\Omega_{re}(s) \quad (12.7)\end{aligned}$$

Where in equation (12.6) and (12.7):

s	Laplace frequency operator, $[1/s]$

The equations are rearranged to derive a transfer function, first for the d-axis:

$$I_d(s) = \frac{1}{R_s + L\, s}\, U_d(s) + \frac{L\,\omega_{re,0}}{R_s + L\, s}\, I_q(s) + \frac{L\, i_{q,0}}{R_s + L\, s}\,\Omega_{re}(s) \quad (12.8)$$

$$I_d(s) = G_{p,el}(s)\, U_d(s) + G_I(s)\, I_q(s) + G_{\Omega_{re},d}(s)\,\Omega_{re}(s) \quad (12.9)$$

And second for the q-axis:

$$I_q(s) = \frac{1}{R_s + L\, s}\, U_q(s) - \frac{L\,\omega_{re,0}}{R_s + L\, s}\, I_d(s) - \frac{L\, i_{d,0} + \lambda_{pm}}{R_s + L\, s}\,\Omega_{re}(s) \quad (12.10)$$

$$I_q(s) = G_{p,el}(s)\, U_q(s) - G_I(s)\, I_d(s) - G_{\Omega_{re},q}(s)\,\Omega_{re}(s) \quad (12.11)$$

The transfer function is rewritten on the standard first order system formula:

$$\begin{aligned}G_{p,el} &= \frac{1}{R_s}\,\frac{1}{\frac{L}{R_s}\, s + 1} \quad (12.12)\\ &= K_{el}\,\frac{1}{\tau_{t,el}\, s + 1} \quad (12.13)\end{aligned}$$

Where in equation (12.13):

$\tau_{t,el}$	Time constant of electric system, $[s]$

If the transfer functions $G_I(s)$, $G_{\Omega_{re},d}(s)$ and $G_{\Omega_{re},q}(s)$ are treated as disturbances, the block diagrams representing equation (12.9) and (12.11) along with two feedback controllers $G_{c,d}$ and $G_{c,q}$ are presented in figure 12.1.

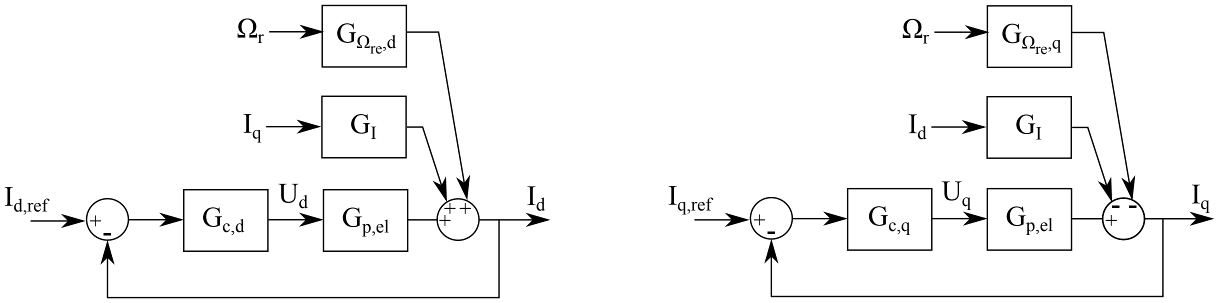

Figure 12.1: Block diagram representation of the linear electrical model.

12.1.2 Linearisation of the mechanical torque

The non-linear torque characteristic of τ_{rot} from section 6.5 is linearised. The rotational torque from equation (6.23) is linearised by a first order Taylor's approximation:

$$\tau_{rot} = K_1 \omega_{rm} + K_2 \tag{12.14}$$

$$\overline{\tau_{rot}} = B_m \, \omega_{rm} \tag{12.15}$$

Where in equation (12.14) and (12.15):

B_m	Linearised rotational torque constant (viscous friction), $[Nm/(rad/s)]$
K_i	Opposing rotational torque coefficients, $[-]$
τ_{rot}	Opposing torque due to rotational loss, $[Nm]$
ω_{rm}	Mechanical angular velocity, $[rad/s]$

The acceleration of the PMSM is described by Newtons 2nd law for rotational motion:

$$J \, \frac{d}{dt}\omega_{rm} = \tau_{em} - \overline{\tau_{rot}} \tag{12.16}$$

Where in equation (12.16):

J	Moment of inertia, $[kg\ m^2]$
τ_{em}	Electro-magnetic torque, $[Nm]$

This is Laplace transformed and rearranged into the transfer function of the mechanical system:

$$J \, \frac{d}{dt}\omega_{rm} = \tau_{em} - B_m \, \omega_{rm} \tag{12.17}$$

$$\Leftrightarrow \frac{\Omega_{rm}(s)}{T_{em}(s)} = \frac{1}{B_m} \, \frac{1}{\frac{J}{B_m} \, s + 1} \tag{12.18}$$

$$G_{p,m}(s) = K_m \, \frac{1}{\tau_{t,m} \, s + 1} \tag{12.19}$$

Where in equation (12.19):

$\tau_{t,m}$	Time constant of mechanical system, $[s]$

A block diagram of the mechanical system is shown in figure 12.2.

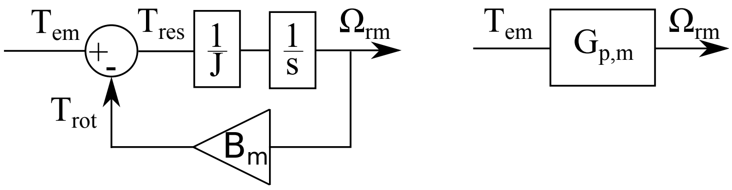

Figure 12.2: Block diagram of the linear mechanical system.

12.1.3 Electric to mechanical conversion

The transformation from the output of the electrical system, i_q, to the input of the mechanical system, τ_{em}, is derived from equation (5.63) as stated in equation (12.20).

$$T_{em} = \frac{3}{2}\frac{p_b}{2}\lambda_{pm}I_q \qquad \Rightarrow \qquad K_{e2m} = \frac{T_{em}}{I_q} = \frac{3}{2}\frac{p_b}{2}\lambda_{pm} \tag{12.20}$$

Where in equation (12.20):

p_b	Number of poles, $[-]$

This gain is inserted between the electric and the mechanical system.

12.1.4 Choice of linearisation point

The linearisation point is chosen where the disturbances from figure 12.1 are highest. The worst case scenario is:

- i_{d0}: Expected to be zero but during operation peaks are expected, why 3 A is chosen.
- i_{q0}: Current to deliver 0.79 Nm (cf. section 6.5) is 5.0 A but a safety margin of 25% is added, why 6.3 A is chosen
- Ω_{re0}: Rated electrical velocity is 1000 Hz (6283 $\frac{rad}{s}$).

High current ripples are expected during operation based on the measurements and simulations in chapter 7, however a constant i_d contribution has more influence on the system response since the ripples are oscillating around a mean value. The choice of i_{d0} as almost half of i_{q0} is conservative as i_{d0} is expected to be eliminated by the current controller.

12.2 Verification of linear system

In this section the linear and the non-linear models of the PMSM are compared to verify the linearised model. It is expected that the models correspond around the linearisation point and deviates the more the operation point is moved from the linearisation point.

To compare the models, a step of 5 V in the q-direction voltage is applied to both models and the d- and q-direction currents are compared. The PMSM operates at 15000 rpm when the voltage step is performed. Figure 12.3 and 12.4 show the response when the linearisation and operating points are coinciding before the step. During the step, the currents oscillate why there is a small current deviation as the oscillations moves the system away from the linearisation point.

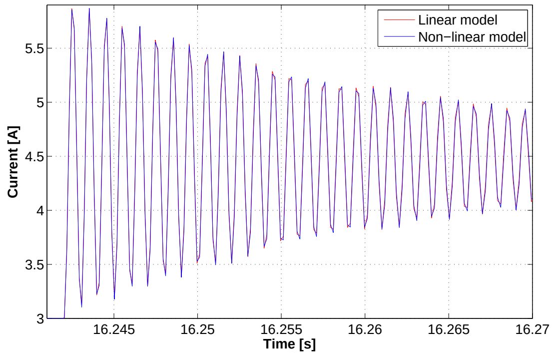

Figure 12.3: i_d current response in the linearisation point.

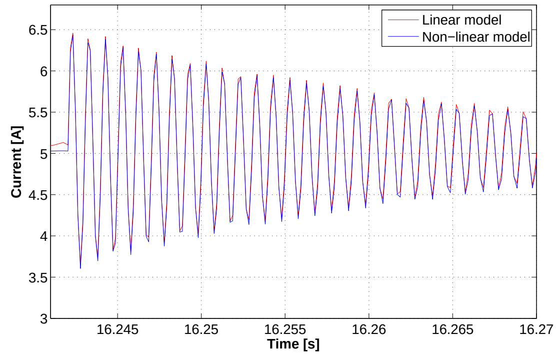

Figure 12.4: i_q current response in the linearisation point.

The responses from the two models are similar in this operating point, why the linearised model is applicable for controller design in the operating point. To check the effect of the chosen linearisation point, a new linearisation point is chosen, where the operating speed and step are repeated. Figure 12.5 and 12.6 show the responses from linear model with the new linearisation point, where the model is linearised to a d-current of 1 A.

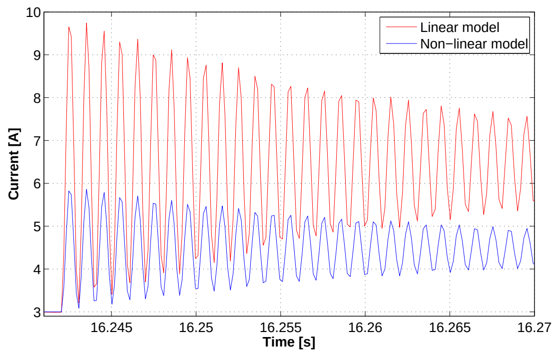

Figure 12.5: i_d current response with altered linearisation point.

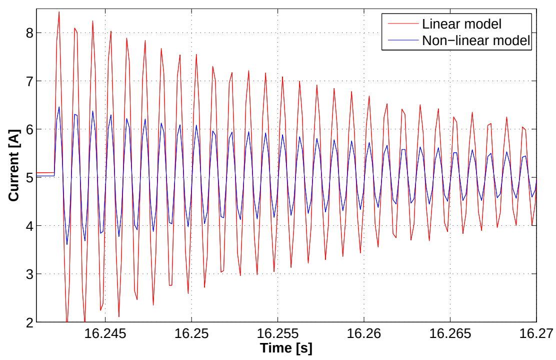

Figure 12.6: i_q current response with altered linearisation point.

As expected, the amplitude of the linearised model deviates from the non-linear model. During the linearisation, constant contributions are disregarded, why an amplitude deviation is expected. However the dynamics are well captured, why the linearised model is found applicable for the design of the PMSM controller.

12.3 PMSM controller design

In this section the controllers are designed. Field weakening is not considered as the PMSM is designed to run 15000 rpm without it [10]. A cascade control structure, with an inner current controller and an outer velocity controller, is chosen for the PMSM controller. The cascade control structure is able to improve the response of the system and to suppress non-linearities [47]. The block diagram, which represents the PMSM and the controllers, is presented in figure 12.7. The inner current controller uses a control strategy known as "Maximum Torque per Ampere" [18]. The Maximum Torque per Ampere has its origin in the torque equation (stated in equation (5.63)), which states that the torque is generated solely from the q-axis current. Therefore the minimum stator current is obtained by elimination of the d-axis current ($i_{d,ref} = 0$). In figure 12.8 a phasor diagram of the PMSM is shown and in figure 12.9 a phasor diagram is shown where the Maximum Torque per Ampere strategy is applied.

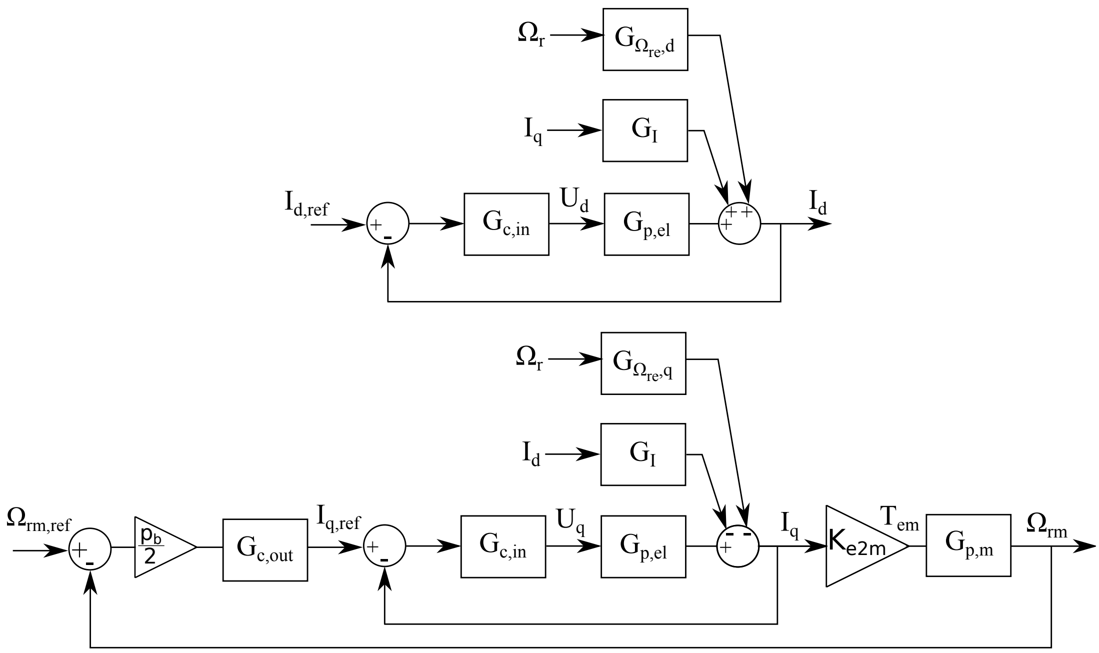

Figure 12.7: Block diagram representation of the linear system model.

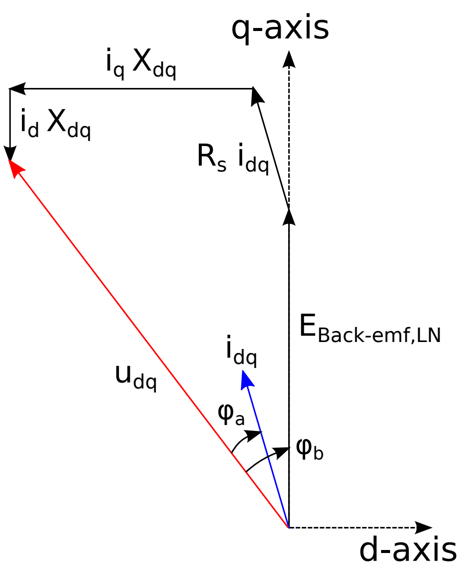

Figure 12.8: Phasor diagram.

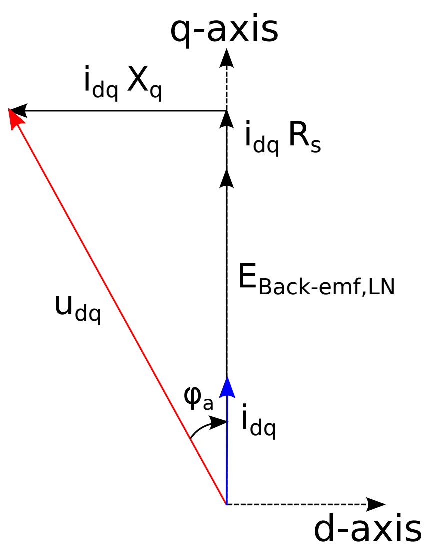

Figure 12.9: Phasor diagram during Maximum Torque per Ampere operation.

Where in figure 12.8 and 12.9:

$E_{back-emf,LN}$	Back electromotive force, line-to-neutral, $[V]$
X_i	Reactance, $[\Omega]$
ϕ	Angle, $[rad]$

12.3.1 Parameter variation

The controllers are designed based on the time constants of the electric and the mechanical system, why the time constants are determined. The time constant of the electrical system is determined by $\tau_{t,el} = \frac{L}{R_s}$, however since the parameters varies, e.g. due to temperature, the variation of the time constant is determined.

The temperature of the windings in the PMSM is estimated to vary between 20°C and 150°C, based on the thermal model of the PMSM presented in chapter 9. The temperature dependency of the resistance is included in equation (6.5), which results in a minimum and maximum resistance of:

$$R_{s,min} = 0.0135\ \Omega(1 + 0.00381 \frac{1}{°C}(20°C - 21°C)) = 0.0134\ \Omega \tag{12.21}$$

$$R_{s,max} = 0.0135\ \Omega(1 + 0.00381 \frac{1}{°C}(150°C - 21°C)) = 0.0201\ \Omega \tag{12.22}$$

The inductance varies between 0.427 mH and 0.433 mH dependent on the direction. Based on these parameters the time constant of the electric system varies between:

$$\tau_{t,el,min} = \frac{0.427\ mH}{0.0201\ \Omega} = 0.0212\ s \quad ; \quad \tau_{t,el,max} = \frac{0.433\ mH}{0.0134\ \Omega} = 0.0322\ s \tag{12.23}$$

The mechanical system has a time constant of $\tau_{t,mech} = \frac{J}{B_m}$. The inertia of the PMSM is constant, however the viscous friction (B_m) may vary. It is assessed B_m does not vary more than ±30% based on the analysis from section 6.5, where mechanical resonance influences the simplified first order polynomial of the rotational torque. This means the time constant of the mechanical system is between:

$$\tau_{t,m,min} = \frac{0.02577\ kg\ m^2}{1.3 \cdot 0.4745\ \frac{mNm}{s}} = 41.77\ s \quad ; \quad \tau_{t,m,max} = \frac{0.02577\ kg\ m^2}{0.7 \cdot 0.4745\ \frac{mNm}{s}} = 77.57\ s \tag{12.24}$$

The time constants are used and further discussed in the following section.

12.3.2 Design of current controller

It is chosen to design PI-controllers for i_d and i_q. PI-controllers are chosen to remove the steady state error and due to simplicity. The transfer function, $G_{p,el}$, of both i_d and i_q are the same, why the same controller is designed for both. The transfer function of a PI-controller is written in equation (12.25).

$$G_{c,in}(s) = \frac{K_p\ s + K_i}{s} \tag{12.25}$$

Where in equation (12.25):

K_i	Integral gain, $[-]$
K_p	Proportional gain, $[-]$

The mechanical system is neglectable during the design of the current controller, if the relationship, stated in equation 12.26, is fulfilled [47]. The relationship means the mechanical system is much slower than the electrical system. The time constants from equation (12.23) and (12.24) show the relationship is fulfilled.

$$\tau_{t,m} > 10\ \tau_{t,e} \tag{12.26}$$

The open loop transfer of the electric system including the controller becomes:

$$G_{el,OL}(s) = G_{c,in}(s)\ G_{p,el}(s) \tag{12.27}$$
$$= \frac{K_p\ s + K_i}{s} \frac{1}{R_s} \frac{1}{\frac{L}{R_s}\ s + 1} \tag{12.28}$$
$$= \frac{1}{R_s} \frac{K_p\ s + K_i}{s\ (\frac{L}{R_s}\ s + 1)} \tag{12.29}$$

It is chosen to cancel the system pole out by the zero from the controller. This is done if the controller parameters are chosen as stated in equation (12.30). $G_{el,OL}(s)$ is simplified to equation (12.31).

$$K_p = \frac{L}{R_s} = \tau_{t,el} \qquad ; \qquad K_i = 1 \tag{12.30}$$
$$G_{el,OL}(s) = \frac{1}{R_s\ s} \tag{12.31}$$

The controller is designed to cancel the pole out from $\tau_{t,el}$ which is desirable if the system transfer function is ideal. Parameter variations affect the system pole location, why the location of the system pole and the controller zero relative to each other, is investigated. In figure 12.10 and 12.11 the effects of the parameter variation (and thereby the pole location) is shown, where the PI-controller is not varied (black circle on the figure 12.11). Only the root locus from the system with $\tau_{t,el,max}$ is visible since the others are located on the real axis. As seen from figure 12.10 $\tau_{t,el,max}$ shifts the phase towards -180° and furthermore as seen from figure 12.11 the system might have an overshoot depending on the chosen gain. Since no performance requirements are determined, it is chosen to design the controllers to the slowest electrical and mechanical system poles ($\tau_{t,el,max}$ and $\tau_{t,m,max}$) and thereby avoid overshoot.

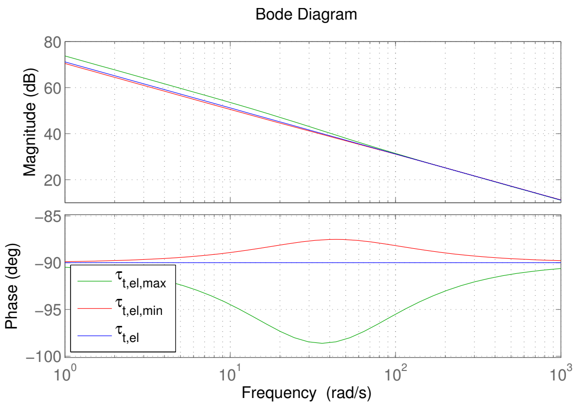

Figure 12.10: Bode plot where the effects of varying the time constant are shown.

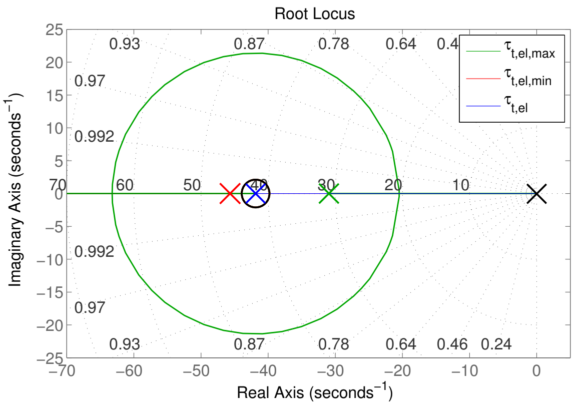

Figure 12.11: Root locus plot where the effects of varying the time constant are shown.

The system can now be gained, however it is important to avoid saturation of the inner loop otherwise the cascade structure does not have the desired performance. In this system it means the controller must not require more than $230V\sqrt{2} \approx 325V$, due to the chosen PWM strategy from chapter 11, however for conservative considerations 310 V is considered to be the maximum demanded output. Through simulations it has to be verified if the system saturates, which is done in section 12.5. Since the system is designed to avoid saturation, no anti-windup is designed.

The gain is determined to $K_{c,in} = 50$ through iterations, which is a balance between overshoot and settling time. The open loop frequency response is shown in figure 12.12. A bandwidth of $f_{BW} = 592\ Hz$ is determined from the closed loop transfer function. The system could be gained further to increase the bandwidth, however a faster system increases discretisation effects as described later in section 12.4.

$$G_{el,OL} = K_{c,in} \frac{1}{R_s \, s} \tag{12.32}$$

Where in equation (12.32):

$K_{c,in}$	Gain of inner controller, $[-]$

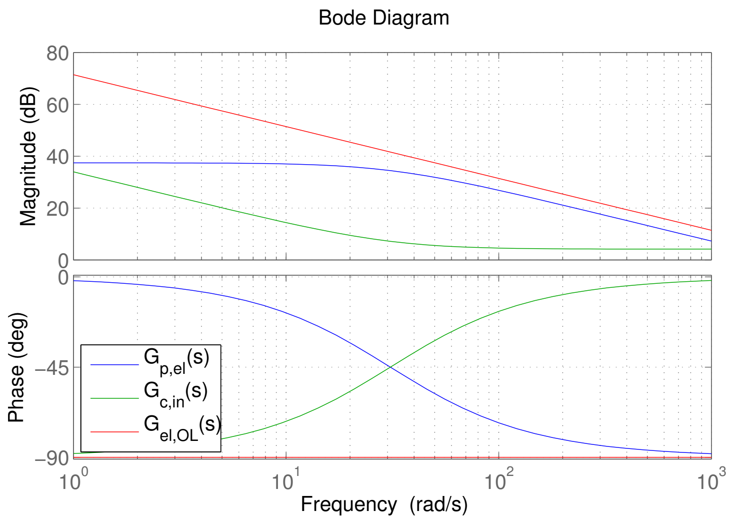

Figure 12.12: Open loop bode plot of electrical system and the controller.

12.3.3 Design of velocity controller

In the velocity controller design, the current loop is considered ideal due to the small time constant compared to the mechanical system, which means the loop can be neglected. The velocity controller is designed from the same procedure as the current controller. The open loop transfer of the mechanical system including the controller is:

$$G_{mech,OL}(s) = G_{c,out}(s) \; G_{p,m}(s) \tag{12.33}$$

$$= \frac{K_p \; s + K_i}{s} \; \frac{1}{B_m} \; \frac{1}{\frac{J}{B_m} \; s + 1} \tag{12.34}$$

$$= \frac{1}{B_m} \; \frac{K_p \; s + K_i}{s \; (\frac{J}{B_m} \; s + 1)} \tag{12.35}$$

Like the electric controller, it is chosen to cancel the system pole out by the zero from the controller. This is done in equation (12.36), where $G_{mech,OL}(s)$ is simplified in equation (12.37).

$$K_p = \frac{J}{B_m} \qquad ; \qquad K_i = 1 \tag{12.36}$$

$$G_{mech,OL}(s) = \frac{1}{B_m \; s} \tag{12.37}$$

The system can now be gained, which is determined to be $K_{c,out} = 0.015$ by iterations, as no performance criteria are set up. The open loop frequency response is shown in figure 12.13. The bandwidth of the mechanical system is around $f_{BW} = 1.1\ Hz$, which is caused by the iterative design where no overshoot is weighted higher than tracking performance.

$$G_{mech,OL} = K_{c,out} \frac{1}{B_m\ s} \tag{12.38}$$

Where in equation (12.38):

$K_{c,out}$	Gain of outer controller, $[-]$

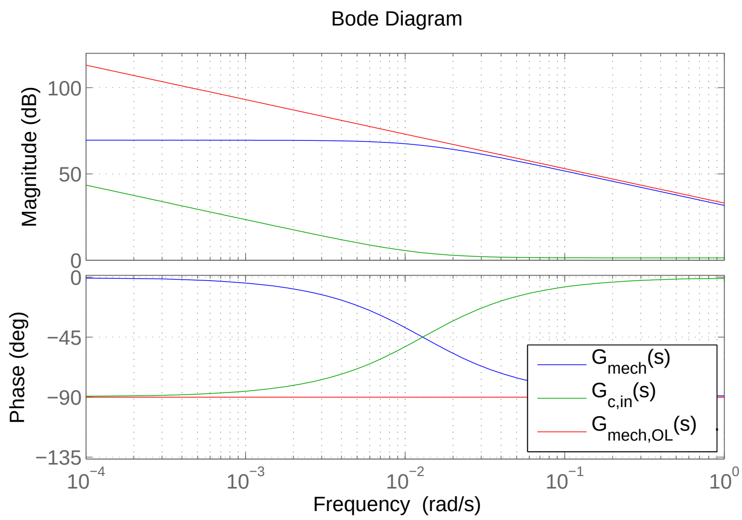

Figure 12.13: Open loop bode plot of the mechanical system and the velocity controller.

12.4 Discretisation of controllers

Despite the PMSM controller is not implemented in this project, the controllers are discretised to include potential discretisation effects. According to [48] the discretisation effects are neglectable if equation (12.39) is fulfilled, where f_{BW} is the bandwidth of the current loop. The switching frequency of the VSI is determined to 6.0 kHz which is assumed to also define the sample frequency. This means discretisation effects should neglectable, however the controllers are discretised for conservative considerations.

$$f_s \geq 10\ f_{BW} \tag{12.39}$$

Where in equation (12.39):

f_{BW}	Bandwidth, $[Hz]$
f_s	Sample frequency, $[Hz]$

The designed controllers are stated in equation (12.40) and (12.41).

$$G_{c,in}(s) = K_{c,in} \frac{\frac{L}{R_s}\ s+1}{s} = \frac{1.616s+50}{s} \tag{12.40}$$

$$G_{c,out}(s) = K_{c,out} \frac{\frac{J}{Bm}\ s+1}{s} = \frac{1.164s+0.015}{s} \tag{12.41}$$

The controllers are discretized according to Tustin's method, which maps the transfer functions from the s- to the z-domain, as stated in equation (12.42) [49]. The discretized controllers are stated in (12.43) and (12.44).

$$s = \frac{2}{T_s}\left(\frac{1-z^{-1}}{1+z^{-1}}\right) \tag{12.42}$$

$$G_{c,in}(z) = K_{c,in}\,\frac{R_s\,T_s - 2L + (2\,L + R_s\,T_s)\,z}{2R_s\,(z-1)} \tag{12.43}$$

$$G_{c,out}(z) = K_{c,out}\,\frac{B_m\,T_s - 2J + (2\,J + B_m\,T_s)\,z}{2B_m\,(z-1)} \tag{12.44}$$

Where in equation (12.42) to (12.44):

T_s	Sample time, $[s]$
z	Discrete operator, $[-]$

The discrete controllers are implemented as shown in figure 12.14. The zero order hold block is used to simulate the discrete feedback signal. The rate transition block is used by MATLAB when a discrete controller is connected to a continuous plant.

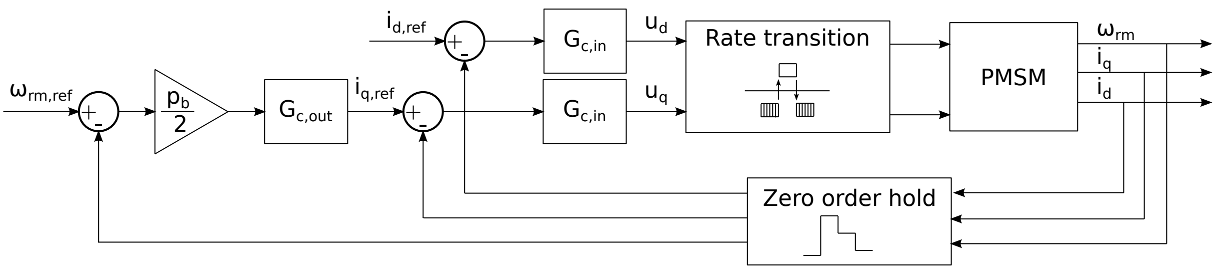

Figure 12.14: Implementation of discrete controllers.

12.5 Test of controllers without VSI

To test the controllers, the PMSM is ramped to 15000 rpm (1570.8 $\frac{rad}{s}$) and a velocity step of 10 $\frac{rad}{s}$ is applied. First the test is performed on the non-linear PMSM without the VSI model and afterwards, in section 12.6, the controllers are tested on the non-linear PMSM with the VSI model.

In figure 12.15, 12.16 and 12.17, the performance of the controllers are shown. Discrete controller-v1 is the controllers stated in equation (12.43) and (12.44). Discrete controller-v2 is the same current controller as previous however the velocity controller is gained by 2, to illustrate why the original gain was chosen. The maximum output voltage from the controllers is 225 V, which means the system is not close to saturation as required. From the figures it is seen the velocities before and after the step are lower than the references, which is caused by the small integral gain in the velocity controller. The offsets are removed if the simulation times are increased, however it is accepted to use these results to test the current ripples. Tuning or redesign of the controllers may remove this offset, however it has to be further investigated.

As seen from the figures the controllers are able to handle the 10 $\frac{rad}{s}$ step and the preceding ramp without getting unstable, however some oscillations occur dependent on the gain. In section 12.3.3 the gain was chosen to reduce the oscillations which are dominant from the gained discrete controller-v2. The oscillations are caused by the disturbances since the electric and mechanical systems are of first order. The responses from the first order systems without the disturbances are shown in figure 12.18 and 12.19. The disturbances are known why they could be used as a feed forward compensation and thereby improve the performance, however it will not be investigated further. The system with the controllers is able to step 10 $\frac{rad}{s}$ and reach steady state within 0.5 s.

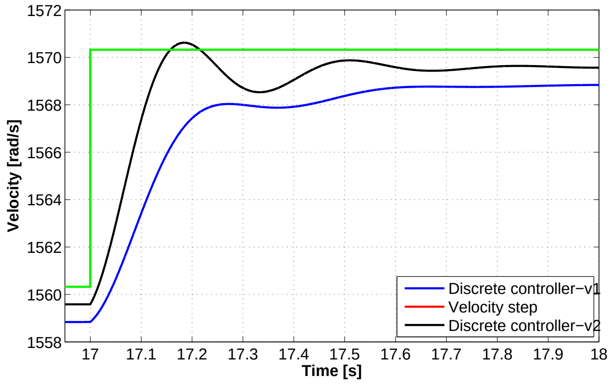

Figure 12.15: Velocity of PMSM with controllers.

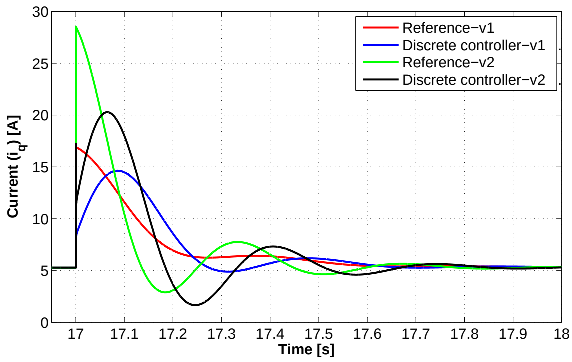

Figure 12.16: I_q current of PMSM with controllers.

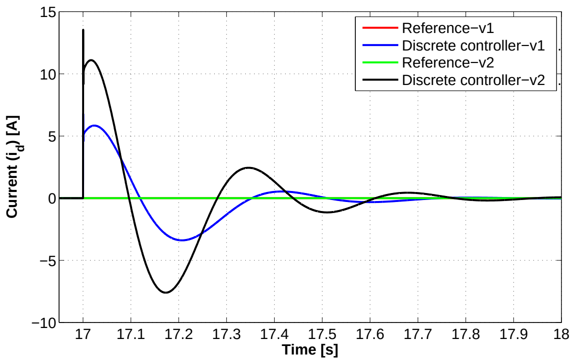

Figure 12.17: I_d current of PMSM with controllers.

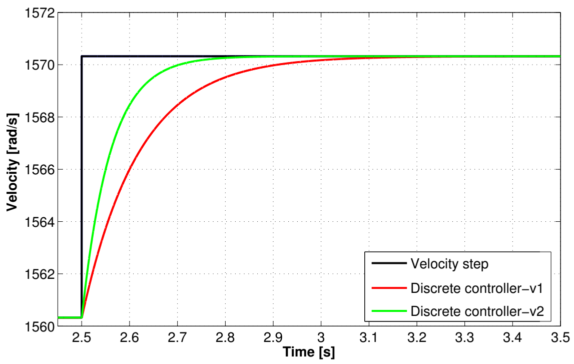

Figure 12.18: Velocity response of the linear model without disturbances.

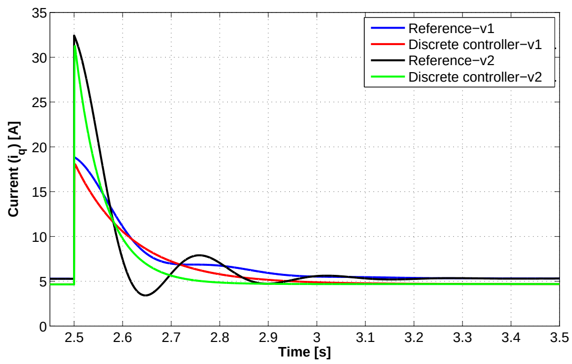

Figure 12.19: I_q current response of the linear model without disturbances.

12.6 Test of controllers with VSI

The VSI is included to see how it influences the performance of the controllers and to analyse the current ripples, due to the low number of switches per revolution described in section 1.1. The VSI model is inserted between the PMSM and the rate transition block in figure 12.14. Three simulations are performed to see the influence of the switching frequency, one with $f_{sw} = 6.0\ kHz$, one with $f_{sw} = 10\ kHz$ and one with $f_{sw} = 16\ kHz$. The results of the first two simulations are shown in figure 12.20 to 12.25. No saturation occurs in the simulations as required.

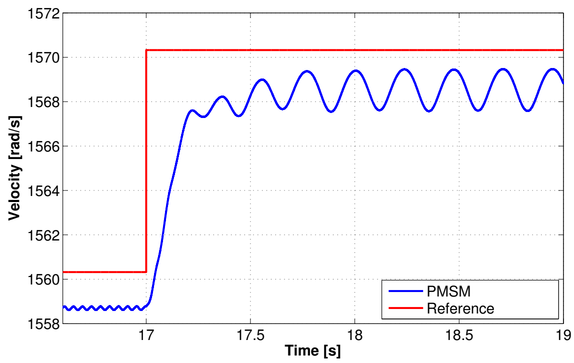

Figure 12.20: Simulated velocity from PMSM including VSI ($f_{sw} = 6.0\ kHz$).

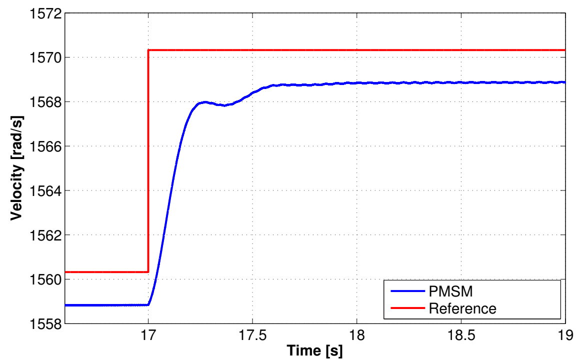

Figure 12.21: Simulated velocity from PMSM including VSI ($f_{sw} = 10\ kHz$).

Figure 12.20 shows the velocity oscillations, which the controllers are not able to eliminate. The oscillations are reduced significantly in figure 12.21, why the oscillations are caused by the low switching frequency of the VSI, as that is the only difference between the simulations. To reduce the current ripples, a higher switching frequency is desired, however a higher switching frequency increases the switching losses in the VSI. Based on these simulations a switching frequency of 6.0 kHz is assessed to be too low to operate the PMSM. The oscillations are also observed during open loop operation as described in section 7.

Figure 12.22 and 12.23 show the simulated i_q currents at a switching frequency of 6.0 kHz and 10 kHz. The amplitude of the current ripples is reduced from approximately 20 A to 14 A, which reduces the losses significantly. From figure 12.24 and 12.25 it is seen the amplitude of the i_d current is almost the same.

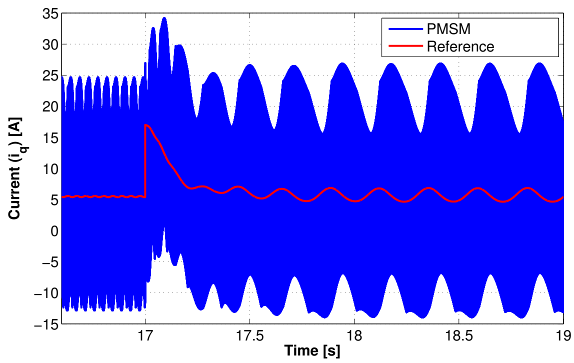

Figure 12.22: Simulated i_q current from PMSM including VSI ($f_{sw} = 6.0\ kHz$).

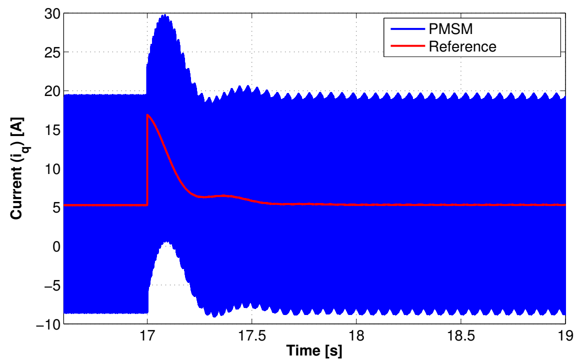

Figure 12.23: Simulated i_q current from PMSM including VSI ($f_{sw} = 10\ kHz$).

Zooms of the current ripples with a switching frequency of 10 kHz are shown in figure 12.26 and 12.27. From the figures it is seen the i_d controller is not able to regulate the i_d current to a mean of 0 A within

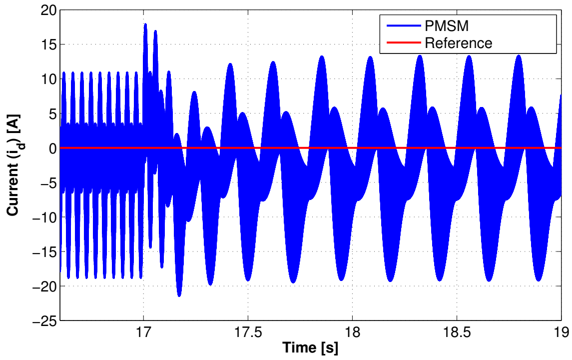

Figure 12.24: Simulated i_d current from PMSM including VSI ($f_{sw} = 6.0\ kHz$).

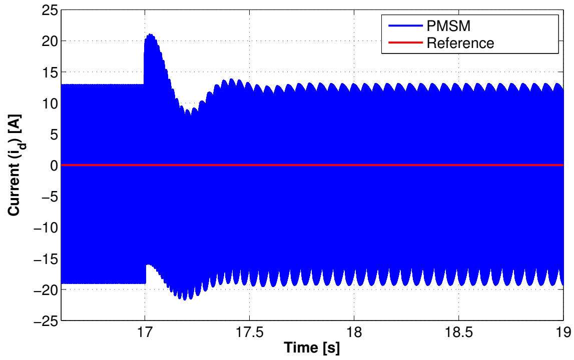

Figure 12.25: Simulated i_d current from PMSM including VSI ($f_{sw} = 10\ kHz$).

the simulated time interval. The average i_d current is around -0.83 A. The characteristics of the i_q and i_d current ripples differ. The i_q has slow oscillations and high ripples. The i_d current has also some slow oscillations however the ripples are reduces compared to the i_q current. The i_q controller is able to regulate to an average close to the reference, which indicates the velocity controller causes the small velocity offset.

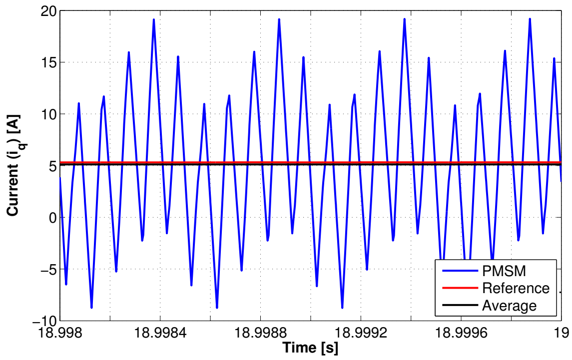

Figure 12.26: Simulated i_q current ripples from PMSM including VSI ($f_{sw} = 10\ kHz$).

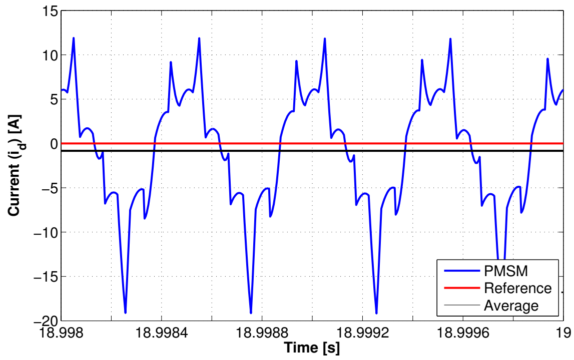

Figure 12.27: Simulated i_d current ripples from PMSM including VSI ($f_{sw} = 10\ kHz$).

A simulation is performed with a switching frequency of 16 kHz to investigate the effects of a further increased switching frequency. The results from the simulations are shown in figure 12.28 to 12.30. From the simulations it is seen the velocity oscillations are further reduced as expected. Both the i_q and the i_d current ripples are reduced to around an amplitude of approximately 7 A in this simulation. Furthermore the controller is now able to regulate the i_d current to an average of 0 A. Based on this simulation it may be beneficial to increase the switching frequency from 10 kHz, however the losses in the VSI must be estimated. It is chosen to use a switching frequency of 10 kHz in the following simulations as the losses in the VSI are unknown.

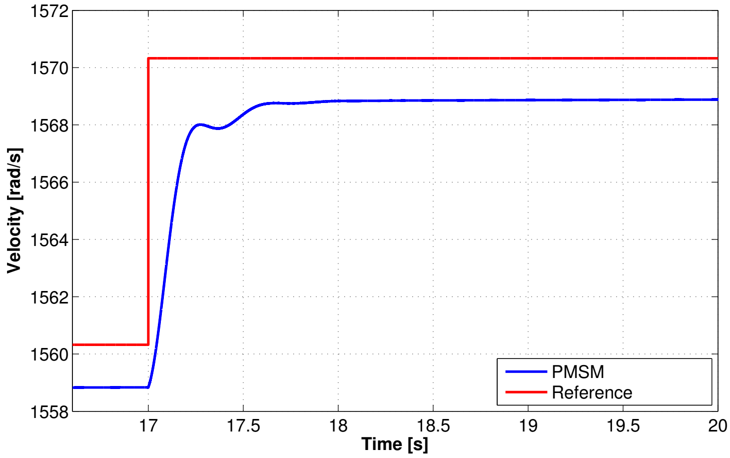

Figure 12.28: Simulated velocity from PMSM including VSI ($f_{sw} = 16\ kHz$).

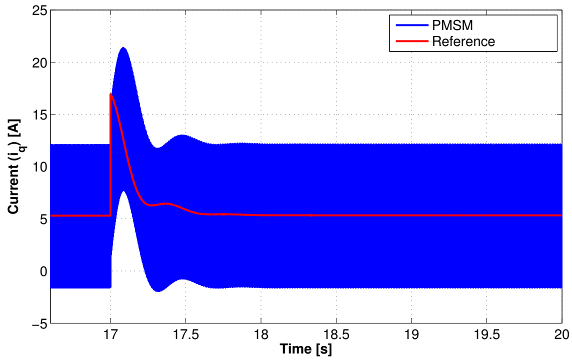

Figure 12.29: Simulated i_q current from PMSM including VSI ($f_{sw} = 16\ kHz$).

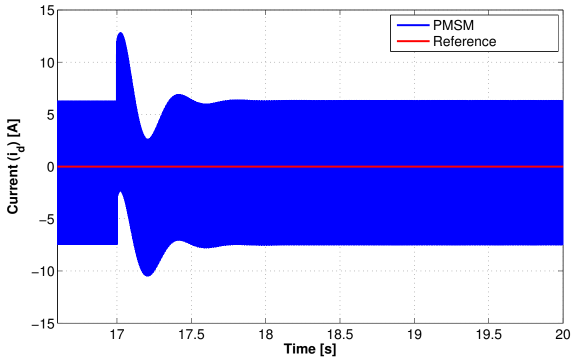

Figure 12.30: Simulated i_d current from PMSM including VSI ($f_{sw} = 16\ kHz$).

12.7 Test of controllers with VSI and load

Load is added to the test if the controllers are able to operate the PMSM with load and a switching frequency of 10 kHz. The load is assumed to be quadric cf. section 5.5, however the parameters are unknown. Two different quadratic loads are arbitrary determined, one where the load at 1570 $\frac{rad}{s}$ is 6.8 Nm and the one where the load at 1570 $\frac{rad}{s}$ is 14.2 Nm. The quadric loads are determined as:

$$\tau_{load1} = 0.000002\ \frac{Nm}{(rad/s)^2}\ \omega_{rm}^2 + 0.001\ \frac{Nm}{rad/s}\ \omega_{rm} + 0.3\ Nm \tag{12.45}$$

$$\tau_{load2} = 0.000005\ \frac{Nm}{(rad/s)^2}\ \omega_{rm}^2 + 0.001\ \frac{Nm}{rad/s}\ \omega_{rm} + 0.3\ Nm \tag{12.46}$$

The PMSM with load is ramped up to 1560 $\frac{rad}{s}$ and after 5 s a step of 10 $\frac{rad}{s}$ is performed. The results from the simulations are shown in figure 12.32 to 12.36.

The controllers are not designed to this load scenario, however they are able to ramp the PMSM to full speed and perform the step as seen from figure 12.31 and 12.32. It is seen the difference between the reference velocity and the actual velocity increases at increased load. The difference is caused by the low integral gain of the velocity controller. From the simulations it is seen the PMSM with load can be ramped up to 15000 rpm in 20 s without saturation. The current ripples remain approximately 14 A with the added load as seen from figure 12.33 to 12.36, which corresponds to theory as current ripples should be independent of the power transferred according to [12].

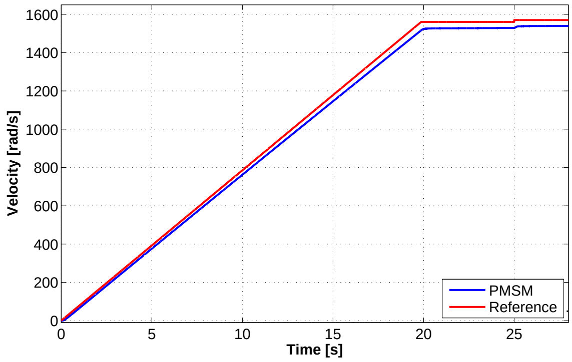

Figure 12.31: Simulated velocity from τ_{load1} ($f_{sw} = 10\ kHz$).

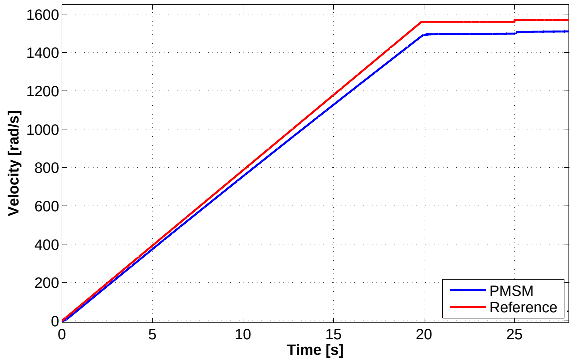

Figure 12.32: Simulated velocity from τ_{load2} ($f_{sw} = 10\ kHz$).

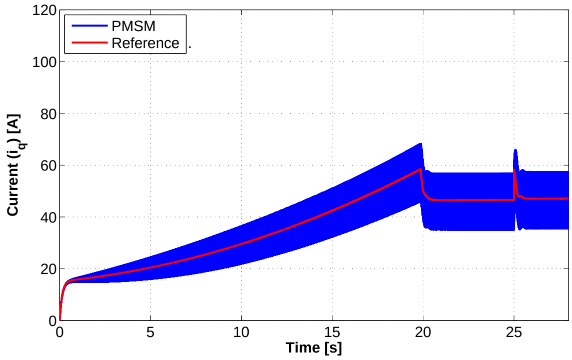

Figure 12.33: Simulated i_q current from τ_{load1} ($f_{sw} = 10\ kHz$).

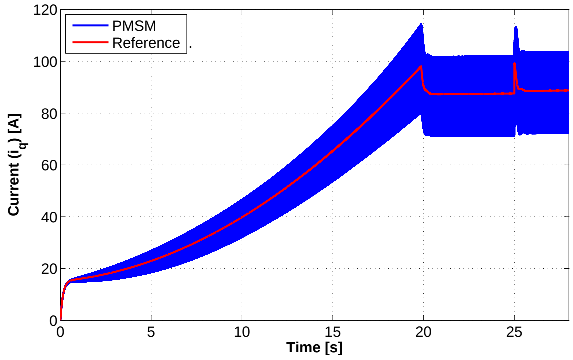

Figure 12.34: Simulated i_q current from τ_{load2} ($f_{sw} = 10\ kHz$).

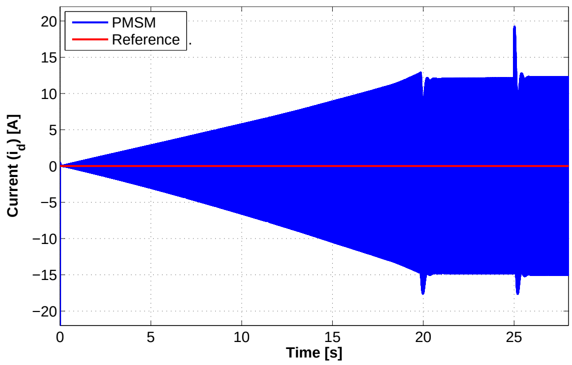

Figure 12.35: Simulated i_d current from τ_{load1} ($f_{sw} = 10\ kHz$).

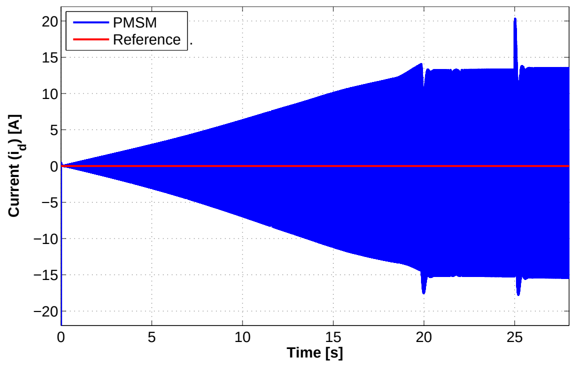

Figure 12.36: Simulated i_d current from τ_{load2} ($f_{sw} = 10\ kHz$).

12.8 Test of the open loop U/F controller with load

The open loop U/F controller is tested with the load to further investigate the open loop oscillations from chapter 7 and 11. It is tested if the oscillations are reduced by loading the PMSM. The simulations of the 0.17 $\frac{V}{Hz}$ open loop U/F relation are shown in figure 12.37 and 12.38, where a switching frequency of 10 kHz is used.

As seen from figure 12.37 increased load reduces the velocity oscillations. The amplitude of the current is increased from the increased load as shown in figure 12.38, however the current oscillations are reduced. The open loop U/F measurements from section 11.3 with a switching frequency of 6.0 kHz have higher

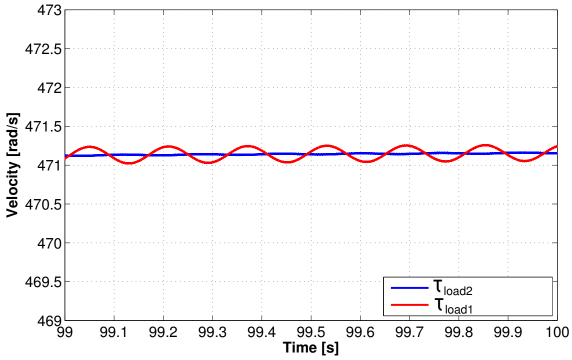

Figure 12.37: Simulated open loop velocity oscillations.

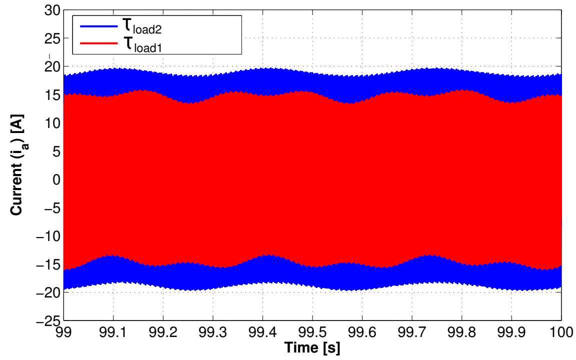

Figure 12.38: Simulated open loop current oscillations.

oscillations, why a high load and high switching frequency decreases the oscillations.

12.9 Influences from switching frequency and load

A brief summation of the influences from the switching frequency and load are stated following. The controllers are able to remove the slow oscillations, which occur during open loop operation, discussed in chapter 7. The PMSM is able to operate despite high current ripples, however a switching frequency of 6.0 kHz is assessed to be too low, why a switching frequency of minimum 10 kHz should be used. The controllers are able to ramp the PMSM and perform a velocity step, however they should be tuned to improve the tracking performance. The current ripples and the power losses should be investigated further, to choose a switching frequency, which reduces the total power losses in the PMSM and the VSI.

CHAPTER

13 CONCLUSION

The goal of this Master's Thesis has been to manufacture, analyse, test and control a Permanent-Magnet Synchronous Machine (PMSM). The overall focus has been solving the issues regarding manufacturing of a functional prototype, the application in a low pressure environment and the influence of the Voltage Source Inverter (VSI) at the high operational speed.

Manufacturing

Two prototypes of the PMSM were manufactured, which included assembling, wounding and resin casting. The purpose was to test if the motor design was realisable and perform experimental tests. The first prototype (PMSM-v1) revealed issues related to the resin casting, since it was not able to seal the cooling system. Repairs by epoxy adhesive and a leak sealing product could not prevent the leakages, why it was discarded to operate PMSM-v1 with liquid cooling. The resin casting process resulted in resin located on the rotor and stator laminations, which was removed in a turning lathe and by machining to enable the assembling of PMSM-v1. Contact between the rotor and stator laminations was unintentionally created in the turning lathe and from the machining. Several shorts occurred in the PMSM during the manufacturing and testing, which showed the importance of insulation materials to prevent this in the second prototype. It was possible to manufacture and assemble PMSM-v1 and operate it at 15000 rpm. Improvement proposals were presented based on the gained experiences.

The end plates were redesigned to avoid leakage in PMSM-v2. Vacuum was applied during the resin casting which improved the resin casting significantly. The improved end plates and resin casting reduced the leakages, but leakages occurred because the casting mould only allowed a thin resin layer at the joint between end plate and shaft, why PMSM-v2 was not assembled. Shorts were avoided in PMSM-v2 by heat shrinkable tubing and care taking during the manufacturing.

Electric and thermal modelling of PMSM

Electrical models of the PMSM and VSI were developed to test controllers and investigate the influence of the VSI. A model of a PMSM with voltage equations in the rotating dq reference frame was developed, where the d-inductance and the q-inductance were assumed to be equal to simplify the electrical model.

Experimental parameter determination showed justification of the assumed equal inductances. The VSI was modelled with ideal IGBTs to reduce the comprehensive simulation time.

The electric models were verified through tests, however the inaccessible star point and lack of position feedback limited the verification to the ABC reference frame. The measured and simulated current ripples were compared, which showed good agreement why the ideal IGBTs were assessed to be acceptable for the VSI model. Inconsistent system oscillations were discovered during the verification.

Mechanical resonance affected the determination of the rotational power losses, however the losses were estimated to be 1300 W, which was almost twice the expected value. The reason for the high losses was assessed to be too tight fittings of the bearings and the contact created between the stator and rotor laminations. The bearing fittings were loosened which reduced the losses.

The cooling system was tested to investigate if the PMSM overheats during operation. Only the stator of PMSM-v1 was tested, why no core losses were included, and the tests were performed at room temperature and atmospheric pressure. The nominal AC current of 70 A was applied to the windings, which resulted in measured winding temperatures of approximately 70°C when liquid cooling of 20°C was enabled. This means the additional core losses must not cause a temperature increment of more than 80°C. It was concluded that further analysis should be performed to include the operation environment and core losses.

A 3D thermal Lumped Parameter model of the PMSM was developed. A literature review did not reveal any models of similar motor topology but several temperature compensation approaches to model distributed power losses were discovered. The novel GD compensation approach was chosen from test scenarios where the simulated temperatures were compared to FEM solutions. A thermal network of the PMSM was set up and the thermal resistances were determined by material properties, geometry and assessments from the manufacturing process. It was not possible to verify the thermal resistances through measurements, which could have verified some of the simplifications made to calculate the resistances.

The lumped parameter model was compared to a 2D FEM model which showed an under-prediction of temperatures from the lumped parameter model. The under-prediction was caused by how a transition between two elements of different size was modelled in the two models.

The lumped parameter model was compared to experimental tests which showed temperatures within an acceptable margin. The heat transfer coefficient for liquid cooling was fitted by the measured temperatures. The simulated radiation and convection showed a deviation in heat flow of -8.3% which was because radiation and convection were not assigned to all surfaces in the lumped parameter model.

The thermal model showed the PMSM is able to operate in the thermal test scenario if the rotational losses are reduced to the expected 750 W. If 1300 W rotational losses are present, the winding and stator temperatures approach 155°C, which is not acceptable. However the accuracy of the model must be investigated to gain more trustworthy results. Tests with liquid cooling and core losses are required verify the thermal model thoroughly. Furthermore additional thermocouples must be incorporated to verify the thermal resistances.

Controller design

A PMSM controller, designed from a linearised model of the PMSM, was developed to investigate the influence of the current ripples on a control strategy and investigate discovered system oscillations. The PMSM controller was designed to a no load scenario, however the load should have been included, as the PMSM controller was not implemented in the test bench. It was chosen to use a cascade control structure with an inner current controller and an outer velocity controller to suppress non-linearities. PI controllers were chosen for both velocity and current loop to remove steady state errors. Tests showed a good performance without the VSI model and on the linearised system. However the PI controller did not perform as it was designed to which was caused by discarded system dynamics during the linearisation.

A switching frequency of 6 kHz was initially chosen based on test runs with the PMSM. Simulations were performed to test the influence of the VSI and the chosen switching frequency which revealed system oscillates and high current ripples at a switching frequency of 6 kHz. The switching frequency was increased to 10 kHz, which reduced the oscillations and current ripples why the initially chosen switching frequency is assessed to be too low.

An open loop voltage/frequency (U/F) control strategy was designed and implemented to bypass the control software in the VSI which enabled the verification of the electrical models of the PMSM. Space Vector Pulse Width Modulation (SVPWM) was chosen to generate PWM signals for the VSI due to the ease of implementation, utilisation of the DC link and low amount of total harmonic distortion. In the low frequency range an offset was added to the U/F relation to compensate for a lowered voltage output from the VSI. The SVPWM and U/F relation was implemented and tested, which showed the PMSM was able to start up and operate at 15000 rpm. Oscillations occurred in the measured currents why simulations were performed with the U/F relation and a load, which indicated the oscillations were lowered by an increased load. Simulations also showed the U/F relation was able to run the PMSM with load at 15000 rpm, however a closed loop control strategy is desirable for future implementation.

CHAPTER

14
FUTURE WORK

The conclusions and experiences gained from this project are used to discuss future work of the development of a PMSM for the water vapour chiller. The influences of the demarcations made in this project are included in the discussion.

Manufacturing and design of cooling system

To improve the resin casting, and thereby seal of the cooling system, a new tight stator mould that prevents resin on the bearing surfaces and does not require silicon sealing is required. The designed rotor mould must also be manufactured and tested. Furthermore the leakage from the joint between the end plate and shaft must be sealed e.g. by an increased layer of resin, as discussed in section 4.3.4. Alternatively a solution to keep the windings away from the joint between the end plate and shaft must be designed, to ensure the resin enters and seals the leakage from the joint.

If it succeeds to prevent leakages, the PMSM must be tested to see how the resin and end plate behave in a hot and moisture environment over a longer time period. It might be beneficial to look into casting materials with better temperature resistivity, as the experiences from Huntsman resin show it changes properties over time.

It might be beneficial to discard the idea of sealing the cooling system by resin, if the above solutions do not prove reliable. A safer and widely used approach is to use a hose system for the coolant. The risk of both external and internal leakages is reduced by using hoses, as no sealing of joints or gaps are required to prevent leakages. It is still beneficial to cast the stator into resin to improve the heat transfer from the windings and stator to the coolant. A solution with hoses could imply hoses passing through where the cooling channels are now or a total redesign of the cooling system. The drawback of using hoses is the manufacturing process involves further steps and hoses with a small bending radius must be utilised if the hoses are to run as the cooling channels. The heat transfer is not assessed to be reduced significantly compared to a solution with closed end plates, if hoses with a sufficiently large diameter and small bending radius are available.

Estimation of temperatures

To assess the applicability of the PMSM in the water vapour chiller, further details of how the application affects temperatures of the PMSM, must be known. To reduce the temperatures cooling by condensing water vapour could be investigated. The estimated temperatures from the thermal model are discussed in section 10.6. A simulation is performed to see the effect of excluding internal and external convection and radiation. The temperatures of the rotor housing are $100°C$ when external convection is removed. The removal of external convection corresponds to the situation if the impeller is mounted directly on the rotor housing. It implies that as long as the temperature of the impeller is beneath $100°C$ the rotor temperature is not increased.

The PMSM-v2 must be assembled to determine if the rotational losses are reduced to the expected rotational loss of 750 W instead of the measured rotational loss. If the high rotational losses persist the estimated temperatures in the test scenario are above the allowable.

Investigation of control strategies

As mentioned in section 1.1 a sensor-less control strategy is desirable to avoid implementation of a position sensor. The developed U/F control can be used to ramp the PMSM to a speed where the amplitude of the currents are sufficiently large to be used for sensor-less position estimation. Care must be taken to select a sensor-less control strategy that is not influenced by the current ripples generated by the VSI. In general, the influence of the current ripples must be investigated to assess their influence on the heat generation in the PMSM. A low pass filter at the VSI output terminals might be advantageous to reduce the losses in the PMSM that are generated by higher order harmonics. However drawbacks (e.g. phase shift) from a low pass filter must be investigated and accounted for in the control strategies for the PMSM.

A more advanced control strategy for the PMSM might be beneficial, as the linearisation of the system results in exclusion of system dynamics in the controller design. An advanced control strategy may render possible to include the contributions which the linear controller design treats as disturbances.

To test the control strategies in a load scenario on the PMSM a load mechanism must be designed. The challenge is to attach a balanced load mechanism to the outer rotor without heat is transferred to the rotor. This could be accomplished by mounting the PMSM in one end of the shaft and then attach a shaft to the rotor in the other end as shown in figure 14.1, however this should be further investigated.

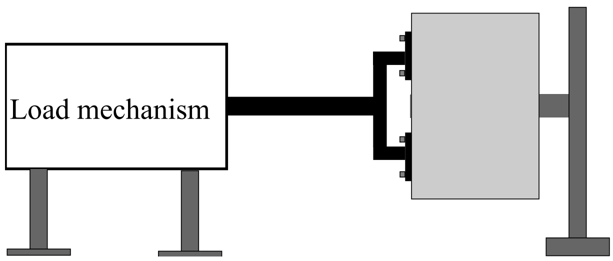

Figure 14.1: Sketch of a load mechanism to test control strategies and efficiency.

BIBLIOGRAPHY

[1] Energiforskning.dk. (2013, Oct. 21) Fremtidens køleanlæg. [Online]. Available: http://www.energiforskning.dk/node/2315

[2] H. Madsboell, "Competitive chiller concept with water as refrigerant," Danish Technological Institute, Centre for Refrigeration and Heat Pump Technology, Tech. Rep., 2013.

[3] Johnson Controls, Inc., "Water as refrigerant: Water vapor chiller, lego prototype," 2013, internal presentation.

[4] Chubu Electric Power. (2011, Oct. 20) Development of world's first water vapor chiller with axial compressor. [Online]. Available: http://www.chuden.co.jp/english/corporate/ecor_releases/erel_pressreleases/3139472_11098.html

[5] T. V. Frandsen *et al.*, "Improved motor intergrated permanent magnet gear for traction applications," pp. 3332–3339, 2013. [Online]. Available: http://ieeexplore.ieee.org/stamp/stamp.jsp?tp=&arnumber=6342334

[6] L. S. Andersen, "Internal note on application of the pmsm in the chiller." 2014, unpublished.

[7] B. Andersson, "Lumped parameter thermal modelling of electric machines," Chalmers University of Technology, Goteborg, Sweden, Tech. Rep., 2013. [Online]. Available: http://publications.lib.chalmers.se/records/fulltext/185192/185192.pdf

[8] B. Yang, "Development of thermal models for permanent-magnet traction motors," Royal Institute of Technology, Stockholm, Sweden, Tech. Rep., 2009. [Online]. Available: http://www.ee.kth.se/php/modules/publications/reports/2009/XR-EE-EME_2009_005.pdf

[9] D. Staton and T. Barucki, "Industrial/ph.d. course in heat management of power electronics and electrical machines," Lecture slides, Department of Energy Technology, Aalborg, Denmark, 2010.

[10] T. V. Frandsen and P. O. Rasmussen, "Internal note on estimations of losses, number of turns and pmsm specifications." 2013, unpublished.

[11] W. H. Yeadon and B. M. Frustaglio, "Current density," *SMMA Fall Conference*, 2010. [Online]. Available: http://www.smma.org/pdf/conferences/2010/F10%20Current%20Density.pdf

[12] N. Mohan *et al.*, *Power Electronics - Converters, Applications and Design*, 2nd ed. New Jersey, USA: John Wiley & Sons, 1995.

[13] Schaeffler Technologies GmbH & Co. (2014, Feb. 10) Deep groove ball bearings. [Online]. Available: http://medias.schaeffler.com/medias/en!hp.ec.br/60..-2Z?#60..-2Z

[14] D. M. Mathiasen *et al.*, "Modelling and implementation of a line-start permanent magnet synchronous motor in a ventilation test set-up," Department of Mechanical and Manufacturing Engineering, Aalborg University, Tech. Rep., 2013.

[15] M. Rossi *et al.*, *Residual Stress, Thermomechanics and Infrared Imaging, Hybrid Techniques and Inverse Problems*. New York City, USA: Springer, 2013.

[16] P. C. Krause *et al.*, *Analysis of Electric Machinery and Drive Systems*. Piscataway, NJ: IEEE Press, 2002.

[17] P. D. C. Perera, *Sensorless Control of Permanent-Magnet Synchronous Motor Drives*. Aalborg, Denmark: Aalborg University, 2002.

[18] T. Frandsen *et al.*, "Development, characterisation, and sensorless control of an integrated permanent magnet gear and -motor prototype for automotive applications," Department of mechanical engineering - Aalborg University, Tech. Rep., 2010.

[19] T. N. Matzen, "Sensorless control of permanent magnet synchronous machines," Department of Energy Technology - Aalborg University, Tech. Rep., 2010.

[20] M. P. Kazmierkowski and H. Tunia, *Automatic Control of Converter-Fed Drives*. Elsevier Science, 1994.

[21] P. Rasmussen, "Control of fluid power and electrical servomechanisms," Lecture slides, Department of Energy Technology, Aalborg, Denmark, 2012.

[22] L. Popova, "Combined electromagnetic and thermal design platform for totally enclosed induction machines," Department of Electrical Engineering, Lappeenranta University of Technology, Tech. Rep., 2010.

[23] B. Andersson, "Lumped parameter thermal modelling of electric machines," Department of Energy and Environment, Chalmers University of Technology, Tech. Rep., 2013. [Online]. Available: http://publications.lib.chalmers.se/records/fulltext/185192/185192.pdf

[24] G. Dajaku and D. Gerling, "Novel lumped-parameter thermal model for electrical systems," *IEEE*, 2005, institute for Electrical Drives, University of Federal Defense Munich. [Online]. Available: http://ieeexplore.ieee.org/stamp/stamp.jsp?tp=&arnumber=1665415

[25] D. Kuehbacher *et al.*, "An improved approach for transient thermal modeling using lumped parameter networks," *IEEE*, 2013. [Online]. Available: http://ieeexplore.ieee.org/stamp/stamp.jsp?tp=&arnumber=6556188

[26] G. Dajaku and D. Gerling, "Thermal calculation of systems with distributed heat generation," *IEEE*, 2006, institute for Electrical Drives, University of Federal Defense Munich. [Online]. Available: http://ieeexplore.ieee.org/stamp/stamp.jsp?tp=&arnumber=1645406

[27] D. Meeker, "Finite element method magnetics - user's manual," 2010. [Online]. Available: http://www.femm.info/Archives/doc/manual42.pdf

[28] G. Kylander, "Thermal modelling of small cage induction motors," Department of Electrical Machines and Power Electronics, Chalmers University of Technology, Tech. Rep., 1995.

[29] S. T. Lee *et al.*, "Thermal analysis of interior permanent-magnet synchronous motor by electromagnetic field-thermal linked analysis," *Journal of Electrical Engineering and Technology*, 2012. [Online]. Available: http://home.jeet.or.kr/archives/view_articles.asp?seq=565

[30] G. Dajaku and D. Gerling, "An improved lumped parameter thermal model for electrical machines," Institute for Electrical Drives, University of Federal Defense Munich, Tech. Rep., 2006. [Online]. Available: https://dokumente.unibw.de/pub/bscw.cgi/1362341

[31] T. L. Bergman *et al.*, *Fundamentals of Heat and Mass Transfer*, 6th ed. New Jersey, USA: John Wiley & Sons, 2006.

[32] D. Staton *et al.*, "Solving the more difficult aspects of electric motor thermal analysis," *IEEE*, vol. 20, no. 3, pp. 620–628, Sep. 2005. [Online]. Available: http://ieeexplore.ieee.org/stamp/stamp.jsp?arnumber=01495534

[33] D. Gerling and G. Dajaku, "Thermal calculation of systems with distributed heat generation," *IEEE*, 2006. [Online]. Available: http://ieeexplore.ieee.org/stamp/stamp.jsp?tp=&arnumber=1645406

[34] A. G. Bluman, *Elementary Statistics*, 7th ed. New York City, USA: McGraw Hill, 2009.

[35] M. Saidi and R. H. Abardeh, "Air pressure dependence of natural-convection heat transfer," *WCE*, 2010, proceedings of the World Congress on Engineering 2010.

[36] J. Nerg *et al.*, "Thermal analysis of radial-flux electrical machines with a high power density," *IEEE*, 2008. [Online]. Available: http://ieeexplore.ieee.org/stamp/stamp.jsp?arnumber=04555649

[37] D. Dave and T. Barucki, "Industrial/ph.d. course in heat management of power electronics and electrical machines," Lecture slides, Department of energy technology, Aalborg, Denmark, 2010.

[38] IAEA, *Thermophysical Properties of Materials for Nuclear Engineering: A Tutorial and Collection of Data*. Vienna, Austria: Nuclear Power Technology Development Section, 2008.

[39] Huntsman Advanced Materials, "Araldite casting resin system technical data sheet," 2004.

[40] Schmolz + Bickenbach, "416rs technical data sheet," 2014. [Online]. Available: http://www.schmolz-bickenbach.us/fileadmin/files/schmolz-bickenbach.us/documents/Ugitech/416RS.pdf

[41] E-magnets UK. (2014, Jan. 15) Characteristics of ndfeb magnets. [Online]. Available: http://www.ndfeb-info.com/characteristics.aspx

[42] D. Svechkarenko, "Thermal modelling and measurements of permanent magnet machines," Department of Electrical Engineering, School of Electrical Engineering, Tech. Rep., 2013.

[43] National Institute of Standards and Technology. (2014, Jan. 19) Thermophysical properties of fluid system. [Online]. Available: http://webbook.nist.gov/chemistry/fluid/

[44] DuPont, "Dupont nomex paper type 410 technical data sheet," 2013. [Online]. Available: http://www2.dupont.com/Energy_Solutions/en_US/assets/downloads/Nomex410_TechSheet_r6.pdf

[45] D. Meeker, "Femm heat flow tutorial," 2005. [Online]. Available: http://www.femm.info/wiki/HeatFlowTutorial

[46] Nippon Steel Corporation, "Non-oriented electrical steel sheets typical properties for 35H210 and 20HTH1200," 2013.

[47] H. C. Pedersen, "Reguleringsteknik," Lecture slides, Department of Mechanical and Manufacturing Engineering, Aalborg, Denmark, 2011.

[48] T. Glad and L. Ljung, *Control Theory - Multivariable and Nonlinear Methods*. Taylor and Francis, 2000.

[49] G. F. Franklin *et al.*, *Feedback Control of Dynamic Systems*, 6th ed. New Jersey, USA: Pearson Prentice Hall, 2009.

[50] R. Parekh, "Vf control of 3-phase induction motor using space vector modulation," 2005, unpublished.

[51] A. Sumper and A. Baggini, *Electrical Energy Efficiency: Technologies and Applications*, 1st ed. New Jersey, USA: John Wiley & Sons, 2012.

[52] A. von Jouanne and B. Banerjee, "Assessment of voltage unbalance," *IEEE*, 2001. [Online]. Available: http://ieeexplore.ieee.org/xpl/articleDetails.jsp?arnumber=956770

APPENDIX

A

PMSM SPECIFICATIONS

In figure A.1 to A.4 the lengths of some of the PMSM components are shown. In table A.1 extra geometry specifications are stated.

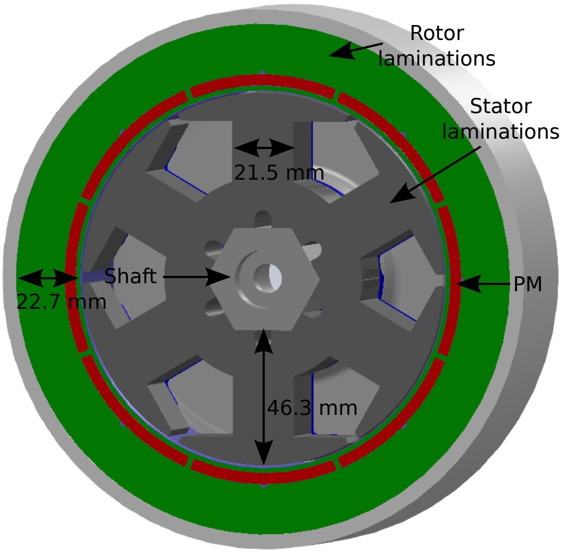

Figure A.1: Radial sectional view of the PMSM without windings and stator resin.

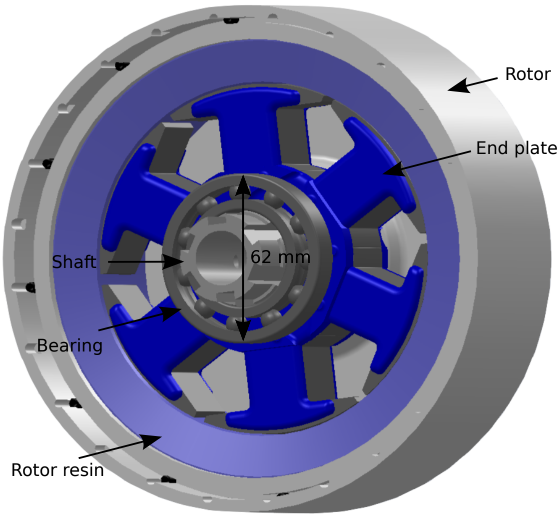

Figure A.2: Radial view of the PMSM without windings and stator resin.

Location	Length/Diameter/Distance
Air gap between rotor resin and stator	0.7mm
Air gap between rotor laminations and stator	1 mm
Thickness of PMs	3.85 mm
Gap between PMs	1.82 mm
Diameter of cooling channels in shaft	5 mm

Table A.1: Specifications of PMSM geometry.

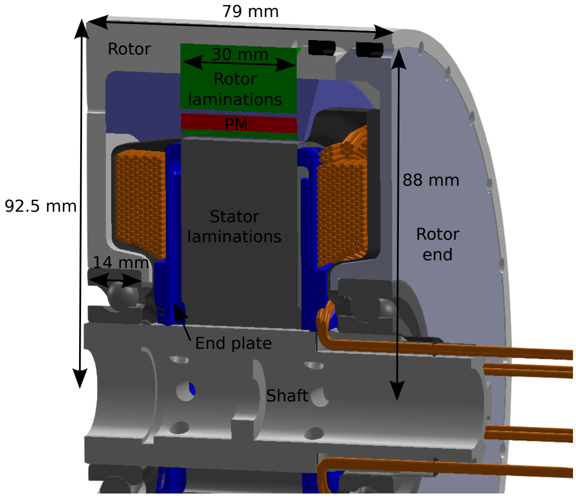

Figure A.3: Axial sectional view of the PMSM.

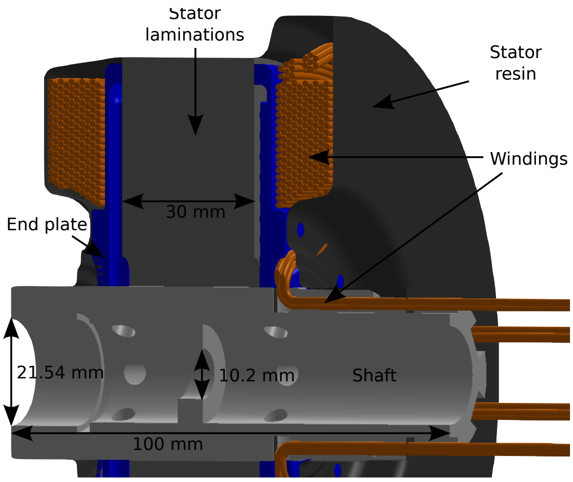

Figure A.4: Axial sectional view of the stator parts and the shaft.

APPENDIX

B

MANUFACTURING OF THE PMSM

This appendix is intended to support the description of the manufacturing process of the PMSM.

B.1 Test stator

Pieces of insulation plastic are placed in the stator slot, as seen in figure B.1, to prevent shorts between the stator laminations and the windings. Figure B.2 shows how the windings lock itself in the test stator. This is done to be able to tighten the windings and ensure a high fill factor. However this is not possible in the two PMSMs, as the windings must be guided along the channels in the shaft and down through the inlets in the end plates.

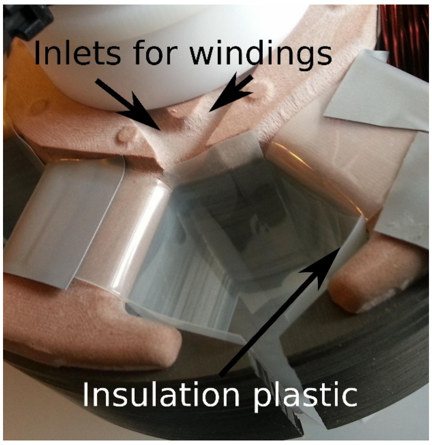

Figure B.1: Insulation plastic in the stator slot.

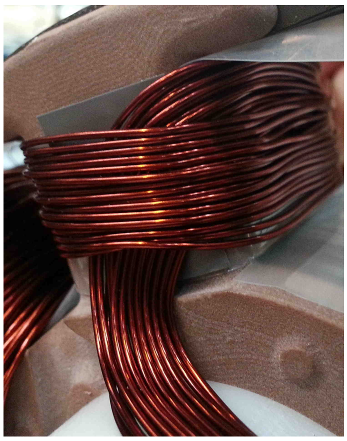

Figure B.2: Locking of the windings in the test stator.

The laminations are mounted on a dummy shaft with two different end plates, one made of Polyurethan (PUR) and one made of (polyoxymethylen) POM. The end plate made of PUR is tested due to the ability to glue it to the stator laminations, and thereby seal the gap between the end plate and the stator. It is also tested if impregnation is able to seal the gap between the PUR end plate and stator since impregnation is able to bind to PUR, but this is not prove a feasible solution. The PUR end plate broke during the winding process as shown in figure B.3. It is considered to be too fragile, why it is not investigated further.

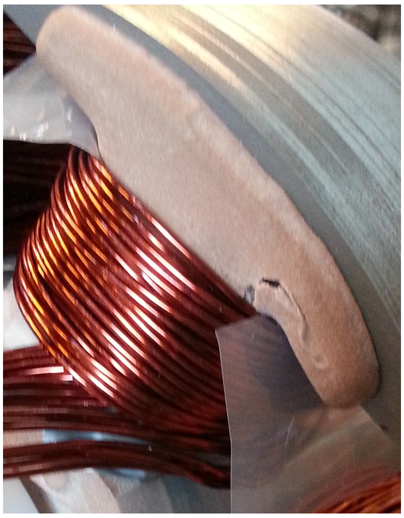

Figure B.3: Broken end plate of PUR.

Figure B.4: Conductors in a bundle.

To reduce the entanglement of the conductors, the conductors are separated into bundles of 3-4 copper conductors, as shown in figure B.4. This proves good results why it is performed for the two PMSMs, however instead of using copper conductors as separation, a cable tie is used to minimise the risk of scratches to the conductors.

After the stator is wound, it is fixed in a clamp and the windings are tensioned as shown in figure B.5 and B.6. This is done to tighten the windings and get them to settle and thereby remain tightened after the stator is removed from the clamp.

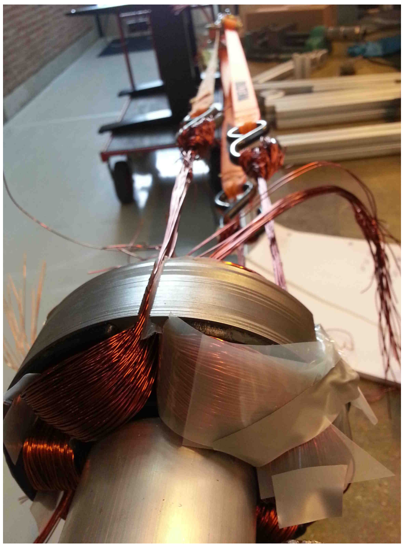

Figure B.5: Fixing and tensioning of the windings.

Figure B.6: Fixing and tensioning of the windings.

One purpose of the test stator is to test the resin casting. The test stator is cast into resin to check how well the Huntsman resin penetrates into the air gaps between the windings. To avoid resin from penetrating into the cooling channels, wax is injected into the cooling channels prior to the resin casting. After the resin has cured, the wax is melted out by heating the stator in an oven.

B.2 Slicing of test stator

The test stator is sliced in a band saw as shown in figure B.7. It is sliced to investigate how the resin has penetrated into the windings and gaps between the windings and stator. It is sliced into five pieces, of which four of them are shown in figure B.8.

Figure B.7: Band saw and the test stator being sliced into pieces.

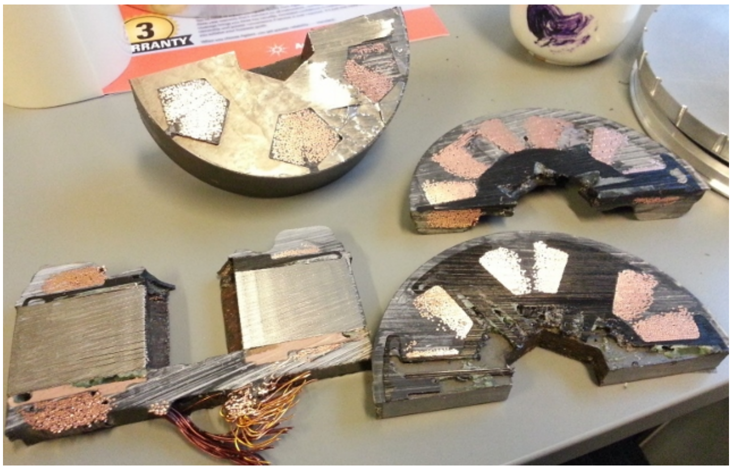

Figure B.8: The sliced pieces of the test stator.

Two of the stator slots sliced in the middle of the stator stack are shown in figure B.9 and B.10. The conductors are tighter near the end plates as shown in figure B.11.

Figure B.9: Slot in a radial slice in the middle of the stator stack.

Figure B.10: Slot in a radial slice in the middle of the stator stack.

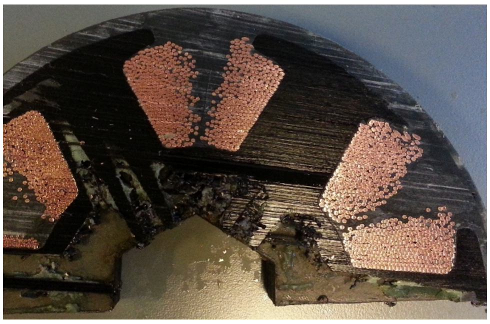

Figure B.11: A radial slice through the end plate.

B.3 Heat test of resin samples

Samples of Huntsman and RAMPF resin are heat tested to test the thermal properties after the samples have been heated in an oven. The samples are tested at the following temperatures and periods:

- $100°C$ in 2 hours and 10 minutes
- $130°C$ in 2 hours and 10 minutes
- $147°C$ in 2 hours and 5 minutes
- $164°C$ in 18 hours and 30 minutes

Figure B.12: Digging in the samples just after the samples had been removed from the oven.

Figure B.13: Samples after heat in 2 hours and 10 minutes at $130°C$. Huntsman resin to the left and RAMPF resin to the right.

The test method do not yield any quantifiable results, but the following observations are made:

- At room temperature, the RAMPF resin is soft and the Huntsman resin is hard. Neither of them break by digging with a screw driver in them.
- At $100°C$ both Huntsman and RAMPF resin get softer and more fragile compared to room temperature. However they are still hard and robust.
- From 100-$164°C$ the materials are soft and fragile and break easily. There is no significant difference in hardness and robustness, only a small advantage to the Huntsman resin over RAMPF resin.
- Both the Huntsman and RAMPF resin return to their originally properties at room temperature. Only the RAMPF becomes slightly more ductile after heating to $164°C$.

The conclusion of the test is that Huntsman resin is chosen as casting material for the PMSM due to the slight advantage in material properties at high temperatures, the hardness and robustness at room temperature. The test stator is cast in Huntsman resin and this also proves good results.

B.4 Wax injection

The wax is injected at DANTRAFO A/S in the machine shown in figure B.14. The stator is fixed by a clamping of 100 *kg* as shown in figure B.15.

Figure B.14: Injection machine at DANTRAFO A/S.

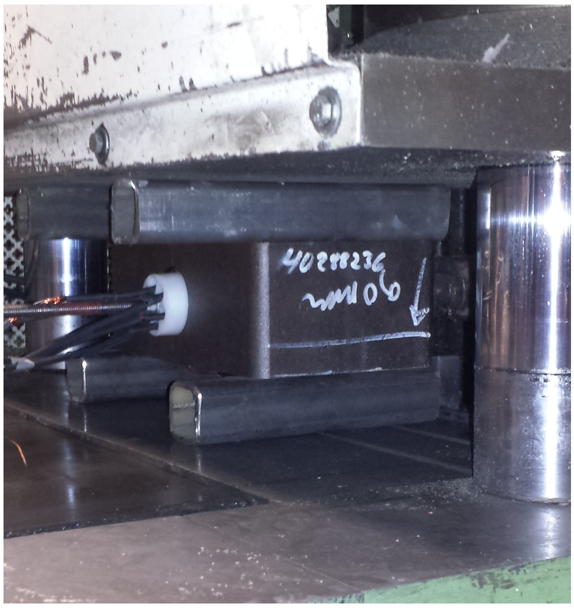

Figure B.15: The fixed stator in the machine.

The wax is injected by the machine through the injection tube shown in figure B.16. The excess wax that has penetrated through the gaps between the stator teeth and end plates is shown in figure B.17.

B.5 Permanent Magnets

This section describes how the PMs are manufactured. At semester start, the demagnetised magnet segments, shown in figure B.18, are provided. Three steps are performed to enable the PMs to be used in the PMSM.

Gluing magnets

First, the segmented magnets are glued together in order to form a complete magnet. In figure B.18 the segments are shown and in figure B.19 the mould, used to align the magnets, is shown.

Figure B.16: The injection tube that is connected to the inlet hole in the shaft.

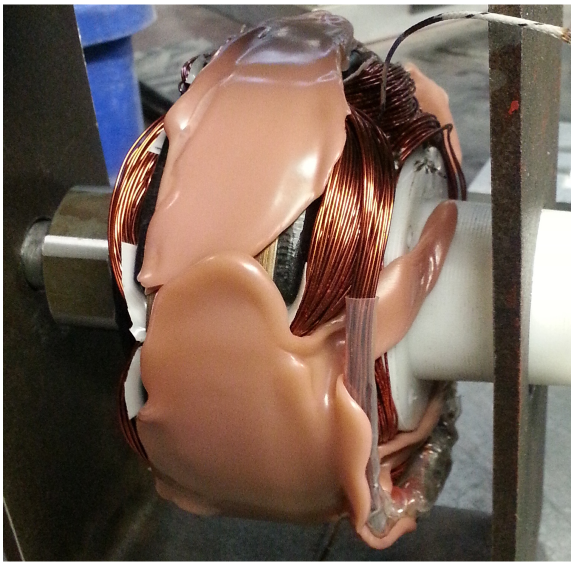

Figure B.17: The stator after the wax injection.

Figure B.18: Segments of the magnets, which are glued together.

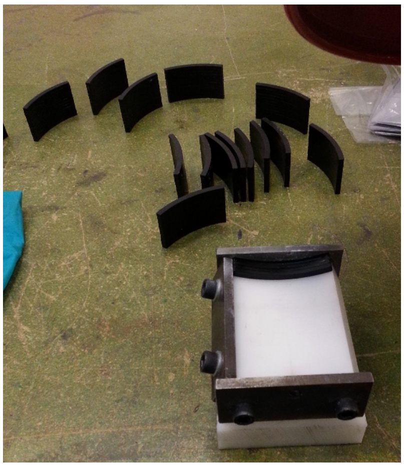

Figure B.19: Mould for the magnets.

Burnishing and painting

After the magnet segments are glued together the ends are burnished in order to assure alignment. This is necessary as the tolerances of the magnet segments are poor, and thereby burnishing ensures the PMs are able to fit in the rotor laminations. The burnishing of the magnet segments is shown in figure B.20.

The ends of the magnets are painted to ensure the magnets do not corrode. Figure B.20 shows a picture of the magnets being burnished and figure B.21 shows a picture of the magnets after the burnishing. To ensure no contact exists between the magnet segments the resistance is measured, which showed an infinite resistance.

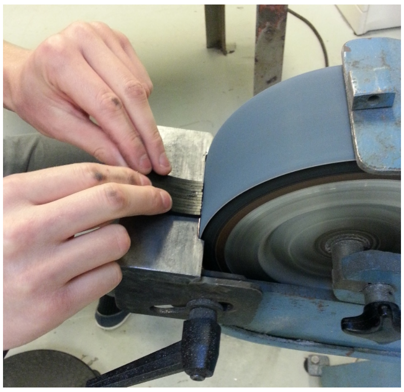

Figure B.20: Glued magnet segments being burnished.

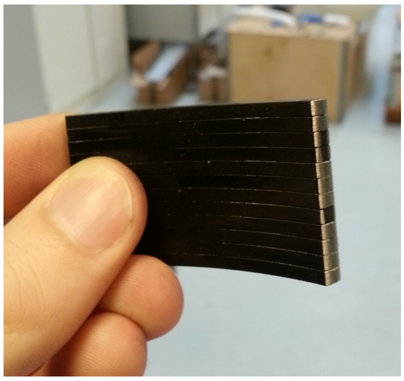

Figure B.21: The glued magnet segments after the burnishing.

Magnetisation

The magnet segments are magnetised at Sintex. To evaluate the magnetisation, the PMs are all measured with a *Gauss-meter*. This is done by aligning two edges and fixing the Gauss-meter probe as shown in figure B.22. The PMs are aligned along the edges and the Gauss-meter is read off. Three PMs are discarded due to deviation from the strength of the remaining PMs.

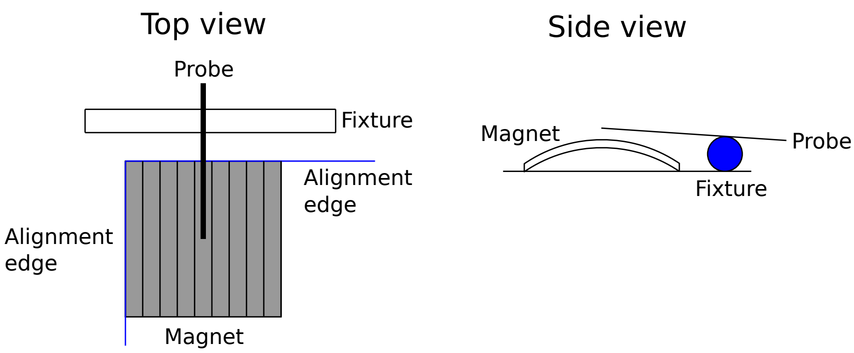

Figure B.22: Set up for gauss measurement.

B.6 Resin casting

During the assembling of the casting mould, it is discovered that the mould does not fit both around the stator teeth and between the mould parts. This results in a gap as shown in figure B.23. It is attempted to fix the gap, which partly succeeded. Two of the bolts are not tightened as it results in an increased gap. After one hour, resin starts to run out of the holes for the two bolts, why it is necessary to tighten the bolts and thereby increasing the gap in the mould. To seal the casting mould, silicone is applied to all potential leakage areas as shown in figure B.24. The silicone is able to seal the mould.

The rotor and stator are filled with resin in the oven while the rotor rotates. Too much resin was filled in the rotor, why it was removed while it rotated. To ensure the resin is distributed evenly, the DC motor is supplied with 40 V for one hour, after which it is supplied with 35.5 V for the remaining time. This is above the rated voltage of 24 V but the current is beneath 0.4 A why the risk by an increased voltage is primarily an increased wear of the commutator. The temperatures during the casting are:

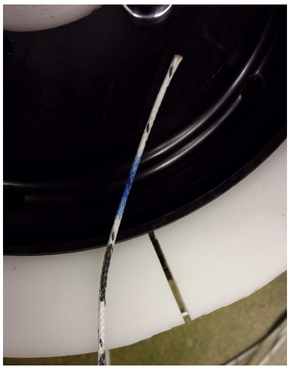

Figure B.23: Gap in casting mould.

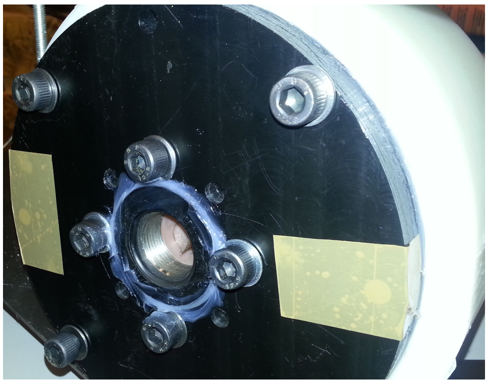

Figure B.24: Silicone sealing the casting mould.

- Around 30 $°C$: two hours, due to the opening and closing of the door to refill the stator and to check the rotor.
- $50°C$: 21 hours
- $60°C$: 2 hours
- $70°C$: 18 hours
- $100°C$: 1 hour
- $115°C$: 5 hours

The rotor is removed after 3 hours at $150°C$ to avoid overheating of the DC motor and demagnetization of the permanent magnets. The voltage is reduced to 27 V as the temperature exceed 80 $°C$.

The cast rotor is shown in figure B.25. The laminations are seen through the resin layer.

Figure B.25: The cast rotor with the excess resin on the rotor laminations.

The resin layer on the laminations is removed in a turning lathe set to 129 mm as the inner diameter of the laminations is 129.6 mm. The result is shown in figure B.26 and B.27. It is seen that some of the laminations have been touched by the cutting tool and this might be due to an offset during the mounting, as it is only a few areas on one side of the rotor. Other than the excess resin, the centrifugal casting shows good results as the resin is concentric with the air gap between the rotor and stator.

The result from the casting of the stator is seen in figure B.28 and B.29. The poor fit of the mould resulted in a large amount of resin on the end of the stator teeth. Figure B.30 shows resin on the shaft, where the bearing is to be mounted. This resin is removed by hand.

The viscosity of the resin resulted in gaps between the laminations and end plates as shown in figure B.31. The resin on the stator laminations is removed by manual machining and the result is shown in figure B.32.

Figure B.26: Rotor after removal of the excess resin.

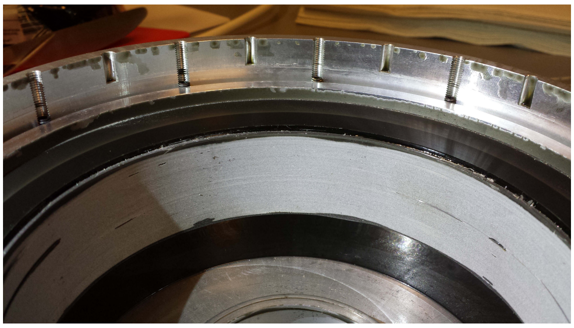

Figure B.27: Rotor after removal of the excess resin.

Figure B.28: One side of the stator with only a small amount of excess resin on the stator teeth. The mould is still attached to the top.

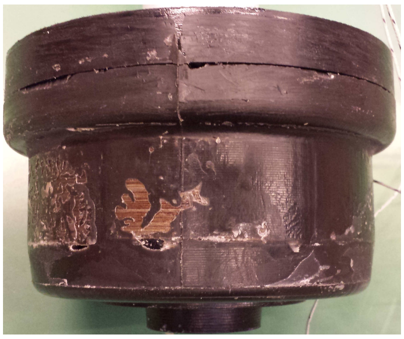

Figure B.29: The other side of the stator with a large amount of excess resin.

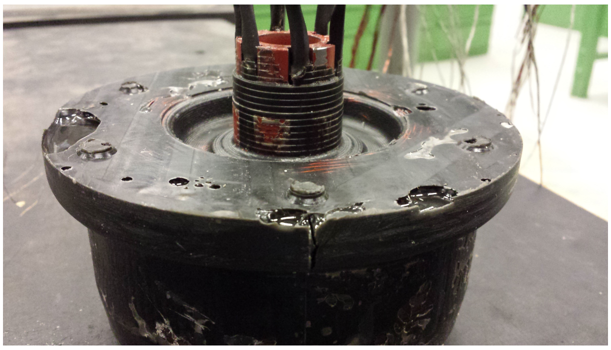

Figure B.30: Resin on the bearing surface.

Figure B.31: Hole between the laminations and the end plate.

Figure B.32: The stator after the machining.

B.7 Vacuum resin casting

Pictures from the resin casting of stator-v2 in the vacuum oven are shown in this section. Figure B.33 shows the gas bubbles from degassing the resin after the resin is mixed. The degassing is performed in a vacuum chamber. Figure B.34 shows how the degassed and preheated ($55°C$) resin is filled into the mould, which is placed in the vacuum oven shown in figure B.35. An extra trench is build around the mould to be able to fill more resin in the stator before the vacuum is applied. Figure B.36 shows the degassing process in the oven when vacuum is applied. When vacuum is released, the bubbles collapse as shown in figure B.37.

Figure B.33: Degassing of the resin after it is mixed.

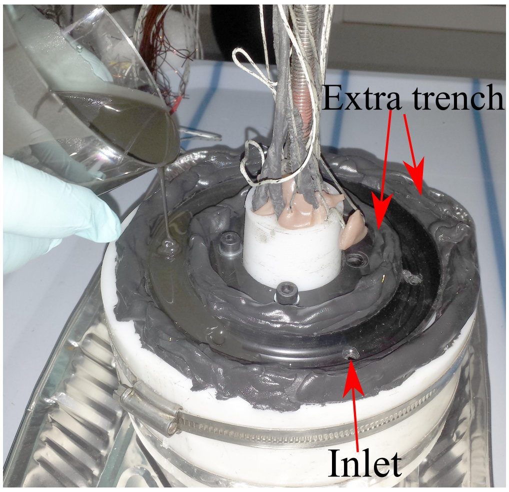

Figure B.34: The resin is filled into the stator mould.

Figure B.35: Vacuum oven used for resin casting.

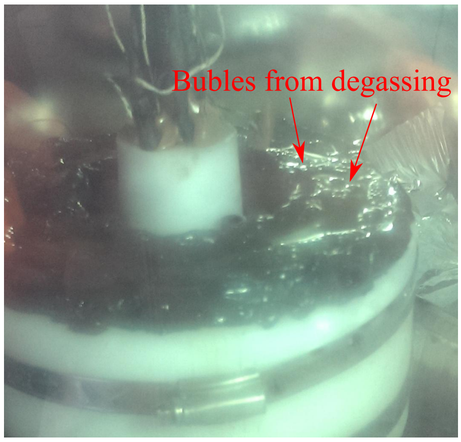

Figure B.36: Bubles from degassing in the oven.

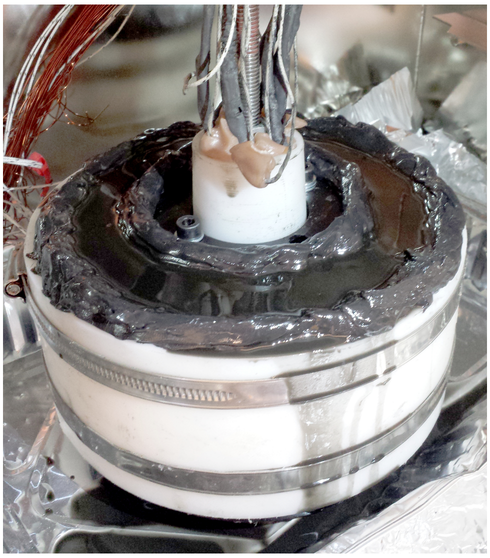

Figure B.37: Stator mould and resin during the casting process when vacuum is released.

APPENDIX

C

UNBALANCED SYSTEM

An unbalanced electrical system might cause oscillations. A three phase unbalanced system can be split into of three balanced systems with three positive sequence components, three negative sequence components and three zero-sequence components [52]. This can be described by phasors that represent voltage, current or impedance:

$$I_a = I_{a0} + I_{a+} + I_{a-} \tag{C.1}$$

$$I_b = I_{b0} + I_{b+} + I_{b-} \tag{C.2}$$

$$I_c = I_{c0} + I_{c+} + I_{c-} \tag{C.3}$$

- The positive-sequence components are balanced, equal in magnitude, displaced by $120°C$ and phase sequence is a,b,c.
- The negative-sequence components are balanced, equal in magnitude, displaced by $120°C$ and phase sequence is a,c,b.
- The zero-sequence components are equal in magnitude and not displaced from each other.

In a balanced system, the negative-sequence-components and zero-sequence-components equal to zero. If the resistance in one phase is increased e.g. due to the broken conductors, the current in this phase is decreased and the system becomes unbalanced. A phasor diagram of a unbalanced current phasors is shown in figure C.1, where the amplitude of I_a is reduced.

The phase sequence of the negative-sequence components results in currents that rotates the opposite direction of the unbalanced system and the positive-sequence components, which generates positive torque. The opposing torque generated by the negative-sequence components results in a decreased resulting torque and possibilities for large torque pulsations [52].

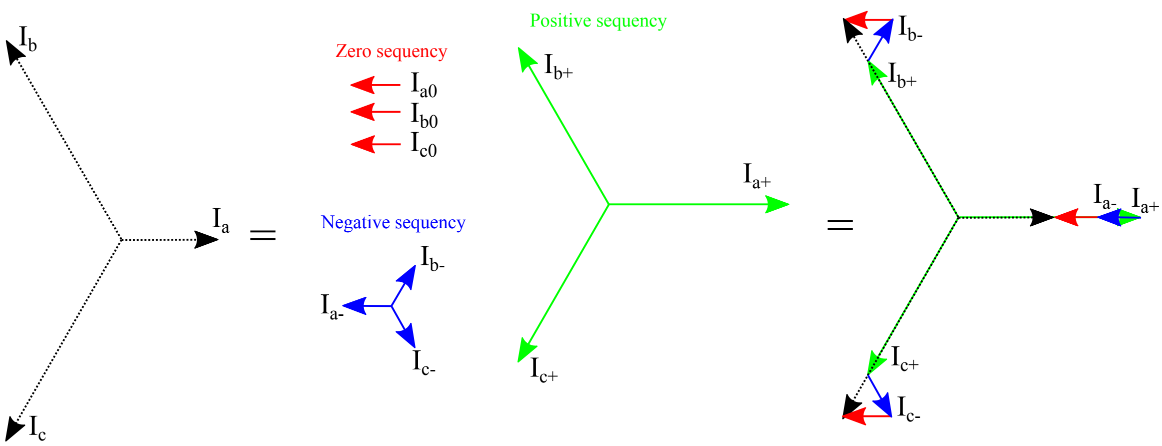

Figure C.1: Phasor diagram of an unbalanced three phase system.

APPENDIX

D
THERMAL MODEL

This appendix supports the thermal model.

D.1 FEM model of compensation approach tests

In this appendix the FEM models of the compensation tests are described.

D.1.1 Test of compensation approaches with 1-D heat flow

In table D.1 the parameters used for the test is stated and in figure D.1 the FEM model is shown. Figure D.2 shows the contour plot from the FEM model.

Parameters	**Thickness**	**Height**	**Length**	$\mathbf{k_{th}}$	**q**
Values	10 mm	60 mm	100 mm	40 $\frac{W}{m\ K}$	1 $\frac{MW}{m^3}$

Table D.1: Parameters for FEM model.

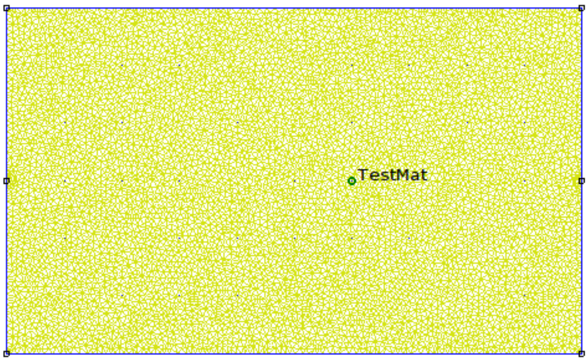

Figure D.1: FEM model of test scenario.

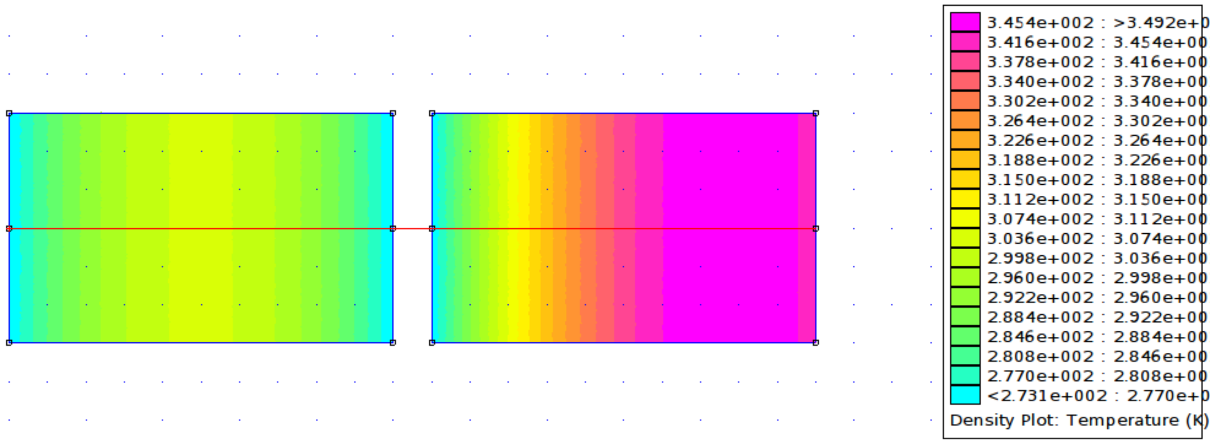

Figure D.2: Results from the FEM model in test scenario 1 and 2.

D.1.2 Test of compensation approaches with 2-D heat flow

In table D.2 the parameters used for the test is stated and in figure D.3 the FEM model is shown. Figure D.4 shows the contour plot from the FEM model in test 3 and figure D.5 shows the contour plot from the FEM model in test 4.

Parameters	Thickness	Height	Length	$k_{th,x}$	$k_{th,y}$
Values	6 mm	100 mm	100 mm	40 $\frac{W}{m\ K}$	20 $\frac{W}{m\ K}$

Table D.2: Parameters for FEM model.

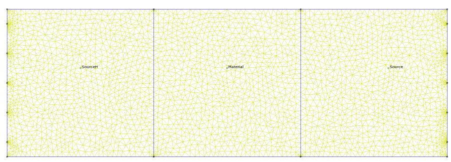

Figure D.3: FEM model of test scenario.

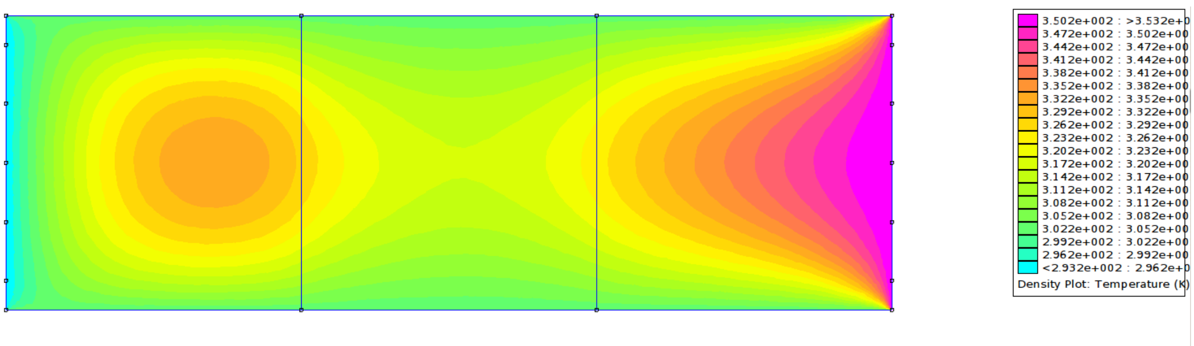

Figure D.4: Results from the FEM model in test scenario 3.

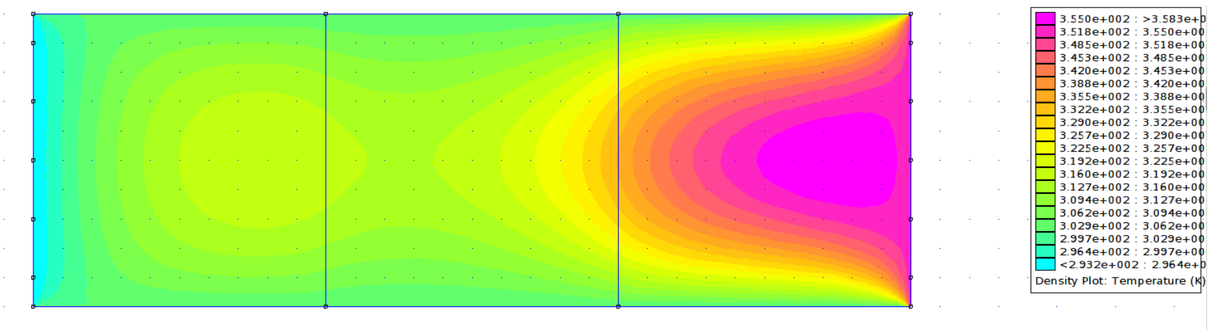

Figure D.5: Results from the FEM model in test scenario 4.

D.1.3 Test of compensation approaches in an element where several heat sources are located next to each other

In table D.3 the parameters used for the test is stated and in figure D.6 the FEM model is shown. Figure D.7 shows the contour plot from the FEM model.

Parameters	Thickness	Height	Length	$k_{th,x}$	$k_{th,y}$
Values	6 mm	100 mm	100 mm	40 $\frac{W}{m\ K}$	20 $\frac{W}{m\ K}$

Table D.3: Parameters for FEM model.

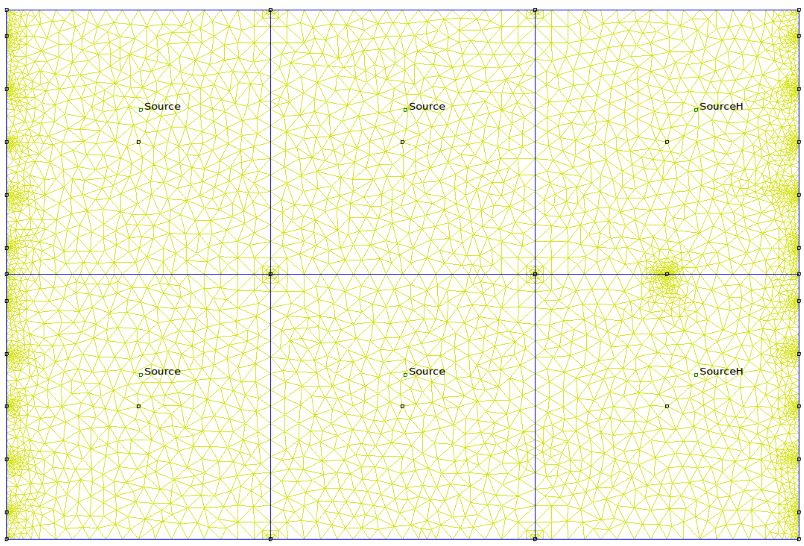

Figure D.6: FEM model of test scenario.

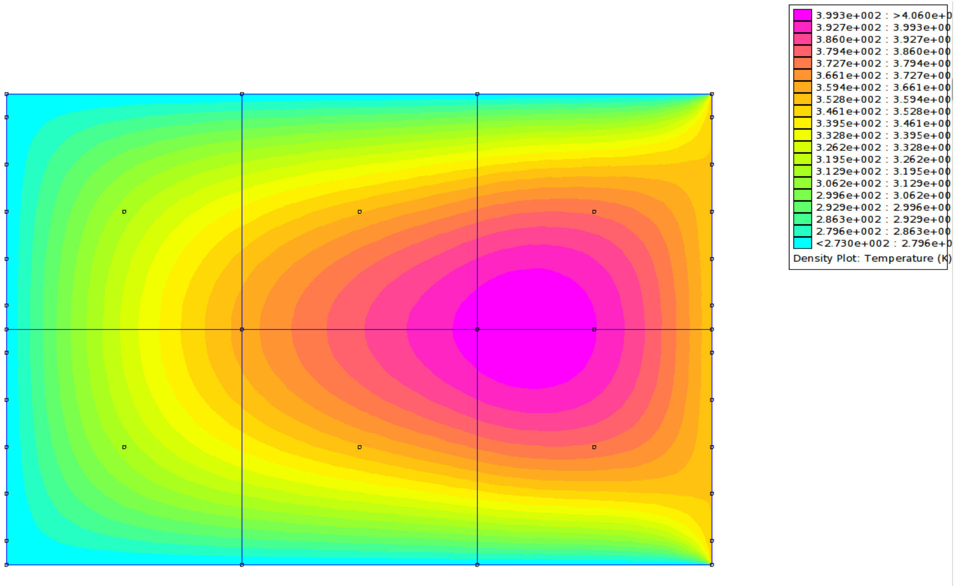

Figure D.7: Results from the FEM model in test scenario.

D.1.4 Additional compensation test

An additional test is stated in this section, which proves that the novel GD compensation approach is able to estimate the temperature when several heat sources are located next to each other. The scenario is set up as shown in figure D.8 where the parameters are the same as test 3 from table 9.5. The results are shown in figure D.9.

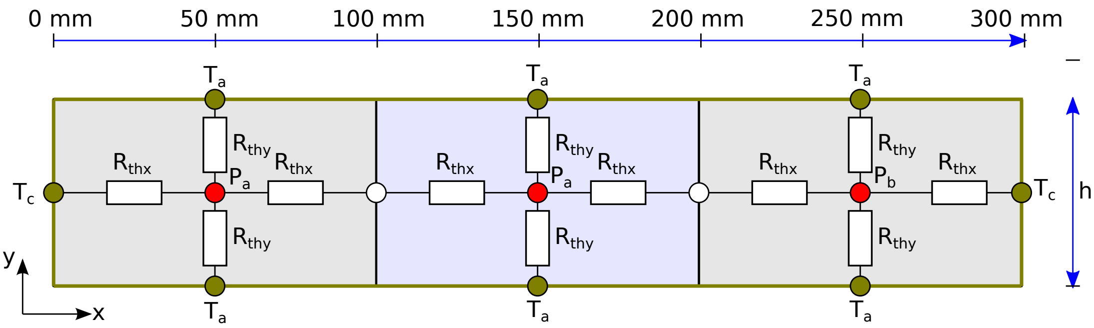

Figure D.8: Test of compensation approaches with several heat sources located next to each other.

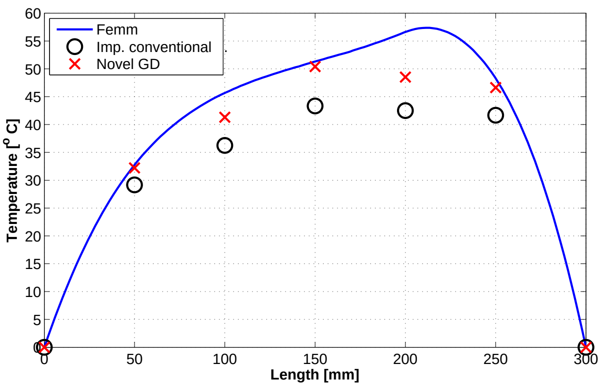

Figure D.9: Temperature estimation from improved conventional, novel GD and Reduced novel GD approaches in test with unevenly distributed heat flow.

D.2 Conduction and contact resistances calculations

In this section the conduction and contact resistances for the PMSM are calculated. As stated in equation (9.3) to (9.5), the conduction resistances are calculated as:

$$R_{th,A}(L,A,k_{th}) = \frac{L}{k_{th}\,A} \tag{D.1}$$

$$R_{th,R}(r_0,r_1,L,\theta,k_{th}) = \frac{ln(r_0/r_1)}{\theta\,k_{th}\,L} \tag{D.2}$$

$$R_{th,C}(r_0,r_1,L,\theta,k_{th}) = \frac{\theta}{2\,k_{th}\,L}\frac{r_1+r_0}{r_0-r_1} \tag{D.3}$$

Lengths are stated in $[m]$, angles in $[rad]$, conductivities in $[W/(m\,K)]$ and areas in $[m^2]$.

D.2.1 Stator resistances

In this section the resistances for the stator and the windings are calculated, as stated in table D.4, where the equation (D.1) to (D.3) are used. The resistances in table D.4 are used to calculate the resistances in table 9.11.

Thermal resistance		Equation (quantities)	Value $[K/W]$
$R_{syoke,A}$	=	$R_{th,A}$ (15e-3, 204e-6, 1.5)	49
$\frac{1}{2}R_{syoke,R}$	=	$R_{th,R}$ (20.5e-3, 35.1e-3, 15e-3, 0.209, 30)/2	2.9
$\frac{1}{2}R_{syoke1,R}$	=	$R_{th,R}$ (20.5e-3, 35.1e-3, 15e-3, 0.21, 30)/2	2.8
$\frac{1}{2}R_{syoke1,C}$	=	$R_{th,C}$ (20.5e-3, 35.1e-3, 15e-3, 0.21, 30)/2	0.4
$R_{syoke2,C}$	=	$R_{th,C}$ (20.5e-3, 35.1e-3, 15e-3, 0.31, 30)	1.3
$R_{stator1,A}$	=	$R_{th,A}$ (15e-3, 2.21e-04, 1.5)	45
$\frac{1}{2}R_{stator1,R}$	=	$R_{th,R}$ (20.5e-3, 1.61e-04, 30)/2	2.1
$R_{stator1,C}$	=	$R_{th,C}$ (10.8e-3, 308e-6, 30)	1.2
$R_{stator2,A}$	=	$R_{th,A}$ (15e-3, 218e-6, 1.5)	46
$\frac{1}{2}R_{stator2,R}$	=	$R_{th,R}$ (54.1e-3, 63.8e-3, 15e-3, 0.2, 30)/2	0.9
$R_{stator2,C}$	=	$R_{th,C}$ (54.1e-3, 63.8e-3, 15e-3, 0.20, 30)	2.7
$\frac{1}{2}R_{stator3,R}$	=	$R_{th,R}$ (54.1e-3, 63.8e-3, 15e-3, 0.21, 30)/2	0.9
$\frac{1}{2}R_{stator3,C}$	=	$R_{th,C}$ (54.1e-3, 63.8e-3, 15e-3, 0.21, 30)/2	1.4
R_{wind}	=	$R_{th,A}$ (39.4e-3 , 1.2768e-04, 401)	0.8
R_{ep}	=	$R_{th,A}$ (1e-3 , 717e-6, 0.37)	3.8

Table D.4: Thermal resistances of the stator and windings.

D.2.2 Shaft and bearings resistances

In this section the resistances for the shaft and bearings are calculated, as stated in table D.5, where the equation (D.1) to (D.3) are used. The resistances in table D.5 are used to calculate the resistances in table 9.12.

Thermal resistance		Equation (quantities)	Value $[K/W]$
$\frac{1}{2}R_{shaft1,A}$	=	$R_{th,A}$(0.015, 5e-5, 25)/2	6
$\frac{1}{2}R_{shaft1,R}$	=	$R_{th,R}$(0.01077, 0.0175, 0.015, π/6, 25)/2	1.2
$\frac{1}{2}R_{shaft2,A}$	=	$R_{th,A}$(0.0259, 6e-5, 25)/2	8.6
$\frac{1}{2}R_{shaft2,R}$	=	$R_{th,R}$(0.010, 0.0175, 0.0259, π/6, 25)/2	0.8

Table D.5: Thermal resistances of the shaft and bearings.

D.2.3 Rotor resistances

In this section the resistances for the rotor are calculated, as stated in table D.6, where equation (D.1) to (D.3) are used. In figure D.10 the resistances from table 9.13 are shown. The resistances in table D.6 are used to calculate the resistances in table 9.13. The thermal resistances of the aluminium rotor housing could easily have been disregarded due to their size.

Thermal resistance		Equation (quantities)	Value $[K/W]$
$\frac{1}{2}R_{rotor1,R}$	=	$R_{th,R}$(0.031, 0.036, 0.015, π/6, 237)/2	0.04
$\frac{1}{2}R_{rotor2,R}$	=	$R_{th,R}$(0.0364, 0.0645, 0.005, π/6, 237)/2	0.5
$\frac{1}{2}R_{rotor3,A}$	=	$R_{th,A}$(0.005, 5.61e-04, 237)/2	0.02
$\frac{1}{2}R_{rotor3,R}$	=	$R_{th,R}$(0.0645, 0.08, 0.005, π/6, 237)/2	0.2
$\frac{1}{2}R_{ryoke1,R}$	=	$R_{th,R}$(0.08, 0.0925, 0.005, π/6, 237)/2	0.1
$\frac{1}{2}R_{ryoke1,A}$	=	$R_{th,A}$(0.005, 0.00056, 237)/2	0.02
$\frac{1}{2}R_{ryoke2,A}$	=	$R_{th,A}$(0.019, 0.00056, 237)/2	0.07
$\frac{1}{2}R_{ryoke2,R}$	=	$R_{th,R}$(0.08, 0.0925, 0.01937, π/6, 237)/2	0.03
$\frac{1}{2}R_{ryoke3,A}$	=	$R_{th,A}$(0.005, 5.608e-04, 237)/2	0.02
$\frac{1}{2}R_{ryoke3,R}$	=	$R_{th,R}$(0.065, 0.08, 0.005, π/6, 237)/2	0.2
$\frac{1}{2}R_{resin,A}$	=	$R_{th,A}$(0.0194, 5.61e-04, 0.61)/2	28
$\frac{1}{2}R_{resin,R}$	=	$R_{th,R}$(0.065, 0.08, 0.01937, π/6, 0.61)/2	17
$R_{lam,A}$	=	$R_{th,A}$(0.015, 710e-6, 2)	11
$\frac{1}{2}R_{lam,R}$	=	$R_{th,R}$(0.0703, 0.0875, 0.015, π/6, 40)/2	0.4
$R_{PM,A}$	=	$R_{th,A}$(0.015, 0.00013, 7.7)	15
$\frac{1}{2}R_{PM,R}$	=	$R_{th,R}$(0.0664, 0.0702, 0.015, π/6, 7.7)/2	0.5

Table D.6: Thermal resistances of the rotor. The resistances of the rotor housing are negligible small.

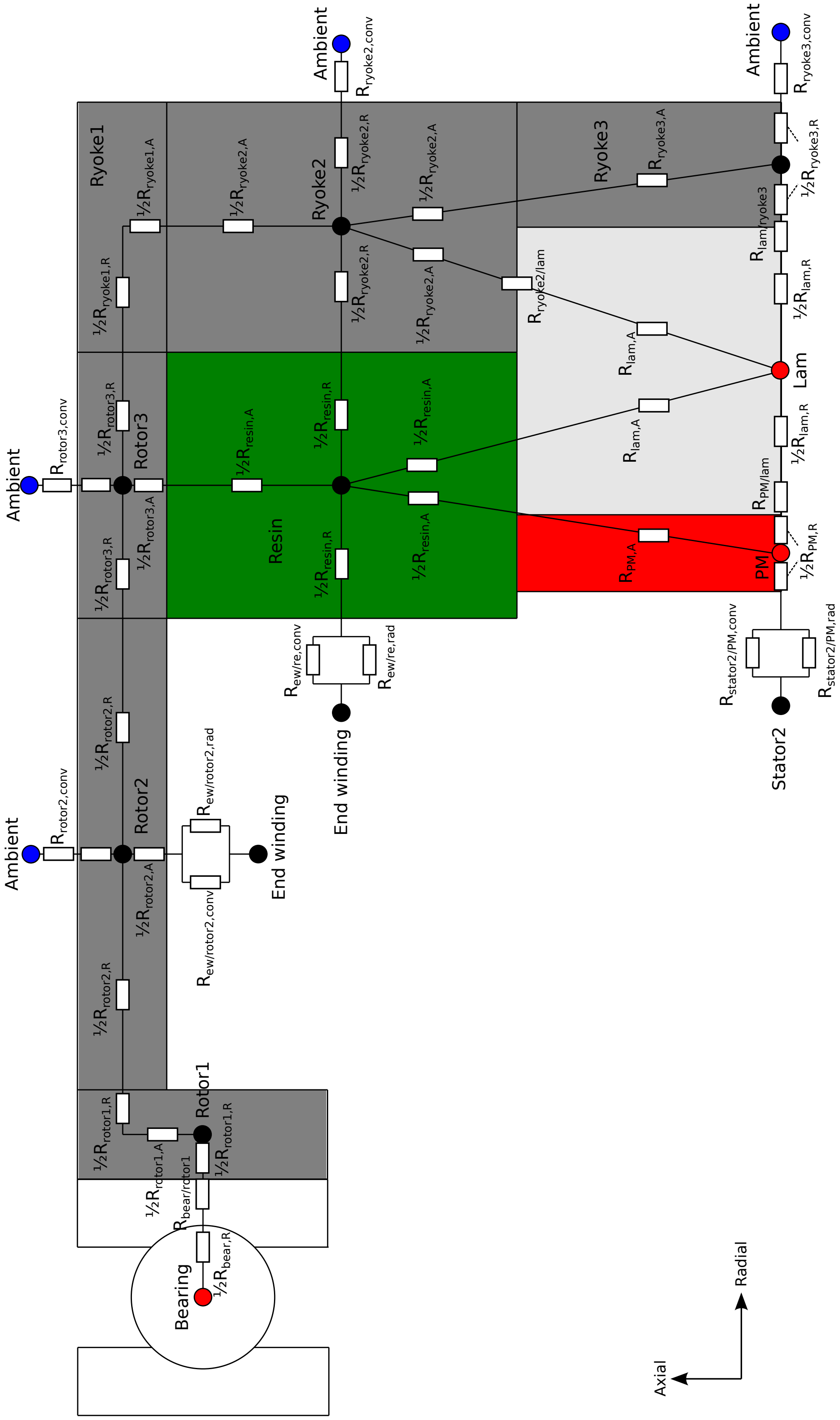

Figure D.10: Rotor resistances.

D.3 Available properties in FEMM

Available properties in FEMM are listed below. The point and boundary properties are assigned throughout the thickness of the planar problem.

- Point properties
  - Specify a temperature [K] or heat generation [W/m] in a point.
- Boundary properties
  - Specify a fixed temperature [K] or a fixed heat flux [W/m^2] on a line or curve.
  - Specify convection or radiation on a line by specifying the ambient temperature and the heat transfer coefficient or the emissivity respectively.
- Material properties
  - Specify a constant or non-linear temperature dependant conductivity of the material in two directions.
  - Specify a volumetric distributed heat generation [W/m^3].
- Conductor properties
  - Specify a total amount of heat flow [W] through a surface.

To assign the boundary conditions in a heat flow problem, the boundary conditions are mathematically modelled in FEMM. The heat flux boundary is modelled by equation (D.4), a convection boundary condition is modelled by equation (D.5) and a radiation boundary is modelled as equation (D.6).

$$k_{th} \frac{\partial T}{\partial n} + f = 0 \tag{D.4}$$

$$k_{th} \frac{\partial T}{\partial n} + h(T_a - T_b) = 0 \tag{D.5}$$

$$k_{th} \frac{\partial T}{\partial n} + \varepsilon \, \sigma_{SB}(T_a^4 - T_b^4) = 0 \tag{D.6}$$